Superconducting Multicell Cavities for Linear Colliders

Matthias U. Liepe
aus Berlin

Dissertation
zur Erlangung des Doktorgrades
des Fachbereichs Physik
der Universität Hamburg

Hamburg
im Oktober 2001

Gutachter der Dissertation:	Prof. Dr. P. Schmüser Priv. Doz. Dr. A. Gamp
Gutachter der Disputation:	Prof. Dr. P. Schmüser Dr. D. Proch
Datum der Disputation:	17. Oktober 2001
Dekan des Fachbereichs Physik und Vorsitzender des Promotionsausschusses:	Prof. Dr. F.W. Büßer

Abstract

For the proposed superconducting TESLA linear collider an energy upgrade towards $E_{cm} = 800$ GeV is envisioned. This appears feasible in the future, since electrolytic polishing of niobium cavities is promising accelerating gradients well above 30 MV/m. But reaching 800 GeV center-of-mass energy needs to be supported by the so-called superstructure concept of coupled cavities and a fast resonance frequency control scheme. Building the TESLA main linac with superstructures increases its active acceleration length by about 6 % whereas a fast frequency tuner permits an efficient cavity operation at high gradients above 25 MV/m.
While electrolytic polishing of cavities is discussed elsewhere, this dissertation covers studies performed for the superstructure concept as well as for the fast resonance frequency control during pulsed cavity operation.

Zusammenfassung

Für den vorgeschlagenen supraleitenden TESLA Linearbeschleuniger wird eine Energieerhöhung auf $E_{cm} = 800$ GeV angestrebt. Dieses scheint in Zukunft möglich, da die Elektropolitur von Niobresonatoren Beschleunigungsgradienten über 30 MV/m in Aussicht stellt. Um jedoch eine Schwerpunktsenergie von 800 GeV zu erreichen, ist es zudem notwendig, sogenannte Superstrukturen mit gekoppelten Resonatoren und ein schnelles Reglungssystem für deren Resonanzfrequenz einzusetzen. Die Verwendung von Superstrukturen im TESLA Beschleuniger erhöht dessen aktive Beschleunigungslänge um 6 %. Desweiteren erlaubt der schnelle Frequenzabstimmer einen effizienten Beschleunigerbetrieb bei hohen Feldgradienten jenseits von 25 MV/m.
Während die Elektropolitur von Hohlraumresonatoren anderweitig beschrieben wird, befasst sich die vorliegende Dissertation mit Untersuchungen zu dem Superstrukturkonzept, sowie mit der schnellen Regelung der Resonanzfrequenz im gepulsten Beschleunigerbetrieb.

To my wife

Preface

Working in an international collaboration is always a great experience and I would not like to be without it. Apart from the scientific work the international relationships are the most important thing the collaborations can give.
So for me the hostility towards foreigners in Germany and elsewhere is not only disgusting and unacceptable but incomprehensible.
For being able to learn from each other in the future it is important to cultivate these relationships. Because this learning might be the first step to a worldwide friendship or peace.

Acknowledgements

This dissertation would not exist without the indescribable help from so many people and friends. They always helped me to let my deep pleasure in physics grow.

I would like to express my deep gratitude to my advisor and Doktorvater, Peter Schmüser, whose never ending help, advice, encouragement and believe in me and my work has helped me through all the problems on my way. His interest in me covers not only the interest in my work but helped me through a very difficult private time. Without his words and his sympathy I would not have been able to recover so soon.
For all the help, his rich ideas and his willingness to share his outstanding knowledge with me I would like to extend a huge thank to Jacek Sekutowicz.
I owe sincere thank to Dieter Trines, Alexander Gamp and Martin Leenen for their support of the work of a young scientist.
My cries for help were always answered by Stefan Simrock, who supported me with his ideas, his incredible knowledge and his friendship.
In the same way, I thank the members of the FDET group, past and present. Discussions with all of them have always been of great help. The chats after lunch were always an enrichment in scientific and private ways. A special thank I owe to Markus Hüning and Jan Menzel, who were always willing to take over my shifts.
The piezo-tuner would still not exist without the help, especially in constructing, of Jens Iversen, Wolf-Dietrich Möller and Hans-Bernd Peters.
For their cooperation in running MAFIA calculations and measuring HOMs I would like to thank Huabi Chen, V. Puntus and Huang Wenhui. Without them I would still sit in front of the copper cavities, trying to finish the HOM measurements on superstructures.
Similarly I thank Nikolai Ignachine, Nicolas Nährig and Yuri Tchernousko for building the drive-electronics for the piezo-tuner.
For the cooling of uncountable cavities and the cooperation with the piezo-tuner I express my thank to the members of the Cryogenic group.
A special thank I extend to Ingrid Nikodem, who not only helped in all official questions but helped with words and the willingness to listen. Without her the FDET group would not be the same and we would be lost in a huge chaos.
I also thank all other involved DESY groups for their help and for providing a stimulating and friendly work environment.
Hasan Padamsee and Jens Knobloch from the Cornell University enabled me to enjoy a great and wonderful time during a research stay at the Newman Laboratory. I would like to thank them not only for their help, advice and encouragement but also for their friendship.

In a more personal way I would like to thank my family. Especially my parents enabled me to find my own way and they always supported me with all their believe, their strength and their love. They gave me wings to fly and always a wonderful home to come back to.
Finally, a deep thank and a huge hug to my best friend and wife Lexa for all her love and her everlasting believe in me. She always stays with me in the good days and in the bad days. Her willingness to cook late dinner meals and sometimes stay the weekend with me at DESY helped me in finishing this dissertation. There are a lot of things I am not able to mention, but I thank her for all of them.

Contents

Part II Superstructures: The Concept of Coupled Cavities

CHAPTER 1

1 Introduction

1.1 Motivation

Past and present particle accelerators have been of fundamental importance in changing our picture of nature at the level of its smallest constituents. Presently the so-called Standard-Model is accepted as the basis of our understanding of particle physics. Accelerators have provided the experimental evidence that vindicates the Standard Model. Nevertheless, some predictions of this model remain to be proven and questions beyond this model arise. It is hoped that future particle accelerators will provide the tool to answer some of these questions.
Currently under construction is the Large Hadron Collider (LHC) at CERN, a proton-proton storage ring with 14 TeV center-of-mass energy[1]. There is a broad agreement in the high energy physics community that a linear e^-e^+ collider with a center-of-mass energy well beyond the reach of the LEP storage ring ($E_{cm} \approx 200$ GeV) and a high luminosity above 10^{33} cm^{-2}s^{-1} should be built next, since this machine is roughly complementary to the LHC. The precise measurements at LEP have demonstrated the need of e^-e^+ machines.
Worldwide several groups are working on different linear collider designs. The TESLA-Collaboration[2] is proposing to use 1.3 GHz *superconducting standing-wave accelerating structures* made from niobium [TDR 01]. In the baseline layout of the TESLA collider 9-cell cavities (see figure 1.1) accelerate the particle beams of electrons and positrons to energies of 250 GeV. The design gradient at $E_{cm} = 500$ GeV

[1] Note that the collision energy is shared among the constituents (quarks) of the protons.
[2] TESLA stands for TeV Energy Superconducting Linear Accelerator.

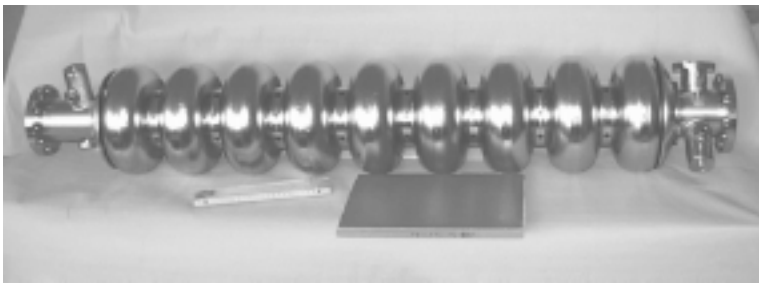

Figure 1.1: Picture of a TESLA-type 9-cell niobium cavity. Parameters are listed in table 4.3.

is 23.4 MV/m. The 9-cell cavities are cooled by superfluid helium to T =2 K to achieve a small power dissipation in the cavity walls (which is quantified by the so-called unloaded quality factor Q_0, see section 5.5). For high accelerating gradients above 20 MV/m it is necessary to go to pulsed cavity operation to keep the average cryogenic losses within acceptable limits. Still, long RF pulses of about a millisecond can be produced, which has to be compared to the microsecond pulses in copper accelerating structures. The long RF pulses allow to use a relative large bunch spacing (337 ns at TESLA-500). Therefore a bunch-to-bunch feedback is feasible to correct the beam orbit within a bunch-train. Further advantages of the superconducting technology are a high RF to beam power transfer efficiency and the large aperture of the 1.3 GHz cavities, which allows to accelerate and conserve small emittance beams.

Over the past years the performance of superconducting cavities and the reliability of achieving high accelerating gradients have been improved significantly. By now, the superconducting technology for a 500 GeV linear collider is available. The 9-cell cavities routinely reach accelerating gradients of 25 MV/m (see figure 1.2), which provide sufficient overhead to safely drive the beams in TESLA to 250 GeV.

In the last years it became also obvious, that a cavity surface preparation by chemi-

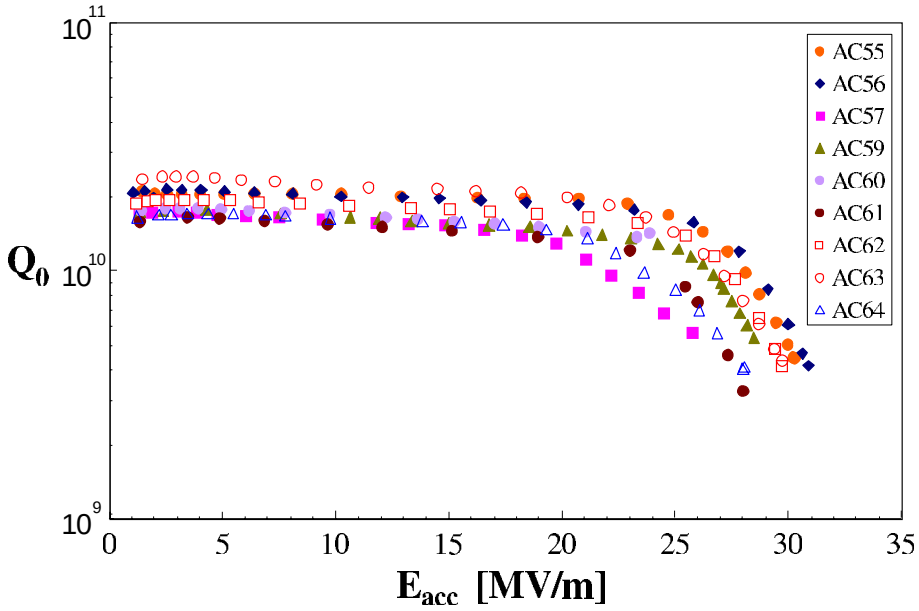

Figure 1.2: Excitation curve of TTF 9-cell cavities of the latest production series. The cavities were cooled by superfluid helium of 2 K [TDR 01]. The surface of the cavities has been prepared by chemical etching.

cal etching is not a suitable method for achieving gradients above 30 MV/m [Lil 01], which is well below the superconductor limit of about 50 MV/m. However, results of single-cell cavities after electrolytic polishing the niobium surface (see figure 1.3) justify the optimism that the accelerating gradient in the 9-cell cavities can be increased beyond 30 MV/m [Lil 01]. Therefore an energy upgrade towards E_{cm} = 800 GeV is envisioned for the TESLA collider [TDR 01]. Electrolytic polishing the cavity

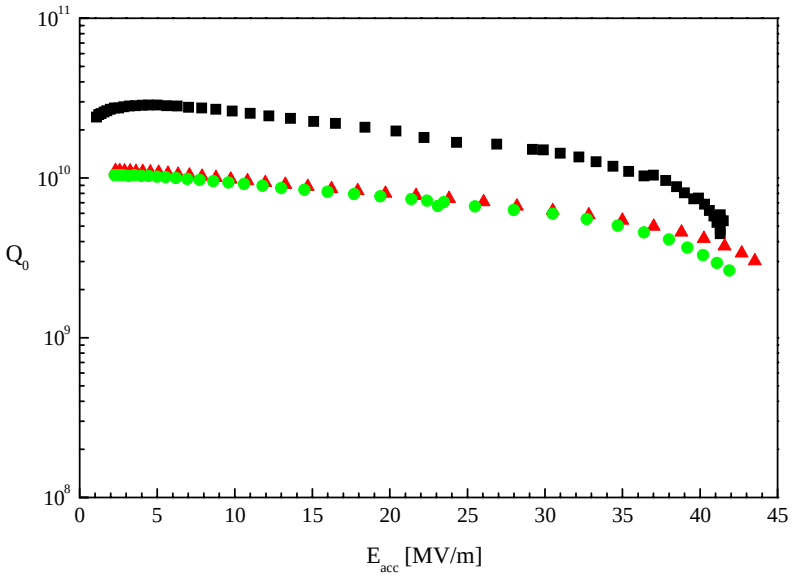

Figure 1.3: Excitation curve of three electropolished 1.3 GHz single-cell cavities [TDR 01]. The tests have been performed in different cyostats and under slightly different helium temperatures.

surface is essential for TESLA-800, but further steps are important to support the high field gradients, since

- The cavities are operated in pulsed mode. The major concern in pulsing cavities are the time-varying Lorentz-forces of the RF field, since they cause mechanical deformations and thereby shift the resonance frequency of the cavities. This so-called Lorentz-force detuning increases as the square of the accelerating gradient and becomes substantial above 25 MV/m, since superconducting cavities are susceptible to small changes in resonance frequency due to their narrow bandwidth. Maintaining the accelerating field constant in a detuned structure requires extra RF power. The stiffening of the TTF[3] 9-cell cavities is not sufficient to permit an efficient cavity operation at the TESLA-800 gradient of 35 MV/m. Therefore the stiffening must be improved, or alternatively, the resonance frequency must be stabilized actively. This frequency control has been studied at the TTF using a fast piezoelectric frequency tuner.

- The achievable high accelerating gradients have to be used effectively, i.e. the active acceleration length for a fixed site length of the linac has to be maximized. In a so-called superstructure several multicell cavities are combined together with reduced inter-cavity spacing [Sek 99]. Building the TESLA linac with superstructures instead of 9-cell cavities increases the active acceleration length by about 6 %. It is believed that the combination of the superstructure

[3]The TESLA Test Facility has been set up at DESY, providing the infrastructure for cavity R&D towards higher gradients [TTF 95].

concept with a surface preparation by electrolytic polishing provides the technology for a 800 GeV linear collider. Moreover the concept of coupled cavities promises a significant cost reduction, since it requires a factor of 2-3 fewer main power couplers in the machine. In order to validate the expected benefits and the operability of a structure with a weak cavity-to-cavity coupling, superstructures have been extensivly studied since 1999.

This dissertation covers the fast resonance frequency control during pulsed cavity operation as well as studies performed for the superstructure concept. Correspondingly the thesis is divided in two parts.

1.2 Organisation of the Dissertation

The first chapter of part I (chapter 2) serves as an introduction to the question of pulsed cavity operation. The Lorentz-force detuning of superconducting cavities and its consequences for the RF power requirements are discussed. In the third chapter the concept of Lorentz-force detuning cancellation is described and initial results with a piezoelectric tuner are shown. Moreover this chapter provides information on the mechanical resonances of a 9-cell cavity.

Chapter 4 at the beginning of part II introduces the superstructure concept. The layout of the prototype structures and of the structures, which have been proposed for the TESLA collider are presented. In chapter 5 a circuit model for coupled multicell cavities is derived. This model provides the basis of the theoretical studies, which are presented in the subsequential chapters.
The remainder of this dissertation covers the different aspects which have been investigated for coupled cavities.
Chapter 6 descibes the amplidude profile measurement in superstructures and the adjustment for a homogeneous profile of the accelerating mode. A special cavity tuning procedure is described, which allows to balance the storred energy of the accelerating mode in the individual cavities of a superstructure during linac operation. In chapter 7 measured and computed transient states of the accelerating mode are discussed and computations of the bunch-to-bunch variation of the energy gain in superstructures are shown. Chapter 8 studies how the TTF field control system can be adapted for the superstuctures. The higer-order mode damping in superstructures is discussed in chapter 9. Measurements on copper versions of the structures are compared with the requirements on damping for the TESLA collider. Presently under construction are two prototype superstructures, which will be installed in the linac at the TESLA-Test-Facility for a beam test beginning of 2002. The main components of the prototyps and the proposed measurement program are presented in chapter 10. Finally, chapter 11 concludes with a summary and an outlook to future studies.

PART I

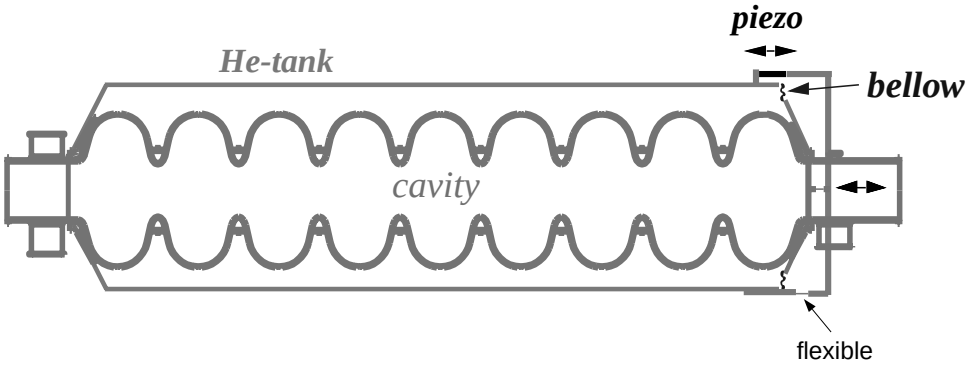

Active Compensation of Lorentz-Force Detuning:

The Piezoelectric Tuner

CHAPTER 2

2 Pulsed Operation and Lorentz-Force Detuning

This chapter serves as an introduction to the question of pulsed operation of superconducting cavities. The pulsed operation requires an advanced RF field control system. The major concern in pulsing cavities are the time dependent Lorentz-forces of the RF field, since they cause time-varying mechanical deformations of the cavity. These deformations result in changes of the accelerating mode frequency within the pulses, i.e. in a detuning of the resonance frequency. For the high gradients at the proposed TESLA collider this Lorentz-force detuning will be in the order of the cavity bandwidth. Amplitude and phase of the accelerating field can be maintained constant in a detuned cavity, but as we will see, this requires additional input power which can be excessive at high gradients.

2.1 Pulsed Operation

The superconducting cavities at the TESLA-Test-Facility linac ([TTF 95]) as well as the cavities at the proposed TESLA collider will be operated at high accelerating gradients above 20 MV/m. However, the cryogenic losses of a superconducting cavity increase with the square of the gradient, for the ideal case of a gradient independent surface resistance. Usually also the surface resistance increases at high gradients. Therefore the superconducting cavities are operated in pulsed mode, to reduce the average cryogenic load. The pulse structure of the accelerating field at the TTF linac and its related parameters are shown in figure 2.1. At the beginning of each pulse the cavity is filled to its nominal accelerating voltage. Subsequentely beam is accelerated at a constant accelerating gradient and phase. The total RF pulse length at the TTF linac is approximately 1300 μs, from which 800 μs are used for beam acceleration (flat-top duration of the pulse). The pulses at the TESLA main linacs will have 950 μs flat-top with beam injection. The repetition rate of the pulses is 5 to 10 Hz.

Amplitude and phase control of the accelerating field is required during the filling to ensure proper beam injection conditions. During beam acceleration the field needs to be maintained constant in amplitude and phase by an RF control system. The pulsed structure of the field and the beam current put demanding requirements on the RF control system.

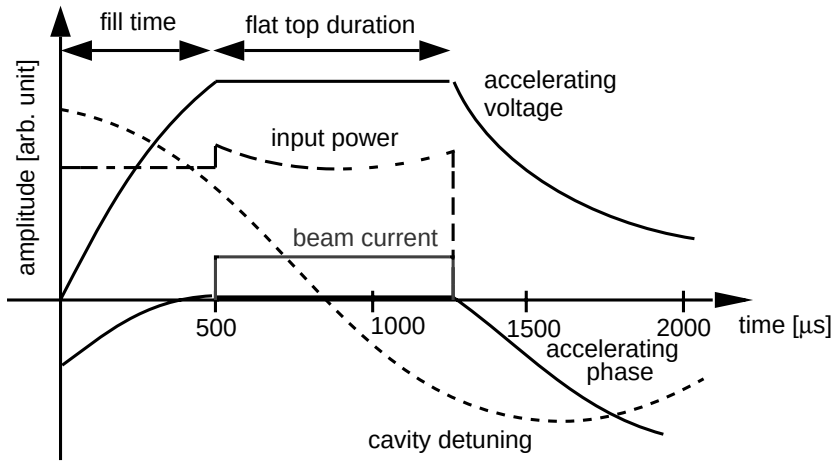

Figure 2.1: Schematic view of various parameters, which are related to the pulsed cavity fields [TDR 01]. At the TESLA-Test-Facility linac the accelerating field is increased during 0.5 ms filling time, followed by 0.8 ms constant gradient with beam acceleration.

There are two major sources of field perturbations in a superconducting cavity:

- beam loading and fluctuation of the beam current
- modulation of the accelerating mode resonance frequency.

Modulation of the cavity resonance frequency is caused by external mechanical vibrations (microphonics), and is induced by the time dependent Lorentz forces of the cavity RF field, see section 2.3 and 2.4. Without control, the resulting amplitude and phase perturbations are in the order of 5% and 20°, respectively [TDR 01]. In order to stay within the energy spread limitations for the TESLA collider ($5 \cdot 10^{-4}$ bunch-to-bunch energy variation [TDR 01]) the RF control system has to suppress these errors by two orders of magnitude. Fortunately, the dominating perturbations (Lorentz force detuning and beam loading) are repetitive from pulse to pulse. Therefore they can be compensated by a feedforward control. This feedforward control is made adaptive to follow slow parameter drifts [Lie 98]. The remaining non-repetitive errors need to be suppressed by feedback control.

2.2 Design of the TTF RF Control System

The digital TTF field control system has been developed for the pulsed operation of superconducting cavities. The overall scheme of this system is shown in figure 2.2. A combination of feedback and feedforward control is stabilizing the sum of the accelerating field vectors of a group of cavities [Schi 98]. By this methode one klystron can drive a group of cavities, which is desirable for cost reasons. Accordingly control of an individual cavity field is not possible, and for relativistic electrons not needed. The real and imaginary part of the field vector-sum in a complex

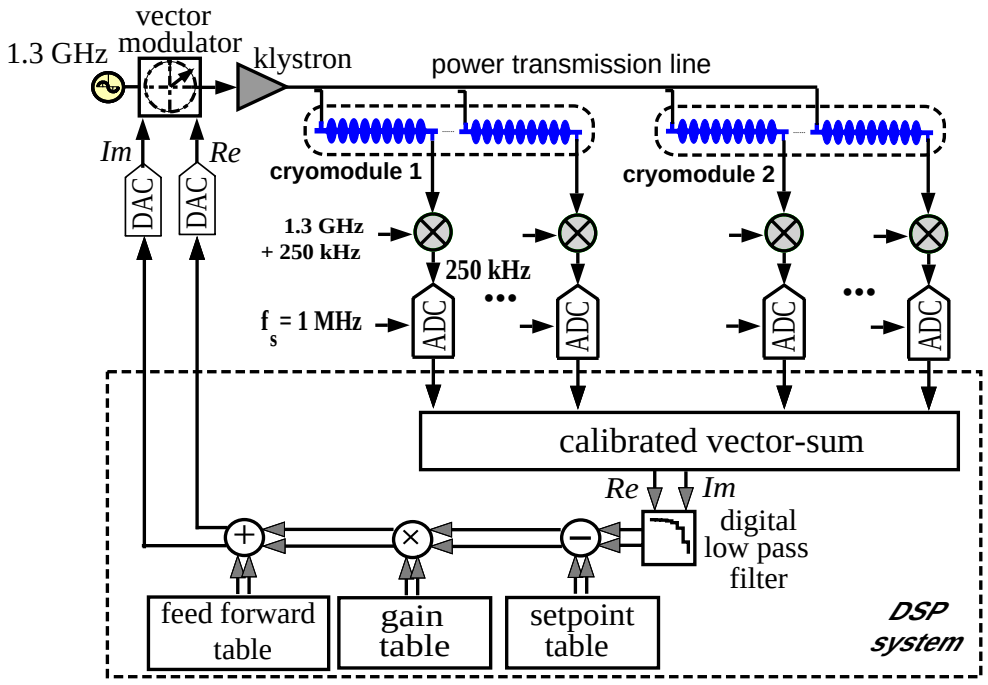

Figure 2.2: Schematic of the digital TTF RF control system [TDR 01].

representation are regulated by modulation of the incident RF wave. The control procedure consists of the following steps (see figure 2.2):

- The 1.3 GHz RF field in the cavities is measured via pick-up antennas close to end-cells.
- The 1.3 GHz RF cavity probe signals are converted to an intermediate frequency (IF) of 250 kHz. The IF signals still have the full amplitude and phase information of the antenna signals (see [Schi 98]).
- The IF signals are sampled with a rate of 1 MHz. Accordingly two subsequential sampled voltages are 90° spaced and describe the real and the imaginary part of the cavity field vector in a complex representation.
- The individual cavity field vectors are multiplied by 2×2 matrices to correct for different gains and cable delays.
- The vector-sum of the fields is calculated and filtered by a digital low-pass filter.
- A proportional feedback control is realized by substracting the measured vector-sum from a setpoint of the vector-sum. The difference is multiplied by a gain factor and gives the new actuator setting of the feedback control. The setpoint and gain values are listed in tables for every microsecond of the RF pulse.
- Feedforward contol is added to the feedback actuator setting. The feedforward table is adaptively updated to follow slowly drifting parameters.

- The digital actuator setting is converted to analog signals for the control of the real and imaginary part of the field vector sum. The analog control signals are held constant for 1 μs until they are updated.

- The analog control signals adjust the driving signal of the klystron via a vector-modulator.

Refer to [Schi 98] for details.
Presently the total time delay of the control loop is about 5 μs. Stability analysis shows, that the maximum feedback gain is limited to about 80 [Schi 98]. Initial measurements at the TTF linac with a 800 μs bunch train indicate, that the combination of feedback and feedforward control stabilises the accelerating field sufficiently with respect to the TESLA requirements ($6 \cdot 10^{-4}$ total rms energy spread at linac exit) [TDR 01]. It is important to note, that the demonstrated high degree of field stability is mainly due to the low level of fast fluctuations, like microphonics.

2.3 Microphonics

Usually superconducting cavities are operated with high loaded quality factors. The optimal loaded quality factor (see section 5.8) for the TESLA-500 parameters is approximately $2.5 \cdot 10^6$. This results in a bandwidth of the accelerating mode of $f_{1/2} = 260$ Hz (half width at half maximum). Compared to the mode eigenfrequency of 1.3 GHz this indicates the high sensitivity of superconducting cavities to mechanical deformations: If the cavity is lengthened by 1 μm, its resonance frequency increases by approximately 315 Hz [TDR 01], i.e. more than one bandwidth. Moreover superconducting cavities have a thin wall thickness (a few mm). This makes them susceptible to mechanical disturbances.
External mechanical vibrations can be transferred to the cavities via the supporting system of the cryostat, the beam pipes and the helium. The excited vibration of the cavity modulates the resonance frequency of the cavity (so-called microphonics). This results in an amplitude and phase jitter of the accelerating field, which has to be suppressed by the RF feedback control. The microphonics level at the TTF linac has been measured to be below 10 Hz (rms) [Schi 98], which is small for a superconducting cavity system.
In order to investigate the spectrum of the microphonics, a TESLA 9-cell cavity has been operated in continuous-wave-mode (cw-mode) in a test-cryostat. The modulation of the accelerating mode frequency has been measured via a phase-locked-loop. Figure 2.3 (a) shows the variation of the detuning versus time. The frequency has a Gaussian distribution, as can be seen in figure 2.3 (b). The spectrum of the microphonics is shown in figure 2.4. It is found that the fluctuations are dominated by a few frequencies, which are vibration frequencies of the vacuum pumps and the helium compressors as well as resonance frequencies of mechanical cavity modes. A mechanical resonance at 287 Hz shows the strongest excitation. The frequencies of the excited mechanical vibrations are well below 1 kHz. Accordingly in pulsed cavity operation (1.3 ms pulse length) microphonics mainly modulate the electrical resonance frequency from pulse to pulse, but not within the pulses.

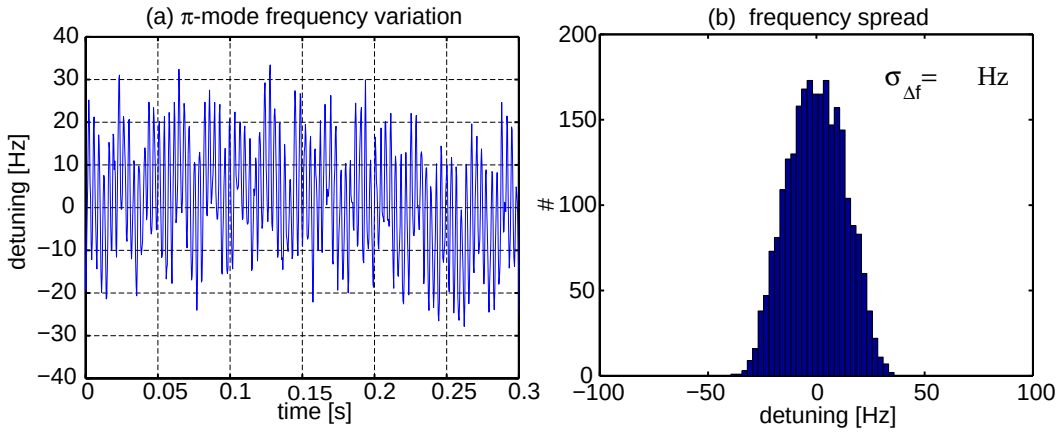

Figure 2.3: Variation of the π-mode frequency in a TESLA 9-cell cavity, which is operated in cw-mode in a test-cryostat. (a) Variation due to microphonics as function of time. (b) Resonance frequency spread.

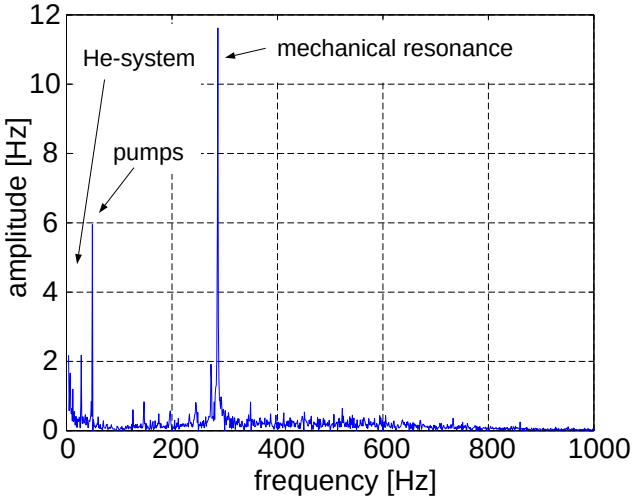

Figure 2.4: Spectrum of the frequency variation due to microphonics, which is shown in figure 2.3.

It is important to note, that the amplitudes of the cavity vibrations depend on the sources which are exciting the cavity vibrations. It can be expected, that also the spectrum of the microphonics in the TTF linac shows a few dominant frequencies. To study the amplitudes of excitation and possible correlations from cavity to cavity, cw-operation of the cavities at the TTF linac is desirable.

2.4 Lorentz-Force Detuning

The electromagnetic fields in a cavity exert Lorentz-forces on the cavity walls. The force per unit area (i.e. the pressure) is given by [Jack 75]

$$P_R = \frac{1}{4}\left(\mu_0 |\vec{H}|^2 - \varepsilon_0 |\vec{E}|^2\right) \quad , \tag{2.1}$$

where $\vec{H}$ and $\vec{E}$ denote the magnetic and electric field on the walls. The Lorentz-forces near to the irises try to contract the cells, while the forces around the equators try to increase the radius of the cells. The resulting deformation of the cavity shape shifts the resonance frequency of the accelerating mode from its design value. According to [Sla 50] the resonance frequency is shifted by

$$\frac{\Delta f_L^{(acc)}}{f^{(acc)}} \approx \frac{1}{2U} \int_{\Delta V} \left(\frac{\mu_0}{2} \left| \vec{H}_0 \right|^2 - \frac{\varepsilon_0}{2} \left| \vec{E}_0 \right|^2 \right) dv \quad , \tag{2.2}$$

where ΔV is the small change in the cavity volume, U is the stored energy and $\vec{E}_0$ and $\vec{H}_0$ are the unperturbated fields of the accelerating mode. The electromagnetic pressure is small (below 1 N/cm^2), but nevertheless important, since superconcucting cavities are very sensitive to tiny mechanical deformations. Assuming that the cavity volume changes linearly with the electromagnetic pressure and that the change in volume is small, the steady-state Lorentz-force frequency shift Δf_L at constant accelerating gradient E_{acc} is proportional to the square of the gradient

$$\Delta f_{L,stat}^{(acc)} = -K_L \cdot E_{acc}^2 \quad . \tag{2.3}$$

The quantity K_L is the so-called Lorentz-force detuning constant. This relation has been verified by measurements on several cavities. The Lorentz-force detuning constant depends on the stiffness of the cavity and on the stiffness of the frequency tuning mechanism. The TESLA cavities have been designed for a steady-state detuning constant $K_L = 1$ Hz/(MV/m)^2 [CDR 97]. This has been acieved by welding stiffening rings between adjacent cells, see figure 2.5. The stiffening rings compensate part of the electromagnetic forces near to the irises, which try to contract the cells. Measurements on two TESLA 9-cell cavities have confirmed, that the steady-state Lorentz-force detuning constant is close to the design value of $K_L = 1$ Hz/(MV/m)^2 [Schi 98].
However, the cavities at the TESLA-Test-Facility linac and at the proposed TESLA collider are operated in pulsed mode, i.e. with time-dependent gradients. On account of the resulting time-dependent Lorentz-forces and the inertia of the cavity

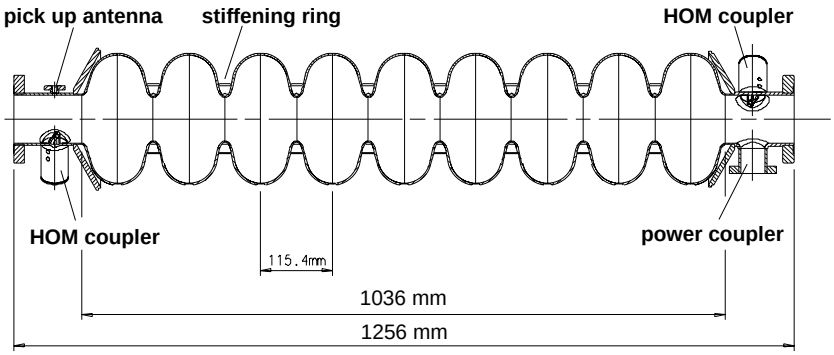

Figure 2.5: Side view of the TESLA 9-cell cavity with main power coupler flange, two higher-order-mode couplers and stiffening rings [TDR 01].

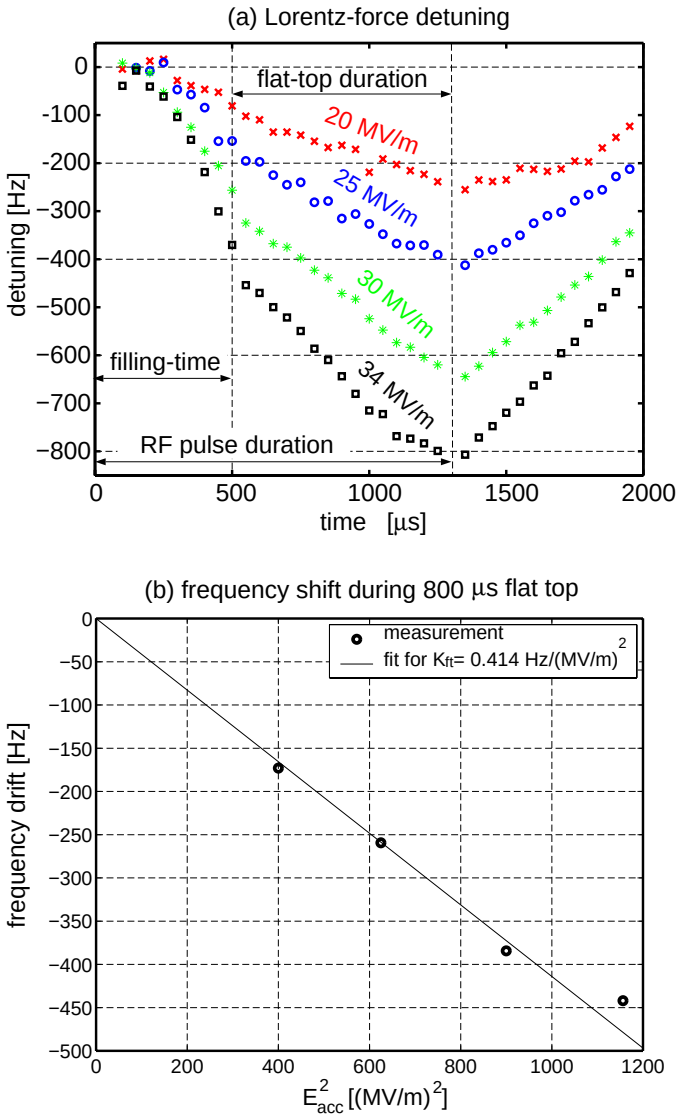

Figure 2.6: Measured Lorentz-force detuning during pulsed operation of a TESLA 9-cell cavity with different flat-top accelerating gradients (20, 25, 30 and 34 MV/m). The pulse structure of the field is shown in figure 2.1. (a) Dynamic behavior. (b) Frequency shift during the 800 μs flat-top of the RF pulse versus accelerating gradient to the square. The line shows the linear fitting curve $\Delta f_{L,ft}^{(acc)} = -K_{ft} \cdot E_{acc,ft}^2$.

walls, the resonance frequency changes with a dynamic behavior. Figure 2.6 (a) shows the dynamic behavior of the Lorentz-force detuning for a TESLA 9-cell cavity, which has been operated in pulsed mode with different flat-top gradients. The time-varying cavity detuning is reproduced very accurately from pulse to pulse. Only a small modulation of some Hz is caused by microphonics, as is discussed in the previous section. This fact is important for field regulation, since feedforward control can be used to precisely stabilize the accelerating gradient, which is perturbed by the Lorentz-force detuning. Moreover the reproducibility enables to apply an active

feedforward cancellation of the Lorentz-force detuning, see next chapter. Figure 2.6 shows a fast inrease of the dynamic frequency shift with increasing flat-top gradients. During the 800 μs flat-top duration of the RF pulses the Lorentz-force detuning is changing almost linearly with time. Figure 2.6 (b) shows the frequency shift during the flat-top as function of the accelerating gradient to the square. As for the static Lorentz-force detuning a quadratical dependence on the gradient is found. The frequency changes by approximately 260 Hz during the 800 μs flat-top duration with 25 MV/m. For 34 MV/m approximately 440 Hz frequency change have been measured, which is almost twice the cavity bandwidth ($f_{1/2} \approx 230$ Hz (half width at half maximum) for TESLA-800). It is important to note, that these values have been measured on one selected TESLA cavity. Preliminary measurements with different TESLA 9-cell cavities indicate that some cavities have up to twice the frequency change shown in figure 2.6 [Sim 01]. Detailed studies at the TTF linac with high gradients above 20 MV/m are planned to determine the distribution of the Lorentz-force frequency change. In section 2.5 the consequences of the Lorentz-force detuning for the power requirements at high gradients will be discussed.
The dynamic behavior of the Lorentz-force detuning during pulsed operation depends on the mechanical properties of the cavity. The dynamic behavior of the cavity wall can be described in terms of mechanical modes, which are excited by the Lorentz-forces. For small changes in the cavity shape, each mode k can be considered as a harmonic oscillator with a given resonance frequency ω_k and damping time constant τ_k. Accordingly the dynamics of the detuning is described by a set of second order differential equations

$$\frac{d^2\Delta f_k^{(acc)}}{dt^2} + \frac{\omega_k}{Q_k}\frac{d\Delta f_k^{(acc)}}{dt} + \omega_k^2 \Delta f_k^{(acc)} = -\omega_k^2 K_k \cdot E_{acc}^2(t) \quad ; k = 1, 2, ... \quad , \tag{2.4}$$

where $\Delta f_k^{(acc)}$ is the detuning of the accelerating eigenmode, which is caused by the mechanical mode k. The quantity Q_k is the quality factor of the mechanical mode k, which is related to the mechanical time constant $\tau_k = 2Q_k/\omega_k$ of the damping. Each mode has its own Lorentz-force detuning constant. The total Lorentz-force detuning is obtained by summing up all modes

$$\Delta f_L^{(acc)}(t) = \sum_k \Delta f_k^{(acc)}(t) \qquad . \tag{2.5}$$

Using equation (2.4) to model the dynamic behavior of the Lorentz-force detuning requires detailed knowledge about the mechanical mode parameters of the cavity. In section 3.5 initial measurements of the mechanical modes of a superconducting TESLA 9-cell cavity will be presented.

2.5 Power Requirements

Amplitude and phase of the accelerating field have to be kept constant during the flat-top duration of the RF pulses, where beam is accelerated by the cavities. A sufficient stability must be guaranteed by the RF control system. The required extra power for keeping amplitude and phase constant depends on the detuning of the cavity. If the accelerating mode frequencyis on its design value for a bunched beam (1.3 GHz for the TESLA cavities) the minimum power required is equal to the power transferred to the beam (the power dissipated in the superconducting cavity walls can be neglected). However, if the accelerating mode frequency is shifted from its design value by $\Delta f^{(acc)}$, additional power is needed to maintain a constant accelerating field. For steady-state conditions the required generator power per cavity is given by (for 'on-crest' acceleration, i.e. 0° accelerating phase)

$$P_g = V_{acc} I_b \left(1 + \frac{1}{4} \left(\frac{\Delta f^{(acc)}}{f_{1/2}} \right)^2 \right) \quad , \tag{2.6}$$

see section 5.8. Here V_{acc} is the accelerating voltage of the cavity, I_b is the average beam current and $f_{1/2}$ is the half bandwith of the accelerating mode resonance. Taking further into account that the Lorentz-force detuning increases quadratically with the accelerating gradient (see eqation (2.3)), it is obvious that the required additional power becomes substantial at high gradients. An example is given in figure 2.7, where a computed RF pulse with TESLA-800 parameters (35 MV accelerating voltage, 12.7 mA average beam current during flat-top [TDR 01]) and the required klystron power per 9-cell cavity is shown. The average power transferred

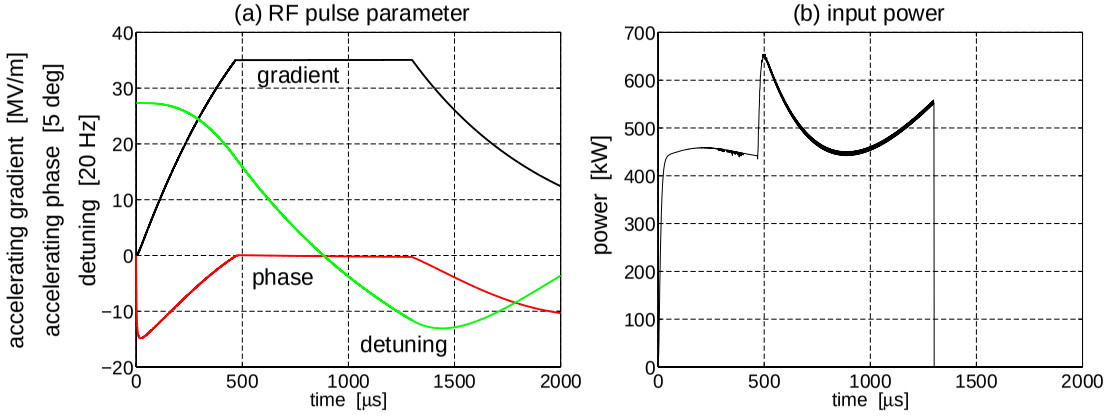

Figure 2.7: Computed RF pulse with TESLA-800 parameters (35 MV/m accelerating voltage, 12.7 mA average beam current during flat-top [TDR 01]). (a) Accerating gradient, phase and cavity detuning versus time. (b) Klystron power per 9-cell cavity versus time.

to the beam is $V_{acc} I_b = 446$ kW. During cavity filling there is no need to keep the accelerating phase Φ_b constant. Therefore the change in frequency by the Lorentz-forces can be followed according to the relation $2\pi \Delta f^{(acc)}(t) = d\Phi_b/dt$. However,

when beam is accelerated during the flat-top of the pulse, a constant accelerating phase is required and a peak RF power of 650 kW is needed, see figure 2.7 (b).
The extra power can be estimated from the measured detuning curves of a TESLA 9-cell cavity, which are shown in figure 2.6. For TESLA-500 the operating gradient is 23.4 MV/m, the flat-top duration is 950 μs and the optimal bandwidth of the accelerating mode is $f_{1/2} \approx 260$ Hz, [TDR 01]. The total Lorentz-force frequency change of the cavity during the 950 μs flat-top duration approximately amounts to $0.414 \cdot (23.4)^2$ Hz $\cdot\, (950/800) \approx 270$ Hz (the factor 0.414 is the fitting parameter for the frequency change during flat-top, see figure 2.6 (b), and the factor (950/800) takes into account, that the flat-top duration is 950 μs instead of 800 μs, as it was in the detuning measurement). Considering that the accelerating mode frequency of the cavity at the beginning of the pulse is properly adjusted, the maximum additional power during the flat-top of the pulse is $0.25 \cdot (135 \text{ Hz}/260 \text{ Hz})^2 \approx 7$ %, see equation (2.6). The TESLA specifications allow for an exta RF power of 10%. Accordingly the 7 % are tolerable. However, for the TESLA-800 parameters (35 MV/m accelerating gradient, 860 μs flat-top duration, $f_{1/2} \approx 230$ Hz, [TDR 01]) the maximum additional power during the flat-top exceeds 30 %, which is intolerably high. Note that this power would be needed just to compensate the field perturbation by the Lorentz-force detuning. Microphonics further increases the required power margin for amplitude and phase control.
Therefore to allow for highest gradients, the stiffening of the cavity must be improved (e.g. by a plasma-sprayed outer copper layer [Bou 99]), or alternatively, the Lorentz-force detuning must be compensated by a fast frequency control scheme. A fast frequency tuner would improve the power efficiency of the TESLA collider significantly, see figure 2.8 and compare to figure 2.7. In a proof of principle experiment fast tuner has been studied, as is discussed in the following chapter.

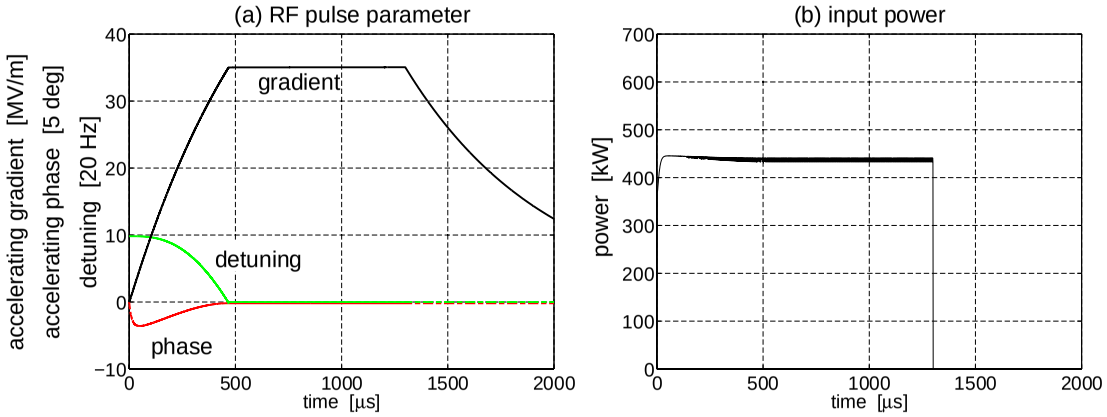

Figure 2.8: Computed RF pulse with TESLA-800 parameters (35 MV/m accelerating gradient, 12.7 mA average beam current during flat-top). During the flat-top of the pulse the Lorentz-force detuning is assumed to be compensated by a fast frequency tuner. (a) Accerating gradient, phase and cavity detuning versus time. (b) Klystron power per 9-cell cavity versus time.

CHAPTER 3

3 Fast Frequency Tuning

In the previous chapter it has been shown, that a fast frequency control would be a desirable option to reduce the overhead in RF power in pulsed cavity operation. Fast frequency tuning within the RF pulses would allow to compensate the time-varying frequency detuning induced by the Lorentz-forces. This chapter explains the concept of detuning cancellation and presents initial experiments with a piezoelectric tuner.

3.1 The Concept of Lorentz-Force Detuning Cancellation

In pulsed cavity operation the object of a Lorentz-force detuning cancellation is to maintain the cavity detuning close to zero during the flat-top duration. By this the required klystron power is minimized, see equation (2.6) and figure 2.8.
The Lorentz-force is distributed over the entire surface of the cavity. It is technically not feasible to generate an counteracting force distribution, which cancels the Lorentz-force at all locations of the cavity surface. However, to reduce the overhead in the RF power it is sufficient to compensate the Lorentz-force frequency shift $\Delta f_L^{(acc)}(t)$ of the accelerating mode by varying the length of the cavity. Accordingly it is sufficient to locally apply a force $F_c(t)$, which generates a time-varying frequency shift $\Delta f_c^{(acc)}(t)$ via a cavity length change. Properly adjusted, this fast frequency correction cancels the Lorentz-force detuning during the flat-top duration in pulsed cavity operation. i.e. $\Delta f_c^{(acc)}(t) = -\Delta f_L^{(acc)}(t)$.

3.2 Principle of a Fast Frequency Tuner

Piezoelectric actuators (see next section) are widely used as positioning elements, since they provide nanometer resolution, high dynamic operation (several kHz), high forces (several 100 N) and high reliability [Zick 96]. These properties make piezoelectric actuators also suitable for a fast frequency tuner. A piezoelectric tuner can be realized by integrating a piezo-element into the tuning frame of the motor driven frequency tuner, see figure 3.1. Alternatively a piezo-element can tune a cavity by modulating the length of the He-vessel, which is surrounding the cavity. Applying a voltage to the piezo-element changes its length and thereby the length of the cavity. The frequency of the accelerating mode depends on the lenght of the cavity. In a TESLA 9-cell cavity the accelerating mode frequency is increased by approximately 315 Hz if the cavity is lengthened by 1 μm, [TDR 01]. Accordingly a maximum piezo stroke of a few micrometers is sufficient for compensating the Lorentz-force

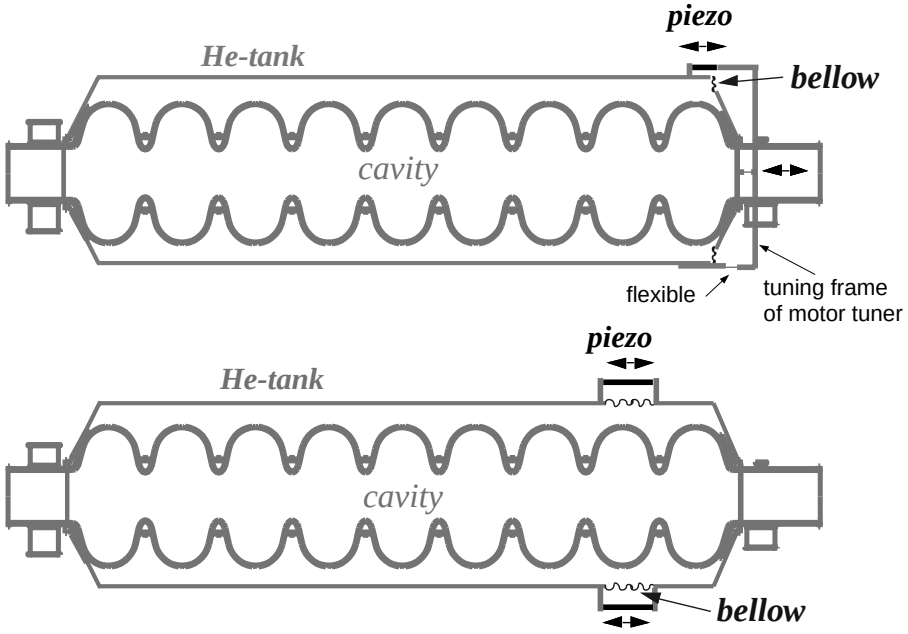

Figure 3.1: Principle of a fast frequency tuner based on piezotranslators. The piezo-element can be integral part of the motor controlled frequency tuner (upper figure) or can tune the cavity by modulating the length of the cavity surrounding He-vessel (lower figure, the additional motor controlled frequency tuner is not shown).

detuning in pulsed mode operation. This is in agreement with the travel-range, which can be provided at cryogenic temperatures by a piezoelectric actuator of a few centimeter length, see next section. A motor driven frequency tuner is needed to pre-adjust the accelerating mode frequency of a cavity, whereas the piezoelectric tuner controls the resonance frequency during pulsed operation. It is important to note that the fast response time of the piezoelectric tuner must be supported by a tuning frame and He-vessel with sufficient stiffness.
The voltage applied to the piezo has to be controlled. Proportional feedback control is however not feasible, since the required high bandwidth of several kHz cannot be realized due to mechanical resonances of the cavity below 1 kHz (see section 3.5). Fortunately, the Lorentz-force detuning is very reproducible from pulse to pulse. Therefore feedforward control can be applied. An adaptive scheme similar to the one which is used in the RF field control at the TESLA-Test-Facility ([Lie 98]) will be used to obtain the voltage signal applied to the piezotranslator, see figure 3.2. The dynamic behavior of the tuner-cavity-system is determined by measuring the response of the cavity detuning curve to a small voltage step applied to the piezo. Considering a time invariant system, the appropiate control voltage curve for the piezo-element can be calculated from the known step response curve and the measured Lorentz-force detuning curve in pulsed mode operation. The obtained voltage curve is then applied to the piezo-element in the subsequent RF pulses to compensate the Lorence-force detuning. Slow drifts in the operating parameters are covered by regularly updating the feedforward control voltage curve.

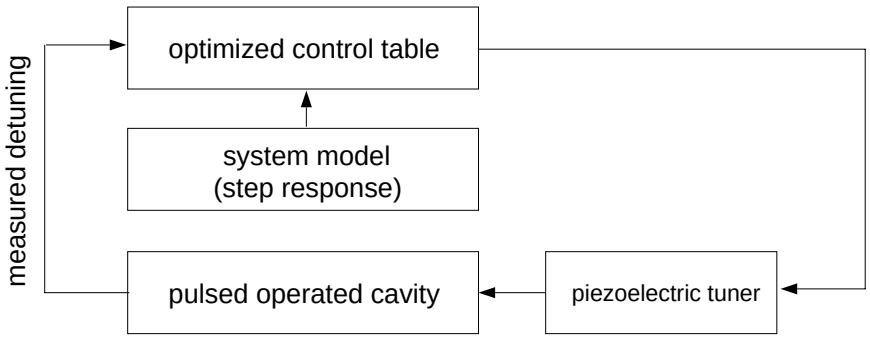

Figure 3.2: Principle of an adaptive feedforward scheme for resonance frequency control during pulsed operation. Based on a system model and on the measured cavity detuning curve during the pulses, the voltage curve applied to the piezotranslator is updated between the RF pulses.

3.3 Piezoelectric Actuators

In 1880 Jacques and Pierre Curie discovered that an electric charge is created in a quartz crystal, if pressure is applied. This so-called piezo-effect is widely used in sensor applications. Later it was shown, that an electric field applied to the crystal leads to a deformation of the crystal. This so-called inverse piezo-effect offers the possibility to be used for actuators. The first actuators using this effect became available around 20 years ago. Today ceramic material based on Lead Zirconate Titanate ($Pb(Zr,Ti)O_3$; PZT) based ceramic material is most often used [PI 01]. The crystal structure of this ferroelectric material is centro-symmetric above the Curie temperature ($T_c \approx 150°$ C for low voltage actuators [PI 01]). Below the Curie temperature and after a poling process the PZT material becomes piezoelectric. The PZT crystallites are then tetragonal-symmetric [Kop 93] with a dipole behaviour on account of the charge distribution, see figure 3.3 (a). The dipoles arrange themselves in groups (so-called Weiss domains) with parallel orientation. In raw PZT material these Weiss domains have randomly orientated dipole moments. However, by applying a strong electric field (>2 kV/mm) the PZT material expands along the field axis and the electric dipoles align. After this poling process the material has a remanent polarization, since part of the dipole alignment remains, see figure 3.3 (b). If now a electric voltage is applied to the piezoelectric material, the Weiss domains increase their alignment and the material expands along the field axis.
In order to keep the operating voltage within practical limits, PZT actuators usually are constructed from thin layers of PZT ceramic material. The layers are electrically connected in parallel. The total displacement of this multilayer design is given by the sum of the strain of the individual layers. So-called low-voltage actuators have layers of 20 μm to 100 μm thickness and a maximum operating voltage in the order of 100 V [PI 01]. By applying the maximum allowable voltage to a PZT stack its length is expanded by approximately 10^{-3} (without load). Table 3.1 gives some parameters of the piezo stack, which has been used in the proof of principle

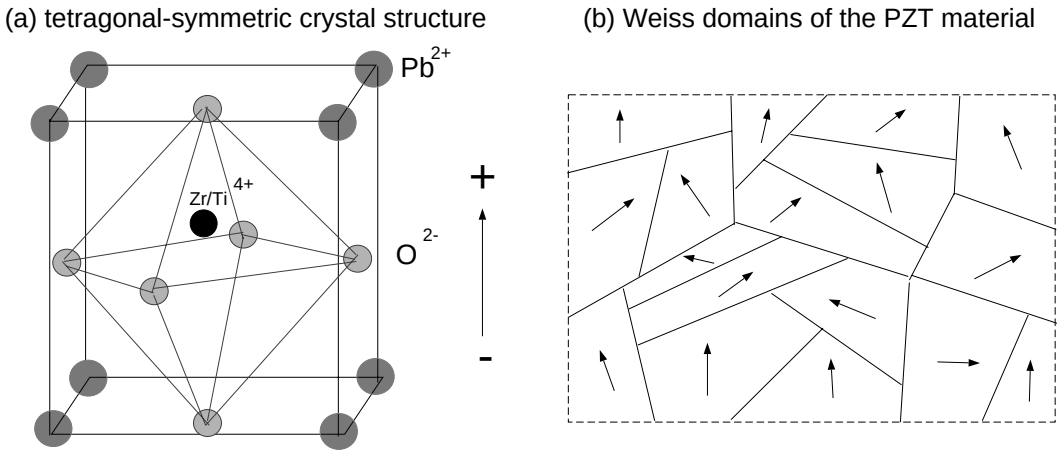

Figure 3.3: Lead Zirconate Titanate ($Pb(Zr,Ti)O_3$; PZT) material after poling. (a) Tetragonal-symmetric crystal structure with dipole behaviour. (b) Weiss domains in PZT material after poling with remanent polarization.

parameter	unit	value
length	[mm]	39
motion at room temp. (±10%)	$[\mu m]$	35
motion at 2 K (±50%)	$[\mu m]$	6
stiffness at room temperature	$[N/\mu m]$	25
maximum load	[N]	1000
capacitance at room temp. (±20%)	[nF]	3600
capacitance at 2 K (±20%)	[nF]	220
operating voltage	[V]	-10 to 150

Table 3.1: Parameters of the piezo stack used in the proof of principle experiment of Lorentz-force detuning cancellation (see section 3.4).

experiment.

The driving piezo-element of the fast frequency tuner has to work reliably under special conditions:

- ***Dynamic operation***
  In order to cancel the Lorentz-force detuning within the RF pulse duration of about 1 ms, a fast response of the piezoelectric tuner is required. Fortunately one of the properties of piezoelectric actuators is a rapid position chance by a rapid drive voltage change. A PZT element can reach its nominal dispacement in approximately 1/3 of its lowest mechanical resonance frequency period [PI 01]. Without load, a piezotranslator has a typical resonance frequency of some kHz, thus it can reach its nominal displacement within some 10 μs. However, when the piezo-element is loaded by the cavity, the time response of the tuner-cavity system is determined by the lowest mechanical resonance, which can be driven by the piezo translator.

- ***Pulsed operation at 2 K***
  The piezo-element is integral part of the cavity tuning mechanism which is operated at cryogenic temperatures (2 K). Piezo translators work at a wide range of temperatures, including cryogenic temperatures. However, the piezoelectric effect of the PZT material depends on the temperature. Below -90° C, the PZT crystallites are rhomboidal-symmetric [Kop 93]. At 2 K the maximum stroke of a PZT actuator is approximately 10 % to 30 % of its room temperature value [PI 01], see also table 3.1. This reduction has to be considered in the design of a fast frequency tuner for Lorentz-force detuning compensation. The piezo-element needs to be operated in pulsed mode for the Lorentz-force detuning compensation. Twenty years of TESLA operation at 5 Hz pulse repetition rate correspond to a total of some 10^9 pulses. A typical failure mechanism during pulsed operation of a piezo-stack is the generation of cracks inside the ceramic, which can result in a electrical break-down and subsequentely electrical shortening of the stack [Zick 96]. Traditionally multilayer piezo-stacks are produced by use of an elastic glue which combines the layers. At cryogenic temperatures this glue might become brittle. Recently industry has developed sintered piezo-stacks without glue, which are optimized for a high dynamic pulsed operation with maximum stroke. A typical application for this type of PZT stacks is the piezo triggered diesel fuel injection, where the control valve is piezoactuated. These piezo actuators have shown a performance of more than 10^{10} cycles at room temperature [PM 01]. For this reliability a high preload of the piezo-stack is essential (more than 50 % of the specified maximum load [PM 01]). This preload shifts the zero point of the piezo-stack travel, but does not reduce the maximum displacement. In order to verify that the prospected reliability of the sintered piezo-stacks is also valid at cryogenic temperatures, a pulsed operation test at 77 K (liquid nitrogen dewar) has been started. Two piezo-elements are placed in series, where one is pulsed at 100 Hz with a pulse structure similar to the one used during Lorentz-force detuning cancellation. The second piezo-element is used as a sensor to detect the force created by the first element. Preliminary results have shown no performance degradation during almost six weeks of pulsed opertion, i.e. more than $3 \cdot 10^8$ pulses, which is comparable to two years of TESLA operation at 5 Hz.

- ***Operation in a radiational environment***
  Since the piezotranslator of a fast frequency tuner is placed close to the cavity, it is exposed to radiation (γ and neutrons), which is partly generated by field emission of electrons in the cavities and partly by beam losses. For the TESLA collider the upper limit for the average dose rate is dictated by the capability of the cryogenic system, which can handle an additional heat load of 0.1 W/m at 2K temperature [TDR 01]. This head load corresponds to a dose rate of approximately 10 Gy/h. Assuming an operation time of 20 years this corresponds to a total dose of approximately 2 MGy including a neutron flux of approximately $10^{13} n/20a/cm^2$ (E>1 MeV) [Leu 01]. According to reference [Bat 75] this should not pose a problem, since almost no damage is expected

up to a dose of about 10 MGy to 100 MGy. To test the radiation hardness two sintered piezo-stacks are presently exposed to radiation from a Co^{60} source (600 Gy/h) and are operated in pulsed mode at 77 K. First results will be aviable soon.

It is important to note that more tests are needed to evaluate the reliability of different piezotranslator types in a radiational environment at cryogeninc temperatures. To improve the reliability it might be desirable to place the the piezotranslator of the fast tuner as well as the stepping motor of the slow frequency tuner outside the cryostat. This solution also improves the maintenance capability of the tuning system. Further studies are planned to evaluate the performance and the cost of such a frequency tuning system.

3.4 Proof of Principle Experiment

A piezo-element has been incorporated in the tuning frame of a TESLA 9-cell cavity, see figure 3.4. The piezotranslator replaces a support rod of the motor driven frequency tuner. The cavity has been operated in pulsed mode in a test cryostat with pulse parameters (23.5 MV/m, 900 μs flat-top duration, 10 Hz RF pulse repetition rate) close to the TESLA-500 values. The amplitude, start time and rise time of the piezo drive voltage have been adjusted to compensate the Lorentz-force detuning during the whole flat-top region of the RF pulses. Figure 3.5 demonstrates the successful compensation by comparing the frequency detuning curves, which have been measured without and with frequency control. The detuning of the accelerating mode frequency is maintained close to zero within the flat-top duration of the pulses. This compensation has been applied successfully several hours and could be reproduced on two other TESLA 9-cell cavities. No degradation of the piezotranslator performance has been observed during these initial experiments.
These results show that the time response of the piezoelectric tuner is sufficient for the compensation of the Lorentz-force detuning. This indicates, that the dynamics of the tuner and the dynamics of the Lorentz-force cavity deformation are set by the same mechanical resonances of the cavity, see also section 3.5.

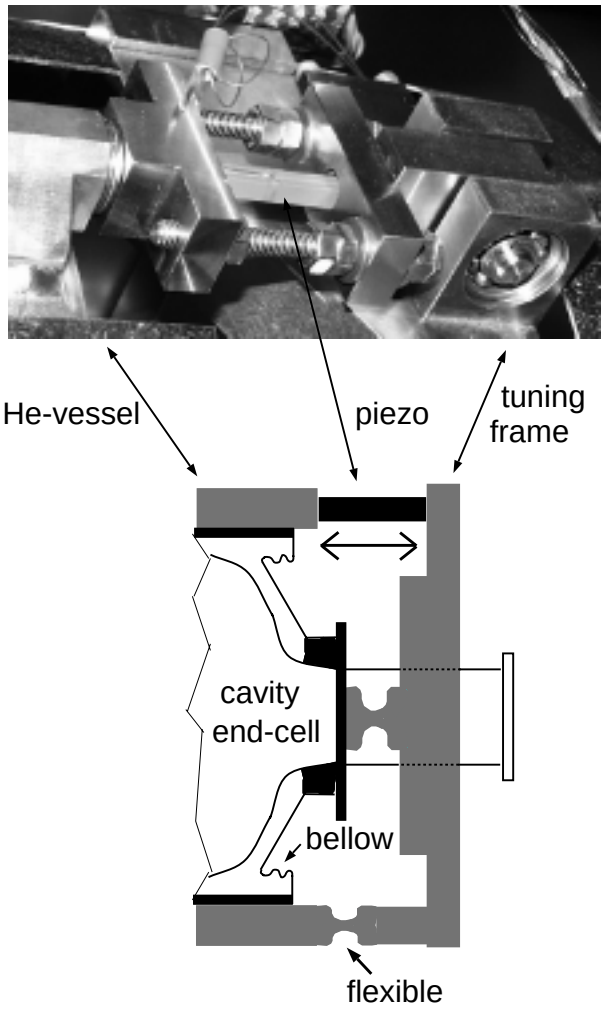

Figure 3.4: Experimental set-up used in the proof of principle experiment of detuning cancellation. Upper figure: A piezotranslator is integral part of the motor controlled frequency tuner of a TESLA 9-cell cavity. Lower figure: Schematic view of the piezoelectric tuner; see also figure 3.1.

3.5 Mechanical Resonances of TESLA 9-cell Cavity

The piezoelectric tuner has also been used for studying mechanical resonances of a TESLA 9-cell cavity at cryogenic temperatures. For this purpose a cavity with He-vessel and high power coupler has been operated in cw-mode in a test cryostat. A sinusoidal voltage has been applied to the piezo-element to excite mechanical modes. The resulting amplitude modulation of the 1.3 GHz resonance frequency has been measured as function of the piezo-voltage frequency, see figure 3.6. The excitation spectrum shows several mechanical modes. Two dominating mechanical resonances are around 300 Hz and 460 Hz and have quality factors in the order of 100. Some of the modes might have quality factors of several 100, but more detailed measurements are required to verify this.
One concern in pulsed mode cavity operation at high gradients is the excitation

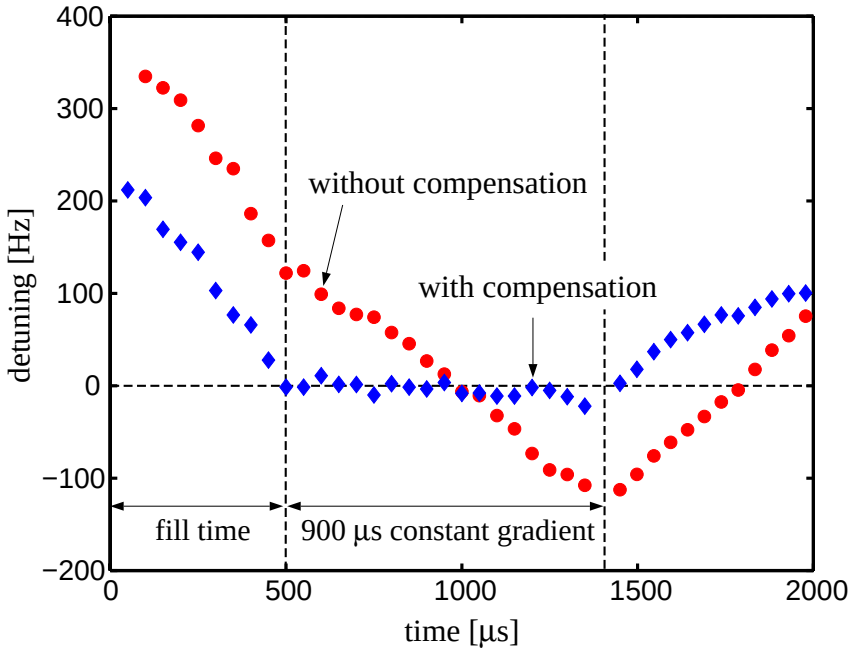

Figure 3.5: Compensation of the Lorentz-force induced frequency shift during the flat-top in pulsed mode cavity operation. Shown is the frequency detuning of the accelerating mode with and without compensation by the piezoelectric tuner. The accelerating flat-top gradient in the TESLA 9-cell cavity is 23.5 MV/m. The pulse structure is shown in figure 2.1.

of mechanical modes by the repetitive Lorentz-forces. For a 10 Hz pulse repetition rate and 1.3 ms long RF pulses the Lorentz-force excitation spectrum has lines every 10 Hz up to frequencies beyond 1 kHz. Accordingly there is potential to resonantly drive a mechanical resonance of the cavity with an amplitude, that depends on the quality factor of the mode. This can result in a significant modulation of the accelerating mode frequency, thus increasing the detuning within the RF pulses. Since piezotranslators can also be used for measuring vibrations they provide a tool to study the excitation of mechanical modes. In an initial experiment the voltage induced in the piezo-element by the vibrations has been monitored during pulsed operation of a 9-cell cavity at high gradients. Figure 3.7 shows the induced voltage at 30 MV/m and 10 Hz pulse repetition rate. As can be seen, a damped oscillation is excited which persists until the next pulse. The pattern of the vibration is largely repetitive from pulse to pulse with a slight modulation, which can be attributed to microphonics. The frequency spectrum of the Lorentz-force excited vibration is shown in figure 3.8 (30 MV/m gradient with 2 Hz pulse repetition rate). Beside two microphonics vibration frequencies (caused by the He-system and pumps) mechanical resonances around 280 Hz and 450 Hz are excited. However, the dominating resonance frequencies are not exact multiples of 10 Hz, thus they are not excited resonantely in a pulsed operation with 10 Hz RF pulse repetition rate.
For more detailed investigations we plan to repeat these measurements with an ad-

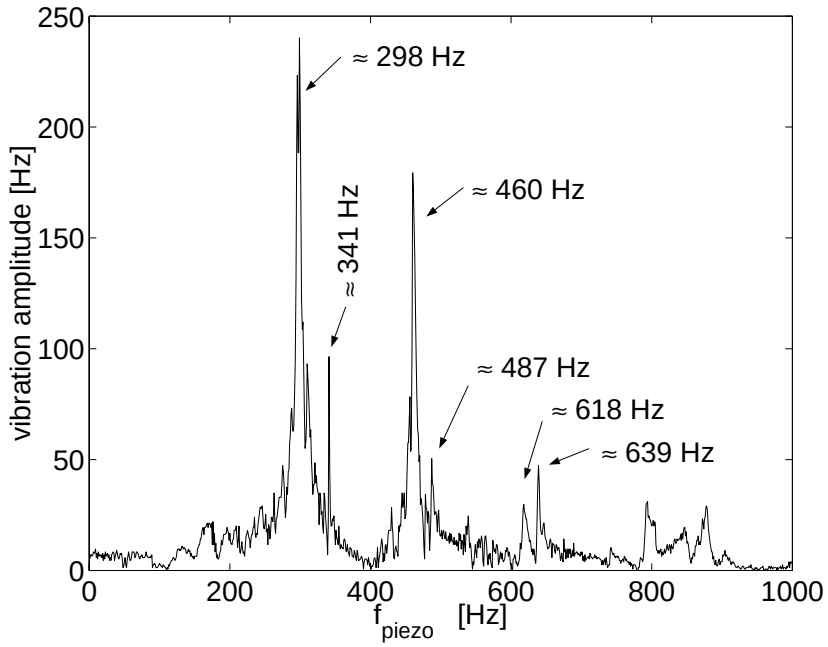

Figure 3.6: Resonance spectrum of mechanical modes measured on a TESLA 9-cell cavity at 2K. The modes are excited by a piezotranslator, which is integral part of the motor controlled frequency tuner, see figure 3.4. Shown is the modulation amplitude of the accelerating mode frequency during cw-operation as function of the vibration frequency of the piezo-element. The sinusoidal voltage applied to the piezo had constant amplitude of V.

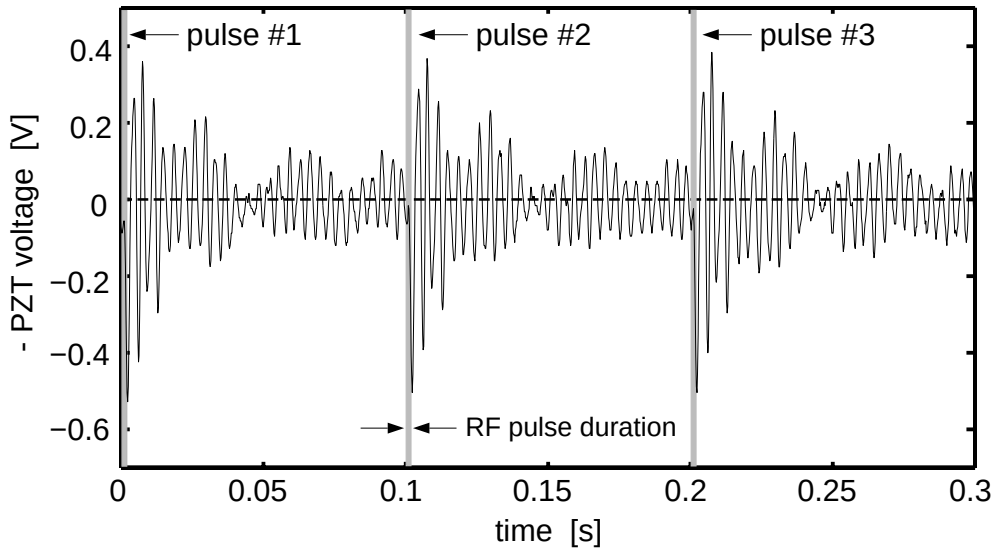

Figure 3.7: Lorentz-force excitation of mechanical vibrations during pulsed mode operation of a TESLA 9-cell cavity (30 MV/m accelerating gradient, 10 Hz pulse repetition rate). Shown is the vibration induced voltage of a piezo-element, which is part of the frequency tuner, see figure 3.4.

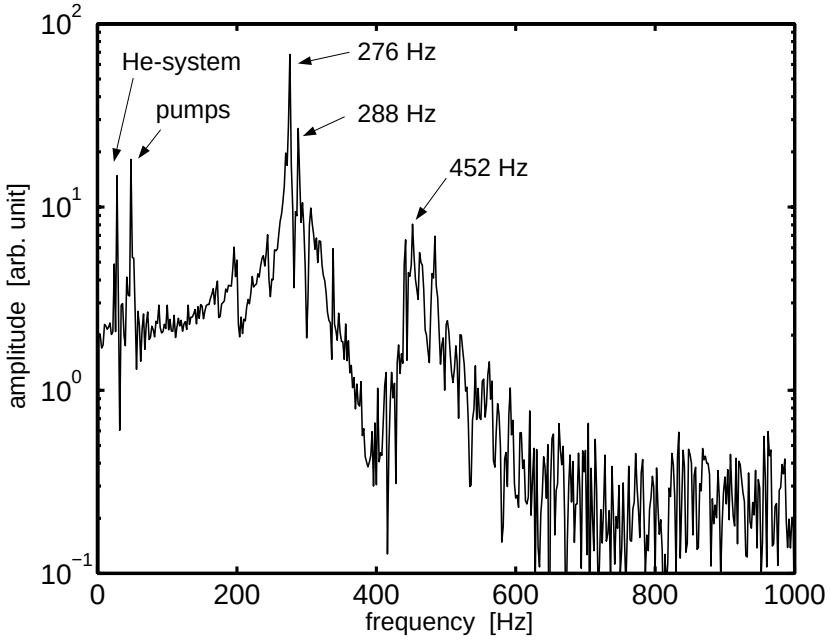

Figure 3.8: Frequency spectrum of the mechanical vibrations excited by the Lorentz-forces during pulsed mode operation of a TESLA 9-cell cavity. The accelerating gradient is 30 MV/m with 2 Hz pulse repetition rate.

justable pulse repetition rate to resonantly excite mechanical cavity modes. This will show the maximum excitation amplitudes and the effect of the mechanical vibrations on the accelerating mode frequency within the RF pulses.

3.6 Outlook

The initial experiments with the piezoelectric tuner have shown that the Lorentz-force detuning can be compensated. In the last years the technique of damping mechanical oscillations by piezo actuators has been studied for several purposes and industrial systems are available now. This technology needs to be transferred to cavities to extend the resonance frequency control to micorphonics detuning. Preliminary cw-measurements have shown a clear correlation between the vibration signal of a piezo-element and the micorphonics detuning. Therefore we believe that also the dominating part of the micorphonics detuning can be compensated via the piezoelectric tuner. The piezoelectric tuner further offers the possibility to actively damp those excited modes, which couple to length variations of the cavity. Note that the Lorentz-forces can also excite other modes.
Detailed investigations of the prospected benefits of a piezoelectric tuner and its reliability are planned. A combination of two piezo-elements will be used: one element serves as actuator while the second element is used as vibration sensor. These studies will increase our knowledge of the mechanical modes of a multicell cavity and their excitation in pulsed operation. Especially for highest gradients this knowledge

is essential to guarantee a narrow energy spread of the beam without excessive RF power requirements.

PART II

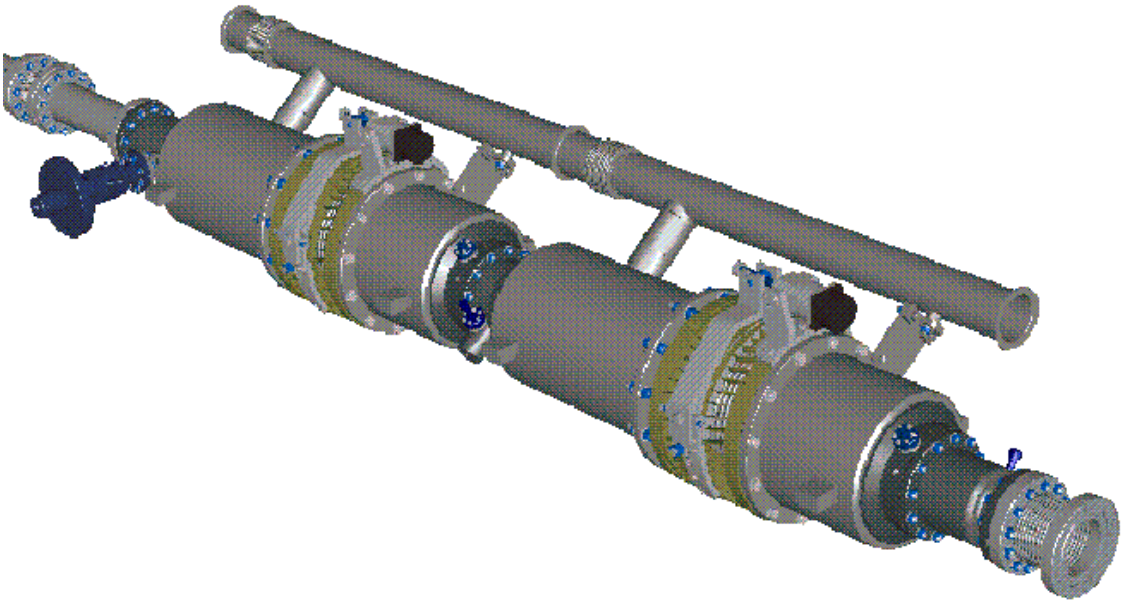

Superstructures: The Concept of Coupled Cavities

4 The Superstructure Concept

4.1 Motivation

A fundamental design goal for a linear accelerator is to minimize the cost of the radio frequency system, representing an essential part of the total investment. It is noteworthy that the cost of the radio frequency (RF) system is not dominated by the accelerating structures. The RF power sources, the waveguide system, the fundamental mode (FM) couplers and the RF control system contribute significantly to the total cost of the radio frequency system [TDR 01]. Further the civil engineering for the tunnel adds considerably to the total investment for a high energy linar collider. Hence the cost of a linear accelerator can be reduced significantly by:

- reducing the number of microwave components, i.e. by reducing the number of accelerating units fed by their own power coupler,
- increasing the filling factor:

$$F = \frac{\text{active acceleration length}}{\text{total length of the accelerator}} \quad . \tag{4.1}$$

Accordingly it is desirable to use multicell cavities with as many cells as possible. Unfortunately the number of cells (N) per accelerating structure is limited by two fundamental effects:

- Firstly, for a standing wave structure operated in the π-mode, the sensitivity of the field homogeneity to small perturbations grows quadratically with the number of cells. A frequency spread δf of the individual cells results in an inhomogeneity in the accelerating field amplitude (A_{cell}) of the cells [Nag 67]:

$$\frac{\delta A_{cell}}{\overline{A}_{cell}} \propto \frac{N^2 \delta f}{\mathcal{K}_{cc}} \quad . \tag{4.2}$$

  Here $\mathcal{K}_{cc}$ is representing the cell-to-cell coupling factor as defined in section 5.6. Each mechanical, chemical or thermal treatment can influence the cell frequencies and disturb the field homogeneity. This reduces the maximum energy gain per cavity, since the achievable gradient in a multicell cavity is usually limited by the cell with the highest amplitude. For the TESLA collider the tolerable reduction is specified to 5 % or less.

- Secondly the probability of trapping higher-order modes (HOM's) within a cavity increases with the number of cells. These trapped modes[1] have a comparatively small field energy stored in the beam tubes as compared to the energy in the cells. Therefore such modes couple only weakly to the HOM couplers, which are located at the beam tubes[2]. This is particularly dangerous for superconducting cavities because of the resulting long damping times of up to several seconds. Depending on the strength of the coupling to the HOM couplers, a trapped mode can even persist between the RF pulses in a pulsed machine[3]. If a mode is weakly damped, already a small coupling to the beam can cause a significant emittance dilution.

For the superconducting cavities of the TESLA Test Facility (TTF) the number of nine cells has been chosen [TTF 95]. This number is a compromise between the requirements - field homogeneity and mode damping - and the desired high number of cells per cavities. In the TTF design, each cavity is equipped with its own input coupler, frequency tuning system and two HOM couplers, one at each end-tube. Experience with the TTF 9-cell cavities ($\mathcal{K}_{cc} = 1.9$ % [TTF 95]) shows that a careful treatment after the final adjustment of the relative field amplitudes allows to reach the specified field homogeneity for TESLA. In the cryomodules of the TESLA Test Facility linac the cavities are spaced by tube sections of $3/2\lambda$ length, see figure 4.1. The wavelength $\lambda = 0.231$ m corresponds to the RF frequency $f = 1.3$ GHz of the accelating mode in the TTF cavities. For the tube diameter of

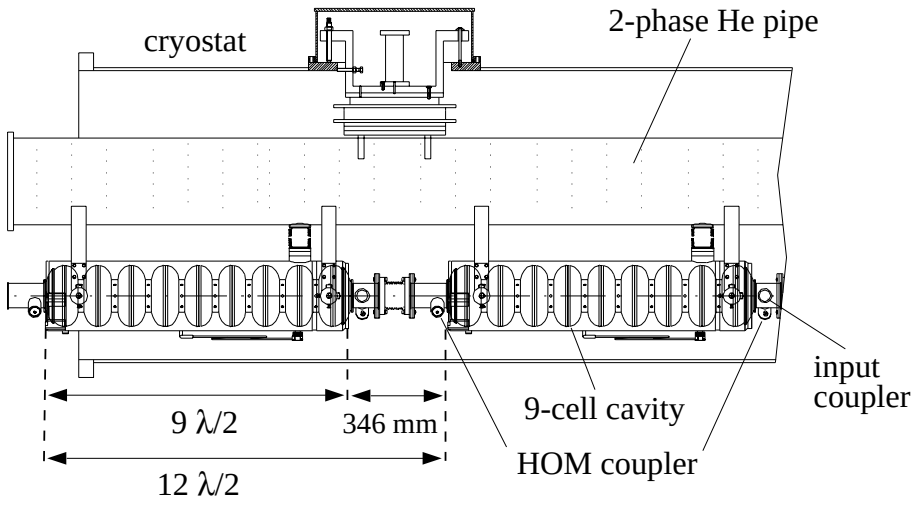

Figure 4.1: Layout of the TTF cryomodule with long ($3/2\lambda$) interconnections between the cavities [CDR 97].

[1] A real trapped mode would have a vanishing field in the beam tubes and is therefore not affected by the HOM couplers. It is common to name all modes with low fields in the tubes as trapped, but no exact definition exists.

[2] The high fields in the cavities discussed here do not allow to place HOM couplers at the cells.

[3] The repetition rate of the RF pulses is 5 Hz to 10 Hz for the proposed TESLA collider and 60 Hz for SNS.

78 mm the mode frequency of 1.3 GHz is below the cut-off frequency of the tube. Hence the $3/2\lambda$ interconnections guarantee a good separation of the accelerating modes of neighboring cavities, i.e. there is no power flow from one cavity to the next. Unfortunately these passive interconnections reduce the filling factor to 75 %[4]. Therefore in the baseline layout of the TESLA collider the distance between the cavities is shortened by 63 mm [TDR 01] to improve the filling factor, see figure 4.2. The resulting tube length of 283 mm is determined by the minimum space needed for the couplers and the flange connection and by a still sufficient separation of the accelerating modes. Due to the limitations on the cell number N the standard TTF

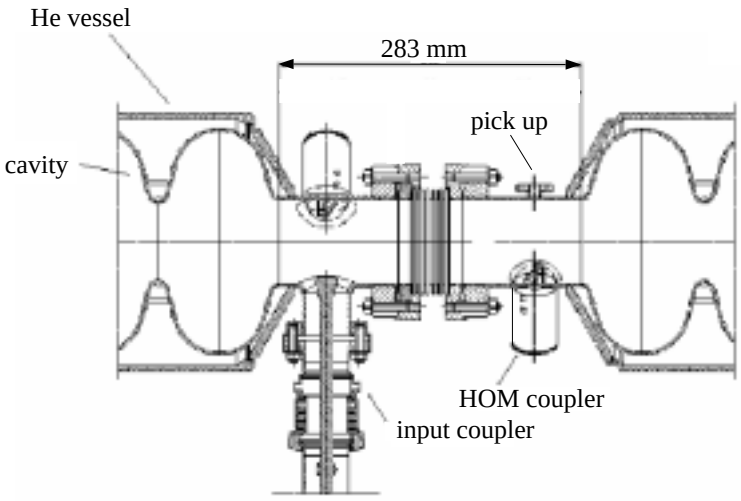

Figure 4.2: Layout of a cavity interconnection with minimized inter-cavity spacing [TDR 01].

multicell cavities do not allow a further improvement of the filling factor. In order to circumvent the limitations, the concept of the so-called superstructure has been proposed by J. Sekutowicz [Sek 99].

4.2 The Concept of Coupled Cavities: the Superstructure

Instead of separating multicell cavities by long tube interconnections, in the superstructure concept several multicell cavities are coupled through short beam tubes [Sek 99], see figure 4.3. The short interconnecting tubes have a sufficiently large diameter (114 mm for 1.3 GHz cells of the TESLA shape) to enable power flow from one cavity to the next. Therefore the electromagnetic fields are coupled through the whole chain of cavities. If the number of joined cavities is M, each mode of a single multicell cavity splits into M resonances, see figure 4.4 and section 5.6. The synchronism between the ultrarelativistic bunches and the accelerating field in a superstructure requires the cavity spacing to be $n\lambda/2$, where n is an integer. Note that

[4]Interconnections between cryomodules are not included in this number.

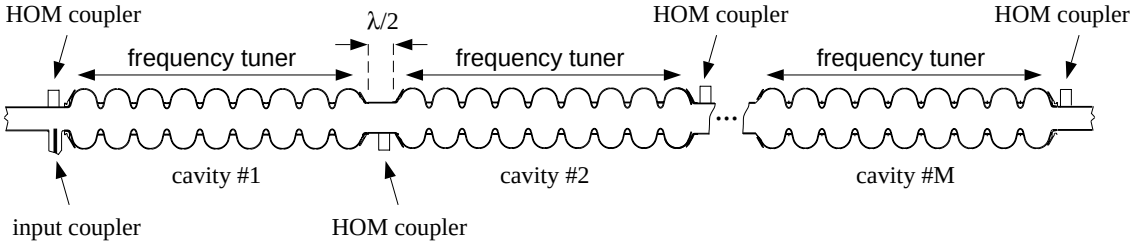

Figure 4.3: Sketch of a superstructure based on M coupled cavities. Each cavity is equipped with its own frequency tuner. The number of input couplers is reduced and the filling factor increased as compared to separate multicell cavities.

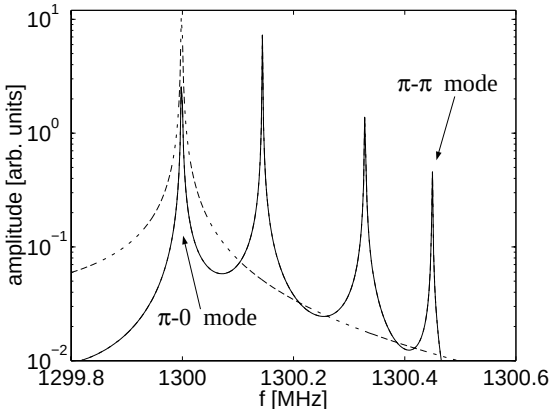

Figure 4.4: Splitting of modes in coupled cavities. The dashed line shows the resonance curve for the accelerating mode of a 7-cell cavity (quality factor $Q_0 = 2 \cdot 10^6$). The solid line shows the corresponding modes in a superstructure composed of four coupled 7-cell cavities.

the phase difference between the fields of two coupled resonators without losses is always 0 or π, see section 5.6. Accordingly the length of the interconnections between the cavities is chosen to be half of the wavelength ($\lambda/2 = 115$ mm for $f = 1.3$ GHz) to optimize the filling factor, as shown in figure 4.3. Also the accelerating mode of the individual cavities splits into M coupled modes. When the number of cells N_c per cavity is an odd number, the mode with a cell-to-cell phase advance of π and a cavity-to-cavity phase advance of zero ($\pi - 0$ mode) can be used for acceleration. This mode is shown in figure 4.5 for a superstructure consisting of 9-cell cavities.

While the short interconnections improve the filling factor, the power flow from cavity-to-cavity enables to feed the M cavities of a superstructure by a single input coupler mounted at one end. Therefore a superstructure composed of M N_c-cell cavities is similar to a $M \cdot N_c$ multicell cavity with respect to the filling factor and the number of RF components, but the total cell number $M \cdot N_c$ is not restricted by the limitations discussed in the section above.

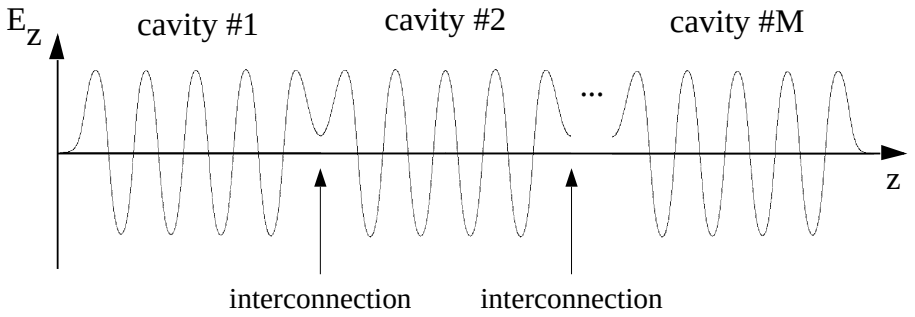

Figure 4.5: Longitudinal electrical field of the accelerating mode along the axis of a superstructure (numerical calculation [Sek 94]).

The reason for this are the following essential differences between a $(M \cdot N_c)$-cell cavity and a $M \times N_c$-cell superstructure:

- HOM couplers are located at the end-tubes and the interconnections, see figure 4.3. Therefore the maximum number of cells between two HOM couples is N_c and not $M \cdot N_c$ as it would be in a multicell cavity with $M \cdot N_c$ cells.
- All cavities of a superstructure are equipped with their own frequency tuning system. This allows to adjust the frequencies of the cavities such, that the field homogeneity of the accelerating mode in the whole structure is optimized, as discussed in section 6.4 in detail. Aside from the economic aspects of the superstructure design, this flexibility in the frequency adjustment means an additional significant advantage: the possibility to adjust, within some boundaries, the frequencies of higher order modes, see chapter 9.5.

Accordingly the HOM damping and the field homogeneity are handled at the N_c-cell sub-unit level. Of course the limitations mentioned in section 4.1 still apply to the number of cells N_c per cavity in a superstructure.
The structures discussed in the following chapters consist of two and four coupled multicell cavities. It is not surprising that also the number M of cavities coupled to a superstructure is restricted. As will be treated later in more detail, there are physical and technical reasons for this:

- propagation time of the RF power through the structure and energy spread,
- perturbation of cavity phasing resulting from beam loading,
- distance of the accelerating mode to the next resonance,
- power capability of the input coupler,
- length of the structure.

Although the coupling of standing wave cavities might appear straightforward, it is noteworthy that this has never been considered before the proposal of the superstructure concept for the TESLA collider. Possible questions are related to the

comperatively weak inter-cavity coupling by the $\lambda/2$ beam tube, being almost two orders of magnitude smaller than the coupling of the cells in a multicell cavity. The superstructure concept has been extensively studied at DESY since 1999 to validate the expected benefits and the operability of a structure with weak coupling and to find its limitations. These studies include the field homogeneity of the accelerating mode (see chapter 6), the energy spread of a beam accelerated in a superstructure (see chapter 7), field stabilisation by a control system (see chapter 8) and damping of the higher order modes (see chapter 9). Moreover the weak inter-cavity coupling requires new concepts in the adjustment of the cell field amplitudes and in the field control.

4.3 Types of Superstructures

Although the analytical derivations in the following chapters will cover a generalized superstructure, the numerical calculations and the measurements on models and prototypes have to focus on a few selected structure layouts. In addition to a 2×7-cell prototype structure [Sek 01], two types of superstructures have been investigated in detail for the TESLA collider: the first one consisting of four 7-cell cavities [Sek 98], and more recently, a 2×9-cell superstructure [Sek 01].

4.3.1 The 2×7-cell prototype structure

A proof of principle experiment for the concept of coupled cavities has to include a beam test. Two niobium prototypes are in preparation for a beam test, which is scheduled for beginning of 2002, see chapter 10. For this test, a cryomodule housing two superstructures will be installed in the linac at the TESLA-Test-Facility. The layout of the inner part of this module is shown in figure 4.6.

Both prototypes consist of two 7-cell 1.3 GHz cavities each, joined by a $\lambda/2$ tube

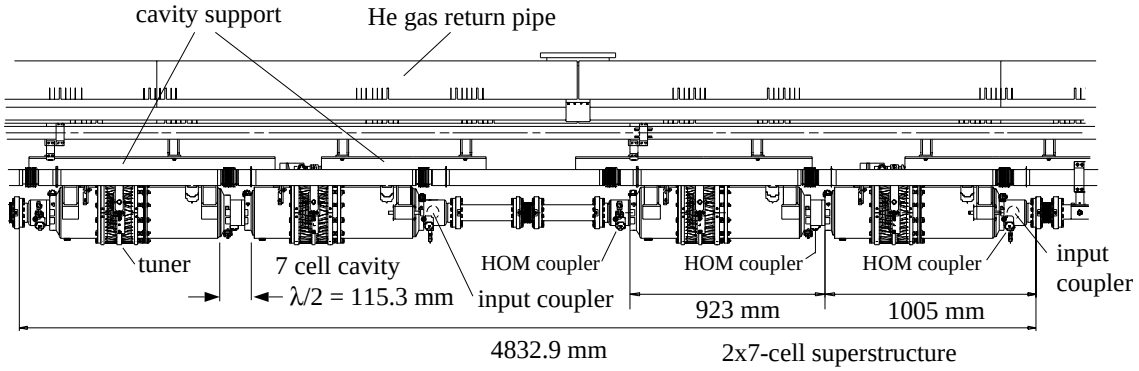

Figure 4.6: Layout of the inner part of the cryomodule, housing two 2×7-cell prototype superstructures. This cavity chain will be used for a proof of principle experiment at the TTF linac.

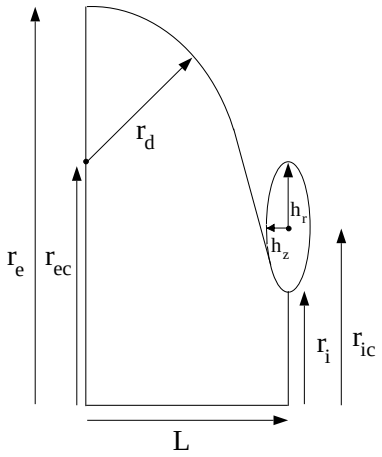

Figure 4.7: Contour of a half-cell (see also table 4.1). The circle and the ellipse are joined by a straight line, which is tangential to them.

parameter	half-cell of centre-cell	inner half-cell of end-cell	outer half-cell of end-cell
equator radius r_e	103.3	104.9	104.9
center point r_{ec}	61.3	62.9	62.9
circle radius r_d	42	42	42
center point r_{ic}	54	54	71
ellipse half axis h_r	19	19	14
ellipse half axis h_z	12	12	13
iris radius r_i	35	35	57
length L	57.7	57.7	57.7

Table 4.1: Parameters for the half-cells of the 2×7-cell prototype superstructure (note that there is a small difference in the shape of the inner end-cells and the outer end-cells, not shown in this table) [Sek 00, Hae 92]. All dimensions are in mm.

with 114 mm diameter [Sek 01]. These 2×7-cell structures[5] will allow to study all aspects that are related to the concept of joining cavities by a comperatively weak coupling. The shape of the centre-cells is identical to those of the TTF 9-cell resonators, whereas the end-cells have been redesigned for the larger aperture of the beam tubes (114 mm instead of 78 mm). The geometrical parameters of the half-cells in the 2×7-cell prototype are listed in table 4.1, see also figure 4.7.

Obviously the resonator-to-resonator coupling $\mathcal{K}_{rr}$ depends on the diameter of the interconnecting tube. Furthermore $\mathcal{K}_{rr}$ depends on the field characteristic within the superstructure, see chapter 5. The 114 mm diameter tube between the two 7-cell cavities results in a coupling $\mathcal{K}_{rr} = 3.6 \cdot 10^{-4}$ for the accelerating mode, whereas the

[5]Initially it was planned to test a 4×7-cell prototype superstructure. Meanwhile the 2×9-cell structure has been proposed and is expected to become the preferred solution for the TESLA collider [TDR 01]. Because the 7-cell cavities had been ordered before we decided to test two structures with 2×7 cells instead to save time and money.

parameter	unit		parameter	unit	
L_{total}	[m]	2.08	type of structure	-	stand. wave
L_{active}	[m]	1.62	accelerating mode	-	TM010, π-0
diameter of tube	[mm]	114	fundamental frequency	[MHz]	1300
L_{tube}	[mm]	115.3	cell-to-cell coupling $\mathcal{K}_{cc}$	[%]	1.9
diam. of mid-cell iris	[mm]	70	cavity-to-cavity coupling for π group, $\mathcal{K}_{rr}$	[%]	$3.6 \cdot 10^{-2}$
no. of cavities, M	-	2			
cells per cavity, N_c	-	7	sensitivity factor, $N_c^2/\mathcal{K}_{cc}$	-	2600
no. of input couplers	-	1	(R/Q) per structure	[Ω]	729
no. of HOM couplers	-	3	geometry factor, G	[Ω]	275
no. of frequ. tuners	-	2	E_{peak}/E_{acc}	-	2.0
no. of pick ups	-	4	B_{peak}/E_{acc}	$\frac{\text{mT}}{\text{MV/m}}$	4.18
			distance to next resonance	[kHz]	350

Table 4.2: Parameters of the 2×7-cell prototype superstructure (note that the definition $R = V_{acc}/(2P_{wall})$ is used for the shunt impedance R, see section 5.5) [Sek 00].

cell-to-cell coupling is $\mathcal{K}_{cc} = 1.9\%$. These and other RF parameters of the 2×7-cell prototype are summarized in table 4.2. Both prototype superstructures will be equipped with an type III TTF input coupler [Moe 99]. Three HOM couplers (based on the TTF design with 40 mm diameter [Sek 93]) will be used per structure, located at the two end-tubes and at the interconnection tube. The frequencies of the cavities can be adjusted individually by newly designed mechanical tuning systems, see also chapter 10. For diagnostic purposes a pick up antenna is located near to each end-cell of the prototype structures. Later superstructures will have fewer pick up antennas.

4.3.2 Superstructures for the TESLA collider

The 4×7-cell superstructure

A superstructure composed of four 7-cell cavities has been first proposed for the TESLA collider [Sek 98]. As in the 2×7-cell prototype the 1.3 GHz cavities are joined by $\lambda/2$ beam tubes with 114 mm diameter, see figure 4.8. Each tube is equipped with a HOM coupler. The input coupler is again located at one end of the structure. The 4×7-cell type of a superstructure is optimized for a high filling factor and a minimum number of RF components. In table 4.3 the parameters of three versions of the TESLA accelerating system are compared. The 4×7-cell layout reduces the number of input couplers by a factor of three[6]. On the other hand the number of helium vessels and frequency tuning systems is higher than in the 9-cell version, since each cavity has only seven cells. The number of cells per cavity (N_c) is reduced from nine to seven to maintain a sufficiently low sensitivity of the whole coupled structure to field inhomogeneities by an improved field stability

[6]The reduced number of input couplers has also major consequences for the cost of the whole RF system.

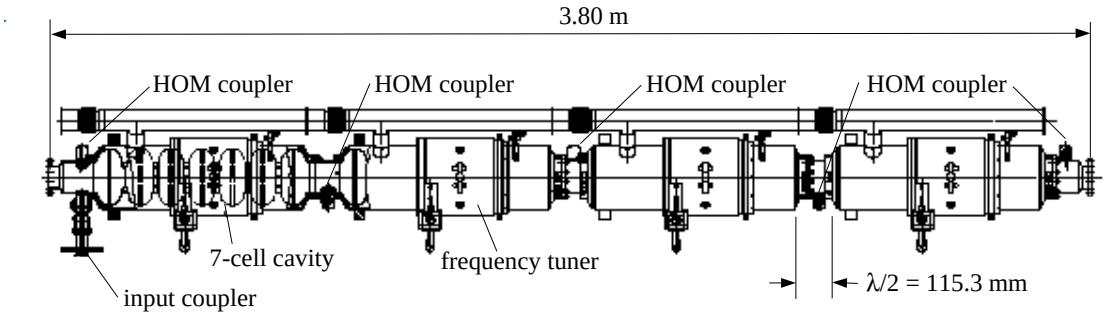

Figure 4.8: Layout of the 4×7-cell superstructure. The four 7-cell resonators are joined by 114 mm diameter $\lambda/2$ beam tubes.

in the individual cavities (see equation 5.2).
The lower number of RF components has the price of an increased overall length of 3.8 m per 4×7-cell structure, which is a clear disadvantage, because it makes cleaning as well as chemical and heat treatments of the entire structure difficult, if not impossible. Therefore it is under study to join two treated and cleaned 2×7-cell halves by a clean welding or a superconducting flange.

The 2×9-cell superstructure

An alternative to the 4×7-cell structure is the combination of two 9-cell cavities [Sek 01], see figure 4.9. With an overall length[7] of 2.45 m this 2×9-cell superstructure can be chemically treated, cleaned and tested as one unit. Therefore the established preparation techniques presently used for the 9-cell resonators can be transferred to the 2×9-cell structures. Moreover this superstructure achieves the same high filling factor as the 4×7-cell structure ($F = 85$ %, see table 4.3). Of course the 2×9-cell layout of the TESLA collider would reduce the number of input couplers not as much as the 4×7-cell layout, but the total number of input couplers is still a factor of two lower than in the layout based on separated 9-cell cavities. In addition this has to be balanced against the lower number of helium vessels and tuners. Because of the high filling factor, the reduced number of RF components and the favorable length the 2×9-cell superstructure is expected to become the preferred layout of the TESLA collider [TDR 01].

4.3.3 Some comments to other types of superstructures

The TESLA 9-cell cavities as well as the superstructures presented above have been designed for a linear collider with a high accelerating gradient and a medium beam current (some mA). For other purposes the optimum type of superstructure may differ. Machines with high demands on the HOM damping can profit from superstructures with a lower number of cells per cavity. The HOM couplers at the interconnecting tubes between the shortened cavitis allow to extract higher-order modes even more efficiently. Ideal candidates for such types of superstructures (for instance a 2×5-cell structure) are the proposed Energy Recovery Linacs (ERL's,

[7] The bellows between two neighboring superstructures are included.

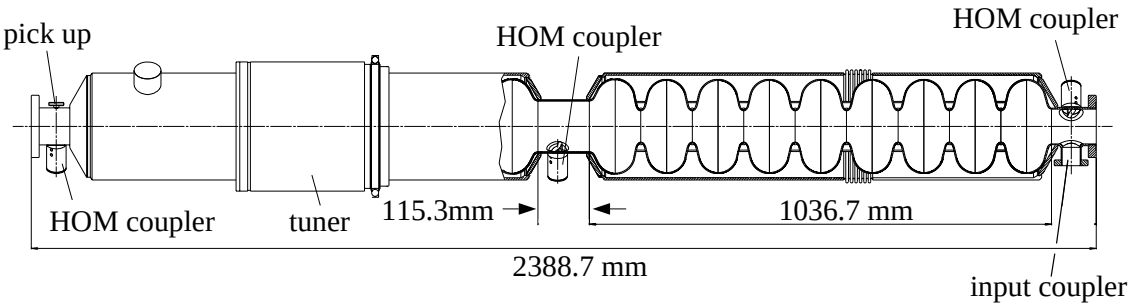

Figure 4.9: Layout of the 2 × 9-cell superstructure. Parameters are listed in table 4.3.

see for example [Gru 00]). They will have a high current recirculating beam[8] in the main linac and a low power transfer by the input couplers. Typical machine parameters under discussion are accelerated beam currents between 10 mA and 100 mA and medium cw gradients of 15 to 20 MV/m.
For beams with a low emittance, a high bunch population or a high average current it may be desirable to enlarge the iris diameter $2r_i$ of the cavities, as compared to the TESLA structures. This leads to a higher surface field for a given accelerating gradient and a lower impedance (R/Q) of the accelerating mode [Sek 98], but on the other hand the loss factor is significantly lowered, since for short bunches the longitudinal loss factor decreases with $1/r_i^2$, see [Nov 98].

[8]After acceleration the beam is routed back to the entrance of the linac, almost 180° out of phase, and decelerated to recover the beam energy. Accordingly the net power transferred to the beam is low (a few kW).

parameter	unit	9-cell	4x7-cell	2x9-cell
L_{total}	[m]	1.30	3.80	2.45
L_{active}	[m]	1.04	3.23	2.08
diameter of intercon. tube	[mm]	-	114	114
diameter of mid-cell iris	[mm]	70	70	70
filling factor	[%]	78.6	84.9	84.8
no. of cells per cavity, N_c	-	9	7	9
no. of cavities per structure, M	-	1	4	2
no. of input couplers per structure	-	1	1	1
no. of HOM couplers per structure	-	2	5	4 (3)
no. of frequency tuners per structure	-	1	4	2
type of structure	-	stand. wave	stand. wave	stand. wave
accelerating mode	-	TM010, π	TM010, π-0	TM010, π-0
fundamental frequency	[MHz]	1300	1300	1300
cell-to-cell coupling $\mathcal{K}_{cc}$	[%]	1.9	1.9	1.9
cavity-to-cavity coupling for π group, $\mathcal{K}_{rr}$	[%]	-	$3.6 \cdot 10^{-2}$	$2.8 \cdot 10^{-2}$
sensitivity factor, $N_c^2/\mathcal{K}_{cc}$	-	4300	2600	4300
(R/Q) per structure	[Ω]	518	1472	986
geometry factor, G	[Ω]	270	275.4	273.2
E_{peak}/E_{acc}	-	2.0	2.0	2.0
B_{peak}/E_{acc}	$\frac{\text{mT}}{\text{MV/m}}$	4.18	4.18	4.18
distance to next resonance	[kHz]	740	158	330
no. of input couplers for TESLA-500GeV	-	20592	7032	10926
no. of HOM couplers for TESLA-500GeV	-	41184	35160	43704 (32778)
no. of tuner, vessels for TESLA-500GeV	-	20592	28128	21852
E_{acc} for TESLA-500GeV	[MV/m]	23.4	22.0	22.0
V_{acc} for TESLA-500GeV	[MV]	24.3	71.1	45.8
Power P_{tr} per RF coupler transm. to 9.5 mA beam	[kW]	232	675	437

Table 4.3: Parameters of the different cavity-chain layouts for the TESLA acclerating system with fixed tunnel length [TDR 01]. The filling factor defined here does not include additional lengths for magnets and module interconnections. Note that the definition $R = V_{acc}/(2P_{wall})$ is used for the shunt impedance R, see section 5.5.

CHAPTER 5

5 A Circuit Model for Coupled Multicell Cavities

Aside from measurements on copper models and prototypes theoretical studies are essential in developing new accelerating RF structures. In common use are numerical codes (for example MAFIA [Kla 86], SUPERFISH [Men 87] and URMEL [Lau 87]) to determine the eigenmode frequencies and their electromagnetic fields in a resonator. On the basis of these computations the parameters of an equivalent circuit model of the accelerating structure can be specified. Once defined, these circuit models allow to study the adjustment of the field amplitudes in the cells (see chapter 6), the transient behaviour and the energy spread of the beam (see chapter 7), as well as the RF field control (see chapter 8). Although we will focus on superstructures in the following chapters, also TESLA 9-cell cavities will be studied as a reference and easier example. This will even allow some new insights into the standard multicell cavities.
In this chapter an equivalent circuit model for coupled multicell cavities will be derived on the basis of the Maxwell equations. We will go through the following steps (see also [Sla 50] for a similar derivation of a differential equation for time dependent field coefficients):

- define a set of orthogonal eigenfunctions for the field in a cavity,
- expand the time dependent electric and magnetic fields in a cavity in terms of these eigenfunctions,
- use the Maxwell equations to find relations between the time dependent expansion coefficients,
- include losses in the walls of the cavity, external losses and a generator drive current,
- include coupling of cells in a multicell cavity and coupling from cavity to cavity in a superstructure and
- transform the obtained differential equation to a circuit diagram with capacitive, inductive and resistive elements.

5.1 A Set of Orthogonal Eigenfunctions

When calculating the electromagnetic fields in a completely enclosed cavity, we have to solve the field equations within the cavity for certain boundary conditions around its surface. A common approach is to expand the electric and magnetic fields in terms of orthogonal eigenfunctions [Sla 50]. These functions are solutions of the vacuum wave equations

$$\left(\nabla^2 - \frac{1}{c^2}\frac{\partial^2}{\partial t^2}\right)\vec{E} = 0 \tag{5.1}$$

$$\left(\nabla^2 - \frac{1}{c^2}\frac{\partial^2}{\partial t^2}\right)\vec{H} = 0 \quad , \tag{5.2}$$

satisfying the boundary conditions for a perfectly conducting cavity surface

$$\vec{n} \times \vec{E} = 0 \qquad \vec{n} \cdot \vec{H} = 0 \quad . \tag{5.3}$$

Here $\vec{n}$ is the outer normal to the cavity surface S. Accordingly the electric field $\vec{E}$ has no tangential component over S, whereas the magnetic field $\vec{H}$ has no component parallel to $\vec{n}$, see figure 5.1.

By general principles of vector analysis, any vector field $\vec{v}$ can be broken up into

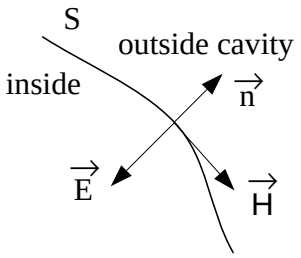

Figure 5.1: Boundary conditions at a perfect conducting surface S with outer normal $\vec{n}$.

two independent parts: one of which is solenoidal ($\vec{\nabla} \cdot \vec{v}_s = 0$) and the other is irrotational ($\vec{\nabla} \times \vec{v}_i = 0$). Consequently also the electric field $\vec{E}$ can be written as a sum of a solenoidal function $\vec{e}(\vec{r})$ and an irrotational function $\vec{f}(\vec{r})$. The irrotational part with $\vec{\nabla} \times \vec{f} = 0$ can be set equal to the gradient of a scalar function Ψ with the boundary condition $\Psi = 0$ at the surface of the cavity

$$\vec{f} = -\vec{\nabla}\Psi \quad . \tag{5.4}$$

From the Maxwell equation $\vec{\nabla} \cdot \vec{D} = \rho$ follows further Poisson's equation

$$\nabla^2\Psi = -\rho/\varepsilon_0 \quad . \tag{5.5}$$

Therefore the irrotational part $\vec{f}$ of the electrical field is the electrostatic field of a given charge distribution within the cavity, which may vary with time. Note that

here the problem of finite velocity of propagation of the disturbance has not been taken into account.
However the fields oscillating in a cavity are given by the solenoidal part of the electric and the magnetic field. In order to expand the electric RF field, we shall define a set of orthogonal solenoidal functions $\vec{e}^{(m)}(\vec{r})$ which are satisfying equation (5.1) with the boundary condition (5.3). The index m denotes the eigenmode. We define

$$\vec{e}^{(m)}(\vec{r}) \;:=\; \sqrt{\frac{\varepsilon_0}{2U^{(m)}}}\vec{E}^{(m)}(\vec{r}) \quad , m = 1, 2, ... \quad , \tag{5.6}$$

with

$$\vec{\nabla} \cdot \vec{e}^{(m)}(\vec{r}) = 0 \quad . \tag{5.7}$$

The eigenmode functions $\vec{e}^{(m)}(\vec{r})$ are normalized with respect to the field energy $U^{(m)}$ stored in the cavity

$$U^{(m)} = \frac{1}{2}\varepsilon_0 \int_V \vec{E}^{(m)}(\vec{r}) \cdot \vec{E}^{(m)}(\vec{r}) dv \quad . \tag{5.8}$$

Exept for some simple cavities like a pill-box cavity, where the eigenmode fields

$$\vec{E}^{(m)}(\vec{r}, t) = \vec{E}^{(m)}(\vec{r}) e^{i\omega^{(m)}t} \tag{5.9}$$

can be calculated analytically (see next section), the eigenmodes $\vec{E}^{(m)}$ have to be calculated numerically. The angular eigenfrequencies $\omega^{(m)}$ are set by the boundary conditions. We can now expand the electric RF field in a loss free cavity in terms of the orthogonal functions

$$\vec{E}(\vec{r}, t) \;=\; \Re e\Big\{ \sum_m \hat{\mathcal{E}}^{(m)} \vec{e}^{(m)}(\vec{r}) e^{i\omega^{(m)}t} \Big\} \quad , \tag{5.10}$$

where $\hat{\mathcal{E}}^{(m)}$ are time independent expansion coefficients.
Similarly we shall expand the magnetic field $\vec{H}$ in a cavity by normal orthogonal modes. The magnetic field itself is solenoidal. Therefore we define a set of orthogonal solenoidal functions by

$$\vec{h}^{(m)}(\vec{r}) \;:=\; \sqrt{\frac{\mu_0}{2U^{(m)}}}\vec{H}^{(m)}(\vec{r}) \quad , m = 1, 2, ... \quad , \tag{5.11}$$

with

$$\vec{\nabla} \cdot \vec{h}^{(m)} = 0 \quad . \tag{5.12}$$

The magnetic eigenmode fields

$$\vec{H}^{(m)}(\vec{r}, t) = \vec{H}^{(m)}(\vec{r}) e^{i\omega^{(m)}t + i\pi/2} \tag{5.13}$$

satisfy (5.2) and correspond to the electric eigenmode fields $\vec{E}^{(m)}(\vec{r}, t)$ for a joint set of eigenfrequencies $\omega^{(m)}$. The phase shift $\pi/2$ follows directly from the Maxwell equation $\vec{\nabla} \times \vec{E} = -\partial\vec{B}/\partial t$, see also equation (5.9). Accordingly the eigenfunctions

$\vec{e}^{(m)}$ and $\vec{h}^{(m)}$ are not independent functions, but related by the Maxwell equations. On the basis of the orthogonal functions $\vec{h}^{(m)}$ we can write for the magnetic field in a loss free cavity

$$\vec{H}(\vec{r},t) \;=\; \Re e\Big\{\sum_m \hat{\mathcal{H}}^{(m)}\vec{h}^{(m)}(\vec{r})e^{i\omega^{(m)}t+i\pi/2}\Big\} \quad , \tag{5.14}$$

where $\hat{\mathcal{H}}^{(m)}$ are the time independent expansion coefficients for the magnetic field. With (5.6), (5.10), (5.11) and (5.14) we find the relation $\hat{\mathcal{E}}^{(m)}/\hat{\mathcal{H}}^{(m)} = \mu_0 c$.
From the general wave equations (5.1) and (5.2) follows with (5.6), (5.9), (5.11) and (5.13)

$$\nabla^2\vec{e}^{(m)} + \left(\frac{\omega^{(m)}}{c}\right)^2\vec{e}^{(m)} = 0 \;, \qquad \nabla^2\vec{h}^{(m)} + \left(\frac{\omega^{(m)}}{c}\right)^2\vec{h}^{(m)} = 0 \quad . \tag{5.15}$$

These equations have an infinite number of independent solutions $\vec{e}^{(m)}$ and $\vec{h}^{(m)}$, corresponding to different eigenvalues $(\omega^{(m)})^2/c^2$. For further discussions we shall derive relations between the electric and magnetic eigenfunctions, $\vec{e}^{(m)}$ and $\vec{h}^{(m)}$ respectively. From Maxwell's equations in vacuum $\vec{\nabla}\times\vec{E}^{(m)}(\vec{r},t) = -\mu_0(\partial\vec{H}^{(m)}(\vec{r},t)/\partial t)$ and $\vec{\nabla}\times\vec{H}^{(m)}(\vec{r},t) = \varepsilon_0(\partial\vec{E}^{(m)}(\vec{r},t)/\partial t)$ we find with (5.6), (5.9), (5.11), (5.13) and $\varepsilon_0\mu_0 = c^{-2}$ the following relations between the functions

$$\vec{\nabla}\times\vec{e}^{(m)} = \frac{\omega^{(m)}}{c}\vec{h}^{(m)} \;, \qquad \vec{\nabla}\times\vec{h}^{(m)} = \frac{\omega^{(m)}}{c}\vec{e}^{(m)} \quad . \tag{5.16}$$

We further get

$$\vec{\nabla}\times(\vec{\nabla}\times\vec{e}^{(m)}) = \left(\frac{\omega^{(m)}}{c}\right)^2\vec{e}^{(m)} \;, \qquad \vec{\nabla}\times(\vec{\nabla}\times\vec{h}^{(m)}) = \left(\frac{\omega^{(m)}}{c}\right)^2\vec{h}^{(m)} \;. \tag{5.17}$$

We shall now prove that the functions $\vec{e}^{(m)}$ and $\vec{h}^{(m)}$ have indeed orthogonality properties with respect to an integration over the cavity volume V

$$\int_V \vec{e}^{(m)}\cdot\vec{e}^{(n)}dv = \delta_{mn} \;, \qquad \int_V \vec{h}^{(m)}\cdot\vec{h}^{(n)}dv = \delta_{mn} \quad , \tag{5.18}$$

where as usual δ_{mn} is unity if $m = n$ and zero if $m \neq n$. To prove the orthogonality of the electric eigenfunction, we use the vector identity [Sla 50]

$$\begin{aligned}\vec{\nabla}\cdot(\vec{e}^{(n)}\times(\vec{\nabla}\times\vec{e}^{(m)})) - \vec{\nabla}\cdot(\vec{e}^{(m)}\times(\vec{\nabla}\times\vec{e}^{(n)})) &= (\vec{\nabla}\times\vec{e}^{(m)})\cdot(\vec{\nabla}\times\vec{e}^{(n)}) \\ -\vec{e}^{(n)}\cdot\vec{\nabla}\times(\vec{\nabla}\times\vec{e}^{(m)}) - (\vec{\nabla}\times\vec{e}^{(m)})\cdot(\vec{\nabla}\times\vec{e}^{(n)}) &+ \vec{e}^{(m)}\cdot\vec{\nabla}\times(\vec{\nabla}\times\vec{e}^{(n)}) \\ = \frac{(\omega^{(n)})^2 - (\omega^{(m)})^2}{c^2}\vec{e}^{(m)}\cdot\vec{e}^{(n)} \quad ,\end{aligned} \tag{5.19}$$

at which in the last step (5.17) has been used. By integrating over the cavity volume V, converting the left side into a surface integral (Gauss's theorem) and inserting (5.16), we get

$$\int_S \vec{n}\cdot\Big(\frac{\omega^{(m)}}{c}\vec{e}^{(n)}\times\vec{h}^{(m)} - \frac{\omega^{(n)}}{c}\vec{e}^{(m)}\times\vec{h}^{(n)}\Big)ds = \frac{(\omega^{(n)})^2 - (\omega^{(m)})^2}{c^2}\int_V \vec{e}^{(m)}\cdot\vec{e}^{(n)}dv \quad . \tag{5.20}$$

The surface integral on the left hand side vanishes because of the boundary conditions (5.3), see also figure 5.1. Usually $(\omega^{(n)})^2 - (\omega^{(m)})^2$ is different from zero for $m \neq n$ and the orthogonality condition (5.18) follows for the functions $\vec{e}^{(m)}$, as we whished to prove. In case of degenerate eigenfrequencies $\omega^{(m)}$ the standard Schmidt orthogonalisation procedure can be used to construct naturally orthogonal eigenfunctions [Bro 89]. The orthogonality condition for the magnetic normal functions $\vec{h}^{(m)}$ can be proven in an entirely analogous manner. Since $\vec{e}^{(m)}$ and $\vec{h}^{(m)}$ are related by (5.16) it has to be proved that these functions can be normalized simultaniously according to (5.18). To prove the consistancy of (5.16) and (5.18) we use the relation (see also (5.16) and (5.17))

$$\begin{aligned} \vec{\nabla} \cdot (\vec{e}^{(m)} \times (\vec{\nabla} \times \vec{e}^{(m)})) &= (\vec{\nabla} \times \vec{e}^{(m)}) \cdot (\vec{\nabla} \times \vec{e}^{(m)}) - \vec{e}^{(m)} \cdot \vec{\nabla} \times (\vec{\nabla} \times \vec{e}^{(m)}) \\ &= \left(\frac{\omega^{(m)}}{c}\right)^2 \vec{h}^{(m)} \cdot \vec{h}^{(m)} - \left(\frac{\omega^{(m)}}{c}\right)^2 \vec{e}^{(m)} \cdot \vec{e}^{(m)} \quad . \end{aligned} \tag{5.21}$$

Again we integrate over the cavity volume V and transform the left side into a surface integral which vanishes on account of the boundary conditions

$$\begin{aligned} \int_V \vec{\nabla} \cdot (\vec{e}^{(m)} \times (\vec{\nabla} \times \vec{e}^{(m)}))dv &= \int_S \vec{n} \cdot (\vec{e}^{(m)} \times (\vec{\nabla} \times \vec{e}^{(m)}))ds = 0 \\ &= \frac{(\omega^{(m)})^2}{c^2}\left\{\int_V \vec{h}^{(m)} \cdot \vec{h}^{(m)} dv - \int_V \vec{e}^{(m)} \cdot \vec{e}^{(m)} dv\right\} \quad . \end{aligned} \tag{5.22}$$

Accordingly $\vec{e}^{(m)}$ and $\vec{h}^{(m)}$ can be normalized simultaniously, such that the volume integrals (5.18) equal unity for $m = n$.
Finally we immediately see that the maximum electric and magnetic field energies are equal

$$\begin{aligned} U_e^{(m)} &= \frac{1}{2}\varepsilon_0 \int_V \vec{E}^{(m)}(\vec{r}) \cdot \vec{E}^{(m)}(\vec{r}) dv = U^{(m)} \int_V \vec{e}^{(m)} \cdot \vec{e}^{(m)} dv = U^{(m)} \\ U_h^{(m)} &= \frac{\mu_0}{2} \int_V \vec{H}^{(m)}(\vec{r}) \cdot \vec{H}^{(m)}(\vec{r}) dv = U^{(m)} \int_V \vec{h}^{(m)} \cdot \vec{h}^{(m)} dv = U^{(m)} \quad . \end{aligned} \tag{5.23}$$

As is well known for a loss free resonator the stored energy oscillates between the electric field and the magnetic field, which are 90° out of phase.
This will end the first step: we have now set up two families of solenoidal functions, which are orthogonal and normalized according to equation (5.18).

5.2 Eigenmodes in a Pill-box cavity

In this section we shall briefly discuss the electromagnetic eigenmodes in a cylindrical pill-box cavity of length L_c and radius R with perfectly conducting surfaces (see [Jack 75] for a detailed discussion). The wave equations (5.1) and (5.2) can be solved analytically for this cavity. One findes that the solutions are Bessel functions, where the lowest frequency mode is described by

$$E_z = E_0 J_0\left(\frac{2.405r}{R}\right) \cos(\omega_0 t) \tag{5.24}$$

$$B_\varphi = \frac{-E_0}{c} J_1\left(\frac{2.405r}{R}\right) \sin(\omega_0 t) \quad . \tag{5.25}$$

All other field components vanish. The zeroth order and first order Bessel functions are denoted by J_0 and J_1 respectively. The electric field vanishes at the radius of the pill-box cavity on account of the first zero of J_0 at 2.405. The resonant frequency of this mode is given by

$$\omega_0 = \frac{2.405c}{R} \quad , \tag{5.26}$$

which is independent of the cavity length. The field pattern of this so-called TM_{010} mode is shown in figure 5.2.

For a pill-box cavity the solutions of the wave equations form two sets of modes, denoted transverse magnetic (TM) modes and transverse electric (TE) modes. TM modes have a longitudinal component of the electric field with respect to the cavity axis (z axis), whereas the magnetic field is transverse everywhere. In contrast to this, TE modes have a longitudinal component of the magnetic field and the electric field is transverse everywhere. The pill-box TM modes are classified by three integer indices and the nomenclature TM_{abp}. The corresponding electric field in z direction is

$$E_z = E_0 \cos\left(\frac{p\pi z}{L_c}\right) J_a\left(\frac{u_{ab} r}{R}\right) \cos\left(a\varphi\right) \quad , \tag{5.27}$$

where u_{ab} is the bth root of the ath order Bessel function J_a. Accordingly the meaning of this indices is as follows:

- Modes with $a = 0$ are rotationally symmetric with respect to the cavity axis z. These so-called monopole modes have a non vanishing longitudinal component of the electric field at the beam axis, since $J_0(0) = 1$. Note that for all other Bessel functions $J_a(0) = 0$, $a \neq 0$. Therefore only modes of the type TM_{0bp} are useful for beam acceleration. Modes with $a = 1$ are called dipole modes because of their field distribution, see figure 5.2. These modes have a net deflecting field on the beam axis and are therefore undesirable in accelerating cavities, but may be used to deflect a beam. Further modes with $a = 2$ are called quadrupole modes, and so on, see (5.27).

- According to equation (5.27), the electric field vanishes at the cylinder wall of the pill-box ($r = R$) on account of the bth root of J_a. Thus b gives the number of sign changes E_z undergoes in radial direction.

- Finally the index p measures the number of sign changes E_z undergoes along the cavity axis (z direction), see also figure 5.2.

The group of TE modes is classified in a similar manner. In an ideal pill-box cavity the TE modes have no longitudinal electric field and thus cannot accelerate the beam nor can the beam excite them. As an example the field pattern of the TE_{111} mode is shown in figure 5.2.

For the elliptical shape of the TESLA cells one can identify eigenmodes similar to the TM and TE modes discussed above. Therefore the same nomenclature is used to classify the modes in elliptical cavities. However, the TM modes have now a non vanishing longitudinal magnetic field and the TE modes a longitudinal electric

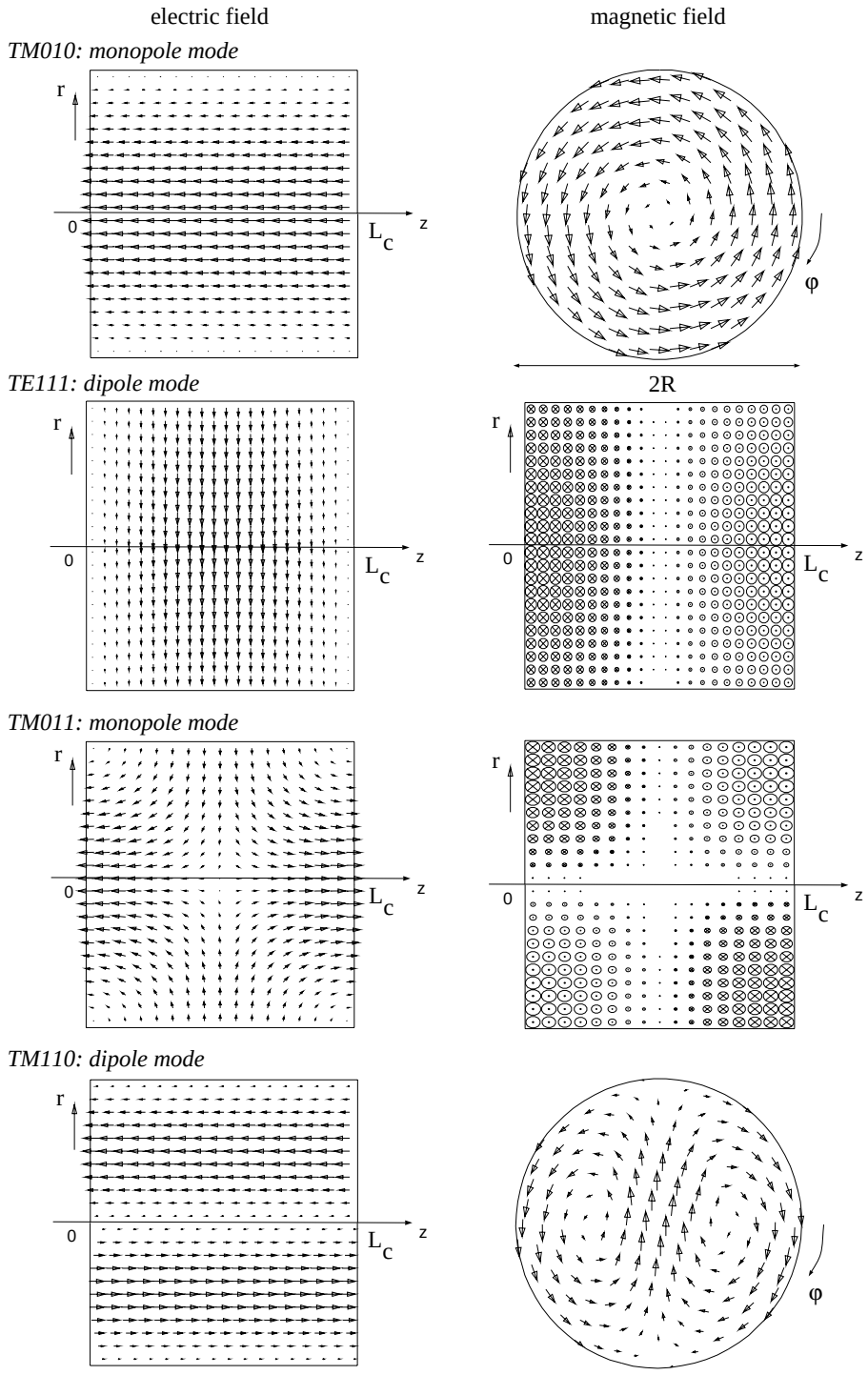

Figure 5.2: Vector plots for selected eigenmode fields in a cylindrical pill-box cavity. The size of the arrows indicates the relative amplitude of the electric field (left column) and the magnetic field (right column) within the cavity.

field. Thus the beam can excite TM as well as TE modes, and both types have to be considered when the beam disruption by higher order modes is studied, see

chapter 9. With increasing frequency a seperation into TM and TE modes becomes less and less meaningful. Accordingly these modes are called hybride modes. Usually from the TM_{0bp} group of modes the TM_{010} mode is chosen for beam acceleration because it has the lowest frequency and the simplest field pattern.
In the following as in the preceding section we will use the superscript m to number consecutively the different eigenmodes of a cavity, starting with the lowest frequency mode. In a TESLA cell the TM_{010} mode has the lowest frequency. Accordingly $\vec{E}^{(1)}$ is the electric field of the TM_{010} mode in the cell.

5.3 Expansion of the RF Fields in a Cavity

In this section we shall expand the electric and magnetic fields within a cavity in terms of the orthogonal eigenfunctions $\vec{e}^{(m)}$ and $\vec{h}^{(m)}$ set up in section 5.1 for the electric and magnetic field respectively. Thus we have for the solenoidal RF fields

$$\vec{E}(\vec{r},t) = \Re e\Big\{\sum_m \mathcal{E}^{(m)}(t)\vec{e}^{(m)}(\vec{r})\Big\} \tag{5.28}$$

$$\vec{H}(\vec{r},t) = \Re e\Big\{\sum_m \mathcal{H}^{(m)}(t)\vec{h}^{(m)}(\vec{r})\Big\} \quad . \tag{5.29}$$

Note that the electrostatic field of any charge distribution within the cavity is not included in this expansion series. In the following section we will insert the expansion series into the Maxwell equations in order to find differential equations for the time dependent expansion coefficients $\mathcal{E}^{(m)}(t)$ and $\mathcal{H}^{(m)}(t)$. From the expansion coefficients the average electric and magnetic field energy within the cavity can be directly calculated

$$\overline{U}_e(t) = \frac{1}{4}\varepsilon_0 \sum_m \mathcal{E}^{(m)}(t)(\mathcal{E}^{(m)}(t))^* \tag{5.30}$$

$$\overline{U}_h(t) = \frac{1}{4}\mu_0 \sum_m \mathcal{H}^{(m)}(t)(\mathcal{H}^{(m)}(t))^* \quad . \tag{5.31}$$

Further we will need the following equations

$$\begin{aligned}\vec{\nabla}\times\vec{E}(\vec{r},t) &= \Re e\Big\{\sum_m \mathcal{E}^{(m)}(t)\vec{\nabla}\times\vec{e}^{(m)}(\vec{r})\Big\} \\ &= \Re e\Big\{\sum_m \mathcal{E}^{(m)}(t)\frac{\omega^{(m)}}{c}\vec{h}^{(m)}(\vec{r})\Big\} \qquad (5.32)\\ \vec{\nabla}\times\vec{H}(\vec{r},t) &= \Re e\Big\{\sum_m \mathcal{H}^{(m)}(t)\vec{\nabla}\times\vec{h}^{(m)}(\vec{r})\Big\} \\ &= \Re e\Big\{\sum_m \mathcal{H}^{(m)}(t)\frac{\omega^{(m)}}{c}\vec{e}^{(m)}(\vec{r})\Big\} \quad , \qquad (5.33)\end{aligned}$$

in which we have used (5.16).

5.4 Differential Equation for the Time Dependent Expansion Coefficients

The next step and object of this section is to insert the expansion series for the fields into Maxwell's equations. This will result in differential equations, which the expansion coefficients have to satisfy. From the Maxwell equation $\vec{\nabla}\times\vec{H} = \partial\vec{D}/\partial t+\vec{j}$ and (5.16) we have

$$\sum_m \mathcal{H}^{(m)}(t)\frac{\omega^{(m)}}{c}\vec{e}^{(m)}(\vec{r}) \;=\; \sum_m \varepsilon_0\frac{d\mathcal{E}^{(m)}(t)}{dt}\vec{e}^{(m)}(\vec{r}) + \frac{\partial\vec{f}}{\partial t} + \vec{j}(\vec{r},t) \quad , \quad (5.34)$$

where $\vec{j}(\vec{r},t)$ is the current density in the cavity and $\vec{f}$ is the irrotational part of the electric field in the cavity, which is related to charges within the cavity. We shall now use the orthogonality of the eigenfunctions (note that the solenoidal and the irrotational part of the electrical field are naturally orthogonal) to separate the differential equation for the individual eigenmodes m. Therefore we multiply by $\vec{e}^{(m)}$ and integrate over the volume of the cavity. This leads to a set of differential equations for the expansion coefficients of the solenoidal RF field

$$\frac{\omega^{(m)}}{c}\mathcal{H}^{(m)}(t) - \varepsilon_0\frac{d}{dt}\mathcal{E}^{(m)}(t) \;=\; \int_V \vec{j}(\vec{r},t)\cdot\vec{e}^{(m)}(\vec{r})dv \quad , m = 1,2,... \quad . \quad (5.35)$$

Similarly from $\vec{\nabla}\times\vec{E} = -\partial\vec{B}/\partial t$ we have

$$\sum_m \mathcal{E}^{(m)}(t)\frac{\omega^{(m)}}{c}\vec{h}^{(m)}(\vec{r}) \;=\; -\mu_0\sum_m \vec{h}^{(m)}(\vec{r})\frac{d}{dt}\mathcal{H}^{(m)}(t) \quad , \quad (5.36)$$

where (5.16) has been used. Again we separate the eigenmodes m by multiplying this equation by $\vec{h}^{(m)}$ and integrating over the cavity volume. We find

$$\frac{\omega^{(m)}}{c}\mathcal{E}^{(m)}(t) + \mu_0\frac{d}{dt}\mathcal{H}^{(m)}(t) \;=\; 0 \quad , m = 1,2,... \quad . \quad (5.37)$$

We shall now consider an additional small tangential component $\vec{E}_{tan}$ of the electric field at the surface S of the cavity [Sla 50]. As we shall shortly see, this gives the possibility to include wall losses and coupling between cells in a multicell cavity. We shall treat the tangential field as a small perturbation of the eigenmode fields of a loss free cavity. Since $\vec{e}^{(m)}\cdot\vec{E}_{tan}$ equals zero at the surface of the cavity, the tangential surface field gives no contribution to equation (5.35), whereas we have an additional therm on the left hand side of equation (5.37)

$$\begin{aligned}
\int_V \vec{h}^{(m)}\cdot\vec{\nabla}\times\vec{E}_{tan}dv &= \frac{c}{\omega^{(m)}}\int_V(\vec{\nabla}\times\vec{e}^{(m)})\cdot(\vec{\nabla}\times\vec{E}_{tan})dv \\
&= \frac{c}{\omega^{(m)}}\int_V\Big\{\vec{\nabla}\cdot(\vec{E}_{tan}\times(\vec{\nabla}\times\vec{e}^{(m)})) + \vec{E}_{tan}\cdot\vec{\nabla}\times(\vec{\nabla}\times\vec{e}^{(m)})\Big\}dv \\
&= \frac{c}{\omega^{(m)}}\int_S\vec{n}\cdot(\vec{E}_{tan}\times(\vec{\nabla}\times\vec{e}^{(m)}))ds + \frac{\omega^{(m)}}{c}\int_V\vec{E}_{tan}\cdot\vec{e}^{(m)}dv \\
&= \int_S\vec{n}\cdot(\vec{E}_{tan}\times\vec{h}^{(m)})ds = \int_S(\vec{n}\times\vec{E}_{tan})\cdot\vec{h}^{(m)}ds \quad . \quad (5.38)
\end{aligned}$$

Accordingly we have now for the amplitude coefficients the differential equation

$$\frac{\omega^{(m)}}{c}\mathcal{E}^{(m)}(t) + \mu_0 \frac{d}{dt}\mathcal{H}^{(m)}(t) = -\int_S (\vec{n} \times \vec{E}_{tan}) \cdot \vec{h}^{(m)} ds \quad , m = 1, 2, \ldots \quad (5.39)$$

The equations (5.35) and (5.39) determine the amplitude coefficients of the RF eigenmode fields in a cavity as function of time. It is convenient to combine (5.35) and (5.39) to get separate differential equations for the coefficients of the electric and magnetic fields. We finally obtain [Sla 50]

$$\frac{d^2}{dt^2}\mathcal{E}^{(m)}(t) + (\omega^{(m)})^2 \mathcal{E}^{(m)}(t) = -\frac{1}{\varepsilon_0}\frac{d}{dt}\int_V \vec{j} \cdot \vec{e}^{(m)} dv - c\omega^{(m)} \int_S (\vec{n} \times \vec{E}_{tan}) \cdot \vec{h}^{(m)} ds \quad (5.40)$$

$$\frac{d^2}{dt^2}\mathcal{H}^{(m)}(t) + (\omega^{(m)})^2 \mathcal{H}^{(m)}(t) = c\omega^{(m)} \int_V \vec{j} \cdot \vec{e}^{(m)} dv - \frac{1}{\mu_0}\frac{d}{dt}\int_S (\vec{n} \times \vec{E}_{tan}) \cdot \vec{h}^{(m)} ds \, . \quad (5.41)$$

The terms on the right hand side correspond to the external forces in the problem of a simple harmonic oscillator. Here the "forces" are currents within the cavity, or disturbances originated from the walls. Our later discussion in this chapter will rely on these differential equations.

5.5 Losses and a Generator Drive

The differential equations (5.40) and (5.41) have no explicit damping term, but as we shall see, by means of the terms on the right hand side we can include them. Later in this section we shall also add a term representing a RF source connected to the cavity.

Wall losses

First we will consider losses in the wall of the cavity which are assumed to have uniform finite conductivity σ. Furthermore we shall assume that the fields which are propagating into the wall vary sinusoidally with time. Accordingly we use the ansatz $\exp(i\omega t)$ for the time dependence of the fields. Maxwell's equations within the wall become then

$$\vec{\nabla} \times \vec{E} = -i\mu_0 \omega \vec{H} \quad \text{and} \quad \vec{\nabla} \times \vec{H} = (\sigma + i\varepsilon_0 \omega)\vec{E} \quad . \quad (5.42)$$

We can consider the cavity wall as a locally plane surface. As is well known the equations (5.42) have then a solution in form of a locally plane wave. If $\vec{n}$ is the outer normal of the cavity surface and x the depth in the cavity wall in direction of $\vec{n}$, so that $x = 0$ at the surface, we shall use the ansatz $\exp(i\omega t - kx)$ for the variaton of $\vec{E}$ and $\vec{H}$ with time t and depth x. Equations (5.42) take the form (with $\vec{n} \times \vec{n} \times \vec{H} = -\vec{H}$)

$$k\vec{n} \times \vec{E} = i\mu_0 \omega \vec{H} \quad \text{and} \quad k\vec{H} = (\sigma + i\varepsilon_0 \omega)\vec{n} \times \vec{E} \quad (5.43)$$

for the propagating fields. From these equations we can derive that the propagation constant k is given by

$$k = \sqrt{-\frac{\omega^2}{c^2}\left(1 - i\frac{\sigma}{\varepsilon_0\omega}\right)} \quad . \tag{5.44}$$

We immediately see from (5.44) that in a conducting medium the fields propagate with attenuation. For a good conductor and not too high frequencies we have $\sigma/(\varepsilon_0\omega) \gg 1$. For copper this is valid for frequencies up to the THz range, but not at optical frequencies. Accordingly for our 1.3 GHz cavities we can use

$$\begin{aligned} \vec{n} \times \vec{E} = \vec{n} \times \vec{E}_{tan} &= \sqrt{\frac{\mu_0}{\varepsilon_0(1 - i\frac{\sigma}{\varepsilon_0\omega})}}\vec{H} \\ &\approx (1+i)\sqrt{\frac{\mu_0\omega}{2\sigma}}\vec{H} \quad \text{for} \quad \frac{\sigma}{\varepsilon_0\omega} \gg 1 \quad , \end{aligned} \tag{5.45}$$

where $\vec{E}_{tan}$ denotes the component of the electric field which is tangential to the surface, i.e. $\vec{n}\cdot\vec{E}_{tan} = 0$. This means that in a good conductor the displacement current $\partial\vec{D}/\partial t$ can be neglected in comparison with the conduction current. Accordingly we have

$$k \approx (1+i)\sqrt{\frac{\mu_0\sigma\omega}{2}} \tag{5.46}$$

for the propagation constant in a good conductor. The value of $\vec{E}$ in the conductor gets smaller and smaller, relative to $\vec{H}$, as the conductivity σ increases, see (5.45). In a good conductor $\vec{E}$ is much smaller than in empty space. Furthermore, the amplitude of the fields is attenuated to $1/e$ of its value in the skin depth $\delta_s = \sqrt{2/\mu_0\sigma\omega}$. At the cavity wall, i.e. a surface of discontinuity between a conductor and empty space, the tangential component of $\vec{H}$ is continous, because genuine surface currents do not exist. In normal conductors the high frequency currents penetrate into the bulk material with exponential attenuation e^{-x/δ_s}. In superconductors the attenuation length is the so-called London penetration depth [Pad 98]. Moreover on account of the condition $\vec{n} \times (\vec{E}_{inside} - \vec{E}_{outside}) = 0$ at the surface, a small tangential component $\vec{E}_{tan}$ of the electric fields exists outside the cavity surface, see also [Jack 75]. The small tangential component at the surface S is given by equation (5.45) for $\vec{H} = \vec{H}|_S$. This shows the relevance of considering a tangential component of the electric surface field in the differential equations of the previous section. Because of the small tangential component of the electric field and the tangential magnetic field outside the cavity surface, energy flows into the wall of the cavity. The average power flow per unit area is given by the Poynting vector at the surface S

$$\frac{d\overline{P}_{wall}}{ds} = \frac{1}{2}\Re e\{\vec{n}\cdot(\vec{E}\times\vec{H}^*)\}\Big|_S = \frac{1}{2}\sqrt{\frac{\mu_0\omega}{2\sigma}}\vec{H}\cdot\vec{H}^*\Big|_S \quad . \tag{5.47}$$

We shall consider now the tangential electric field as a small perturbation and assume that the tangential magnetic field at the wall remains unaffected by the losses in the wall. Further we consider the case that only the eigenmode m is excited in the

cavity. Then the surface field is given by $\mathcal{H}^{(m)}\vec{h}^{(m)}|_S$. Accordingly the average power dissipated in the cavity wall is given by

$$\begin{aligned} \overline{P}^{(m)}_{wall} &= \frac{1}{2}\sqrt{\frac{\mu_0\omega^{(m)}}{2\sigma}}\mathcal{H}^{(m)}(\mathcal{H}^{(m)})^* \int_S \vec{h}^{(m)}\cdot\vec{h}^{(m)}ds \\ &= \frac{1}{2}R_s\mathcal{H}^{(m)}(\mathcal{H}^{(m)})^* \int_S \vec{h}^{(m)}\cdot\vec{h}^{(m)}ds \quad , \end{aligned} \tag{5.48}$$

where we have introduced the surface resistance

$$R_s^{(m)} := \sqrt{\frac{\mu_0\omega^{(m)}}{2\sigma}} = \frac{1}{\sigma\delta_s} \quad . \tag{5.49}$$

Note that here we have assumed that the mode is oscillating with its eigenfrequency $\omega^{(m)}$. If the mode gets excited by a angular frequency ω_g different from its eigenfrequency, the field will have significant amplitudes only near to the resonance[1]. Accordingly we may neglect the difference between ω_g and $\omega^{(m)}$ when calculating wall losses. Moreover we should notice that (5.49) is valid only for normal conducting cavities. In case of superconductivity, the surface resistance is given by the expression

$$R^{(m)}_{s,BCS} \propto \frac{(\omega^{(m)})^2}{T}e^{-1.76T_c/T} \quad , \tag{5.50}$$

according to the Bardeen-Cooper-Schrieffer (BCS) theory, where T_c is the critical temperature of the superconductor. Nevertheless we can asssume that the mode is oscillating with its eigenfrequency $\omega^{(m)}$. It is convenient to introduce a quantity Q_0, the so-called unloaded quality factor

$$\frac{1}{Q_0^{(m)}} := \frac{\overline{P}^{(m)}_{wall}}{\omega^{(m)}U^{(m)}} = \frac{R_s^{(m)}}{\mu_0\omega^{(m)}}\int_S \vec{h}^{(m)}\cdot\vec{h}^{(m)}ds \quad , \tag{5.51}$$

related to the wall losses in a cavity. This dimensionless quantity characterizes the wall losses relative to the stored energy $U^{(m)}$ in the cavity, and does not depend on the field amplitude. Typical values are 10^4 for normal conducting 1.3 GHz cavities and 10^{10} for superconducting 1.3 GHz cavities. A frequently used quantity is the geometry constant G, defined as

$$G^{(m)} := Q_0^{(m)}R_s^{(m)} = \frac{\mu_0\omega^{(m)}}{\int_S \vec{h}^{(m)}\cdot\vec{h}^{(m)}ds} \quad . \tag{5.52}$$

Obviously this quantity depends only on the geometry of the cavity and not on its surface resistance. Moreover by scaling the cavity's linear dimensions by a factor a, one findes that $\omega^{(m)} \propto 1/a$ and that $\int_S \vec{h}^{(m)}\cdot\vec{h}^{(m)}ds \propto 1/a$. Therefore the geometry factor depends on the cavity shape and the eigenmode m, but not on the cavity size. This makes G useful for comparing different cavity shapes. Another important

[1]Normalconducting 1.3 GHz cavities have a relative bandwidth of the resonance curve of $\omega_{1/2}/\omega < 10^{-4}$. For superconducting cavities this factor is much smaller, see also figure 4.4.

quantity is the shunt impedance $R^{(m)}$, used to characterize the wall losses in relation to the maximum accelerating voltage of a cavity, and defined as

$$R_{sh}^{(m)} := \frac{(V_{acc}^{(m)})^2}{2\overline{P}_{wall}^{(m)}} \quad . \tag{5.53}$$

The maximum accelerating voltage V_{acc} of the cavity is given by a line integral along the axis of the cavity

$$\begin{aligned} V_{acc}^{(m)} &= \frac{\text{maximum energy gain possible during transit for mode } m}{\text{charge of the accelerated particle}} \\ &= \left| \int_{-L_c/2}^{L_c/2} E_z^{(m)}(r=0,z) e^{i\omega^{(m)} \frac{z}{\beta c}} dz \right| \quad . \end{aligned} \tag{5.54}$$

Here L_c represents the length of the cavity and $\beta = v/c$ is the normalized particle velocity. Ideally we want the shunt impedance to be large for the accelerating mode, to minimize the dissipated power. This is particularly important for normal conducting cavities. Unfortunately another definition exists for the shunt impedance of a cavity

$$R_{sh,a}^{(m)} := \frac{(V_{acc}^{(m)})^2}{\overline{P}_{wall}^{(m)}} \quad , \tag{5.55}$$

where $R_{sh,a}^{(m)}$ is in ohms per cavity, differing by a factor of 2 from the definition (5.53). Further the shunt impedance per unit length

$$r_{sh,a}^{(m)} := \frac{(E_{acc}^{(m)})^2}{\overline{P}_{wall}^{(m)\prime}} \quad , \tag{5.56}$$

is sometimes used. Here $r_{sh,a}^{(m)}$ is in ohms per meter and $\overline{P}_{wall}^{(m)\prime}$ is the average dissipated power per unit length. The accelerating gradient of a cavity $E_{acc}^{(m)}$ is defined as

$$E_{acc}^{(m)} := \frac{V_{acc}^{(m)}}{\text{active length of the cavity}} \quad . \tag{5.57}$$

In the following the definition (5.53) is used, which is compatible with the standard nomenclature in ac circuits. The ratio $(R_{sh}^{(m)}/Q_0^{(m)})$ of the shunt impedance and the unloaded quality factor is given by

$$\left(\frac{R_{sh}}{Q_0}\right)^{(m)} := \frac{(V_{acc}^{(m)})^2}{2\omega^{(m)} U^{(m)}} = \frac{1}{\varepsilon_0 \omega^{(m)}} \Big\{ \int_{-L/2}^{L/2} e_z^{(m)}(r=0,z) e^{i\omega^{(m)} \frac{z}{\beta c}} dz \Big\}^2 \quad , \tag{5.58}$$

which is independent of the surface resistance. For a given cavity shape and eigenmode, this quantity is also independent of the cavity size, since the line integral scales inversely with the cavity's linear dimensions. The ratio $(R_{sh}^{(m)}/Q_0^{(m)})$ is frequently used for determining the level of interaction between the mode m and the beam, see chapter 9. As $(R_{sh}^{(m)}/Q_0^{(m)})$ of a mode inreases, the accelerating voltage seen by the beam increases, normalized to the stored energy of a mode.

We shall now omit the restriction to one mode and assume that each mode n, $n = 1, 2, ...$, is excited in the cavity with amplitude $\mathcal{H}^{(n)}$. As for equation (5.48) we consider the tangential electric surface field as a small perturbation to the eigenmode fields. Than we have for the surface integral on the right hand side of the differential equation (5.40)

$$\int_S (\vec{n} \times \vec{E}_{tan}) \cdot \vec{h}^{(m)} ds \;=\; (1+i) \sum_n R_s^{(n)} \mathcal{H}^{(n)}(t) \int_S \vec{h}^{(n)} \cdot \vec{h}^{(m)} ds \qquad , \quad (5.59)$$

see (5.29), (5.45) and (5.49). To describe a cavity with wall losses, we add this term to the differential equation (5.40). As we see from (5.59), the differential equations for the eigenmode amplitudes become coupled by means of the wall losses. The physical reason is that the losses are proportional to the square of the magnetic field, see (5.48). Accordingly if several modes are excited simultaneously, the losses must be computed from the complete field. Fortunately, for some important cases the coupling of the eigenmodes vanishes or can be neglected. Firstly the fields in a cavity are normally excited by a frequency near to one resonance m, usually the mode used for beam acceleration. Then the amplitude of the resonant mode dominates. Further we may assume, that the surface integral on the right side of equation (5.59) is small or even zero for $n \neq m$. As we shall see later, this is fulfilled by the group of the TM_{010} modes of a multicell cavity, from which one mode is normally used for beam acceleration. We shall focus on these modes in the following and therefore use

$$\begin{aligned} \int_S (\vec{n} \times \vec{E}_{tan}) \cdot \vec{h}^{(m)} ds &= (1+i) R_s^{(m)} \mathcal{H}^{(m)}(t) \int_S \vec{h}^{(m)} \cdot \vec{h}^{(m)} ds \\ &= (1+i) \mu_0 \frac{\omega^{(m)}}{Q_0^{(m)}} \mathcal{H}^{(m)}(t) \qquad , \end{aligned} \quad (5.60)$$

with the unloaded quality factor $Q_0^{(m)}$ of mode m.

External load

To excite a resonant mode of a cavity one has to power the cavity by a RF source. Thereby the power is carried to the cavity via a coaxial antenna or a waveguide coupler. This power coupler connects the cavity not only to the RF generator, but also to an external load, see figure 5.3. Part of the incoming RF power is reflected

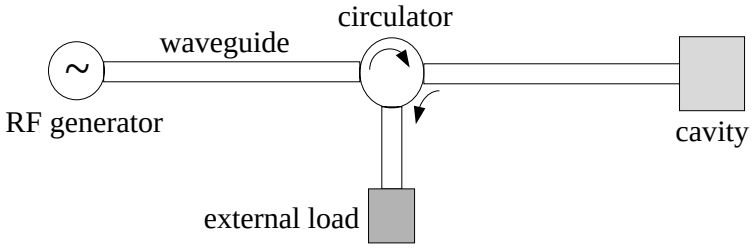

Figure 5.3: Waveguide system with RF source, external load and a cavity.

at the input coupler and is therefore lost for beam acceleration. By proper choice of

the external load the power transferred to the beam can be maximized, see section 5.8 and [Schi 98]. We shall describe the external losses by a current density [Fer 96]

$$\vec{j}_c(t,\vec{r}) = \sigma_c(\vec{r})\vec{E}(t,\vec{r}) = \sigma_c(\vec{r})\sum_k \mathcal{E}^{(k)}(t)\vec{e}^{(k)}(\vec{r}) \qquad , \tag{5.61}$$

which is *driven by the electric field* (5.28) in the cavity at the input coupler location. This current density contributes to the right hand side of the differential equation (5.40), which determines the amplitude coefficients of the electric eigenmode fields in the cavity. Accordingly we have for the integral

$$\begin{aligned} \frac{1}{\varepsilon_0}\frac{d}{dt}\int_V \vec{j}_c \cdot \vec{e}^{(m)} dv &= \frac{1}{\varepsilon_0}\sum_k \frac{d\mathcal{E}^{(k)}(t)}{dt}\int_V \sigma_c(\vec{r})\vec{e}^{(k)}(\vec{r})\cdot\vec{e}^{(m)}(\vec{r})dv \\ &= \sum_k \frac{\omega^{(m)}}{Q_e^{(km)}}\frac{d\mathcal{E}^{(k)}(t)}{dt} \qquad . \end{aligned} \tag{5.62}$$

Similar to the wall losses, where we have defined the unloaded quality factor $Q_0^{(m)}$ for mode m, we introduce here the so-called external quality factors

$$\frac{1}{Q_e^{(km)}} := \frac{1}{\varepsilon_0\omega^{(m)}}\int_V \sigma_c(\vec{r})\vec{e}^{(k)}(\vec{r})\cdot\vec{e}^{(m)}(\vec{r})dv \qquad . \tag{5.63}$$

We notice that by means of the external losses the differential equations for the eigenmode amplitudes become again coupled. The reason for this is a coupling of the eigenmodes via the current density $\vec{j}_c(t,\vec{r})$ at the power coupler.

Driving RF source

The last object of this section is to add a generator current to the differential equation (5.40) of the amplitude coefficients. We represent the RF generator by a current density at the coupler location

$$\vec{j}_g(t,\vec{r}) = \Re e\{J_g(t)\vec{f}_g(\vec{r})\} \qquad , \tag{5.64}$$

with $J_g = \hat{J}_g e^{i\omega_g t}$. Accordingly we find for the integral on the right hand side of (5.40)

$$\begin{aligned} \frac{1}{\varepsilon_0}\frac{d}{dt}\int_V \vec{j}_g \cdot \vec{e}^{(m)} dv &= \frac{1}{\varepsilon_0}\frac{d}{dt}J_g(t)\int_V \vec{f}_g(\vec{r})\cdot\vec{e}^{(m)}(\vec{r})dv \\ &= \frac{1}{\varepsilon_0}K_g^{(m)}\frac{d}{dt}J_g(t) \qquad , \end{aligned} \tag{5.65}$$

where we have defined

$$K_g^{(m)} = \int_V \vec{f}_g(\vec{r})\cdot\vec{e}^{(m)}(\vec{r})dv \qquad . \tag{5.66}$$

Now we shall add the term for the wall losses (5.60), the external load (5.62) and the RF generator (5.65) to the differential equation (5.40), which determines the

amplitude coefficients of the electric eigenmode fields in the cavity. Thus we have for a driven cavity with losses (with (5.35))

$$\begin{aligned}\frac{d^2\mathcal{E}^{(m)}}{dt^2} &+ \frac{\omega^{(m)}}{Q_0^{(m)}}(1+i)\frac{d\mathcal{E}^{(m)}}{dt} + \sum_k \frac{\omega^{(m)}}{Q_e^{(km)}}\left\{\frac{d\mathcal{E}^{(k)}}{dt} + \frac{\omega^{(m)}}{Q_0^{(m)}}(1+i)\mathcal{E}^{(k)}\right\} + (\omega^{(m)})^2\mathcal{E}^{(m)} \\ &= -\frac{K_g^{(m)}}{\varepsilon_0}\left\{\frac{d}{dt}J_g + \frac{\omega^{(m)}}{Q_0^{(m)}}(1+i)J_g\right\} \quad . \end{aligned} \tag{5.67}$$

Since the field in the cavity is normally excited with a frequency near to the resonances of the eigenmodes and $1/Q_e^{(km)} \ll 1$ as well as $1/Q_0^{(m)} \ll 1$ for RF cavities, we find in good approximation

$$\begin{aligned}\frac{d^2\mathcal{E}^{(m)}}{dt^2} &+ \frac{\omega^{(m)}}{Q_0^{(m)}}(1+i)\frac{d\mathcal{E}^{(m)}}{dt} + \sum_k \frac{\omega^{(m)}}{Q_e^{(km)}}\frac{d\mathcal{E}^{(k)}}{dt} + (\omega^{(m)})^2\mathcal{E}^{(m)} \\ &= -\frac{K_g^{(m)}}{\varepsilon_0}\frac{d}{dt}J_g \quad . \end{aligned} \tag{5.68}$$

5.6 Coupling from Cell to Cell and from Cavity to Cavity

The object of this section is to derive a differential equation for the accelerating field in *multicell cavities*. In the TESLA cavities, as in almost all standing-wave RF cavities, the so-called TM_{010} mode is used for beam acceleration, see also section 5.2. For a single cell cavity we can assume that only the accelerating TM_{010} mode is excited by a RF source via the input coupler. This is justified, since the bandwidth of the neighboring modes is in general very narrow as compared to the frequency spacing of the modes. Accordingly only the TM_{010} mode is excited with a significant amplitude, wheras the excitation of other modes can be neglected. Note that this is no longer true for multicell cavities, as we shall see later. Hence we have for the amplitude coefficient of the accelerating mode in a *single cell* cavity

$$\frac{d^2\mathcal{E}^{(1)}}{dt^2} + \left\{\frac{\omega^{(1)}}{Q_0^{(1)}}(1+i) + \frac{\omega^{(1)}}{Q_e^{(1,1)}}\right\}\frac{d\mathcal{E}^{(1)}}{dt} + (\omega^{(1)})^2\mathcal{E}^{(1)} = -\frac{K_g^{(1)}}{\varepsilon_0}\frac{d}{dt}J_g \quad , \tag{5.69}$$

as follows from the differential equation (5.68). Here $m = 1$ denotes the TM_{010} mode. The corresponding eigenfunctions $\vec{e}^{(1)}$ and $\vec{h}^{(1)}$ of the electric and magnetic fields are shown in figure 5.4 for an elliptically shaped cell. If we assume for the moment $J_g = 0$, and use the ansatz $\mathcal{E}^{(1)} = \mathcal{E}_0^{(1)} \exp(-\omega_{1/2}t + i\omega t)$ to solve (5.69), we find for the bandwidth $\omega_{1/2}$ of the mode to the first order (recall that $1/Q_0^{(1)}$ and $1/Q_e^{(1,1)}$ are generally small in RF cavities)

$$\omega_{1/2} \approx \frac{\omega^{(1)}}{2}\left\{\frac{1}{Q_0^{(1)}} + \frac{1}{Q_e^{(1,1)}}\right\} = \frac{\omega^{(1)}}{2Q^{(1)}} \quad . \tag{5.70}$$

Here we introduce the so-called loaded quality factor $Q^{(1)}$ of the TM_{010} mode. Accordingly, for the angular frequency of the RF field we have

$$\omega \approx \omega^{(1)} - \frac{\omega^{(1)}}{2Q_0^{(1)}} \quad . \tag{5.71}$$

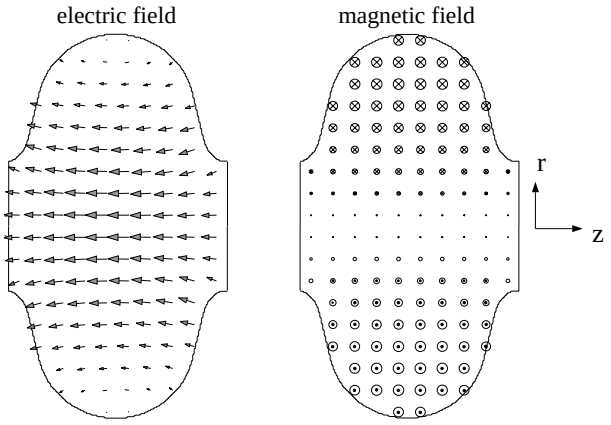

Figure 5.4: TM_{010} mode in a elliptical single cell cavity (numerical calculation). This mode is used for beam acceleration.

We see that the frequency has a first order correction on account of the complex wall loss term $i\omega^{(1)}/Q_0^{(1)}$ in (5.69). For normal conducting 1.3 GHz RF cavities with a unloaded quality factor in the order of 10^4 this correction is small, but has to be considered in an accurate frequency determination. For superconducting cavities with $Q_0^{(1)} \approx 10^{10}$ we can neglect this frequency shift.
We shall now consider a multicell cavity by joining individual cells as shown in figure 5.5. The fields in the cells are coupled through holes, which are cut in the surface of

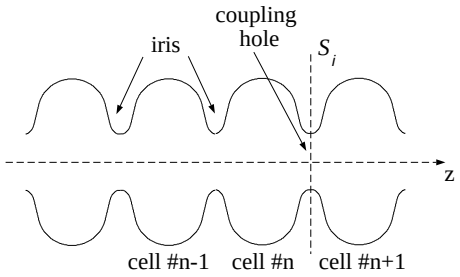

Figure 5.5: Chain of coupled cells. The structure has rotational symmetry with respect to the beam axis z.

the individual cells. These iris holes have a surface S_i. Near an iris the TM_{010} magnetic eigenmode field of a *completely enclosed single cell* is azimuthal, whereas the electric eigenmode field is parallel to the cavity axis. To transfer power between the cells a radial component of the electric field near the iris is required. Together with the azimuthal magnetic field this radial component results in a Poynting vector in direction of the cavity axis. Again, as for the wall losses, we can treat the additional radial electric field $\vec{E}_{rad}$ at the iris S_i as a small perturbation to the eigenmode field $\vec{e}^{(1)}$ of a *single cell*, which is completely enclosed by a perfectly conducting surface. The radial field between cell n and cell $n+1$ is given by a superposition of two contributions, one from the field of each cell. These contributions are proportional

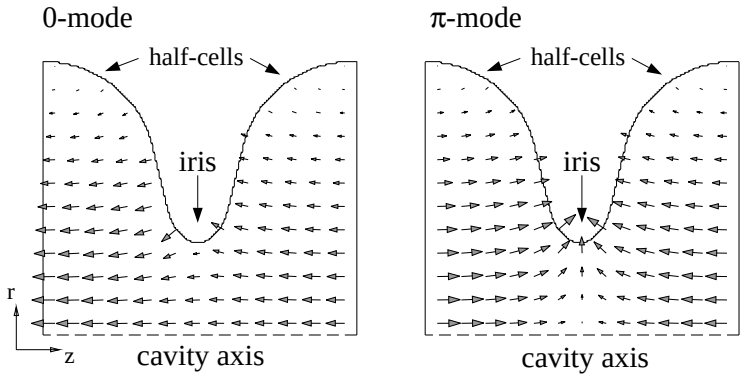

Figure 5.6: Field pattern of the TM_{010} modes in two coupled cells (calculation by MAFIA). The modes in the two cells can either oscillate with zero phase shift (0 mode) or with π phase shift (π mode), as shown on the left and right side respectively. The fields have rotational symmetry with respect to the cavity axis and have even symmetry with respect to the middle plane of the cells.

to the amplitudes $\mathcal{E}^{(1)}$ of the TM_{010} modes in the cells. So we have for two coupled cells excited in the TM_{010} mode [Bev 64]

$$\vec{E}_{rad}\Big|_{S_i} = \mathcal{E}_n^{(1)}\vec{e}_{n,n+1}^{(1)}\Big|_{S_i} - \mathcal{E}_{n+1}^{(1)}\vec{e}_{n,n+1}^{(1)}\Big|_{S_i} \quad , \tag{5.72}$$

where the function $\vec{e}_{n,n+1}^{(1)}$ describes the field pattern for the radial field of *one* cell at the hole surface S_i. In equation (5.72) the minus sign is taken, since the field of the TM_{010} mode is of even symmetry with respect to the middle plane of a cell. Accordingly for identical cells with equal field amplitudes, the radial electric field vanishes for zero phase shift between the fields of the cells (0 mode), see figure 5.6. However at π phase shift, i.e. $\mathcal{E}_n^{(1)} = -\mathcal{E}_{n+1}^{(1)}$, the two contributions to the radial electric field at S_i add up, whereas the longitudinal electric field vanishes at S_i. The field pattern of this π mode is shown on the right side of figure 5.6. We find that the 0 mode corresponds to electric boundary conditions at the hole surface S_i, whereas the π mode matches magnetic boundary conditions at S_i. As we shall see, the two coupled modes, i.e. the TM_{010} 0 mode and the TM_{010} π mode, have different resonance frequencies, depending on the strength of the coupling of the two cells. Thus for two coupled cells we have two TM_{010} modes. Consequently one finds in a structure of N coupled cells N different TM_{010} modes. If we denote the radial field of the π mode at the hole between two identical cells as $\vec{e}_{hole}^{(1)}$, we have

$$\vec{e}_{hole}^{(1)} = 2\vec{e}_{n,n+1}^{(1)} \quad . \tag{5.73}$$

We can now define an important dimensionless quantity for multicell cavities, the cell-to-cell coupling factor k_{cc} for two identical cells

$$\mathcal{K}_{cc} := \frac{c}{\omega_0^{(1)}} \int_{S_i} (\vec{e}_{hole}^{(1)} \times \vec{h}^{(1)}) \cdot \vec{u}_z ds \quad , \tag{5.74}$$

which measures the strength of the coupling. Here $\omega_0^{(1)}$ is the eigenfrequency of the TM_{010} mode in a completely enclosed *single cell* with perfectly conducting walls at the iris surface S_i and $\vec{h}^{(1)}$ is the corresponding eigenfunction for the magnetic field. The unit vector $\vec{u}_z$ points in direction of the cavity axis. For the TESLA multicell cavities the cell-to-cell coupling factor is $\mathcal{K}_{cc} \approx 0.019$.
We shall now come back to the differential equation (5.69) for the amplitude coefficient of the electric TM_{010} eigenfield in a single cell cavity and include cell-to-cell coupling. From the relation (5.72) we find for the surface integral on the right hand side of (5.40)

$$\begin{aligned} \int_{S_i} (\vec{n} \times \vec{E}_{rad}) \cdot \vec{h}^{(1)} ds &= \{\mathcal{E}_n^{(1)} - \mathcal{E}_{n+1}^{(1)}\} \int_{S_i} (\vec{e}_{n,n+1}^{(1)} \times \vec{h}^{(1)}) \cdot \vec{i}_z ds \\ &= \{\mathcal{E}_n^{(1)} - \mathcal{E}_{n+1}^{(1)}\} \frac{\omega_0^{(1)}}{2c} \mathcal{K}_{n,n+1} \quad . \end{aligned} \tag{5.75}$$

Accordingly for the coupling of the cell n to cell $n-1$ we have the integral

$$\int_{S_i} (\vec{n} \times \vec{E}_{rad}) \cdot \vec{h}^{(1)} ds = \{\mathcal{E}_n^{(1)} - \mathcal{E}_{n-1}^{(1)}\} \frac{\omega_0^{(1)}}{2c} \mathcal{K}_{n,n-1} \quad . \tag{5.76}$$

In equation (5.75) and (5.76) we have introduced the coupling constant

$$\mathcal{K}_{n,n+1} := \frac{2c}{\omega_0^{(1)}} \int_{S_i} (\vec{e}_{n,n+1}^{(1)} \times \vec{h}^{(1)}) \cdot \vec{u}_z ds \quad , \tag{5.77}$$

which characterizes the individual coupling of cell n and cell $n+1$. We will use the definition (5.77) for cells, which are connected by an iris as well as for cells, which are joined by an interconnecting tube.
Similar to the cell-to-cell coupling constant, we introduce a resonator-to-resonator coupling constant $\mathcal{K}_{rr}$ for two identical cavities (m and $m+1$), which are coupled by a tube to form a superstructure. Therefore we define

$$\mathcal{K}_{rr} := \frac{c}{\omega_r^{(1)}} \int_{S_T} (\vec{e}_{tube}^{(1)} \times \vec{h}_r^{(1)}) \cdot \vec{u}_z ds \quad , \tag{5.78}$$

where $\omega_r^{(1)}$ is the resonance frequency of a selected mode of the individual cavites and $\vec{h}_r^{(1)}$ the corresponding field pattern of the magnetic field within a *single cavity*. In (5.78) we integrate over the cross section S_T at the center of the interconnecting tube, see figure 5.7. The normalized (see (5.72)) radial electric field along this surface is denoted by $\vec{e}_{tube}^{(1)}$ for the case, that the fields of the connected end-cells are oscillating with π phase difference. Analogous to iris-coupled cells, we get two possibilities for the phase advance from the last cell of the first cavity to the first cell of the second cavity. As shown in figure 5.7, the fields in the two joined cells can build up a 0 mode and a π mode. Accordingly each of the N_c TM_{010} modes of a N_c-cell cavity splits into two modes if two cavities become joined and into M modes in case of a superstructure with M cavities. Since the N_c TM_{010} modes of a N_c-cell cavity have different field patterns, we have to specify the resonator-to-resonator

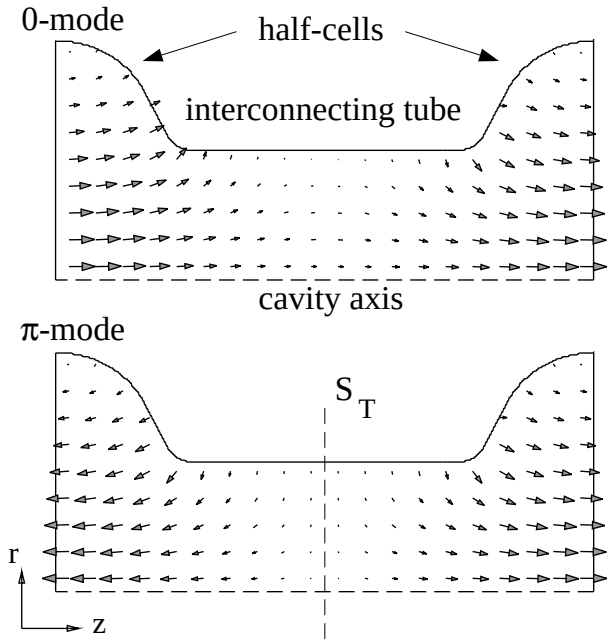

Figure 5.7: Field pattern of the TM_{010} modes in the end-half-cells of cavities joined by a pipe (calculation by MAFIA). The fields in the two cells can either oscillate with zero phase advance (0 mode) or with π phase advance (π mode). The fields have rotational symmetry with respect to the cavity axis.

coupling with respect to a selected mode. Usually this coupling factor is listed for the accelerating mode.
Finally we combine the equations (5.69), (5.75) and (5.76) according to (5.40). Thus we obtain for the amplitude coefficient $\mathcal{E}_n^{(1)}$ of the TM_{010} mode in cell n of a *multicell cavity* the differential equation

$$\frac{d^2\mathcal{E}_n^{(1)}}{dt^2} + \left\{\frac{\omega_0^{(1)}}{Q_0^{(1)}}(1+i) + \frac{\omega_0^{(1)}}{Q_{e,n}^{(1,1)}}\right\}\frac{d\mathcal{E}_n^{(1)}}{dt} + \frac{(\omega_0^{(1)})^2}{2}\{1 + \mathcal{K}_{n,n-1} + \mathcal{K}_{n,n+1}\}\mathcal{E}_n^{(1)}$$
$$-\frac{(\omega_0^{(1)})^2}{2}\{\mathcal{K}_{n,n-1}\mathcal{E}_{n-1}^{(1)} + \mathcal{K}_{n,n+1}\mathcal{E}_{n+1}^{(1)}\} = -\frac{K_{g,n}^{(1)}}{\varepsilon_0}\frac{d}{dt}J_{g,n} \quad . \tag{5.79}$$

Here we assume that the unloaded quality factor $Q_0^{(1)}$ is identical in all cells. Notice that the coupling factors of the form $\mathcal{K}_{n,n+1}$ can either represent a coupling from cell to cell within a cavity, or the coupling of the last cell of a cavity to the first cell of a neighboring cavity in a superstructure.
Further we consider, that the cells, which are coupled to a multicell cavity, have slightly different eigenfrequencies $\omega_n^{(1)}$ near to the design frequency $\omega_0^{(1)}$. Therefore we write

$$\frac{d^2\mathcal{E}_n^{(1)}}{dt^2} + \left\{\frac{\omega_n^{(1)}}{Q_0^{(1)}}(1+i) + \frac{\omega_n^{(1)}}{Q_{e,n}^{(1,1)}}\right\}\frac{d\mathcal{E}_n^{(1)}}{dt} + (\omega_n^{(1)})^2\mathcal{E}_n^{(1)} + \frac{(\omega_n^{(1)})^2}{2}\{\mathcal{K}_{n,n-1} + \mathcal{K}_{n,n+1}\}\mathcal{E}_n^{(1)}$$

$$-\frac{(\omega_n^{(1)})^2}{2}\{\mathcal{K}_{n,n-1}\mathcal{E}_{n-1}^{(1)}+\mathcal{K}_{n,n+1}\mathcal{E}_{n+1}^{(1)}\}=-\frac{K_{g,n}^{(1)}}{\varepsilon_0}\frac{d}{dt}J_{g,n} \quad . \tag{5.80}$$

Note that in this section it is assumed, that the perturbation of the cell's eigenmode fields by the coupling is small, which implies that the cells are of almost identical shape and frequency. As discussed above, for superconducting multicell cavities we may neglect the complex part of the wall loss term and write

$$\frac{d^2\mathcal{E}_n^{(1)}}{dt^2}+\frac{\omega_n^{(1)}}{Q_n^{(1)}}\frac{d\mathcal{E}_n^{(1)}}{dt}+(\omega_n^{(1)})^2\mathcal{E}_n^{(1)}+\frac{(\omega_n^{(1)})^2}{2}\{\mathcal{K}_{n,n-1}+\mathcal{K}_{n,n+1}\}\mathcal{E}_n^{(1)}$$
$$-\frac{(\omega_n^{(1)})^2}{2}\{\mathcal{K}_{n,n-1}\mathcal{E}_{n-1}^{(1)}+\mathcal{K}_{n,n+1}\mathcal{E}_{n+1}^{(1)}\}=-\frac{K_{g,n}^{(1)}}{\varepsilon_0}\frac{d}{dt}J_{g,n} \quad , \tag{5.81}$$

where the loaded quality factor of cell n is defined as

$$\frac{1}{Q_n^{(1)}}=\frac{1}{Q_0^{(1)}}+\frac{1}{Q_{e,n}^{(1,1)}} \quad . \tag{5.82}$$

For normal conducting cavities we may also use the equation (5.81) if $\omega_n^{(1)}$ represents the cell's TM_{010} eigenmode frequency shifted according to (5.71). Usually the input coupler is located at the beam tube near to the first cell of a multicell cavity. Then we have $Q_n^{(1)}=Q_0^{(1)}$ and $K_{g,n}^{(1)}=0$ for $n\neq 1$.

5.7 An Equivalent Circuit Diagram

In this section we shall transform the differential equation (5.81) of the TM_{010} field amplitudes of a multicavity-multicell-structure into an eqivalent series LCR circuit with inductive (L), capacitve (C) and resistive (R) elements. Therefore we make the following substitutions

$$(\omega_n^{(1)})^2=:\frac{1}{LC_n} \qquad \mathcal{K}_{n,n+1}=:\frac{2C_n}{C_{n,n+1}} \qquad Q_n^{(1)}=:\frac{\omega_n^{(1)}L}{R_n} \quad . \tag{5.83}$$

Let the cavity be driven by an input coupler at the beam tube at the first cell of the cavity, then we can write for the resistance $R_1=R_0+R_e$ and $R_n=R_0$ for $n\neq 1$. Here R_0 represents the wall losses and R_e accounts for the energy extraction via the input coupler. The stored field energy in a loss-free cell is given by $U_n=\frac{1}{2}\varepsilon_0\mathcal{E}_n^{(1)}(\mathcal{E}_n^{(1)})^*$, whereas the stored energy in a L-C resonant circuit with a current I_n is given by $U_n=\frac{1}{2}LI_nI_n^*$. Accordingly we substitute the field amplitude factor $\mathcal{E}_n^{(1)}$ of the TM_{010} mode in cell n by

$$\mathcal{E}_n^{(1)}=:\sqrt{\frac{L}{\varepsilon_0}}I_n \quad . \tag{5.84}$$

Similarly we define a driving current in the circuit model by

$$-\frac{K_g^{(1)}}{\varepsilon_0}J_{g,1}=:\sqrt{\frac{1}{\varepsilon_0 L}}R_eI_{g,1} \quad . \tag{5.85}$$

We shall see shortly that this results in a convenient equivalent circuit model and an intuitive expression for the generator power. Since the input coupler is located at the beam tube at cell $n = 1$, we have $I_{g,n} = 0$ for $n \neq 1$.
Substituting the equations (5.83), (5.84) and (5.85) in the differential equation (5.81) we find

$$\frac{d^2 I_n}{dt^2} + \frac{R_n}{L}\frac{dI_n}{dt} + \frac{1}{LC_n} I_n + \frac{1}{L}\left\{\frac{1}{C_{n,n-1}} + \frac{1}{C_{n,n+1}}\right\} I_n$$
$$-\frac{1}{L}\left\{\frac{1}{C_{n,n-1}} I_{n-1} + \frac{1}{C_{n,n+1}} I_{n+1}\right\} = \frac{R_e}{L}\frac{d}{dt} I_{g,n} \quad . \tag{5.86}$$

This differential equation corresponds to the lumped element circuit shown in figure 5.8. To prove the consistancy we use Kirchhoff's voltage summation rule

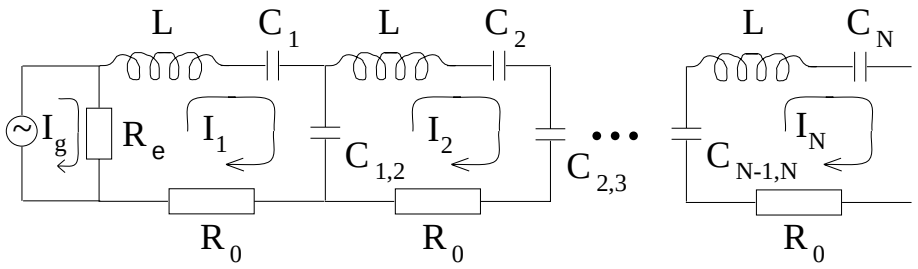

Figure 5.8: Equivalent Series LCR circuit model for the TM_{010} field amplitudes in a multicell cavity with N cells. Note that this circuit model is only valid for fields of even symmetry within the cells with respect to the middle plane of the cells.

$$V_L + V_{C_n} + V_{C_{n,n+1}} + V_R + V_{C_{n,n-1}} = 0 \tag{5.87}$$

for each current loop. Recalling $V_L = L\dot{I}_n$, $\dot{V}_C = I_n/C$ and $V_R = RI_n$ we obtain the differential equation (5.86).
In the discussion of coupled cells the cells were taken to have almost identical shape. Accordingly the cells have only sligthly different angular eigenfrequencies $\omega_n^{(1)}$ near to a design frequency $\omega_0^{(1)}$

$$(\omega_0^{(1)})^2 := \frac{1}{LC} \quad . \tag{5.88}$$

The nominal capacitence C is defind by the cell's nominal frequency $\omega_0^{(1)}$. A small cell detuning is modelled by varying the cell capacitence C_n

$$\frac{C}{C_n} =: 1 + \delta_n \quad . \tag{5.89}$$

Accordingly we find

$$\delta_n = 2\frac{\Delta\omega_n^{(1)}}{\omega_0^{(1)}} + \left(\frac{\Delta\omega_n^{(1)}}{\omega_0^{(1)}}\right)^2 \quad , \tag{5.90}$$

where $\Delta\omega_n^{(1)} = \omega_n^{(1)} - \omega_0^{(1)}$ is the detuning of cell n. Futhermore it is convenient to define a coupling constant $k_{n,n+1}$ for the coupling of the current loops n and $n+1$ in the circuit model as

$$k_{n,n+1} = \frac{C}{C_{n,n+1}} = \frac{(\omega_n^{(1)})^2}{(\omega_0^{(1)})^2}\frac{\mathcal{K}_{n,n+1}}{2} \quad . \tag{5.91}$$

Note that this loop coupling constant is a factor of two smaller than the cell-to-cell coupling constant $\mathcal{K}_{n,n+1}$ in case of ideal cells with $\omega_n^{(1)} = \omega_0^{(1)}$. We can write the differential equations (5.86) for the coupled cells in matrix notation

$$\frac{1}{(\omega_0^{(1)})^2}\ddot{\vec{I}} + \mathbf{B}\dot{\vec{I}} + \mathbf{A}\vec{I} = \frac{\omega_1^{(1)}}{(\omega_0^{(1)})^2 Q_{e,1}^{(1,1)}}\dot{\vec{I}}_g \quad , \tag{5.92}$$

where $\vec{I}$ and $\vec{I}_g$ are column vectors representing the excitation of the loop currents and the generator current, respectively

$$\vec{I} = \begin{bmatrix} I_1 \\ I_2 \\ \vdots \\ I_N \end{bmatrix} \qquad \vec{I}_g = \begin{bmatrix} I_{g,1} \\ 0 \\ \vdots \\ 0 \end{bmatrix} \quad . \tag{5.93}$$

For the square matrices $\mathbf{A}$ and $\mathbf{B}$ with dimension N we have

$$\mathbf{A} := \begin{bmatrix} A_1 & -k_{1,2} & 0 & \cdots & 0 \\ -k_{1,2} & A_2 & -k_{2,3} & & \vdots \\ & & & \ddots & \\ 0 & & \ddots & & 0 \\ & \ddots & & & \\ \vdots & & -k_{N-2,N-1} & A_{N-1} & -k_{N-1,N} \\ 0 & \cdots & 0 & -k_{N-1,N} & A_N \end{bmatrix} \tag{5.94}$$

$$\mathbf{B} := \frac{1}{(\omega_0^{(1)})^2}\begin{bmatrix} \omega_1^{(1)}/Q_1^{(1)} & 0 & \cdots & 0 \\ 0 & \omega_2^{(1)}/Q_2^{(1)} & & \vdots \\ \vdots & & \ddots & 0 \\ 0 & \cdots & 0 & \omega_N^{(1)}/Q_N^{(1)} \end{bmatrix} \quad , \tag{5.95}$$

where the diagonal matrix elements are

$$A_1 := 1 + \delta_1 + k_{1,2} \tag{5.96}$$

$$A_n := 1 + \delta_n + k_{n-1,n} + k_{n,n+1} \qquad , 1 < j < N \tag{5.97}$$

$$A_N := 1 + \delta_N + k_{N-1,N} \quad . \tag{5.98}$$

If the cavity is driven by a RF generator, the time dependent steady state field will oscillate with the generator angular frequency ω_g. Accordingly we separate a rapidly varying term $e^{i\omega_g t}$ and write

$$J_g(t) = \hat{J}_g(t)e^{i\omega_g t} \tag{5.99}$$
$$\mathcal{E}_n^{(1)}(t) = \hat{\mathcal{E}}_n(t)e^{i\omega_g t} \tag{5.100}$$
$$I_g(t) = \hat{I}_g(t)e^{i\omega_g t} \tag{5.101}$$
$$I_n(t) = \hat{I}_n(t)e^{i\omega_g t} \quad . \tag{5.102}$$

The envelope functions $\hat{J}_g$, $\hat{\mathcal{E}}_n$, $\hat{I}_g$, and $\hat{I}_n$ vary slowly on the time scale of the RF period. Accordingly we have

$$\dot{\hat{\mathcal{E}}}_n \ll \omega_g \hat{\mathcal{E}}_n \qquad \ddot{\hat{\mathcal{E}}}_n \ll (\omega_g)^2 \hat{\mathcal{E}}_n \tag{5.103}$$
$$\dot{\hat{I}}_n \ll \omega_g \hat{I}_n \qquad \ddot{\hat{I}}_n \ll (\omega_g)^2 \hat{I}_n \quad . \tag{5.104}$$

Under these assumptions we obtain a system of N coupled first order differential equations from (5.92)

$$\dot{\vec{\hat{I}}} + \frac{(\omega_0^{(1)})^2}{2}\mathbf{B}\vec{\hat{I}} + \frac{i\omega_g}{2}\left\{\mathbf{1} - \left(\frac{\omega_0^{(1)}}{\omega_g}\right)^2 \mathbf{A}\right\}\vec{\hat{I}} = -\frac{i\omega_1^{(1)}}{2\omega_g Q_{e,1}^{(1,1)}}\dot{\vec{I}}_g e^{-i\omega_g t} \quad . \tag{5.105}$$

Similarly we have for the TM_{010} field amplitude coefficients the coupled first order differential equations

$$\dot{\vec{\hat{\mathcal{E}}}} + \frac{(\omega_0^{(1)})^2}{2}\mathbf{B}\vec{\hat{\mathcal{E}}} + \frac{i\omega_g}{2}\left\{\mathbf{1} - \left(\frac{\omega_0^{(1)}}{\omega_g}\right)^2 \mathbf{A}\right\}\vec{\hat{\mathcal{E}}} = \frac{iK_g^{(1)}}{2\varepsilon_0\omega_g}\dot{\vec{J}}_g e^{-i\omega_g t} \quad . \tag{5.106}$$

The differential equations (5.105) and (5.106) can be integrated numerically.
Finally for steady state with constant generator current $\vec{J}_g(t) = \vec{\hat{J}}_g e^{i\omega_g t}$ we find

$$\frac{i\omega_g}{2}\left\{\mathbf{1} - \left(\frac{\omega_0^{(1)}}{\omega_g}\right)^2 \mathbf{A} - \frac{i(\omega_0^{(1)})^2}{\omega_g}\mathbf{B}\right\}\vec{\hat{\mathcal{E}}} = -\frac{K_g^{(1)}}{2\varepsilon_0}\vec{\hat{J}}_g \quad . \tag{5.107}$$

Example: TESLA 9-cell cavity

To illustrate the steady state equation (5.107) we shall apply it to a TESLA 9-cell cavity as an example of a multicell cavity. We assume an ideal cavity, i.e. the cavity is tuned for equal field amplitudes of the accelerating mode in all cells (see chapter 6) and the cell-to-cell coupling is constant. Figure 5.9 shows the result of a simulated resonance spectrum analysis for this cavity. As discussed before, we find nine TM_{010} resonances in the 9-cell structure. The mode designation $j\pi/9$ follows the mode notation in traveling wave RF structures, where it describes the phase advance per cell of the waveguide mode. In standing wave RF structures the phase advance between neighboring cells can only be 0 or π in absence of losses, but the notation $j\pi/9$ is reflected in the TM_{010} amplitude profiles of the cavity eigenmodes. We will discuss this in more detail in section 5.9.

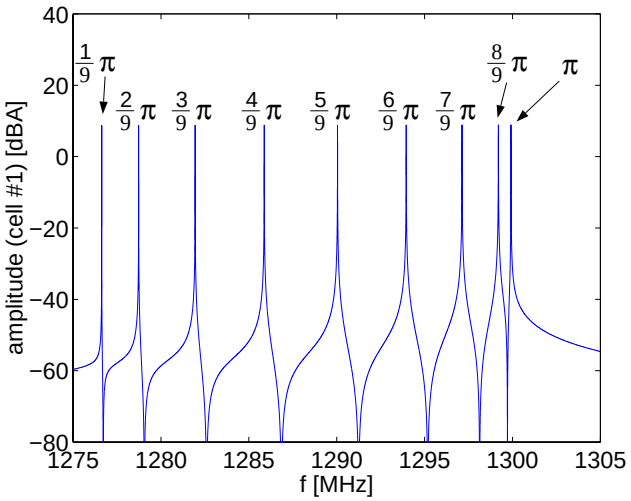

Figure 5.9: Calculated resonance spectrum of the TM_{010} modes in a TESLA 9-cell cavity. Shown is the steady state amplitude of the field in cell #1 as a function of the frequency of the driving RF generator ($\mathcal{K}_{cc} = 1.9\%$, $\omega_0^{(1)}/(2\pi) = 1.276$ GHz, $Q_0^{(1)} = 10^{10}$, $Q_{e,1}^{(1,1)} = 10^5$).

5.8 Generator Power

When calculating the generator power by means of the equivalent cavity circuit model, we have to take into account, that this model does not include the transmission line, the circulator and the coupler between the generator and the cavity, see figure 5.10. In the simplified cavity model the external load is modelled by the transformed waveguide impedance $R_e = n^2 Z_t$ for a coupler transformation ratio $1 : n$. We have to distinguish carefully between the generator current $\tilde{I}_g$ in the model including the transmission line and the fictitious generator current I_g in the simplified cavity model. To illustrate the difference between these currents, we assume that the external load is matched to the wall losses according to $n^2 Z_t = R_0$ and that the single cell cavity (see figure 5.10) is driven on resonace, i.e $\omega_g^2 = 1/(LC_1)$. We will find that for these conditions the field in the cavity is maximized for a given generator current. Accordingly, as is well known, all generator power is transferred to the cavity. From figure 5.10 (a) we find that the cell current I_1 is then given by

$$I_1 = \frac{1}{n}\tilde{I}_g \quad , \tag{5.108}$$

since the LC series has zero impedance for $\omega_g^2 = 1/(LC_1)$. Recall that I_1 is representing the field amplitude in the cell, see (5.84). However, for the simplified model we have

$$I_1 = \frac{1}{2}I_g \quad , \tag{5.109}$$

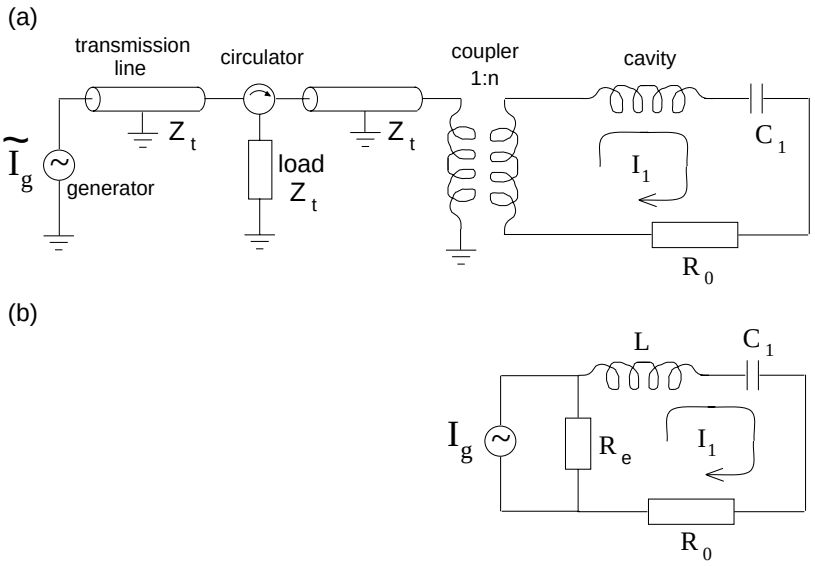

Figure 5.10: (a) Model of a single cell cavity coupled to a RF generator by a coupler and a transmission line. On account of the circulator, the generator is always loaded with the impedance Z_t. (b) Simplified cavity model with a fictitious generator current I_g. The external load Z_t is transformed to the cavity side of the coupler to $R_e = n^2 Z_t$.

since we consider matched conditions ($R_e = R_0$). Accordingly we find for the fictitious generator current I_g in the simplified cavity model the relation

$$I_g = \frac{2}{n}\tilde{I}_g \quad . \tag{5.110}$$

If we define the generator power by $P_g = 1/2 Z_t \tilde{I}_g \tilde{I}_g^*$ we finally obtain with (5.85)

$$P_g = \frac{1}{8} R_e I_g I_g^* = \frac{1}{8\varepsilon_0} \frac{Q_e^{(1,1)}}{\omega_1^{(1)}} {K_g^{(1)}}^2 J_{g,1} J_{g,1}^* \quad . \tag{5.111}$$

Refer to [Schi 98] for a detailed disussion of the dissipated and reflected power.
To analyse the matching of the external load to the wall losses or a beam current passing the cavity, we consider for the moment a single cell cavity. From (5.81) and (5.111) we find for the steady state field amplitude in the cavity without beam

$$\hat{\mathcal{E}}_1 = \sqrt{\frac{8P_g}{\varepsilon_0 \omega_1^{(1)}} \frac{Q_0^{(1)}}{2 + \frac{Q_0^{(1)}}{Q_e^{(1,1)}} + \frac{Q_e^{(1,1)}}{Q_0^{(1)}}}} \quad . \tag{5.112}$$

Here we assumed that the cavity is driven on its TM_{010} mode frequency, i.e. $\omega_g = \omega_1^{(1)}$. Accordingly the power required for a field amplitude $\hat{\mathcal{E}}_1$ is minimized if the external quality factor is identical with the unloaded quality factor of the cavity, i.e. $Q_e^{(1,1)} = Q_0^{(1)}$. For a beam loaded superconducting cavity we may neglect the wall losses in comparison with the beam load. The maximum average power extracted

by a beam is $P_b = V_{acc} I_b$, where I_b is the average beam current. By substituting $Q_0 = (\omega_1^{(1)} U^{(1)})/P_b$ in equation (5.112), we have for the matched external qualtity factor for a superconducting cavity with beam loading (with equation (5.58))

$$(Q_e^{(1,1)})_{opt} = \frac{V_{acc}}{2(\frac{R}{Q})I_b} \quad . \tag{5.113}$$

More generally we find from (5.81) and (5.111) an equation for the power required to maintain a constant accelerating field in a superconducting cavity with $Q_e^{(1,1)} \ll Q_0^{(1)}$

$$P_g = \frac{V_{acc}^2}{8Q_e^{(1,1)}(\frac{R}{Q})}\Bigg\{ \quad \Big(1 + 2\Big(\frac{R}{Q}\Big)Q_e^{(1,1)}\frac{I_b}{V_{acc}}\cos(\Phi_b)\Big)^2 + \Big(\frac{\Delta\omega_1^{(1)} 2Q_e^{(1,1)}}{\omega_1^{(1)}} + 2\Big(\frac{R}{Q}\Big)Q_e^{(1,1)}\frac{I_b}{V_{acc}}\sin(\Phi_b)\Big)^2\Bigg\} \quad . \tag{5.114}$$

Here V_{acc} is the maximum accelerating voltage of the cavity, Φ_b is the accelerating phase of the field when the beam passes the center of the cavity and $\Delta\omega_1^{(1)} = \omega_1^{(1)} - \omega_g$ is the detuning of the cavity; see also chapter 2. Accordingly the voltage seen by the beam is given by $V = V_{acc}\cos(\Phi_b)$.

5.9 Eigenmodes of a Multicell Cavity

As discussed in the previous sections, multicavity-multicell RF structures have $N = MN_c$ TM_{010} modes, if M is the number of coupled cavities and N_c is the number of cells per cavity. To analyse these eigenmodes, we shall consider a loss-free structure (i.e. $\mathbf{B} = 0$) without generator current. According to equation (5.107) the orthonormal TM_{010} cavity eigenmodes $\vec{v}^{(j)}$ are solutions of the eigenmode equation

$$\mathbf{A}\vec{v}^{(j)} = \Omega^{(j)}\vec{v}^{(j)} \quad , \tag{5.115}$$

where the square matrix A with dimension $N = MN_c$ is

$$\mathbf{A} := \begin{bmatrix} A_1 & -k_{1,2} & 0 & \cdots & 0 \\ -k_{1,2} & A_2 & -k_{2,3} & \ddots & \vdots \\ 0 & & \ddots & & 0 \\ \vdots & \ddots & -k_{MN_c-2,MN_c-1} & A_{MN_c-1} & -k_{MN_c-1,MN_c} \\ 0 & \cdots & 0 & -k_{MN_c-1,MN_c} & A_{MN_c} \end{bmatrix}, \tag{5.116}$$

see (5.94). As before we use subscripts on a quantity to refer to the cell number, whereas superscripts label the TM_{010} cavity mode. The eigenvalues $\Omega^{(j)}$ define the mode frequencies $\omega^{(j)}$

$$\Omega^{(j)} := \frac{(\omega^{(j)})^2}{(\omega_0^{(1)})^2}, \qquad j = 1, ..., MN_c \quad . \tag{5.117}$$

Instead of the general circuit model shown in figure 5.8, in this section we shall use a model adapted for a loss-free structure with M coupled cavities, see figure 5.11. Accordingly we have for the diagonal elements of the matrix A

$$\begin{aligned} A_1 &:= 1 + \delta_1 + k_{1,2} && (5.118)\\ A_n &:= 1 + \delta_n + k_{n-1,n} + k_{n,n+1} \quad , 1 < n < MN_c && (5.119)\\ A_{MN_c} &:= 1 + \delta_{MN_c} + k_{MN_c-1,MN_c} \quad . && (5.120) \end{aligned}$$

We know from the previous discussion of superstructures, that the so-called TM_{010} $\pi - 0$ mode with π cell to cell phase advance and zero cavity to cavity phase advance is used for beam acceleration (for $\lambda/2$ interconnecting tubes). It is desirable to have homogeneous field amplitudes for this mode in the cells in order to maximize the energy gain of the beam with a given limitation on the cell's maximum field. Accordingly we have for the normalized eigenvector of this mode

$$\vec{v}^{(M(N_c-1)+1)} = \frac{1}{\sqrt{MN_c}}[1, -1, 1, ..., -1, 1, 1, -1, 1, ..., -1, 1, 1, -1, ...]^T \quad . \quad (5.121)$$

As we shall see, the $\pi - 0$ mode is the $(M(N_c - 1) + 1)^{\text{th}}$ mode in TM_{010} group of modes in a superstructure. We assume a constant cell-to-cell coupling of the cells within the cavities

$$\begin{aligned} k_{j,j+1} &=: k_c \quad , && (5.122)\\ & \quad j = \{1, ..., N_c - 1, N_c + 1, ..., 2N_c - 1, 2N_c + 1, ..., MN_c - 1\} \, , \end{aligned}$$

and a homogeneous coupling of the end-cells of the coupled cavities

$$k_{j,j+1} =: k_e \quad , j = \{N_c, 2N_c, ..., (M-1)N_c\} \quad . \quad (5.123)$$

We now insert (5.121) in the eigenmode equation (5.115) to determine the cell frequencies for a $\pi - 0$ mode with homogeneous field amplitudes. For the center-cells of the cavities we get

$$\begin{aligned} k_c + (1 + \delta_j + 2k_c) + k_c &= \Omega^{(M(N_c-1)+1)} \\ -k_c - (1 + \delta_{j+1} + 2k_c) - k_c &= -\Omega^{(M(N_c-1)+1)} \quad . \end{aligned} \quad (5.124)$$

Solving this equation system we find that $\delta_j = \delta_{j+1}$. Without loss of generality we may use for the center-cells

$$\delta_j = 0 \quad , j = \{2, \cdots, N_c - 1, N_c + 2, ..., MN_c - 1\} \quad . \quad (5.125)$$

Similarly we have for the first two cells of the superstructure the equations

$$\begin{aligned} (1 + \delta_1 + k_c) + k_c &= \Omega^{(M(N_c-1)+1)} \\ -k_c - (1 + 2k_c) - k_c &= -\Omega^{(M(N_c-1)+1)} \quad , \end{aligned} \quad (5.126)$$

with the solution

$$\delta_1 = 2k_c \quad . \quad (5.127)$$

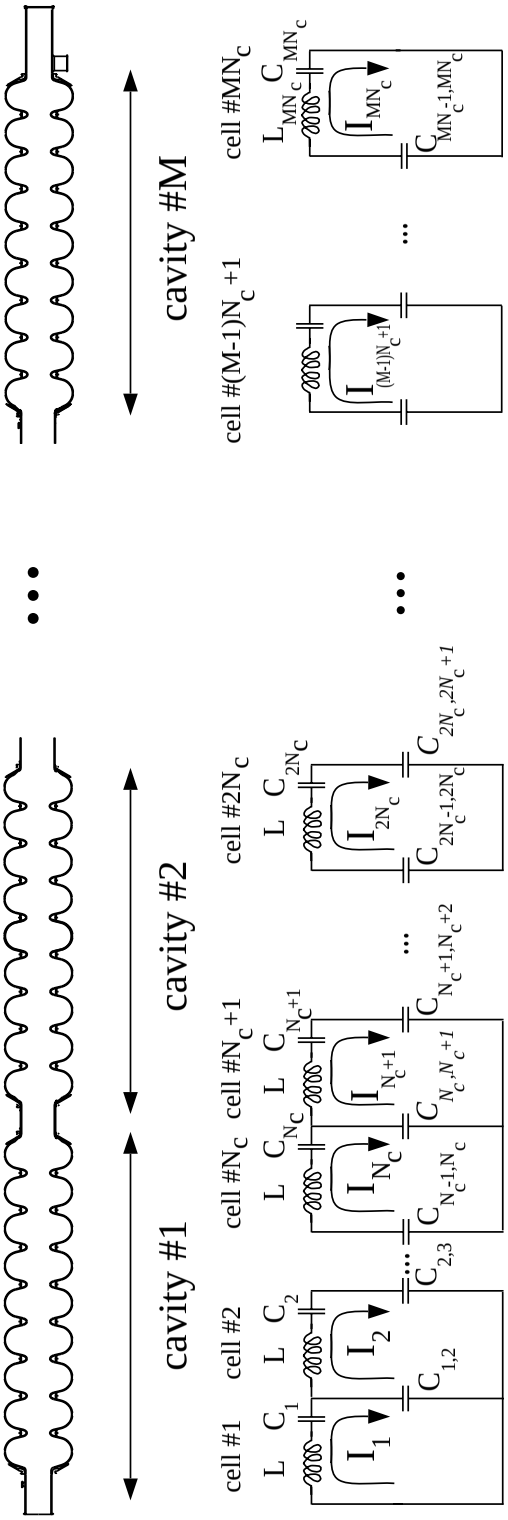

Figure 5.11: Circuit model of a loss-free superstructure for the TM_{010} modes. Each of the M coupled cavities has N_c cells.

Accordingly we find for the last cell of the structure

$$\delta_{MN_c} = 2k_c \quad . \tag{5.128}$$

Finally for the end-cells between the coupled cavities we have to solve the system of equations

$$\begin{aligned} -k_c - (1+2k_c) - k_c &= -\Omega^{(M(N_c-1)+1)} \\ k_c + (1+\delta_j + k_c + k_e) - k_e &= \Omega^{(M(N_c-1)+1)} \end{aligned} \quad , \tag{5.129}$$

and find for these connecting end-cells

$$\delta_j = 2k_c \ , j = \{N_c, N_c+1, ..., (M-1)N_c, (M-1)N_c+1\} \ . \tag{5.130}$$

We have determined now the required frequency adjustments for a $\pi - 0$ mode with homogeneous field amplitudes. Accordingly the general matrix (5.116) becomes

$$\mathbf{A} = \begin{bmatrix} 1+3k_c & -k_c & 0 & & & & \cdots & & 0 \\ -k_c & 1+2k_c & -k_c & & & & & & \\ 0 & & \ddots & & & & & & \vdots \\ & & -k_c & 1+3k_c+k_e & -k_e & & & & \\ \vdots & & & -k_e & 1+3k_c+k_e & -k_c & & & \\ & & & & & \ddots & & 0 & \\ & & & & & -k_c & 1+2k_c & -k_c & \\ 0 & & & \cdots & & 0 & -k_c & 1+3k_c & \end{bmatrix} \tag{5.131}$$

for a tuned superstructure. Solving the eigenvalue problem (5.115) for the system matrix (5.131), we find the TM_{010} eigenmodes in a multicell cavity.

Example: TESLA 9-cell cavity

Before analysing the eigenmodes in a superstructure in section 5.12, we discuss the TM_{010} modes in a TESLA 9-cell cavity. This will serve as a basis for our later studies of the fields in multicavity-multicell RF structures.

Thus we consider a single multicell cavity, which is tuned according to (5.127) and (5.128) for homogeneous field amplitudes of the accelerating mode. Then the solutions of the eigenmode equation (5.115) are given by

$$v_n^{(j)} = \sqrt{\frac{2-\delta_{jN_c}}{N_c}} \sin\left[j\pi\left(\frac{2n-1}{2N_c}\right)\right] \ , j = 1, ..., N_c \quad , \tag{5.132}$$

where $n = 1...., N_c$ is the cell number. According to the number of cells N_c per cavity, we have N_c othonormal eigenmodes $\vec{v}^{(j)}$ in a multicell cavity. Moreover we immediately see from (5.132) the meaning of the eigenmode notation $j\pi/N_c$ for standing wave cavities. For a tuned cavity, the eigenmodes are independent of the cell-to-cell coupling, whereas the spacing of the eigenvalues is determined by the coupling factor k_c

$$\Omega^{(j)} = \left(\frac{\omega^{(j)}}{\omega_0^{(1)}}\right)^2 = 1 + 2k_c\left[1 - cos\left(\frac{j\pi}{N_c}\right)\right] \quad . \tag{5.133}$$

Accordingly the mode frequency spacing increases with stronger cell-to-cell coupling and decreases as the number of cells per cavity increases. The spacing of modes is particularly important when designing a RF control system for the accelerating fields in a cavity, see chapter 8. Figure 5.12 shows the TM_{010} group of eigenmodes for the TESLA 9-cell cavity and the corresponding eigenfrequencies. To verify the validity of our cavity model this figure also shows measured amplitude profiles of the TM_{010} modes. The agreement is quite good. The small differences between the calculated and the measured eigenmode amplitudes reflect minor inhomogeneities in the cell frequencies and in the cell-to-cell coupling of the measured cavity as well as the accuracy of the measurement (see chapter 6). The mode $j = N_c = 9$ is the accelerating mode of the cavity with a amplitude profile according to (5.121). Note that the cell to cell phase advance of the eigenmodes is always 0 or π.

Ideally the TM_{010} frequencies $f_n^{(1)}$ of the cells are tuned for a homogeneous amplitude profile of the accelerating mode. If the frequency of a cell becomes shifted from its design value by $\Delta f_n^{(1)}$, an inhomogeneity in the field amplitudes results. To illustrate this, figure 5.13 shows field amplitude profiles for the accelerating mode in a detuned TESLA 9-cell cavity. The eigenvector is calculated from (5.115) assuming that a selected cell is detuned according to (5.90) (see also (5.97) and (5.131) for uniform cell-to-cell coupling). Alternatively the perturbated eigenvector can be found from the unperturbated eigenmodes by a perturbation calculation, see chapter 6. We find that a positive cell detuning $\Delta f_n^{(1)} > 0$ increases the relative field amplitude of the accelerating mode in the detuned cell. The $\pi-$mode amplitude homogeneity is significantly more sensitive to frequency errors of the end-cells than of the center-cells, see figure 5.14.

For small errors the inhomogeneity is found to be proportional to the detuning of the cell. This is demonstrated in figure 5.15 (a), where the average π-mode amplitude homogeneity $\overline{(v_n^{(acc)})_{mean}/(v_n^{(acc)})_{max}}$ is shown for TESLA 9-cell cavities with detuned cells. In the calculation of the homogeneity it is assumed that the cell frequencies are normally distributed. Experience with the 9-cell cavities for the TTF-linac has shown, that the present preparation technique allows to maintain the cell frequency spread within $\sigma_f^{(1)} = 20$ kHz after the tuning of the cavities for amplitude homogeneity. Figure 5.15 (b) shows the corresponding distribution of the field homogeneity, calculated for 10000 cavities, as one TESLA main linac will have. The average field homogeneity is 98.8 %. Note that we have defined the field homogeneity as the quotient of the mean cell field amplitude and the maximum amplitude. Accordingly if we assume that the maximum field in a cavity is limited by the cell with the highest field, a beam gains 98.8 % of the energy it could have for perfect homogeneity. The 1.2 % reduction is tolerable and well below the limit set for the TESLA collider, see also section 6.1.

To quantify the sensitivity of a RF structure to inhomogeneities in the cell amplitude of the accelerating mode, we define a sensitivity factor S_i and write for the average homogeneity of many cavities

$$\overline{\left(\frac{(|v_n^{(acc)}|)_{mean}}{(|v_n^{(acc)}|)_{max}}\right)} = 1 - S_i \sigma_f^{(1)} \quad . \tag{5.134}$$

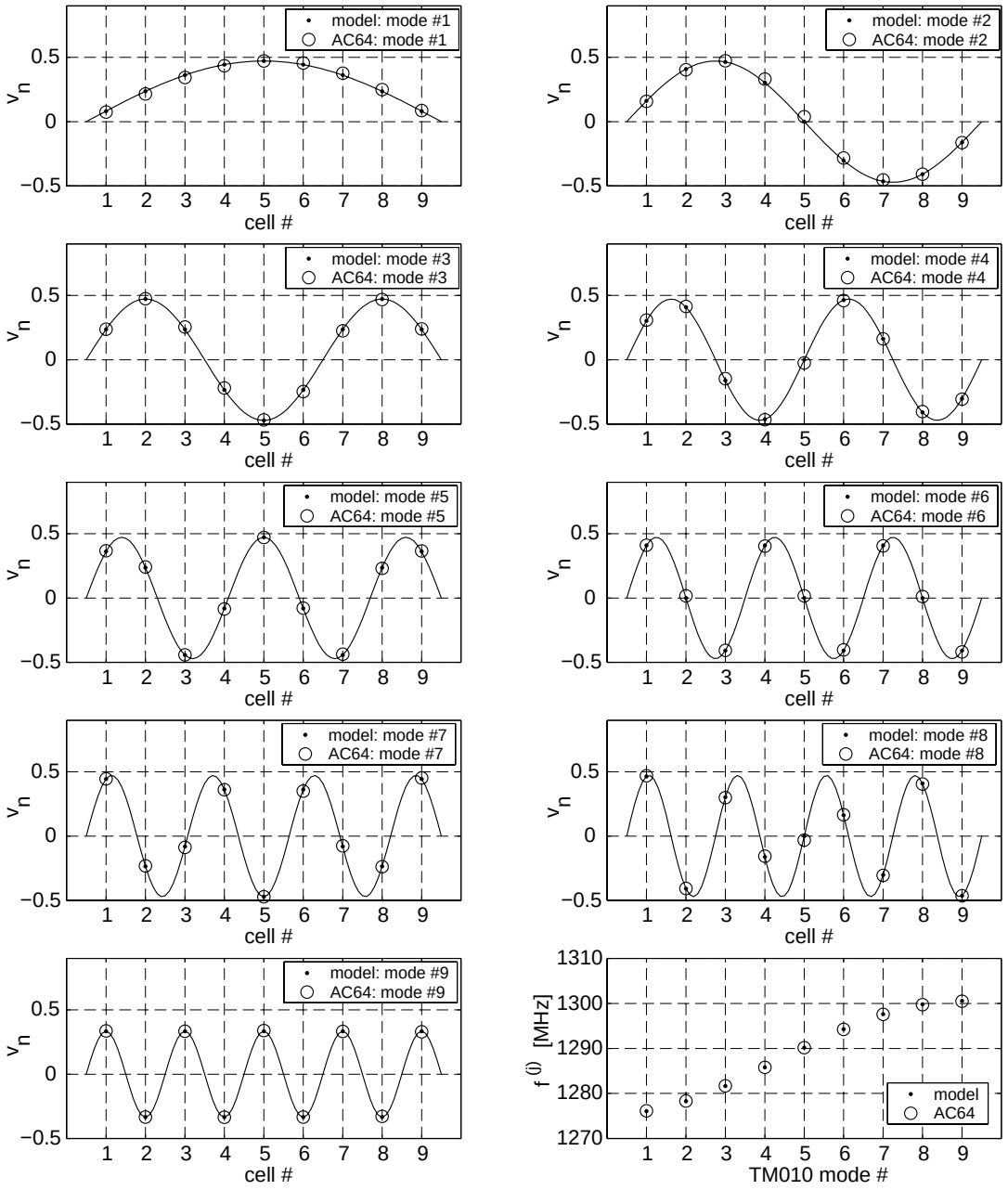

Figure 5.12: TM_{010} eigenmodes of a TESLA 9-cell cavity. Shown are the cell amplitudes of the modes as calculated from (5.132) for an ideal cavity. To verify the calculations, the measured amplitude profiles of cavity AC64 are plotted. According to (5.132) the sinusoidal curves have to be evaluated at discrete points to determine the amplitudes of the eigenmodes in the cells. Note that the phase advance between neighboring cells is always 0 or π. Also shown are the calculated ($2k_c = 0.02$, $\omega_0^{(1)}/(2\pi) = 1.275$ MHz) and measured TM_{010} eigenfrequencies.

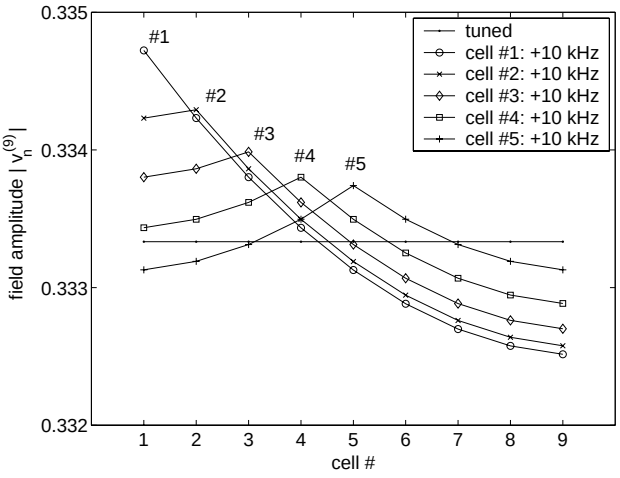

Figure 5.13: Calculated field amplitude profile for the accelerating mode in a TESLA 9-cell cavity with a selected cell detuned by $\Delta f_n^{(1)} = 10$ kHz ($2k_c = 0.019$).

For the definition of S_i we assume, that the cell frequencies of a cavity are normally distributed with $\sigma_f^{(1)}$. In (5.134) we take into account, that the inhomogeneity is proportional to small perturbations of the cell frequencies. For a single multicell cavity, the sensitivity factor S_i will depend on the number of cells N_c per cavity and the cell-to-cell coupling, see figure 5.16 and 5.17, respectively. It can be seen, that the sensitivity grows faster than linear with the number of cell (N_c). Further we find that the inhomogeneity sensitivity inreases proportional to $1/(2k_c)$. Accordingly for the amplitude homogeneity of a multicell cavity sufficient cell-to-cell coupling is required. Based on this computations we have for the sensitivity factor the approximation

$$S_i \approx \frac{4.20}{2k_c\omega_0^{(1)}}(N_c^{1.407} - 1) \qquad . \tag{5.135}$$

Note that (5.134) and (5.135) are valid only for small perturbations of the cell frequencies, typically a few 10 kHz. For larger frequency errors the inhomogeneity grows less than linearly with the cell detuning.

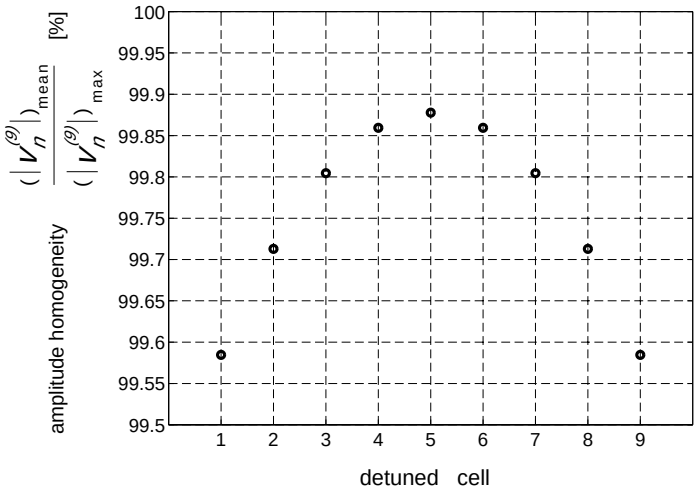

Figure 5.14: Calculated π-mode amplitude homogeneity of a TESLA 9-cell cavity ($2k_c = 0.019$) with a cell detuned by +10 kHz. Each cell has been detuned individually to determine its influence on the amplitude inhomogeneity of the π-mode.

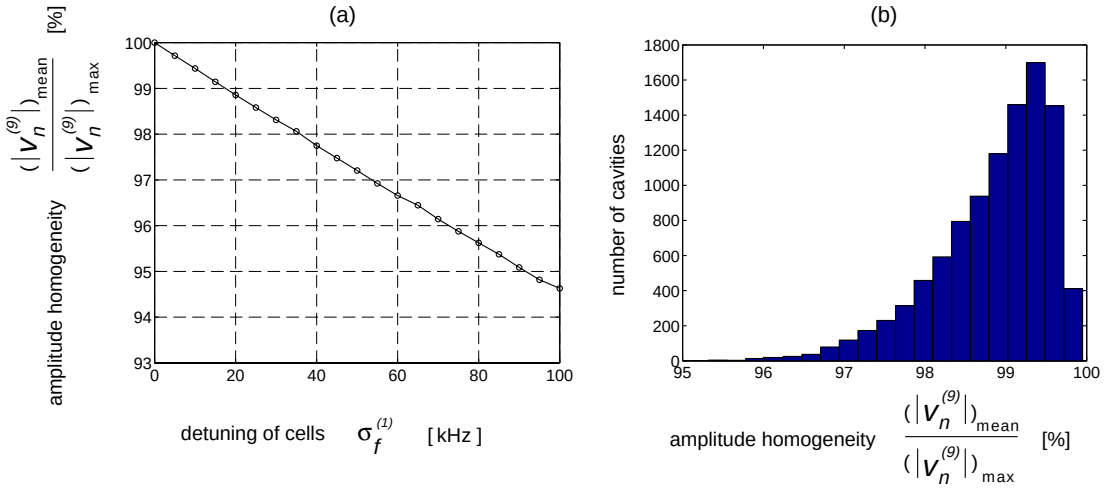

Figure 5.15: (a) Calculated average π-mode amplitude homogeneity for TESLA 9-cell cavities with detuned cells ($2k_c = 0.019$). It is assumed that the cell frequencies are normally distributed. (b) Distribution of the homogeneity for 10000 cavities with cells detuned by $\sigma_f^{(1)} = 20$ kHz.

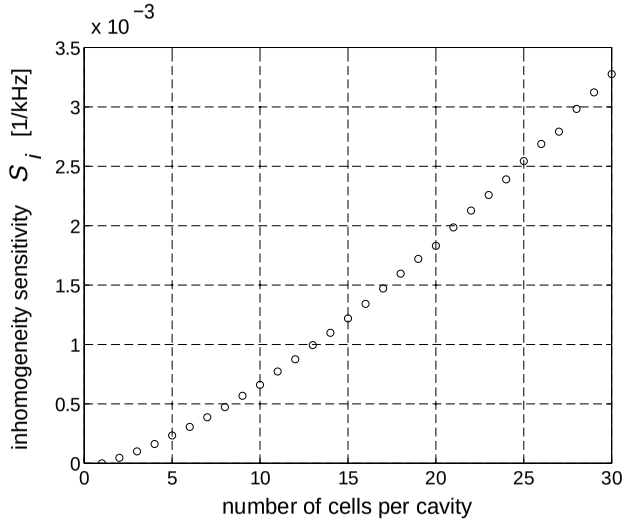

Figure 5.16: Calculated π-mode inhomogeneity sensitivity as function of the cell number N_c per cavity ($2k_c = 0.019$, $\omega_0/(2\pi) = 1.275$ GHz).

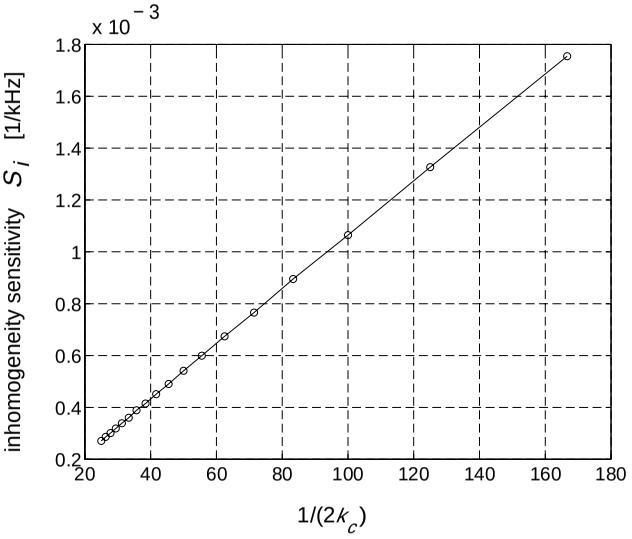

Figure 5.17: Calculated π-mode inhomogeneity sensitivity as function of the cell-to-cell coupling constant for a 9-cell cavity ($\omega_0/(2\pi) = 1.275$ GHz).

5.10 Eigenmode Representation

In this section the time dependent envelope functions of the cell fields are expanded in terms of the cavity TM_{010} orthonormal eigenmodes. Therefore we write

$$\vec{\hat{\mathcal{E}}}(t) = \sum_{j=1}^{N} a^{(j)}(t)\vec{v}^{(j)} \quad , \tag{5.136}$$

where $a^{(j)}(t)$ are the time dependent expansion coefficents and $\vec{v}^{(j)}$ the eigenmodes . Accordingly we transform the differential equation (5.106) for the fields in the cells of a cavity into a differential equation for the excitation of the TM_{010} eigenmodes of the whole cavity. On account of the orthogonality of the modes we have

$$(\vec{v}^{(l)})^T \vec{\hat{\mathcal{E}}}(t) = \sum_{j=1}^{N} a^{(j)}(t)(\vec{v}^{(l)})^T \vec{v}^{(j)} = a^{(l)}(t) \quad . \tag{5.137}$$

To transform (5.106), we insert (5.136), multiply from the left by the transposed vector $(\vec{v}^{(l)})^T$ and use (5.137). We find the differential equations for the coefficents $a^{(l)}(t)$

$$\frac{da^{(l)}}{dt} + \frac{(\omega_0^{(1)})^2}{2} \sum_{j=1}^{N} (\vec{v}^{(l)})^t \mathbf{B} \vec{v}^{(j)} a^{(j)} + \frac{i\omega_g}{2} \left\{ 1 - \left(\frac{\omega_0^{(1)}}{\omega_g} \right)^2 \sum_{j=1}^{N} (\vec{v}^{(l)})^t \mathbf{A} \vec{v}^{(j)} \right\} a^{(j)}$$
$$= \frac{iK_g^{(1)} v_1^{(l)}}{2\varepsilon_0 \omega_g} \dot{J}_{g,1} e^{-i\omega_g t} \tag{5.138}$$

for $l = 1, ..., N$. We can separate the square matrix $\mathbf{B}$ into a term for the wall losses and a term for the external load. The wall losses are practically independent of the small perturbations of the cell frequencies (refer to the disussion in section 5.5). Hence we get

$$\mathbf{B} = \mathbf{B}_0 + \mathbf{B}_e = \frac{1}{\omega_0^{(1)} Q_0^{(1)}} \mathbf{1} + \frac{\omega_1^{(1)}}{Q_{e,1}^{(1,1)} (\omega_0^{(1)})^2} \begin{bmatrix} 1 & & 0 \\ & 0 & \\ 0 & & \ddots \end{bmatrix} \quad . \tag{5.139}$$

As before we consider a cavity driven by a coupler close to the first cell. By inserting (5.139) into (5.138), the damping term due to wall losses in (5.138) yields

$$(\omega_0^{(1)})^2 \sum_{j=1}^{N} (\vec{v}^{(l)})^t \mathbf{B}_0 \vec{v}^{(j)} a^{(j)} = \frac{\omega_0^{(1)}}{Q_0^{(1)}} a^{(l)} \quad . \tag{5.140}$$

We find that the coupling of eigenmodes due to the wall losses vanishes on account of the orthogonality of the TM_{010} amplitude eigenvectors. By way of contrast for the damping term due to the external load the intermode coupling remains

$$(\omega_0^{(1)})^2 \sum_{j=1}^{N} (\vec{v}^{(l)})^t \mathbf{B}_e \vec{v}^{(j)} a^{(j)} = \frac{\omega_1^{(1)}}{Q_{e,1}^{(1,1)}} v_1^{(l)} \sum_{j=1}^{N} v_1^{(j)} a^{(j)} =: \sum_{j=1}^{N} \frac{\omega^{(l)}}{Q_e^{(jl)}} a^{(j)} \quad . \tag{5.141}$$

Further we find from the orthogonality of the eigenvectors and the equation (5.115) that $(\vec{v}^{(l)})^t \mathbf{A} \vec{v}^{(j)} = \delta_{lj}(\omega^{(j)})^2/(\omega_0^{(1)})^2$. Moreover we can consider that the mode frequency $\omega^{(j)}$ and the generator frequency ω_g are nearly equal and use the approximation

$$\frac{\omega_g}{2}\left\{1 - \left(\frac{\omega^{(l)}}{\omega_g}\right)^2\right\} \approx -(\omega^{(l)} - \omega_g) =: -\Delta\omega^{(l)} \quad , \tag{5.142}$$

where $\Delta\omega^{(l)}$ is the frequency deviation between the resonance frequency of mode l and the generator frequency. Finally by this we have for the differential equation (5.138) for the mode l

$$\frac{da^{(l)}}{dt} + \frac{\omega_0^{(1)}}{2Q_0^{(1)}} a^{(l)} + \sum_{j=1}^{N} \frac{\omega^{(l)}}{2Q_e^{(jl)}} a^{(j)} - i\Delta\omega^{(l)} a^{(l)} = \frac{iK_g^{(1)} v_1^{(l)}}{2\varepsilon_0 \omega_g} \dot{J}_{g,1} e^{-i\omega_g t} \, . \tag{5.143}$$

Accordingly we have a system of N coupled differential equations of first order. By numerical integration we can solve this system and compute the transient TM_{010} field amplitudes in superstructures, see chapter 7. Note that a slowly varying envelope approximation for the mode expansion coefficents $\mathcal{E}^{(m)}$ in the second order differential equation (5.68) results also in the first order differential equation (5.143). The TM_{010} field envelope amplitude of cell n can be obtaind from a summation on the modes of the TM_{010} group (see (5.136))

$$\hat{\mathcal{E}}_n(t) = \sum_{l=1}^{N} a^{(l)}(t) v_n^{(l)} \quad . \tag{5.144}$$

Here $v_n^{(l)}$ is the value of the eigenvector of mode l for cell n and $a^{(l)}(t)$ is the envelope function for the excitation of mode l. Similarly the TM_{010} field in a cavity is given by a summation on the TM_{010} eigenmodes of the cavity

$$\vec{E}(\vec{r},t) = \sum_{l=1}^{N} \mathcal{E}^{(l)}(t) \vec{e}^{(l)}(\vec{r}) = \sum_{l=1}^{N} a^{(l)}(t) e^{i\omega_g t} \vec{e}^{(l)}(\vec{r}) \quad , \tag{5.145}$$

where the normalized eigenmode functions $\vec{e}^{(l)}(\vec{r})$ (see (5.6)) can be obtained from the TM_{010} eigenmode functions $\vec{e}_n^{(1)}(\vec{r})$ of the individual cells

$$\vec{e}^{(l)}(\vec{r}) = \sum_{n=1}^{N} v_n^{(l)} \vec{e}_n^{(1)}(\vec{r}) \tag{5.146}$$

or, more accurate, can be computed by numerical eigenmode codes like MAFIA [Kla 86]. The ratio $(R_{sh}/Q_0)^{(l)}$ determines the level of interaction between the mode l and the beam (see (5.58)) and amounts for a multicell cavity approximately to

$$\left(\frac{R_{sh}}{Q_0}\right)^{(l)} \approx \left(\frac{R_{sh}}{Q_0}\right)_1^{(1)} \left| \sum_{n=1}^{N} v_n^{(l)} e^{in\pi f^{(l)}/f^{(acc)}} \right|^2 \quad , \tag{5.147}$$

where $(R_{sh}/Q_0)_1^{(1)}$ is the corresonding value of a single cell. This equation is valid for a multicell cavity with a cell length $l = c/(2f^{(acc)})$ for a relativistic beam ($v \approx c$),

where $f^{(acc)}$ is the eigenfrequency of the accelerating mode. For a tuned multicell cavity with an accelerating mode eigenvector $\vec{v}^{(acc)} = [1, -1, 1, ...]^T$, we see from (5.147), that the ratio $(R_{sh}/Q_0)^{(l)}$ almost vanishes for all other modes on account of the orthogonality of the modes ($\frac{f^{(l)}}{f^{(acc)}} \approx 1$). Alternatively to equation (5.147), $(R_{sh}/Q_0)^{(l)}$ can be computed by numerical eigenmode codes for the TM_{010} modes of a complete multicell cavity.
Measurements of the field profile along the cavity axis are usually performed at room temperature. During such kind of room temperature studies, the losses are normally dominated by the wall losses, i.e. $Q_{e,1}^{(1,1)} \gg Q_0^{(1)}$. For this case and for a constant amplitude generator current $J_{g,1} = \hat{J}_g e^{i\omega_g t}$ the analytical solution of (5.143) is

$$a^{(l)}(t) = C^{(l)} \left\{ e^{-\left(\frac{\omega_0^{(1)}}{2Q_0^{(1)}} - i\Delta\omega^{(l)}\right)(t-t_0)} - 1 \right\} + a_0^{(l)} e^{-\left(\frac{\omega_0^{(1)}}{2Q_0^{(1)}} - i\Delta\omega^{(l)}\right)(t-t_0)} \quad , \qquad (5.148)$$

where $a_0^{(l)} = a^{(l)}(t_0)$ is the initial condition at $t = t_0$ and

$$C^{(l)} = \frac{K_g^{(1)} v_1^{(l)} \hat{J}_g}{2\varepsilon_0 \left(\frac{\omega_0^{(1)}}{2Q_0^{(1)}} - i\Delta\omega^{(l)}\right)} \quad . \qquad (5.149)$$

This completes our discussion of a model for the TM_{010} mode amplitudes in a multicell cavity. In the following chapters we shall apply this model to superstructures to study the field homogeneity and its tuning, the transient state and the RF field control. In the last section of this chapter we will begin this studies with the steady state field amplitudes in superstructures.

5.11 Summary

The basis of our cavity circuit model is the expansion (5.28) of the cavity fields in terms of orthonormal eigenmode functions (5.6). We found a second order differential equation (5.40) for the time dependent expansion coefficients. After introducing wall losses, an external load and a generator drive, we discribed the cavity eigenmode amplitudes by a system of coupled differential equations (5.68).
To study the group of **TM_{010} modes in a multicell cavity** we defined a cell-to-cell coupling constant (5.74) and derived a system of second order differential equations (5.81) for the TM_{010} *amplitude coefficients* $\mathcal{E}_n^{(1)}$ *of the individual cells.* We showed that this equation corresponds to the equivalent circuit diagramm of figure 5.8. The RF fields in a cavity oscillate with a frequency nearly equal to the generator frequency (ω_g). Accordingly we wrote $\mathcal{E}_n^{(1)} = \hat{\mathcal{E}}_n e^{i\omega_g t}$ and made a slowly varying envelope approximation to obtain a first order differential equation (5.106) for the cell's envelop amplitude coefficents $\hat{\mathcal{E}}_n$.
The orthonormal TM_{010} amplitude eigenmodes $\vec{v}^{(j)}$ of a multicell cavity can be calculated from the equation (5.115). The eigenvectors $\vec{v}^{(j)}$ describe the TM_{010} cell amplitude profile for the different TM_{010} modes of a multicell cavity.
Alternatively to the amplitude coefficients $\mathcal{E}_n^{(1)}$ of the cells, we used the *amplitude*

coefficients $a^{(j)}$ *of the individual* TM_{010} *modes of a multicell cavity* to represent the TM_{010} fields in a multicell cavity. We found a system of first order differential equations (5.143) for the mode amplitude coefficients. Both representations are equivalent.

5.12 Superstructures: Steady State Field Amplitudes

In this section we shall discuss the steady state TM_{010} field properties of superstructures. Exemplary we will consider the 2x9-cell structure proposed for the TESLA collider. We can easily conclude from the results for this structure on the properties of other superstructures.
For the beginning let us assume that the superstructure is perfectly tuned for homogeneous field amplitudes of the accelerating mode, see (5.121). Then we can use (5.131) to model the TM_{010} properties of the cavity and can compute the steady state field coefficients from (5.107). Figure 5.18 shows the resulting field amplitude of cell #1 as a function of the generator frequency. On the left side of this figure

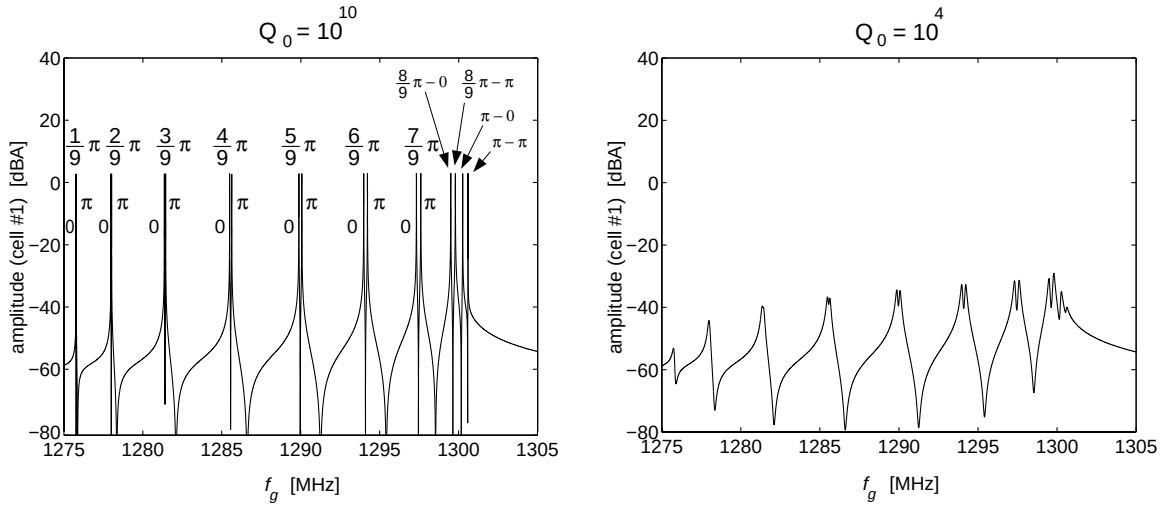

Figure 5.18: Computed resonance spectrum of the TM_{010} modes in a 2x9-cell superstructure. Shown is the steady state amplitude of the field in cell #1 as a function of the frequency of the driving RF generator ($\mathcal{K}_{cc} = 0.02$, $\mathcal{K}_{rr} = 2.8 \cdot 10^{-4}$, $\omega_0/(2\pi) = 1.275$ GHz). On the left side a frequency scan is plotted for a superconducting structure ($Q_{e,1}^{(1,1)} = 5.5 \cdot 10^4$, $Q_0^{(1)} = 10^{10}$), whereas the right side shows a frequency scan for a superstructure at room temperature ($Q_{e,1}^{(1,1)} = 5.5 \cdot 10^4$, $Q_0^{(1)} = 10^4$).

the resonance spectrum is plotted for a superconducting structure ($Q_0^{(1)} = 10^{10}$) at cryogenic temperatures, whereas on the right side the spectrum is shown for a niobium structure at room temperature ($Q_0^{(1)} = 10^4$). As discussed before, it is found that a 2x9-cell superstructure has 18 TM_{010} modes, designated by $\frac{1}{9}\pi - 0$, $\frac{1}{9}\pi - \pi$, ..., $\pi - \pi$. This modes built up $N_c = 9$ subgroups with $M = 2$ modes each. Because of the comparatively weak resonator-to-resonator coupling, the frequency spacing of

the two modes per group is smaller than the spacing of the nine subgroups. At room temperature the resonances overlap significantly. Therefore the two modes of the lower frequency subgroups cannot be separated at room temperature. It can be seen from figure 5.19, that the mode $M(N_c-1)+1=17$ is the accelerating mode for a cell length $l=c/(2f^{(17)})$ and a relativistic beam ($v\approx c$). This mode is the so-called TM_{010} $\pi-0$ mode of the 2x9-cell superstructure. As aimed by the tuning of the

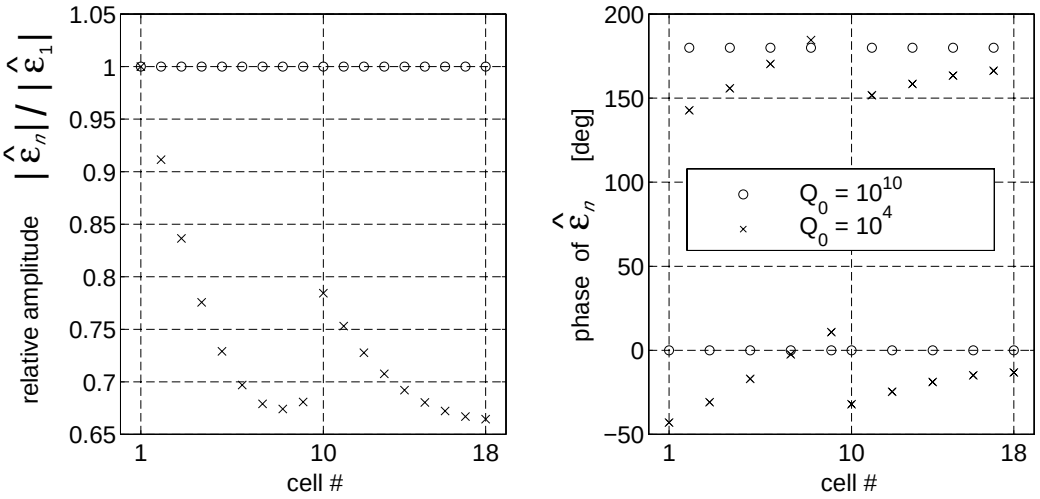

Figure 5.19: Computed steady state envelope coefficients of a tuned 2x9-cell superstructure ($\mathcal{K}_{cc}=0.02$, $\mathcal{K}_{rr}=2.8\cdot10^{-4}$, $\omega_0/(2\pi)=1.275$ GHz, $Q_{e,1}^{(1,1)}=5.5\cdot10^4$) driven on its 17^{th} resonance (maximum field amplitude in cell #1). Shown are amplitude and phase of the TM_{010} coefficients for the individual cells for a superconducting structure ($Q_0^{(1)}=10^{10}$) and for a superstructure at room temperature ($Q_0^{(1)}=10^4$).

cell's frequency, we find homogenious field amplitudes for this mode in a superconducting superstructure. At room temperatures the neighboring modes (mainly the $\frac{8}{9}\pi-0$, $\frac{8}{9}\pi-\pi$ and $\pi-\pi$ mode) overlap with mode 17 and influence the amplitude profile considerably, see figure 5.19. Obviously this becomes important, when the cell's amplitude profile is measured at room temperature to tune the cell frequencies for homogenious field amplitudes at cryogenic temperatures, see chapter 6.
Figure 5.20 shows the amplitude profiles of the TM_{010} group of eigenmodes for a lossfree 2x9-cell superstructure. The eigenvectors are calculated from (5.115) with the square matrix (5.131) for a tuned structure. Comparing the amplitude profiles of a TESLA 9-cell cavity (figure 5.12) and the 2x9-cell superstructure, it is found that the profile of the odd numbered 2x9-cell modes is composed of the eigenvectors of the 9-cell cavity. Moreover for the same cell-to-cell coupling the eigenfrequencies of the odd numbered 2x9-cell modes equals the mode frequencies of the 9-cell cavity. If the frequency of a cell is shifted from its design value for a homogeneous $\pi-0$ mode amplitude profile, this will cause an inhomogeneity, see figure 5.21 and compare to figure 5.13. A positive cell detuning $\Delta f_n^{(1)}=f_n^{(1)}-f_0^{(1)}>0$ increases the fields amplitude of the $\pi-0$ mode in this cell, as in the 9-cell cavity, but lowers the average field amplitude of the cavity containing the detuned cell. Similarly, if all

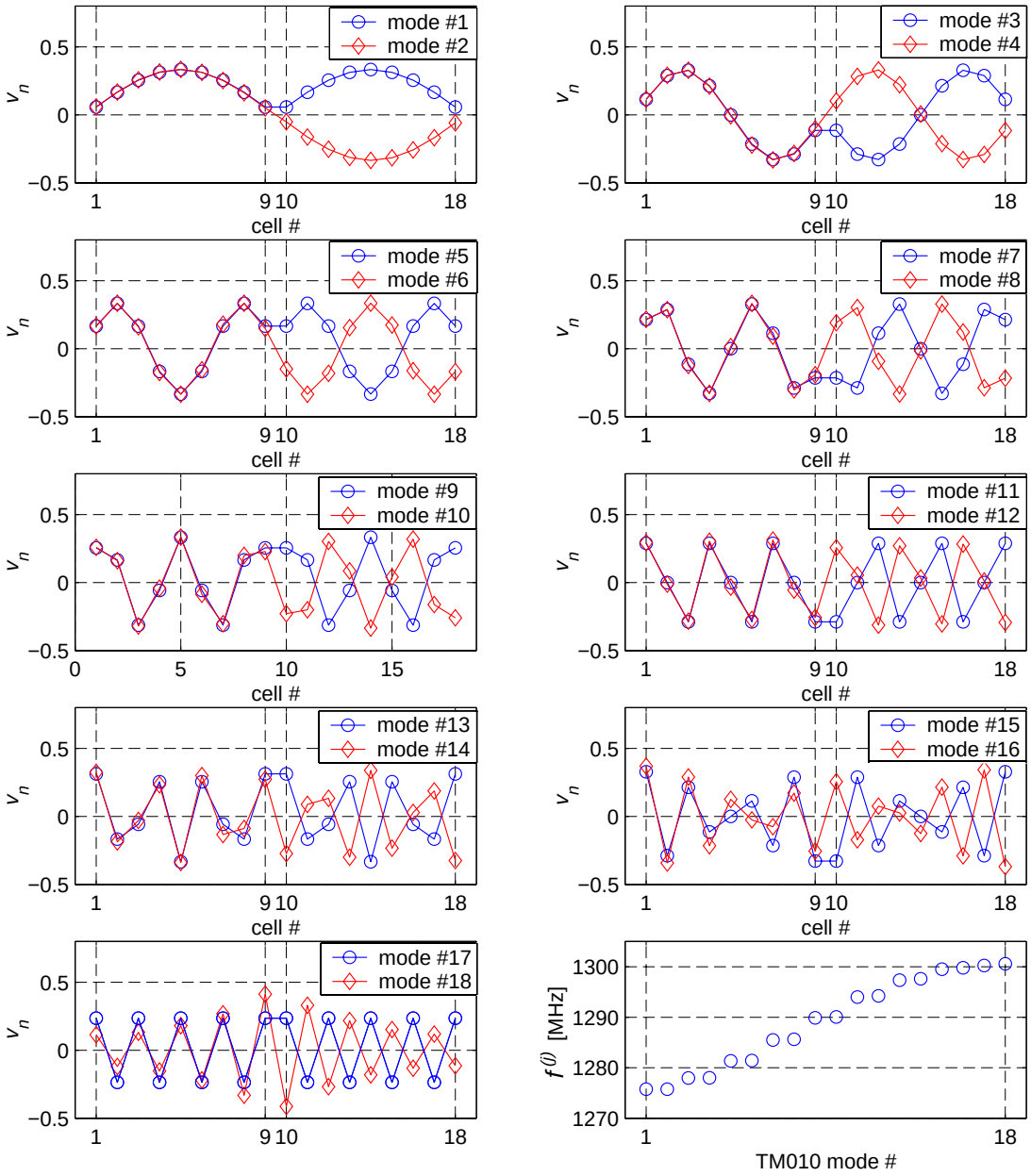

Figure 5.20: TM_{010} eigenmodes of a 2x9-cell superstructure. Shown are the cell amplitudes of the modes as calculated from (5.115) for a tuned superstructure ($\mathcal{K}_{cc} = 0.02$, $\mathcal{K}_{rr} = 2.8 \cdot 10^{-4}$, $\omega_0/(2\pi) = 1.275$ GHz). Note that the profile of the cell's TM_{010} field amplitudes is shown, and not the field profile along the cavity axis. The values are connected by lines to guide the eye. Also shown are the calculated eigenfrequencies.

cell frequencies of a coupled cavity are increased, the relative $\pi - 0$ field amplitudes of this cavity are lowered.

Finally we can use the solution (5.148) of the differential equation (5.143) to determine the steady state envelope coefficients of the TM_{010} eigenmodes of the su-

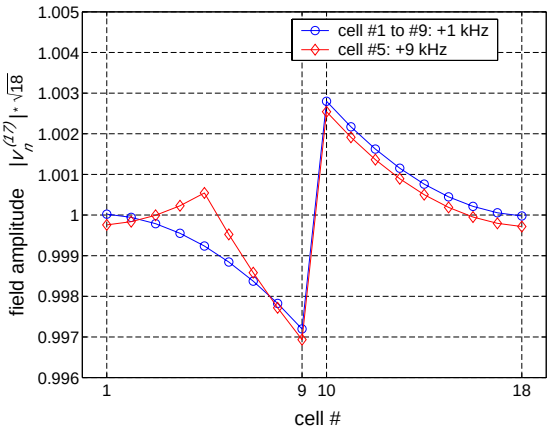

Figure 5.21: Calculated field amplitude profile for the accelerating eigenmode in a detuned 2x9-cell superstructure. Shown are the amplitude profiles for a structure with a single detuned cell and for a structure with a detuned cavity ($\mathcal{K}_{cc} = 0.02$, $\mathcal{K}_{rr} = 2.8 \cdot 10^{-4}$, $\omega_0/(2\pi) = 1.275$ GHz).

perstructure. Based on the eigenvectors $\vec{v}^{(j)}$ the envelope field amplitudes of the individual cells can then be calculated, see (5.144). As an example, this separation into the TM_{010} eigenmodes is shown in figure 5.22 for the room temperature amplitude profile plotted in figure 5.19. As discussed before, the profile is modified considerably by overlapping modes.

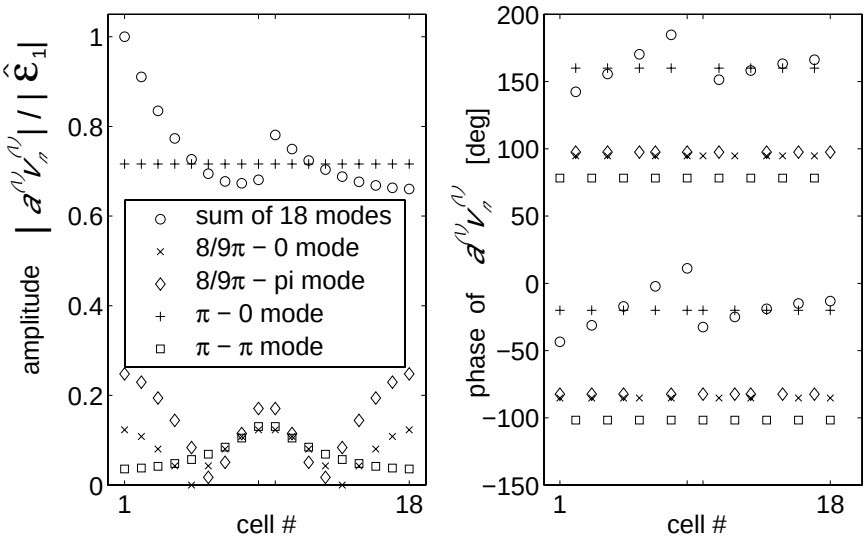

Figure 5.22: Computed steady-state envelope coefficients of a tuned 2x9-cell superstructure at room temperature ($\mathcal{K}_{cc} = 0.02$, $\mathcal{K}_{rr} = 2.8 \cdot 10^{-4}$, $\omega_0/(2\pi) = 1.275$ GHz, $Q_0^{(1)} = 10^4$) driven on its 17^{th} resonance (maximum field amplitude in cell #1). Shown are the TM_{010} amplitude coefficents of the cells for the dominating TM_{010} modes. In addition the sum of all 18 TM_{010} cavity modes is plotted; compare to figure 5.19.

CHAPTER 6

6 Amplitude Profile Measurement and Tuning

6.1 Requirements on Amplitude Homogeneity

Ideally the accelerating TM_{010} eigenmode of a multicell cavity should have equal field amplitudes in all cells. This has two advantages: For a given amount of stored energy the net accelerating voltage of the cavity is maximized and the peak surface RF field is minimized. The fundamental field limit of superconducting cavities is set by the RF critical magnetic field [Pad 98]. However, usually the field is limited below by technical reasons like defects in the material and field emission. Consider that a multicell cavity is is operated at its maximum field. Then the TM_{010} amplitude homogeneity of the cavity

$$\text{amplitude homogeneity} := \frac{\text{mean field amplitude of the cells}}{\text{maximum amplitude}} \tag{6.1}$$

is particular important, since any amplitude inhomogeneity reduces the maximum possible energy gain of a beam, if the field limit is set by the cell with the highest field.
It is desirable to operate superconducting cavities below their field-break-down limit to provide a safety margin. The TESLA cavities of the recent production series have shown a maximum average gradient of 28.3 MV/m, whereas the design accelerating gradient for TESLA-500 is 23.4 MV/m, i.e. in average more than 15 % below the present maximum performance. Obviously this relaxes the requirements on the TM_{010} amplitude homogeneity of the accelerating mode considerably. Accordingly the lower limit for the *average amplitude homogeneity* is set to 95 % for the TESLA collider. This homogeneity has to be achieved by properly tuning the cell frequencies. Amplitude profile tuning is usually needed only after the fabrication of the cavity and after major cavity preparation steps, like strong surface etching or heat treatment, since they may perturb the cell geometry.
In this chapter we will discuss the measurement and the tuning of the amplitude profile for standard multicell cavities as well as for superstructures. We will find major differences. Moreover during operation of a superstructure in a linac, the stored energy in the cavities has to be balanced by proper cavity tuning. The method developed for this adjustment is presented in section 6.4.

6.2 Amplitude Profile Measurements

The standard technique to measure the amplitude profile of electromagnetic eigenmodes in cavities at room temperature is based on perturbing the mode eigenfrequencies [Mai 52]. This is realized by mounting a small metal bead on a Nylon string along the cavity axis, see figure 6.1. The perturbing bead is pulled through

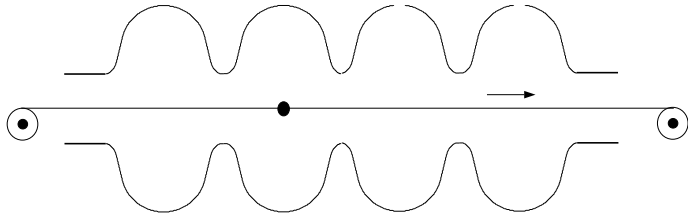

Figure 6.1: Setup to measure the field profile on the axis of a cavity. A tiny metal bead is sent through the cavity to perturb the cell frequencies.

the axis of a cavity. Due to the volume occupied by the metal bead the resonance frequency of a eigenmode j is shifted according to [Sla 50] by

$$\left(\frac{f^{(j)\prime}}{f^{(j)}}\right)^2 \approx 1 + \frac{1}{U^{(j)}} \int_{\Delta V_{bead}} \left(\frac{\mu_0}{2} \left|\vec{H}^{\,(j)}\right|^2 - \frac{\varepsilon_0}{2} \left|\vec{E}^{\,(j)}\right|^2 \right) dv \quad . \tag{6.2}$$

Here $\vec{E}^{\,(j)}$ and $\vec{H}^{\,(j)}$ are the unperturbated fields, $U^{(j)}$ is the stored energy and ΔV_{bead} is the volume occupied by the metal bead. Since the TM_{010} eigenmodes have a vanishing magnetic field on the cavity axis, we can use the following approximation for a small metal bead placed on the cavity axis at $z = z_{bead}$

$$\frac{\delta f^{(j)}_{bead}}{f^{(j)}} \approx -\frac{\varepsilon_0 \Delta V_{bead}}{4} \frac{|\vec{E}^{\,(j)}(z_{bead})|^2}{U^{(j)}} = -\frac{\Delta V_{bead}}{2} |\vec{e}^{(j)}(z_{bead})|^2 \quad . \tag{6.3}$$

Here $\vec{e}^{(j)}(\vec{r})$ is the normalized eigenfunction of the electric eigenmode field, see section 5.1. We see from (6.3), that the profile of the electric field amplitude along the cavity axis can be measured by measuring the eigenfrequency shift $\delta f^{(j)}_{bead}$ due to the bead. Note that a bead-bull measurement gives no phase information.
During a field profile measurement the cavity is driven by a RF generator via an input antenna close to one of the end-cells. The RF field in the cavity is measured via an output antenna. Two methods can be used to approximately determine the frequency shift $\delta f^{(j)}_{bead}$ of an eigenmode j from the output antenna signal:

- measure the frequency shift δf_{amp} of the field amplitude maximum on the j^{th} resonance curve, see figure 6.2 (a), or
- measure the frequency shift δf_{ph} by tracking a constant phase, which is set by the phase at the unperturbated field maximum, see figure 6.2 (b). The phase of the RF field signal is measured with respect to the generator RF signal. For tracking the phase, a network analyzer or a phase looked loop is used.

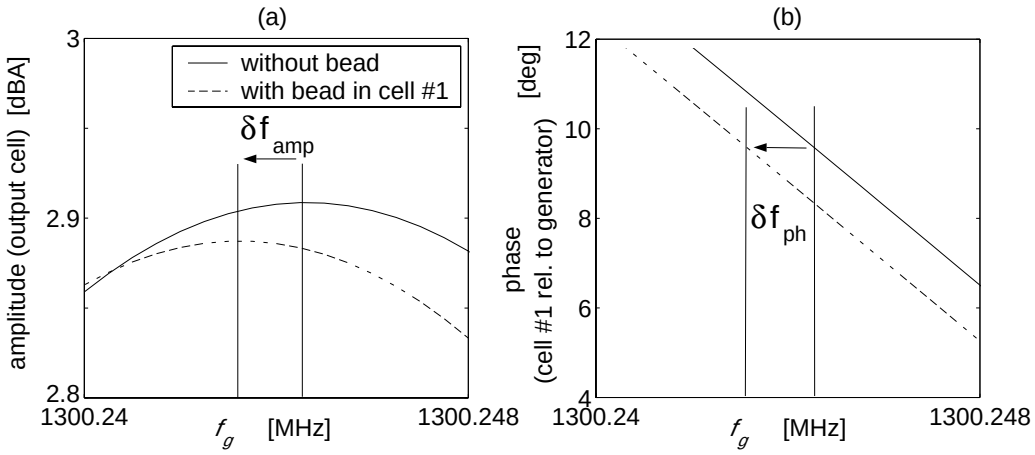

Figure 6.2: Two different methods to approximately determine the eigenfrequency shift due to the metal bead at room temperature. (a) The frequency shift of the resonance maximum is measured. (b) Tracking a nominal phase, which is set by the phase at the unperturbated field maximum.

It can be seen from figure 6.2 that the amplitude is almost constant near to resonance, thus finding the maximum is noise-sensitive. In contrast to this, measuring of the frequency shift δf_{ph} is less sensitive to noise, because near to resonance the phase is changing almost linearly. Therefore δf_{ph} is usually measured to approximately determine the frequency shift $\delta f_{bead}^{(j)}$ of an eigenmode. According to equation (6.3), the *measured profile* is given by $\sqrt{|\delta f_{ph}|/1\text{kHz}}$. As an example, figure 6.3 (a) shows the measured on-axis electric field amplitude profile of the TM_{010} π mode in a 7-cell cavity before tuning for amplitude homogeneity.

The values $\sqrt{|\delta f_{ph}|/1\text{kHz}}$ at the *center of the cells* give the bead-pull measured profile of the TM_{010} cell amplitudes, see figure 6.3 (b). Accordingly by moving the

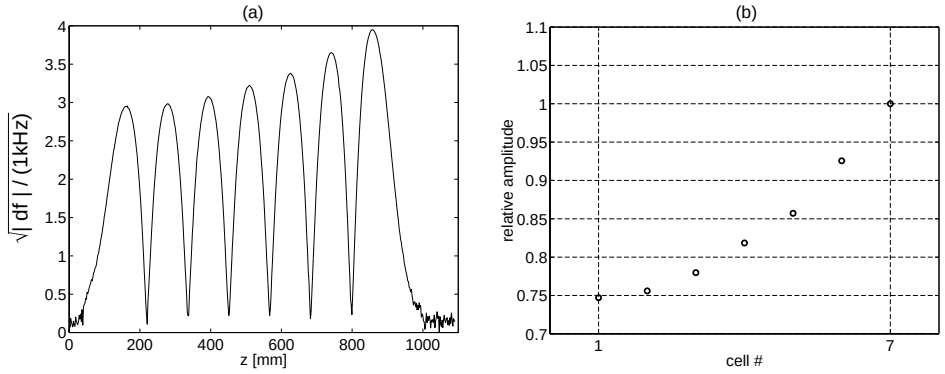

Figure 6.3: (a) On-axis electric field amplitude profile of the TM_{010} π-mode in a 7-cell cavity. Bead-pull measurement before tuning for amplitude homogeneity. (b) Corresponding TM_{010} cell amplitudes profile.

metal bead to the center of the cells in succession, the cell amplitude profile of a TM_{010} eigenmode in a multicell cavity can be measured. At the center of a cell the bead perturbs the TM_{010} frequency $\omega_n^{(1)}$ of the corresponding cell by a small detuning $\delta\omega_b$. In our lumped element circuit for a multicell cavity we can model this by the out-of-tune parameter

$$\delta_n = \delta_{bead} = 2\frac{\delta\omega_b}{\omega_0^{(1)}} + \left(\frac{\delta\omega_b}{\omega_0^{(1)}}\right)^2 \approx 2\frac{\delta\omega_b}{\omega_0^{(1)}} \quad , \tag{6.4}$$

see (5.90). Recall that $\omega_0^{(1)}$ is the TM_{010} nominal frequency of the cells.
For the small perturbation $\delta_n \ll 1$ we can apply standard perturbation techniques to find how the bead affects the TM_{010} eigenfrequencies and eigenmodes of the cavity. The unperturbated eigenmodes of the cavity are the solution of the matrix equation (5.115)

$$\mathbf{A}\vec{v}^{(j)} = \Omega^{(j)}\vec{v}^{(j)} \quad . \tag{6.5}$$

As before j designates the TM_{010} cavity eigenmode number ($j = 1, ...,$ number of cells). For given perturbations δ_n of the cells we define a diagonal perturbation matrix $\mathbf{P}$ with the diagonal elements $P_{nn} := \delta_n$. Accordingly we can write for the perturbated eigensystem

$$(\mathbf{A} + \mathbf{P})(\vec{v}^{(j)})' = (\Omega^{(j)})'(\vec{v}^{(j)})' \quad , \tag{6.6}$$

see (5.116) to (5.120). The primed quantities are the perturbated solutions. The TM_{010} eigenfrequencies of the cavities are non-degenerate, see (5.133). Using a *first order* non-degenerate perturbation approach we find for the perturbated eigenvectors

$$(\vec{v}^{(j)})' \approx \vec{v}^{(j)} + \sum_{r\neq j} a_{jr}\vec{v}^{(r)} \quad , \tag{6.7}$$

with

$$a_{jr} = \frac{1}{\Omega^{(j)} - \Omega^{(r)}} \sum_n v_n^{(j)}\delta_n v_n^{(r)} \quad , \tag{6.8}$$

and for the perturbated eigenvalues

$$(\Omega^{(j)})' = \left(\frac{\omega^{(j)\prime}}{\omega_0^{(1)}}\right)^2 \approx \Omega^{(j)} + \sum_n v_n^{(j)}\delta_n v_n^{(j)} \quad . \tag{6.9}$$

Refer to [Pad 98] for a detailed derivation of these equations.
In an amplitude profile measurement the metal bead is successively placed at the center of the cells. Considering that the bead is in the center of cell b, we find from (6.7) and (6.9)

$$\delta\vec{v}_{bead}^{(j)} = (\vec{v}^{(j)})' - \vec{v}^{(j)} \approx \sum_{r\neq j} \frac{1}{\Omega^{(j)} - \Omega^{(r)}} v_b^{(j)}\delta_{bead}v_b^{(r)}\vec{v}^{(r)} \tag{6.10}$$

$$\delta\Omega_{bead}^{(j)} = (\Omega^{(j)})' - \Omega^{(j)} \approx \delta_{bead}\left(v_b^{(j)}\right)^2 \approx 2\Omega^{(j)}\frac{\delta f_{bead}^{(j)}}{f^{(j)}} \quad . \tag{6.11}$$

Again we see, that the normalized mode amplitude $|v_b^{(j)}|$ in a cell can be determined by measuring the eigenfrequency shift of a mode due to the small bead at the center

of the cell. Note that a bead-pull measurement gives absolut values $|v_b^{(j)}|$.
It is discussed above that the frequency shift $\delta f_{bead}^{(j)}$ is usually determined by measuring the frequency shift Δf_{ph} for tracking a constant phase. We shall see that Δf_{ph} and $\delta f_{bead}^{(j)}$ are in good agreement for 7-cell and 9-cell cavities, as long as the two antennas are mounted at opposite end-cells. Accordingly measuring Δf_{ph} is the standard procedure to determine the amplitude profiles of the TM_{010} eigenmodes in TESLA multicell cavites. The eigenmode profile of the accelerating mode then needs to be tuned for homogeneity.
It is important to note, that the first order perturbation approximation (6.11) is used to determine the mode amplitude profiles. More accurately we have for the perturbated eigenvalues in a second order perturbation approach

$$\delta\Omega_{bead}^{(j)} = (\Omega^{(j)})' - \Omega^{(j)} \approx \delta_{bead}\left(v_b^{(j)}\right)^2 + \sum_{r\neq j} \frac{1}{\Omega^{(j)} - \Omega^{(r)}}\left(\delta_{bead} v_b^{(j)} v_b^{(r)}\right)^2 \quad . \tag{6.12}$$

As before we consider that the metal bead is in the center of cell b. To ensure that the second order term in (6.12) can be neglected, the frequency perturbation due to the bead has to be sufficient small. From (6.4) and (6.12) we find the condition $\delta f_b \ll \Delta f_{modes}$. We will see later in this section, that a perturbation $\delta f_b < 100$ kHz should be used for an accurate bead-pull measurement.
The amplitude profiles measurement in superstructures needs to be studied more carefully. The reason for this is, that the spacing of modes is significantly smaller in a superstructure than in a TESLA 9-cell cavity. Accordingly we have to take into account, that the modes overlap at room temperature (see figure 6.4), which is perturbing the bead-pull measurement. Figure 6.5 shows measured on-axis profiles for selected TM_{010} resonances of a 2×7-cell prototype superstructure. The measured

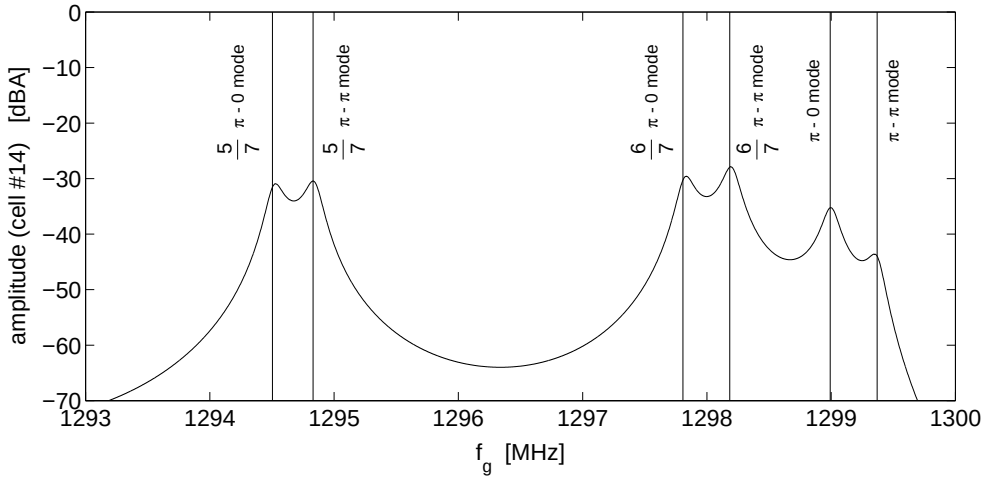

Figure 6.4: Calculated resonance spectrum of the higher frequency TM_{010} modes in a TESLA 2×7-cell superstructure at room temperature ($Q_0^{(1)} = 10^4$). Shown is the steady state amplitude of the field in cell #14 as function of the driving RF generator frequency. The vertical lines mark the eigenfrequencies of the TM_{010} eigenmodes.

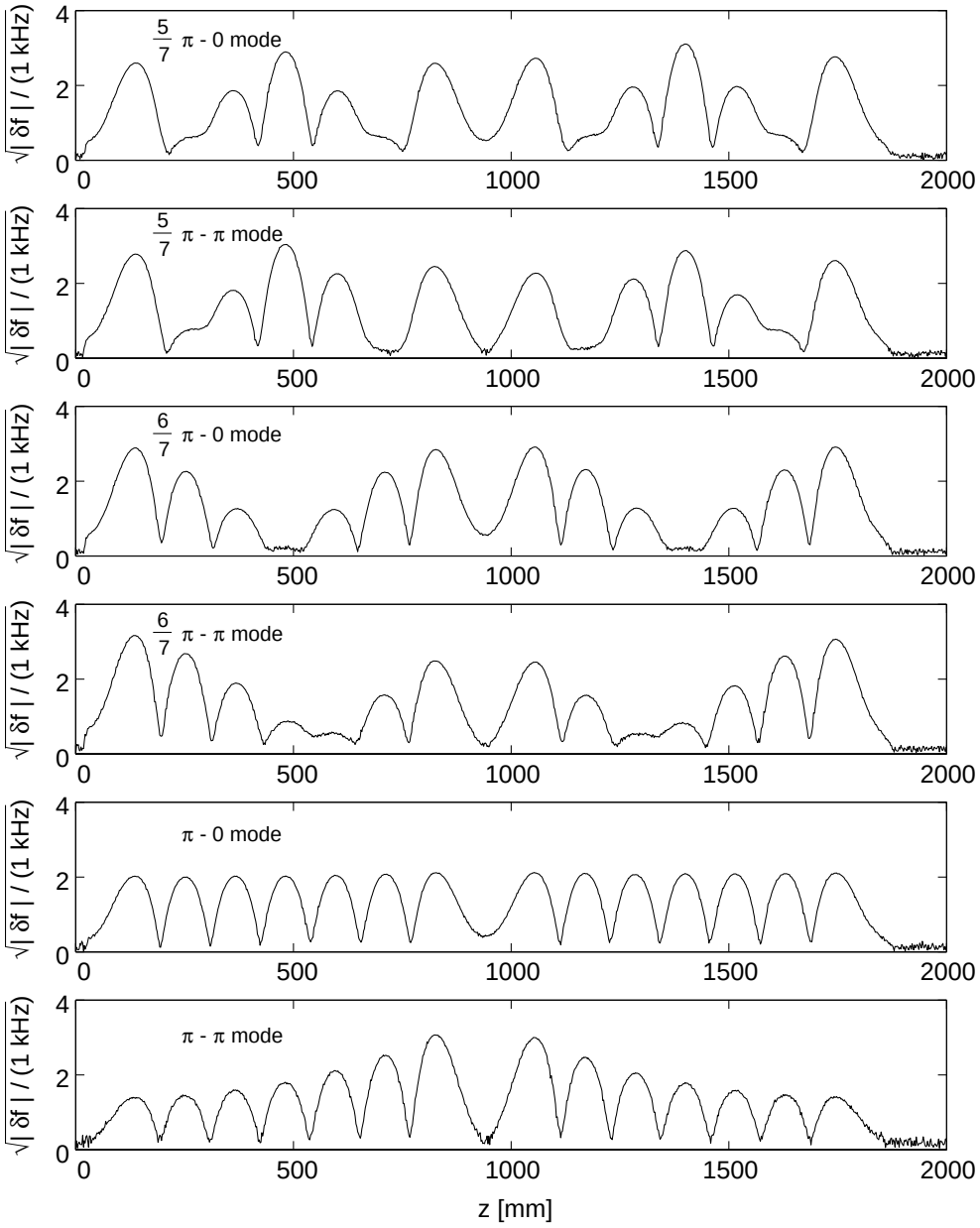

Figure 6.5: Bead-pull measured on-axis profiles $\sqrt{|\delta f_{ph}|/1\text{kHz}}$ for selected TM_{010} resonances of a 2×7-cell prototype superstructure at room temperature.

profiles are labeled according to the eigenmode which is dominating at the selected resonance curve, see also figure 6.4. In the following we have to distinguish carefully between three profiles:

- the amplitude profile of the TM_{010} eigenmode j, which is in good approximation also the profile in the *superconducting state* ($Q_0 \approx 10^{10}$),

- the amplitude profile on the j^{th} resonance maximum at *room temperature*,
- the *result* $\sqrt{|\Delta f_{ph}|/1\text{kHz}}$ *of a bead-pull measurement* at the j^{th} resonance maximum at *room temperature*.

We will find major differences between this profiles in superstructures. The eigenmode profile does not depend on the position of the antennas in the bead-pull measurement (as long as the perturbation of the cell frequencies by the antennas is small, as we consider). We can expect that the amplitude profile at room temperature depends on the position of the input antenna, since the coupling of the overlapping modes to the antennas depends on the amplitude profiles, see (5.149). Moreover the bead-pull measured profile depends also on the position of the output antenna. Note that in the *superconducting state* ($Q_0 \approx 10^{10}$) the amplitude profile on the j^{th} resonance maximum and the amplitude profile of the TM_{010} eigenmode j agree well, since there is almost no overlapping of modes. However, at room temperature the neighboring TM_{010} modes are overlapping and therefore are perturbing the bead-pull measurent. According to equation (5.144) and (5.149) the unperturbated steady-state field envelope amplitude in the end-cell with the output antenna is given by

$$\hat{\mathcal{E}}_{out} = |\hat{\mathcal{E}}_{out}|e^{i\phi_{out}} = \sum_{l=1}^{N} \hat{\mathcal{E}}_{out}^{(l)} = \sum_{l=1}^{N} \frac{K_g^{(1)} v_1^{(l)} \hat{J}_g v_{out}^{(l)}}{2\varepsilon_0 \left(\frac{\omega_0^{(1)}}{2Q_0^{(1)}} - i(\omega^{(l)} - \omega_g) \right)} = \sum_{l=1}^{N} \frac{\hat{\mathcal{E}}_{out,0}^{(l)}}{1 - i\frac{f^{(l)} - f_g}{f_{1/2}}} \quad . \tag{6.13}$$

Here we consider that the input antenna is at the end-tube close to cell #1 and that the external quality factor of the antennas is large as compared to the unloaded quality factor $Q_0^{(1)}$ given by wall losses. The quantity $\hat{\mathcal{E}}_{out,0}^{(l)}$ is the envelope coefficient of mode l on resonance, i.e. for $f_g = f^{(l)}$, where f_g is the generator frequency ($J_g = \hat{J}_g e^{i\omega_g t}$). The bandwidth $f_{1/2}$ of the modes at room temperature is defined as $f_{1/2} = f_0^{(1)}/(2Q_0^{(1)})$. Note that a niobium 1.3 GHz cavity has a bandwidth of $f_{1/2} \approx 65$ kHz at room temperature. Accordingly the the overlapping of neighboring TM_{010} modes is significant in superstructures, see figure 6.4 and equation (6.13). In a bead-pull mesurement the generator frequency f_g is choosen for a maximum amplitude $\hat{\mathcal{E}}_{out}$ on a resonance curve. We denote this frequency by f_{max}. If now a small bead is placed in the center of a cell the perturbated steady-state envelope amplitude in the end-cell with the output antenna is

$$\hat{\mathcal{E}}'_{out} = |\hat{\mathcal{E}}'_{out}|e^{i\phi'_{out}} = \sum_{l=1}^{N} \frac{\left(\hat{\mathcal{E}}_{out,0}^{(l)} \frac{(v_1^{(l)})'}{v_1^{(l)}} \frac{(v_{out}^{(l)})'}{v_{out}^{(l)}} \right)}{\left(1 - i\frac{f^{(l)} + \delta f_{bead}^{(l)} - f_{max} - \delta f_{ph}}{f_{1/2}} \right)} \quad . \tag{6.14}$$

Here $(\vec{v}^{(l)})'$ is the perturbed eigenvector (see (6.10)) and $\delta f_{bead}^{(l)}$ is the shift of the eigenfrequency $f^{(l)}$ due to the bead (see (6.11)). Further δf_{ph} is the measured generator frequency shift for a constant phase, i.e. for $\phi_{out} = \phi'_{out}$, see figure 6.2. We see from (6.14) that the perturbation of the eigenfrequencies as well as the perturbation of the eigenvectors contribute to a changed envelope amplitude $\hat{\mathcal{E}}'_{out}$. Both effects

have to be considered, even for a small bead, since both have a non vanishing first order term in a perturbation calculation, see (6.10) and (6.11).
To illustrate (6.13) and (6.14), consider that the amplitude profile at the j^{th} resonance maximum of $\hat{\mathcal{E}}_{out}$ is measured. According to (6.13) the room temperature amplitude profile differs from the j^{th} eigenmode profile on account of overlapping neighboring eigenmodes $l \neq j$. Further we see from (6.14) that the bead-pull measurement condition $\phi_{out} = \phi'_{out}$ is fulfilled for $\delta f_{ph} \neq \delta f^{(j)}_{bead}$, since $\frac{(v^{(l)}_1)'}{v^{(l)}_1} \neq \frac{(v^{(j)}_1)'}{v^{(j)}_1}$, $\frac{(v^{(l)}_{out})'}{v^{(l)}_{out}} \neq \frac{(v^{(j)}_{out})'}{v^{(j)}_{out}}$ and $\delta f^{(l)}_{bead} \neq \delta f^{(j)}_{bead}$ for $l \neq j$. Accordingly the measured profile differs from the j^{th} eigenmode profile as well as from the room temperature amplitude profile. Obviously the differences in the profiles become more and more significant with increasing overlapping of the modes, i.e. with decreasing mode frequency spacing. We would like to measure the amplitude profile of the TM_{010} eigenmodes by the bead-pull-mesurement at room temperature. To study the error between the measured profiles and the eigenmode profiles, we can use the cavity model developed in the previous chapter to simulate bead-pull measurements by:

1. specifying the cavity matrix **A** (see (5.116)) and finding the unperturbated eigenvalues and the eigenvectors of the TM_{010} modes from (6.5);

2. calculating the unperturbated resonance spectrum at room temperature according to (6.13), selecting a resonance and finding the generator frequency $f_g = f_{max}$ with maximum amplitude $\hat{\mathcal{E}}_{out}$; calculating the phase ϕ_{out} at the maximum;

3. calculating from equation (6.6) the perturbated eigenvectors and eigenfrequencies with a bead (6.4) in one cell;

4. using (6.14) to numerically calculating the shift of the generator frequency δf_{ph} to fulfill the condition $\phi_{out} = \phi'_{out}$; and then

5. repeating the last two steps for all cells of the cavity.

TESLA 9-cell cavity

Figure 6.6 shows a simulated bead-pull measurement for a TESLA 9-cell cavity. The cavity is assumed to be ideally tuned for homogeneous cell amplitudes of the accelerating π-mode in the *superconducting state*. We find that the difference between the π-eigenmode profile and the measured profile is less than 1 %, if a small bead is used and the input and output antennas are mounted at opposite end-cells. This error is acceptable, since we only need to tune the TESLA cavities with an amplitude homogeneity of 95 %. To verify that this accuracy is also valid in a detuned 9-cell cavity, figure 6.7 shows a simulated bead-pull measurement for a detuned cavity. Again the agreement between eigenmode profile and the measured profile is good. As discussed before, this is not the case if the bead used for the profile measurement is too large, see figure 6.8. To stay within 1 % systematic error, a cell frequency perturbation caused by the bead has to be kept below 120 kHz for a 9-cell cavity. Even if a small bead is used, the difference between the measured profile and the

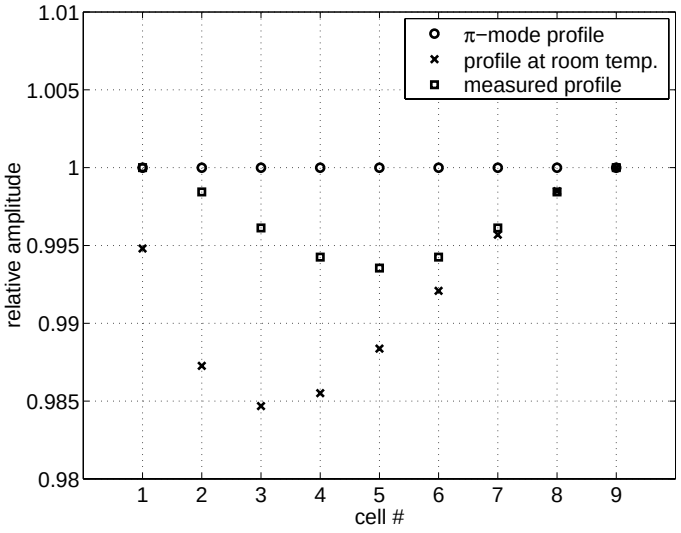

Figure 6.6: Calculated TM_{010} π-mode cell amplitude profile for a tuned TESLA 9-cell cavity ($\mathcal{K}_{cc} = 0.019$, $\omega_0/(2\pi) = 1.275$ GHz, $Q_0 = 10^4$). Shown is the eigenmode profile (i.e. approximately the profile in the *superconducting state*), the amplitude profile at room temperature and the result of a bead-pull measurement simulation ($\delta f_b = -10$ kHz). The input antenna is placed at cell #1 and the output antenna at cell #9.

eigenmode amplitude profile becomes large, if the input and the output antenna are placed at the same end of the 9-cell cavity, see figure 6.8.
Note that a perfectly tuned cavity (uniform field amplitudes in the cells for the accelerating mode) has always a bead-pull profile, which is symmetric with respect to the center cell, if the two antennas are placed symmetrically with respect to the center of the cavity; see figure 6.8. This correspondes to the equations (6.13) and (6.14), where the input and output antennas can be interchanged without changing the cell field amplitude $\hat{\mathcal{E}}_{out}$. In contrast to this the room temperature profile is asymmetric, since it depends only on the position of the input antenna (we consider that the external quality factor of the antennas is large as compared to the unloaded quality factor at room temperature).

TESLA superstructures

The spacing of neighboring TM_{010} modes is smaller in a TESLA superstructure than in a TESLA 9-cell cavity; compare figure 5.9 and 5.18. Accordingly the effect of overlapping modes is stronger. In the following we consider superstructures, which are perfectly tuned for uniform TM_{010} amplitudes of the accelerating $\pi - 0$ mode in the cells. Figure 6.9 shows the result of a bead-pull measurement simulation for a TESLA 2×7-cell superstructure. It can be seen that the room temperature profile, the $\pi - 0$ eigenmode profile and the measured profile are differing significantly, even if a small bead is used. Accordingly a perfectly tuned 2×7-cell superstructure shows a bead-pull measured profile with inhomogeneous cell amplitudes as shown in figure 6.9.

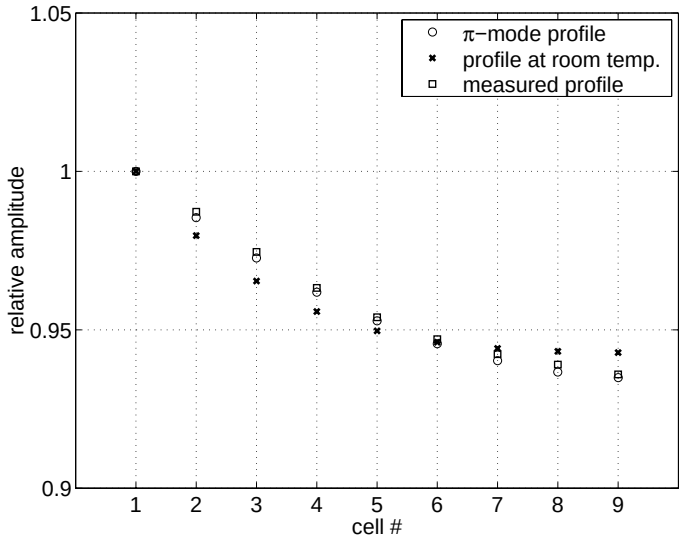

Figure 6.7: Calculated TM_{010} π-mode cell amplitude profile for a detuned TESLA 9-cell cavity ($\mathcal{K}_{cc} = 0.019$, $\omega_0/(2\pi) = 1.275$ GHz, $Q_0 = 10^4$). The first cell of the cavity is detuned by 100 kHz. Shown is the eigenmode profile (i.e. approximately the profile in the *superconducting state*), the amplitude profile at room temperature and the result of a bead-pull measurement simulation ($\delta f_b = -60$ kHz). The input antenna is placed at cell #1 and the output antenna at cell #9.

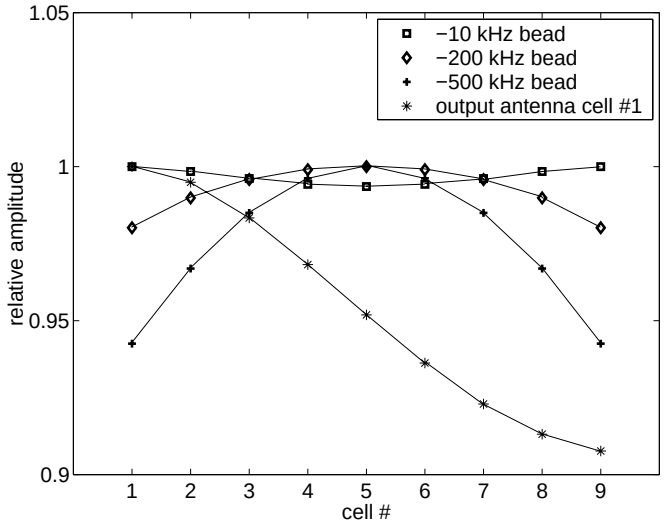

Figure 6.8: Simulated bead-pull measurements for the TM_{010} π-mode of a *tuned* TESLA 9-cell cavity with a *homogeneous* π-mode profile. ($\mathcal{K}_{cc} = 0.019$, $\omega_0/(2\pi) = 1.275$ GHz, $Q_0 = 10^4$, input antenna at cell #1). The first three curves show bead-pull profiles with three different beads and with the output antenna at cell #9. The fourth curve shows the bead-pull profile (-10 kHz bead) if also the output antenna is placed at cell #1. The curves are drawn to guide the eye.

Again the measured bead-pull profile is symmetric, if the two antennas are mounted at oposide ends of the structure, wheras the room temperature profile is asymmetric. To verify this result, figure 6.10 compares the simulation with a

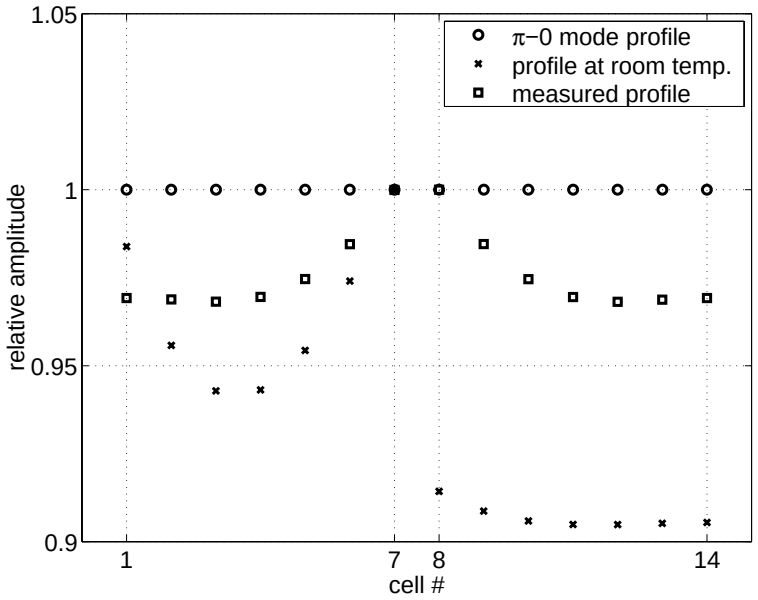

Figure 6.9: Calculated TM_{010} $\pi - 0$ mode amplitude profile for a tuned TESLA 2×7-cell superstructure ($\mathcal{K}_{cc} = 0.019$, $\mathcal{K}_{rr} = 3.6 \cdot 10^{-4}$, $\omega_0/(2\pi) = 1.275$ GHz, $Q_0 = 10^4$). Shown is the eigenmode profile (i.e. approximately the profile in the *superconducting state*), the amplitude profile at room temperature and the result of a bead-pull measurement simulation ($\delta f_b = -30$ kHz). The input antenna is placed at cell #1 and the output antenna at cell #14.

bead-pull measurement on the 2×7-cell prototype superstructure, see also figure 10.2. The cavities of the prototype have been pre-tuned for amplitude homogeneity of their π modes. This tuning procedure is discussed in detail in section 6.3. The measurement and the simulation agree within the 1 % statistical error of the bead-pull measurement (mainly due to phase noise and temperature fluctuations during the bead-pull measurement), thus verifying the result of the cavity model. Moreover this demonstrates that the used pre-tuning procedure allows to achieve sufficient amplitude homogeneity. We can conclude from figure 6.10 that the amplitude homogeneity of the accelerating mode of the 2×7-cell prototype superstructure is 98 % or more; see also section 6.3.
In a 4×7-cell superstructure the spacing of neighboring TM_{010} modes is even smaller. Figure 6.11 and 6.12 show simulated bead-pull results for a niobium 4×7-cell structure and a 4×7-cell copper model, respectively. In the copper model of the superstructure (see also chapter 9) the effect of overlapping modes is smaller because of the higher conductivity of copper at room temperature. Is is found that a well tuned niobium 4×7-cell structure shows a bead-pull result with a 15 % cell amplitude modulation.

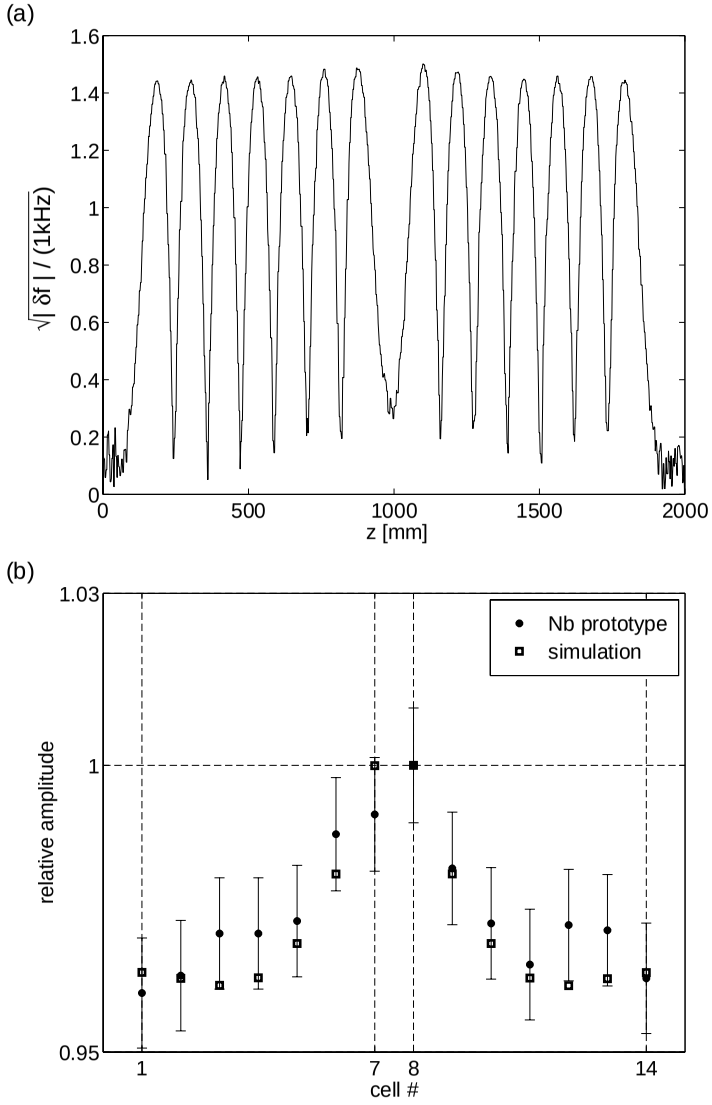

Figure 6.10: Bead-pull result on a 2×7-cell prototype superstructure (input antenna cell #1, output antenna cell #14). (a) Shown is the measured profile of the electric field amplitude at the cavity axis for the TM_{010} $\pi - 0$ resonance. (b) Values at the center of the 14 cells. The statistic measurement error is $\sigma_{rms} = 1\%$. The simulated bead-pull result for a perfecty tuned 2×7-cell superstructure is also shown ($Q_0 = 8900$).

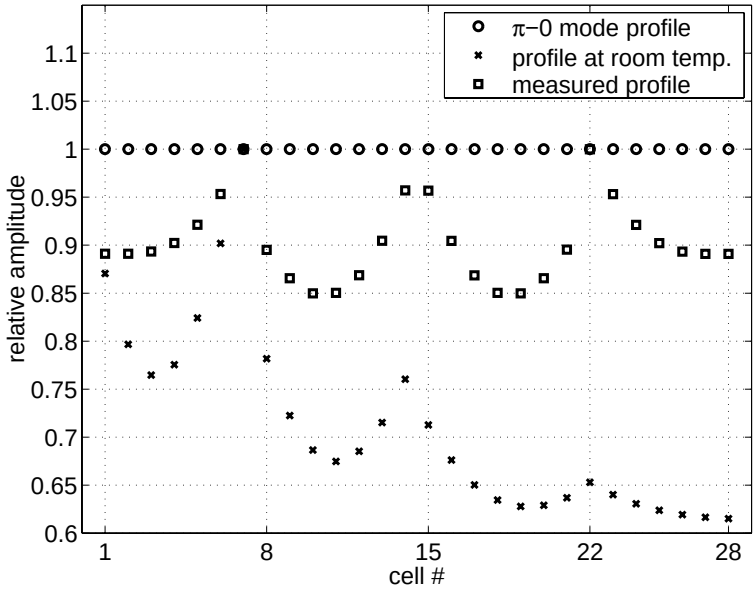

Figure 6.11: Calculated TM_{010} $\pi - 0$ mode amplitude profile for a tuned TESLA 4×7-cell *niobium* superstructure ($\mathcal{K}_{cc} = 0.019$, $\mathcal{K}_{rr} = 2.8 \cdot 10^{-4}$, $\omega_0/(2\pi) = 1.275$ GHz, $Q_0 = 10^4$). Shown is the eigenmode profile (i.e. approximately the profile in the *superconducting state*), the amplitude profile at room temperature and the result of a bead-pull measurement simulation ($\delta f_b = -30$ kHz). The input antenna is placed at cell #1 and the output antenna at cell #28.

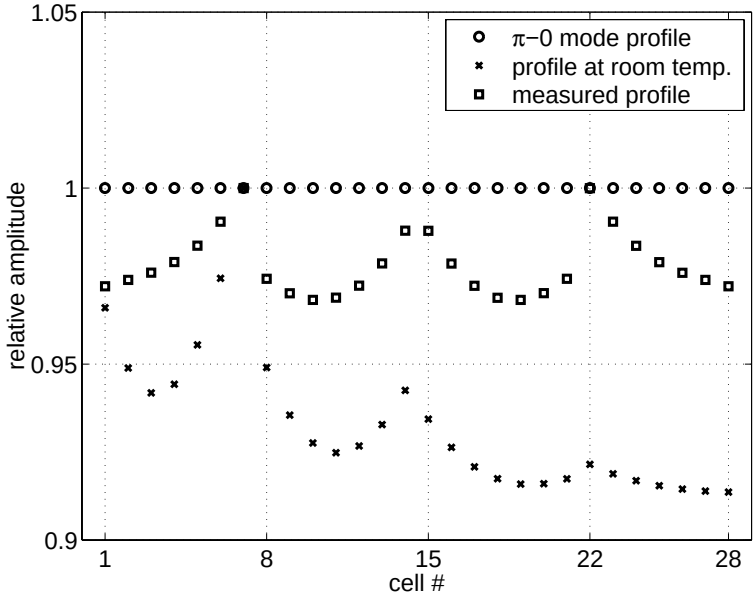

Figure 6.12: Calculated TM_{010} $\pi - 0$ mode amplitude profile of a tuned TESLA 4×7-cell superstructure made from *copper* ($Q_0 = 27000$, other parameters same as in figure 6.11).

Obviously the bead-pull measured profiles of superstructures cannot be used directly for an accurate amplitude profile tuning. To estimate the profile of the accelerating eigenmode one can either compare the bead-pull result with a simulation for a perfectly tuned structure, as shown in figure 6.10, or use a procedure to reconstruct the eigenmode profile from bead-pull measurements $\delta\vec{f}_{ph}^{\,(l)}$ of the accelerating mode and the neighboring modes. The idea of this procedure is, that the distortion of the measurement by mode overlap can be estimated from the bead-pull results of the neighboring modes. One can use the following reconstruction procedure:

- Estimate from a resonance spectrum measurement the eigenfrequencies $f^{(l)}$ and the on-resonance envelope coefficients $\hat{\mathcal{E}}_{out,0}^{(l)}$ of the neighboring modes, see equation (6.13). For the 2×7-cell superstucture it is sufficent to consider the modes $(5/7\pi - 0)$ to $(\pi - \pi)$ for a reconstruction of the accelerating $\pi - 0$ eigenmode profile, see also figure 6.4.

- Use equation (6.13) to calculate the phase ϕ_{out} at the maximum of the accelerating resonance curve.

- Calculate from the first order approximation (6.10) the perturbation of the eigenvectors $(v_n^{(l)})'/v_n^{(l)}$ due to the bead at the center of a cell. Assume for this that the measured bead-pull profiles approximately give the amplitude values of the eigenvectors. Repeat for all cells.

- Use equation (6.14) to numerically compute the frequency shift $\delta f_{bead}^{(acc)}$ of the accelerating mode. For this set $\delta\vec{f}_{ph} = \delta\vec{f}_{ph}^{\,(acc)}$, use the approximation $\delta\vec{f}_{bead}^{\,(l)} \approx \delta\vec{f}_{ph}^{\,(l)}$ for the neighboring modes and find $\delta f_{bead}^{(acc)}$ for the bead-pull condition $\phi'_{out} = \phi_{out}$. The vectors $\delta\vec{f}_{ph}^{\,(acc)}$ and $\delta\vec{f}_{ph}^{\,(l)}$ are the bead-pull measured profiles of the accelerating mode and the neighboring modes, respectively. Repeat for all cells.

- Calculate the eigenmode profile of the accelerating mode from $\delta\vec{f}_{bead}^{\,(acc)}$ by using the first order approximation (6.11).

The systematic error of the bead-pull measurements can be reduced sufficiently by this procedure for the purpose of amplitude profile tuning. Figure 6.15 in section 6.3 shows the reconstructed $\pi - 0$ eigenmode profile for the bead-pull result shown in figure 6.10.

For 9-cell cavities we found that the bead-pull profiles are in good agreement with the eigenmode profiles, provided that a small bead is used and that the antennas are mounted at oposite end-cells. For 2×7-cell superstructures (as well as for 2×9-cell structures) the measured cell amplitude profile differs a few percent form the eigenmode profile. This error can be reduced further as is described above. However, for 4×7-cell superstructures the overlap of modes at room temperature is substantial. Based on the present experience this structure reaches the limit at which the homogeneity of the accelerating mode can still be determined with sufficient accuracy.

6.3 Amplitude Profile Tuning for Multicavity Structures

In the following we will describe the amplitude profile tuning procedure, which has been used for the 2×7-cell prototype superstructures (see also chapter 10) and for a 4×7-cell copper model (see also chapter 9). Based on the experience with the prototypes we shall discuss the tuning of the superstructures for the TESLA collider.

Tuning of the 2×7-cell prototype superstructures

Before joining the two 7-cell cavities to build a superstructure, the separate cavities have been pre-tuned for uniform field amplitudes in the cells for the accelerating TM_{010} π mode. Special end-cups ([Ban 99]) have been used, mounted at the beam tubes of the 7-cell cavities during the profile measurement and tuning, see figure 6.13. These end-cups simulate the TM_{010} $\pi - 0$ mode of a complete superstructure

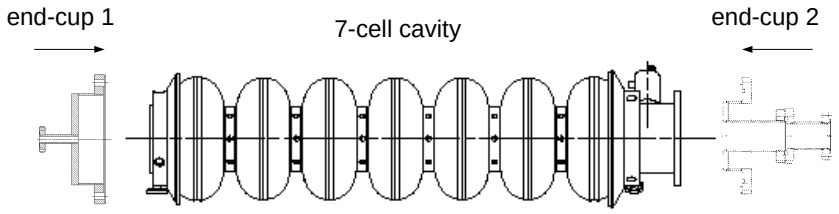

Figure 6.13: End-cups for the tuning of a 7-cell cavity. The end-cups simulate the boundary conditions between the cavities in a superstructure [Ban 99].

by placing an electric boundary at the center plane of the interconnecting tube. Accordingly if two perfectly pre-tuned cavities become joined, the superstructure will have uniform amplitudes in its $\pi - 0$ mode. The π mode tuning of the separate 7-cell cavities has been done analogously to the TESLA 9-cell cavities. In summary, the tuning method used for the multicell cavities consists of the following steps [Sek 90]:

- The amplitude profile of all TM_{010} eigenmodes (N modes in a $N-$cell cavity) and the corresponding eigenfrequencies $f^{(j)}$ are measured. As discussed before, a bead-pull measurement can be used for 7-cell and 9-cell cavities to determine the absolute values $|v_n^{(j)}|$ with sufficient accuracy. The phase relationship of the eigenvector elements is taken from theory by solving of the eigenvalue equation $\mathbf{A}\vec{v}^{(j)} = \Omega^{(j)}\vec{v}^{(j)}$ for a tuned cavity, see (5.115) and (5.131).

- The cavity model matrix $(f_0^{(1)})^2\mathbf{A}$ for the *detuned cavity* is determined by solving the equations

$$\begin{bmatrix} (\vec{v}^{(1)})^T \\ \vdots \\ (\vec{v}^{(N)})^T \end{bmatrix} \cdot \begin{bmatrix} (f_0^{(1)})^2 A_{i1} \\ \vdots \\ (f_0^{(1)})^2 A_{iN} \end{bmatrix} = \begin{bmatrix} (f^{(1)})^2 v_i^{(1)} \\ \vdots \\ (f^{(N)})^2 v_i^{(N)} \end{bmatrix}, \quad i = 1, ..., N \quad . \tag{6.15}$$

  These equations follow from the eigenvalue equation $(f_0^{(1)})^2\mathbf{A}\vec{v}^{(j)} = (f^{(j)})^2\vec{v}^{(j)}$ (see (5.115) and (5.117)), as one can easily find. It is convenient to multiply

(5.115) by $(f_0^{(1)})^2$, since eigenfrequencies are measured and not eigenvalues $\Omega^{(j)} = (f^{(j)})^2/(f_0^{(1)})^2$. The matix element A_{ik} is the i^{th} row k^{th} column element of the matrix $\mathbf{A}$ and T denotes transposed vectors.

- The tuning aim is to get amplitude homogeneity for the π mode

$$\vec{v}^{(tun)} = \left[\ 1, -1, 1, -1, ...\ \right] \tag{6.16}$$

at a required eigenfrequency $f^{(tun)}$. From the obtained system model $(f_0^{(1)})^2\mathbf{A}$ the required TM_{010} frequency adjustments $\Delta f_n^{(1)}$ for the cells of the cavity can be calculated by solving

$$(f_0^{(1)})^2(\mathbf{A} + \mathbf{P})\vec{v}^{(tun)} = (f^{(tun)})^2\vec{v}^{(tun)} \tag{6.17}$$

for the diagonal matrix elements $(f_0^{(1)})^2 P_{nn} = (f_0^{(1)})^2\delta_n \approx 2f_0^{(1)}\Delta f_n^{(1)}$, see (5.90) and (5.119).

- The cells are tuned successively in the model as well as in the real cavity: in the model the first cell is assumed to be tuned and the frequency shift of the π eigenmode due to this tuning is calculated. Then the frequency of the first real cavity cell is tuned until the π mode frequency is shifted by the calculated value. Subsequently the second cell of the model is tuned, the π eigenmode shift is calculated and the second cell of the real cavity is tuned for the calculated π mode frequency shifty, and so on.

Refer to [Sek 90] for a detailed discussion. However, this tuning procedure cannot be used for a complete TESLA superstructure, since the lower frequency modes cannot be separated at room temperature, see figure 5.18. Accordingly even a reconstruction of the higher frequency eigenvectors is not sufficient, because all eigenvectors are needed to determine the cavity model matrix $(f_0^{(1)})^2\mathbf{A}$ according to (6.15). For the 7-cell cavities all eigenvectors can be found with sufficient accuracy by bead-pull measurements. Figure 6.14 shows the field amplitude profile of the TM_{010} π mode in one of the 7-cell cavities before and after tuning. The 7-cell cavities of the two prototype superstructures have been tuned after the major preparation steps. These preparation steps include cavity welding, strong surface chemistry and heat treatments, and may perturbe the cell geometry. Accordingly tuning the cell frequencies is required afterwards. The subsequent preparation steps influence the cell geometry only slightly, and therefore preserve the amplitude homogeneity. After the pre-tuning of the separate cavities, two 2×7-cell prototype superstructures have been built by joining two cavities each via a flange connection, see also chapter 10. The stored energy in the cavities has been balanced by proper tuning the cavity frequencies. Note that each cavity has its own frequency tuning system. Accordingly the stored energy can be balanced, even during operation of a superstructure in a linac, see next section. To verify the pre-tuning procedure, the amplitude profile of the accelerating $\pi - 0$ mode has been measured by a bead-pull measurement on the 2×7-cell prototypes. The result on one of the strutures is shown in figure 6.10. By comparing the measured profile with the simulated profile of a well tuned

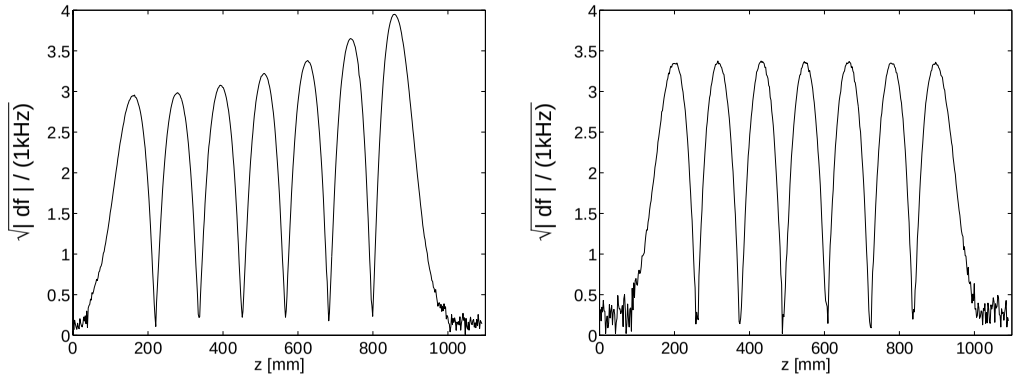

Figure 6.14: On-axis field amplitude profile of the TM_{010} π mode in a 7-cell cavity (bead-pull measurement). Left: *before tuning* the cell frequencies for uniform field amplitudes in the cells. Right: *after tuning*.

2×7-cell superstructure it is found, that the achieved amplitude homogeneity is better than 98 %, thus exceeding the requirements for TESLA. This is confirmed by a reconstruction of the $\pi - 0$ eigenmode amplitude profile, as is discussed in section 6.2. The obtained $\pi - 0$ eigenmode profile is shown in figure 6.15. Also the second

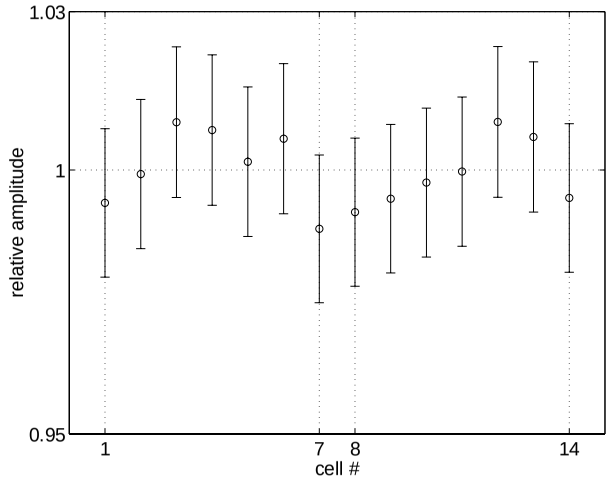

Figure 6.15: Reconstructed amplitude profile of the accelerating $\pi - 0$ mode in a 2×7-cell prototype superstructure. The original bead-pull measured profile of the $\pi - 0$ resonance is shown in figure 6.10.

2×7-cell prototype has exceeded the requirements with an amplitude homogeneity of 97 %.

Tuning of the 4×7-cell copper model superstructure

For the 4×7-cell copper model (see figure 9.2) the same pre-tuning procedure has been used to achieve amplitude homogeneity for the accelerating mode in the structure. After pre-tuning the four 7-cell cavites, the cavity chain of the superstructure

has been assembled. Figure 6.16 (a) shows the bead-pull amplitude profile of the accelerating $\pi-0$ mode, measured after small frequency corrections of the individual cavities (each cavity in a superstructure is equipped with its own frequency tuning system). By comparing the measured cell amplitude profile with a simulation for a

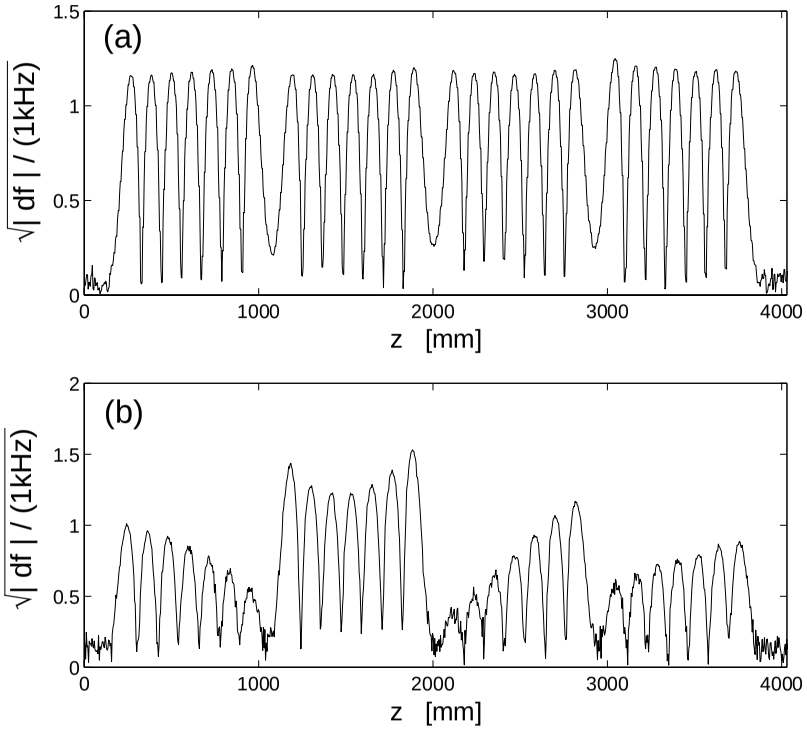

Figure 6.16: Bead-pull results $\sqrt{|\delta f_{ph}|/1\text{kHz}}$ on the 4×7-cell copper model superstructure, see also figure 9.2. (a) Accelerating $\pi-0$ mode after small frequency corrections of the individual cavities. The input antenna is placed at cell #1 and the output antenna at cell #28. Compare to figure 6.12. (b) Same as before, but with cavities detuned to permit high-power-processing of the second cavity. The first cavity is detuned by +25 kHz and the second cavity by -200 kHz.

perfectly tuned superstructure (see figure 6.12) it is found that the achieved amplitude homogeneity of the accelerating $\pi-0$ eigenmode is better than 95 %.
High-power-processing is often used to improve the field performance of superconducting cavities while there are installed in an accelerator [Pad 98]. For the high-power-processing of a superstructure it is desirable to process the cavities of the structure successively, to reduce the maximum power transferred by the input coupler. By proper detuning of the superstructure cavities the dominating part of the input power can be transferred to one of the cavities. As example, the figure 6.16 (b) shows a bead-pull profile on the 4×7-cell copper superstructure with cavities detuned to permit processing of the second cavity.

Tuning of the superstructures for the TESLA collider

Based on the promising experience with the 2×7-cell prototypes and the 4×7-cell copper model, it is proposed to use the pre-tuning procedure also for the TESLA

superstructures. If needed, an additional final tuning can be done on the complete superstructure. For this fine-tuning it is sufficient to measure the amplitude profile of the accelerating eigenmode. As discussed before, the accelerating eigenmode profile $\vec{v}^{(acc)}$ can be reconstructed from bead-pull measurements. To calculate the detuning of the cell frequencies from the measured eigenvector $\vec{v}^{(acc)}$, a *simplified cavity model* can be used, in which uniform cell-to-cell coupling within the cavities and uniform cavity-to-cavity coupling is assumed. In this approximation, the cavity model matrix $\mathbf{A}$ of a well tuned structure is given by (5.131). The uniform cell-to-cell coupling factor and the uniform cavity-to-cavity coupling factor can be easily estimated from the measured TM_{010} resonance spectrum (see (5.133)), to determine $\mathbf{A}$. The detuning of the cell freuqency $\Delta f_n^{(1)}$ is then found by solving (see (5.90), (5.115) and (5.119))

$$(\mathbf{A} + \mathbf{P})\vec{v}^{(acc)} = \left(\frac{f^{(acc)}}{f_0^{(1)}}\right)^2 \vec{v}^{(acc)} \tag{6.18}$$

for the elements $P_{nn} = \delta_n \approx 2\Delta f_n^{(1)}/f_0^{(1)}$ of the diagonal matrix $\mathbf{P}$. Subsequently the superstructure is tuned cell by cell, by analogy with standard multicell cavities, as is described above. This fine-tuning procedure still needs to be tested on a superstucture.

6.4 Amplitude Profile Adjustment at Cryogenic Temperatures

After the installation in the linac, the cavities are evacuated and cooled down to cryogenic temperatures (2 K at the TTF-linac), to achieve superconductivity. Because of the thermal shrinkage of about 0.1 % and the evacuation, the frequencies of the TM_{010} eigenmodes are shifted by more than 2 MHz. For the cavities of a superstructure it cannot be taken for granted, that all cavites are shifted by the same amount within a few kHz. Therefore the electromagnetic field energy of the accelerating mode will be unbalanced in the cavities after cool down, even if the cavites had been well tuned at room temperature for amplitude homogeneity of the accelerating mode. Figure 6.17 (a) shows an example with unbalanced stored energies in the cavities of the 4×7-cell cooper model. To balance the stored energy in the cavities, the frequencies of the coupled cavities have to be adjusted individually. This can be done, even during linac operation at 2 K, since each cavity in a superstructure is equipped with its own frequency tuning system (see also chapter 10). Recall that this is one of the essential differences between a $M \times N_c$-cell superstructure and a $(M \cdot N_c)$-cell cavity, see chapter 4. Obviously, a bead-pull measurement cannot be done on a superstructure installed in a linac. In the following a method will be described, which allows to measure the relative stored energies in the cavities of a superstructure and to adjust the cavity frequencies for a balanced energy in the cavities.

Let us consider a superstructure with M coupled cavities. Each cavity $m = 1, ..., M$ is composed of N_c cells, which are well tuned for amplitude homogeneity at room

temperature. After cool down the cells of each cavity have still uniform TM_{010} frequencies[1], but from cavity to cavity the cell TM_{010} frequencies are different. If we denote the uniform detuning of the cells $n = mN_c - N_c + 1, ..., mN_c$ of the cavity m by $\Delta_m = 2\Delta f_n^{(1)}/f_0^{(1)}$ (see (5.90)), we can use the first order perturbation approach (6.7) to find the perturbation $\delta\vec{v}^{(acc)}$ of the accelerating mode eigenvector $\vec{v}^{(acc)}$ in the superstructure after cool down

$$\delta v_k^{(acc)} = \sum_{r\neq(acc)} \frac{v_k^{(r)}}{\Omega^{(acc)} - \Omega^{(r)}} \sum_{m=1}^{M} \left\{ \sum_{n=mN_c-N_c+1}^{mN_c} v_n^{(acc)} \Delta_m v_n^{(r)} \right\}, \qquad k = 1, ..., MN_c. \tag{6.19}$$

Here $\vec{v}^{(r)}$ are the unperturbated eigenvectors in a perfectly tuned superstructure and $\Omega^{(r)}$ the corresponding unperturbated eigenvalues, see also (5.115) and (5.131). The accelerating mode eigenvector after cool down is then given by $\vec{v}_{cold}^{(acc)} = \vec{v}^{(acc)} + \delta\vec{v}^{(acc)}$. The method proposed to determine the stored energy in the individual cavities uses a perturbation approach, similar to a bead-pull measurement. Instead of a metal bead, the frequency tuner of a cavity is used to perturb the TM_{010} cell frequencies of a *selected cavity* p uniformly by $\Delta_t = 2\Delta f_t^{(1)}/f_0^{(1)}$. According to equation (6.9) in a first order approximation the resulting change $\delta f_{t,p}^{(acc)}$ of the accelerating mode frequency in the superstructure is given by

$$2\Omega_{cold}^{(acc)} \frac{\delta f_{t,p}^{(acc)}}{f_{cold}^{(acc)}} \approx \delta\Omega_{t,p}^{(acc)} = \Delta_t \sum_{k=pN_c-N_c+1}^{pN_c} \left(v_k^{(acc)} + \delta v_k^{(acc)} \right)^2 \qquad , \tag{6.20}$$

where the subscript p denotes that the frequency tuner of cavity p is perturbing cavity p. The accelerating mode eigenvector $\vec{v}_{cold}^{(acc)} = \vec{v}^{(acc)} + \delta\vec{v}^{(acc)}$ and the eigenfrequency $f_{cold}^{(acc)}$ after cool down have to be used in (6.20), since we consider that the eigenmode frequency is perturbed by the tuner after cool down. We find that the relative stored energy $\sum_{k=pN_c-N_c+1}^{pN_c} \left(v_k^{(acc)} + \delta v_k^{(acc)} \right)^2$ in the cavities can be determined by perturbing the cavity frequencies in succession (see also equation (5.30) and (5.144) and consider that only the accelerating mode is excited). Similar to a bead-pull measurement, where the *relative energy of a cell* is found from the measured frequency shift due to the bead in the cell, see (6.11), here the *relative stored energy of a cavity* is measured. Fortunately, the tuner-perturbation measurement is not affected by overlapping modes, because it is done on a superconducting structure, see also figure 5.18. The frequency tuners are driven by stepping motors, with a resolution of better than 1 Hz per step. Accordingly each cavity can be perturbed precisely by the same amount. In the linac the TESLA cavities are operated in pulsed mode, see chapter 2. After the RF input power is turned off at the end of a pulse the accelerating field in a cavity immediately oscillates at the eigenfrequency $f_{cold}^{(acc)}$ of the accelerating mode. The phase $\phi^{(acc)}$ of the accelerating field is

[1] The experience with the TTF 9-cell cavities has shown, that the nine TM_{010} mode eigenfrequencies are changed during cool down by almost the same factor, as one would expect for a uniform shrinkage of the cavity. The maximum relative frequency deviation from the expected values is usually well below 10 kHz [Kre 01]. One can conclude from this, that the relative cell frequencies are only minor changed during cool down.

measured with respect to a 1.3 GHz reference generator. Accordingly the eigenfrequency $f_{cold}^{(acc)}$ can be determined by measuring $d\phi^{(acc)}/dt = 2\pi(f_{cold}^{(acc)} - 1.3\text{GHz})$ after turning of the input power. By averaging over several measurements the influence of microphonics (see chapter 2) cancels out and the average eigenfrequency $f_{cold}^{(acc)}$ is found. The accuracy is approximately 1 Hz. Accordingly a small perturbation $\Delta f_t^{(1)} \approx 100$ Hz by the frequency tuner is sufficient to determine the relative field energies of the cavities. Note that this tuner-perturbation method requires only one pick-up antenna per superstructure. Moreover the pick-up signal needs not to be calibrated. We shall now derive a equation, which allows to calculate the detuning of the cavities after the cool down from the measured frequency shifts $\delta f_{t,p}^{(acc)}$ of a tuner-perturbation measurement ($p = 1, ..., M$).
Successively the cavity frequencies are perturbed by the frequency tuners. The average shift of the accelerating mode frequency is given by

$$< \delta f_{t,p}^{(acc)} >= \frac{1}{M}\sum_{p=1}^{M} \delta f_{t,p}^{(acc)} = \frac{1}{M}\frac{f_{cold}^{(acc)}}{2\Omega_{cold}^{(acc)}}\Delta_t \sum_{k=1}^{MN_c}\left(v_k^{(acc)} + \delta v_k^{(acc)}\right)^2 = \frac{1}{M}\frac{f_{cold}^{(acc)}}{2\Omega_{cold}^{(acc)}}\Delta_t \quad . \tag{6.21}$$

Accordingly (6.20) can be written as

$$\frac{\delta f_{t,p}^{(acc)}}{< \delta f_{t,p}^{(acc)} >} = M \sum_{k=pN_c-N_c+1}^{pN_c}\left(v_k^{(acc)} + \delta v_k^{(acc)}\right)^2 \quad . \tag{6.22}$$

We consider that the inhomogeneity $\delta v_k^{(acc)}$ of the accelerating mode after cool down is small. Thus we can use the approximation

$$\left(v_k^{(acc)} + \delta v_k^{(acc)}\right)^2 \approx \left(v_k^{(acc)}\right)^2 + 2v_k^{(acc)}\delta v_k^{(acc)} = \frac{1}{MN_c} + 2v_k^{(acc)}\delta v_k^{(acc)} \quad , \tag{6.23}$$

where $(v_k^{(acc)})^2 = 1/(MN_c)$ follows from (5.121) for a accelerating eigenvector $\vec{v}^{(acc)}$ with homogeneous amplitudes. Inserting (6.23) into (6.22) yields

$$\frac{\delta f_{t,p}^{(acc)}}{< \delta f_{t,p}^{(acc)} >} = 1 + 2M \sum_{k=(pN_c-N_c+1}^{pN_c} v_k^{(acc)}\delta v_k^{(acc)} \quad . \tag{6.24}$$

On the other hand we find from equation (6.19) the following relation by multiplying with $v_k^{(acc)}$ and a summing over all cells of cavity p

$$\begin{aligned}\sum_{k=pN_c-N_c+1}^{pN_c} v_k^{(acc)}\delta v_k^{(acc)} &= \sum_{m=1}^{M}\left\{\sum_{r\neq(acc)}\left(\sum_{k=pN_c-N_c+1}^{pN_c}\frac{v_k^{(acc)}v_k^{(r)}}{\Omega^{(acc)}-\Omega^{(r)}}\sum_{n=mN_c-N_c+1}^{mN_c} v_n^{(acc)}v_n^{(r)}\right)\right\}\Delta_m \\ &= \sum_{m=1}^{M} H_{pm}\Delta_m \quad . \end{aligned} \tag{6.25}$$

Here we introduced the matrix elements H_{pm} of a square matrix $\mathbf{H}$. Accordingly we can write in matrix notation

$$\begin{bmatrix} \sum_{k=1}^{N_c} v_k^{(acc)}\delta v_k^{(acc)} \\ \vdots \\ \sum_{k=(M-1)N_c+1}^{MN_c} v_k^{(acc)}\delta v_k^{(acc)} \end{bmatrix} = \mathbf{H}\cdot\begin{bmatrix} \Delta_1 \\ \vdots \\ \Delta_M \end{bmatrix} \quad . \tag{6.26}$$

Finally we combine (6.24) and (6.26) and obtain

$$\begin{bmatrix} \frac{1}{2M}\left\{\frac{\delta f_{t,1}^{(acc)}}{<\delta f_{t,p}^{(acc)}>}-1\right\} \\ \vdots \\ \frac{1}{2M}\left\{\frac{\delta f_{t,M}^{(acc)}}{<\delta f_{t,p}^{(acc)}>}-1\right\} \end{bmatrix} = \mathbf{H}\cdot\begin{bmatrix} \Delta_1 \\ \vdots \\ \Delta_M \end{bmatrix} \quad . \tag{6.27}$$

We find, that the matrix $\mathbf{H}$ relates the frequency detunings $\Delta_m = 2\Delta f_n^{(1)}/f_0^{(1)}$ of the superstructure cavities after cool down with a vector containing the frequency shifts $\delta f_{t,p}^{(acc)}$, which are caused by detuning one cavity after the other. According to (6.25), the matix $\mathbf{H}$ can be calculated from the eigenvectors and eigenvalues of a perfectly tuned superstructure with uniform cell-to-cell coupling and uniform cavity-to-cavity coupling. Since the cell-to-cell coupling factor and the cavity-to-cavity coupling factor of a superstructure are known, these eigenvectors and eigenvalues can be calculated from equation (5.115), using the cavity matrix given by (5.131).
Since $\mathbf{H}$ is known from theory and the frequency shifts $\delta f_{t,p}^{(acc)}$ are measured, the cavity detunings $\Delta f_{cavity\ m} = \Delta_m f_0^{(1)}/2$ of the superstructure cavities can be found by solving (6.27). The nominal frequency $f_0^{(1)}$ of the cells can easily be estimated from $f_0^{(1)} = f_{cold}^{(acc)}/\sqrt{\Omega^{(acc)}}$, where $\Omega^{(acc)}$ is the calculated eigenvalue of the accelerating mode for the ideal superstructure and $f_{cold}^{(acc)}$ is the measured frequency of the accelerating mode. It is important to note, that the detuning vector on the right hand side of (6.27) is not unique, since uniformly tuning all cavities will not change the amplitude profile and the relative energies stored in the cavities. Accordingly the matrix $\mathbf{H}$ cannot be inverted. This difficulty can be removed by using the last cavity as a reference and setting $\Delta_M = 0$. Accordingly we strip off the last column and row of $\mathbf{H}$ to get a reduced matrix $\tilde{\mathbf{H}}$, which is invertible. Then the detuning of the the cavities is found from

$$\begin{bmatrix} \Delta f_{cavity\ 1} \\ \vdots \\ \Delta f_{cavity\ M-1} \end{bmatrix} = \frac{f_0^{(1)}}{2}\left(\tilde{\mathbf{H}}\right)^{-1}\cdot\begin{bmatrix} \frac{1}{2M}\left\{\frac{\delta f_{t,1}^{(acc)}}{<\delta f_{t,p}^{(acc)}>}-1\right\} \\ \vdots \\ \frac{1}{2M}\left\{\frac{\delta f_{t,M-1}^{(acc)}}{<\delta f_{t,p}^{(acc)}>}-1\right\} \end{bmatrix} \quad . \tag{6.28}$$

Correspondingly the cavities have to be tuned to balance the energy stored in the cavities. This can easily be done, since the frequency tuners are driven by stepping motors with well known resolution xHz/step. Subsequently all cavities have to be tuned uniformly to restore the frequency of the accelerating mode at its specified value (1.3 GHz for the TESLA linac). The required uniform tuning can be measured after balancing the stored energy, or can be calculated from the cavity model. For this the accelerating mode frequency has to be calculated before and after tuning the cavities of the model. The calculated frequency shift has to be compensated by tuning all cavities uniformly.
If the stored energy in the cavities is strongly unbalanced, the tuning procedure has to be applied iteratively to balance the field energy sufficently. The reason for this

is given by the approximation (6.23), which we have used in deriving (6.28).
The proposed method of balancing the stored energy in the cavities of a superstructure has been tested by computer simulations (see next section) as well as on the copper 4×7-cell superstructure at room temperature. In figure 6.17 one example on the copper superstructure is given. Figure 6.17 (a) shows the initial bead-pull measured field profile of the accelerating $\pi - 0$ mode. The stored energy in the cavities is strongly unbalanced. Successively the relative stored energy in the cavities has been measured by the tuner-perturbation method, see (6.22). From this values the frequency corrections have been calculated, which are needed to balance the stored energies. After tuning the cavities according to the calculated frequency corrections, the field profile of the accelerating $\pi - 0$ mode has been re-measured, see figure 6.17 (b). It can be seen, that the amplitude homogeneity is almost sufficient

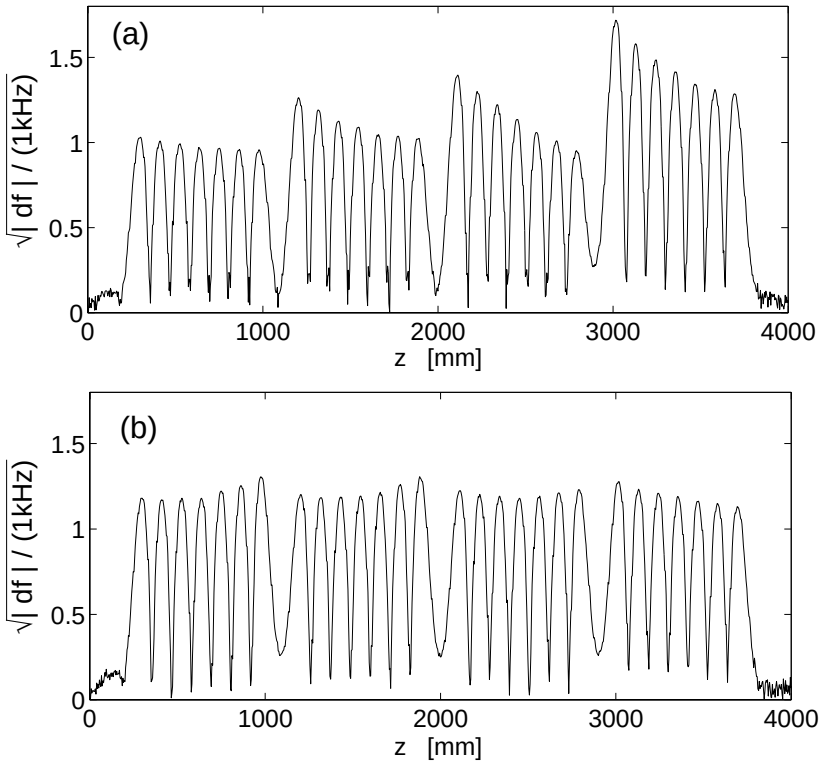

Figure 6.17: Test of the energy balancing method on the 4×7-cell copper supersturcture, see also figure 9.2. (a) On-axis profile of the accelerating $\pi - 0$ mode *before balancing* the stored energies of the cavites (bead-pull result $\sqrt{|\delta f_{ph}|/1\text{kHz}}$). (b) On-axis profile of the $\pi - 0$ mode *after* the frequencies of the cavities have been adjusted by using the method described in this section.

already after the first iteration of the energy balance procedure (compare to figure 6.12 and figure 6.16). Further iterations impove the stored energy distrubution, until the stored energy in the cavities is balanced. Note that the entire cavities are tuned, but not the cells within a cavity. Accordingly only the stored energy in the cavities can be balanced, and not the energy stored in the individual cells. Therefore

the achievable amplitude homogeneity by adjusting the cavity frequencies is finally limited by detuned cells.

6.5 Distribution of Amplitude Homogeneity

In order to verify the benefit from the energy-balancing method the amplitude homogeneity in 4×7-cell superstructures has been studied by computer simulations. Based on the experience with the TESLA 9-cell cavities, a frequency variation of $\sigma_f^{(1)} = 20$ kHz is considered for the individual cells. The amplitude homogeneity of the accelerating mode is calculated before and after balancing the stored energy in the cavities, according to the method described in the preceding section. The resulting homogeneity statistics of 3500 4×7-cell superstructures (as one TESLA linac would have) is shown in figure 6.18 (b) and (c), before and after adjusting the cavity frequencies, respectively. The benefit from balancing the stored energy is obvious. The mean inhomogeneity is 1.8 times smaller after cavity tuning. Recall that the energy balancing in a superstructure is possible, since each cavity is equipped with its own frequency tuner. However, 28-cell cavities would have a homogeneity distribution as shown in figure 6.18 (a). The average inhomogeneity is 2.5 times larger than in the superstructure. This demonstrates that the sensitivity of a 4×7-cell superstructures to field inhomogeneities is essentially lower than the sensitivity of a 28-cell cavity. There are two reasons for this: the $\pi - 0$ mode of the superstructure itself is less sensitive than the π mode of the 28-cell cavity (see figure 6.19) and the cavities in the superstructure can be tuned individually.
Figure 6.20 summarizes the distribution of amplitude homogeneity for the three different structures under discussion for the TESLA collider. Again a frequency variation of $\sigma_f^{(1)} = 20$ kHz is considered for the individual cells. In all three cases the average homogeneity exceeds the lower limit set for the TESLA collider.

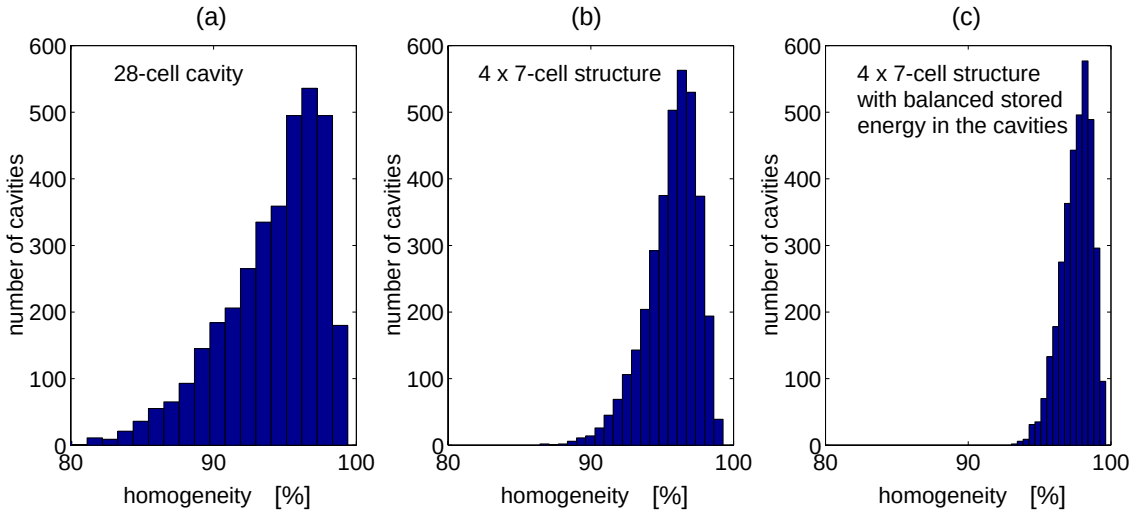

Figure 6.18: Computed distribution of amplitude homogeneity $(|v_n^{acc}|)_{mean}/(|v_n^{acc}|)_{max}$ of the accelerating mode for different structures. The cells of the cavities are assumed to be randomly detuned with $\sigma_f^{(1)} = 20$ kHz. (a) 3500 28-cell cavities with TESLA shaped cells. Average homogeneity: 94.0 %. (b) 3500 TESLA 4×7-cell superstructures before balancing the stored energy in the cavities. Average homogeneity: 95.7 %. (c) 3500 TESLA 4×7-cell superstructures after balancing the stored energy in the cavities by the method described in section 6.4. Average homogeneity: 97.6 %.

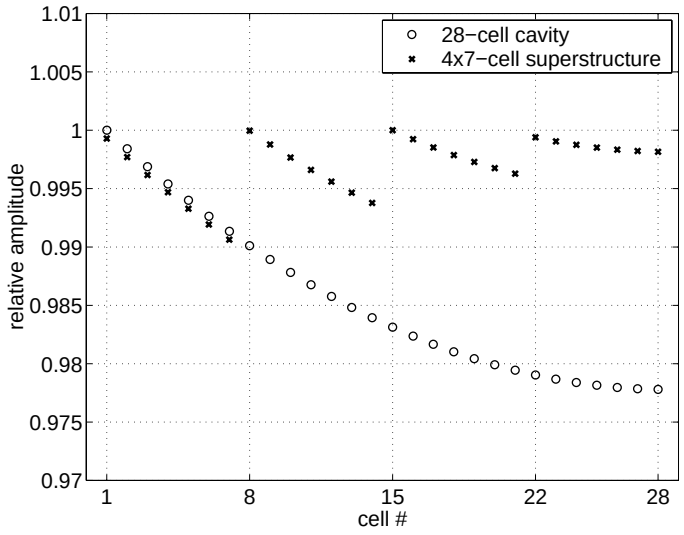

Figure 6.19: Computed cell amplitude profile of the accelerating eigenmode in a TESLA 4×7-cell superstructure and in a 28-cell cavity with TESLA shaped cells. For both structures, the first cell is assumed to be detuned by 10 kHz.

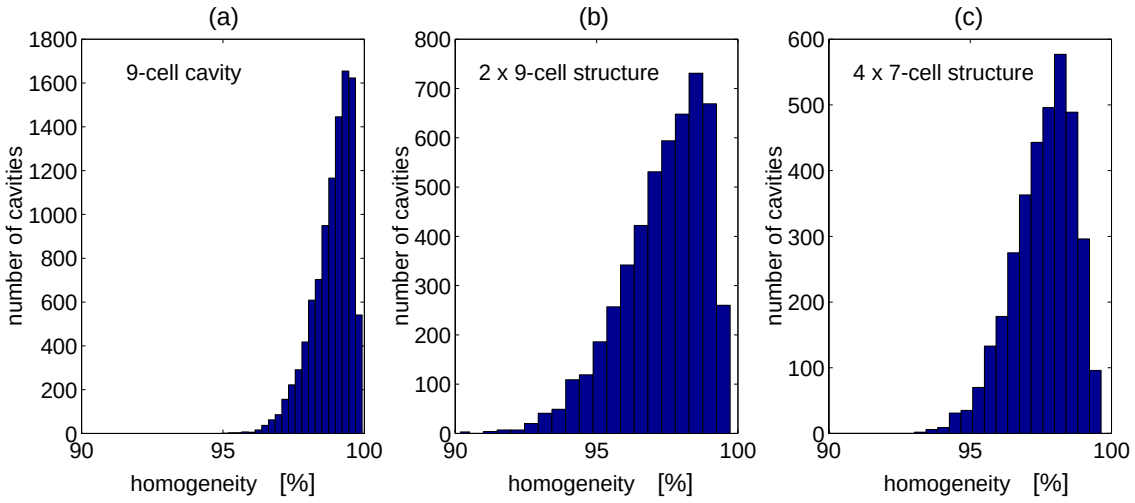

Figure 6.20: Computed distribution of the accelerating mode amplitude homogeneity $(|v_n^{acc}|)_{mean}/(|v_n^{acc}|)_{max}$ for the structures proposed for TESLA. The cells of the cavities are assumed to be randomly detuned with $\sigma_f^{(1)} = 20$ kHz. (a) 10000 TESLA 9-cell cavities. Average homogeneity: 98.8 %. (b) 5000 TESLA 2×9-cell superstructures after balancing the stored energy in the cavities by the method described in section 6.4. Average homogeneity: 97.3 %. (c) 3500 TESLA 4×7-cell superstructures after balancing the stored energy in the cavities by the method described in section 6.4. Average homogeneity: 97.6 %.

7 Transient Behaviour and Bunch-to-Bunch Energy Variation

The filling of a superstructure at the beginning of an RF pulse and the refilling of the stored energy between sequential bunches is discussed in this chapter. We will find, that not only the accelerating mode (also called fundamental mode) is involved, but all TM_{010} eigenmodes of a multicell structure. This causes a bunch-to-bunch fluctuation of the beam energy, since some of the non-fundamental modes have (R/Q)-values of a few 10^{-3} of the fundamental mode (R/Q). The coupling of the cavities in a superstructure is small. Therefore the energy flow through a superstructure has been studied to ensure, that *all* cells of the structure can be refilled between two sequential bunches without causing unacceptable energy spread. For the TESLA-collider it is desirable to keep the bunch-to-bunch energy variation below the intra-bunch energy spread of $5 \cdot 10^{-4}$ [TDR 01]. By numerical codes the bunch-to-bunch energy variation in superstructures has been computed for the TESLA bunch-train of 2820 bunches [TDR 01]. Although the results appear satisfactory, it is important to note, that they have to be confirmed by beam measurements, see chapter 10.

7.1 Transient State of the Accelerating Mode

The superconducting standing-wave cavities in the TESLA collider will be operated in pulsed mode, see chapter 2. At the beginning of each RF pulse the cavites are filled with RF energy until the nominal accelerating voltage is reached. Subsequently the beam is injected. The input coupler is close to an end-cell, thus the field energy has to propagate from this cell through the entire structure to fill each cell. Accordingly for $t \approx 0$ the field energy is concentrated in the first cell. Therefore the accelerating eigenmode cannot be excited individually during cavity filling, since the eigenmode has uniform field in all cells. The propagation of field energy and the filling of the cells in a multicell cavity can be described by a time-dependent superposition of all TM_{010} eigenmodes, see also [Doh 98]. To study this for the superstructures, the transient state has been computed for the normal state at room temperature as well as for the superconducting state. At room temperature the excitation of the TM_{010}

eigenmode l by a generator current $J_g = \hat{J}_g e^{i\omega_g t}$ for $t > 0$ is given by

$$a^{(l)}(t) = \frac{K_g^{(1)} v_1^{(l)} \hat{J}_g}{2\varepsilon_0 \left(\frac{\omega_0^{(1)}}{2Q_0^{(1)}} - i(\omega^{(l)} - \omega_g) \right)} \left\{ e^{-\left(\frac{\omega_0^{(1)}}{2Q_0^{(1)}} - i(\omega^{(l)} - \omega_g) \right) t} - 1 \right\} \quad , l = 1, ..., \tag{7.1}$$

where $a^{(l)}$ is the envelope expansion coefficent of mode l; see (5.148) and (5.149) in section 5.10. The quantity $\omega^{(l)}$ is the eigenfrequency of mode l and $\omega_0^{(1)}/(2Q_0^{(1)})$ is the bandwidth of the modes at room temperature. The field envelope coefficient of cell n is obtained from a summation over all eigenmodes

$$\hat{\mathcal{E}}_n(t) = \sum_{l=1}^{N} a^{(l)}(t) v_n^{(l)} \quad . \tag{7.2}$$

For the superconducting state the coupling of modes via the external losses has to be included in the calculation. For this the first order differential equation (5.143) has to be solved numerically. The eigenvectors $\vec{v}^{(l)}$ and eigenfrequencies $\omega^{(l)}$ are computed by solving the matrix equation (5.115) for the matrix $\mathbf{A}$ of a well tuned structure, see (5.131).

Figure 7.1 compares computed field amplitudes during the filling with measurements on the 4×7-cell copper superstructure. The structure is exited by an RF wave, which is switched on at t=0. The frequency of the RF wave equals the accelerating mode frequency. It is found, that the measured and calculated tran-

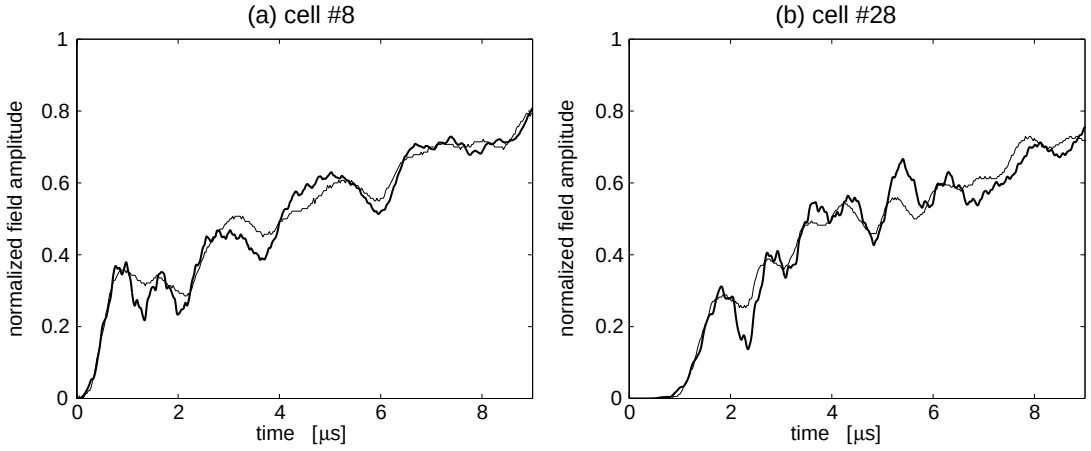

Figure 7.1: Transient state measured on the 4×7-cell copper superstructure (standard lines) and computed (bold lines) for an ideal superstructure ($\mathcal{K}_{cc} = 0.019$, $\mathcal{K}_{rr} = 3.6 \cdot 10^4$, $f_0^{(1)} = 1.275$ GHz, $Q_0^{(1)} = 27000$). The RF input power is switched on at $t = 0$ μs. The frequency of the input wave equals the accelerating mode frequency. The structure is driven via an input antenna close to cell # 1. (a) Transient in cell #8. (b) Transient in cell #28.

sient states are in good agreement. The small differences in the substructure of the transients can be attributed to imperfections of the copper model. The cell-to-cell

coupling and the cell frequencies are slightly varying, whereas the calculation is done for an ideal 4×7-cell superstructure. The propagation time of the RF pulse through the structure of about 1 μs can be inferred from the time offset in filling cell #8 and #28. Figure 7.2 (a) shows the contributions of several coupled TM_{010} eigenmodes to the field amplitude in the last cell. The accelerating $\pi - 0$ mode increases with $1 - e^{-\omega t/(2Q)}$ as in a single-cell cavity, but also the neighboring modes have significant amplitudes. After 50 μs steady-state is almost reached. Note that the non-fundamental modes have small, but non-vanishing steady-state amplitudes. Figure 7.2 (b) shows the transient behaviour for the last cell of a 2×7-cell niobium superstructure at room temperature. Again the field is modulated by the neighboring eigenmodes. For a superconducting 2×7-cell superstructure the field amplitude of the first and the last cell are shown in figure 7.3 for the first microsecond of filling. Note that the time constant $2Q_e^{(13,13)}/\omega^{(13)}$ of the accelerating mode is 667 μs for the selected parameters. Accordingly the steady-state is approximated after several milliseconds.

Figure 7.4 shows the stored field energy $U^{(l)} = \frac{1}{2}\varepsilon_0 a^{(l)}(a^{(l)})^*$ for selected eigenmodes during cavity filling. After the filling time $t_f = 2Q_e^{(13,13)}/\omega^{(13)} ln(2) = 462$ μs the first bunch of a TESLA bunch-train would be injected into the superstructure. At this time the field of the non-fundamental TM_{010} eigenmodes is still fluctuating with decreasing amplitude. Accordingly also the accelerating voltage has a small fluctuation on account of the small, but non-vanishing (R_{sh}/Q_0) values of the non-fundamental eigenmodes. In the following section the resulting energy gain variation will be studied. The fluctuation amplitude of the interfering TM_{010} eigenmode fields is decaying on account of the external losses and the coupling of modes via the losses. Note that the excitation of the neighboring TM_{010} eigenmodes during filling is not a special property of superstructures, but happens in all multicell cavities, see for example [Fer 96]. However, the amplitude of excitation depends on the distance of a mode to the generator frequency, see (7.1).

7.2 Bunch-to-Bunch Energy Variation

To compute the bunch-to-bunch energy variation, we have to add the pulsed beam current in the simulation. This is done by superposing the RF field, which is excited by the generator current with the beam induced field. Let us consider a relativistic point charge q passing the a cavity on the axis. The transit time of the relativistic charge is much shorter than the decay time of the field in the cavity. Therefore wall losses and losses due to the external load can be neglected for the calculation of the mode coefficient $\Delta\mathcal{E}_q^{(l)}(t)$ induced by the charge in mode l.

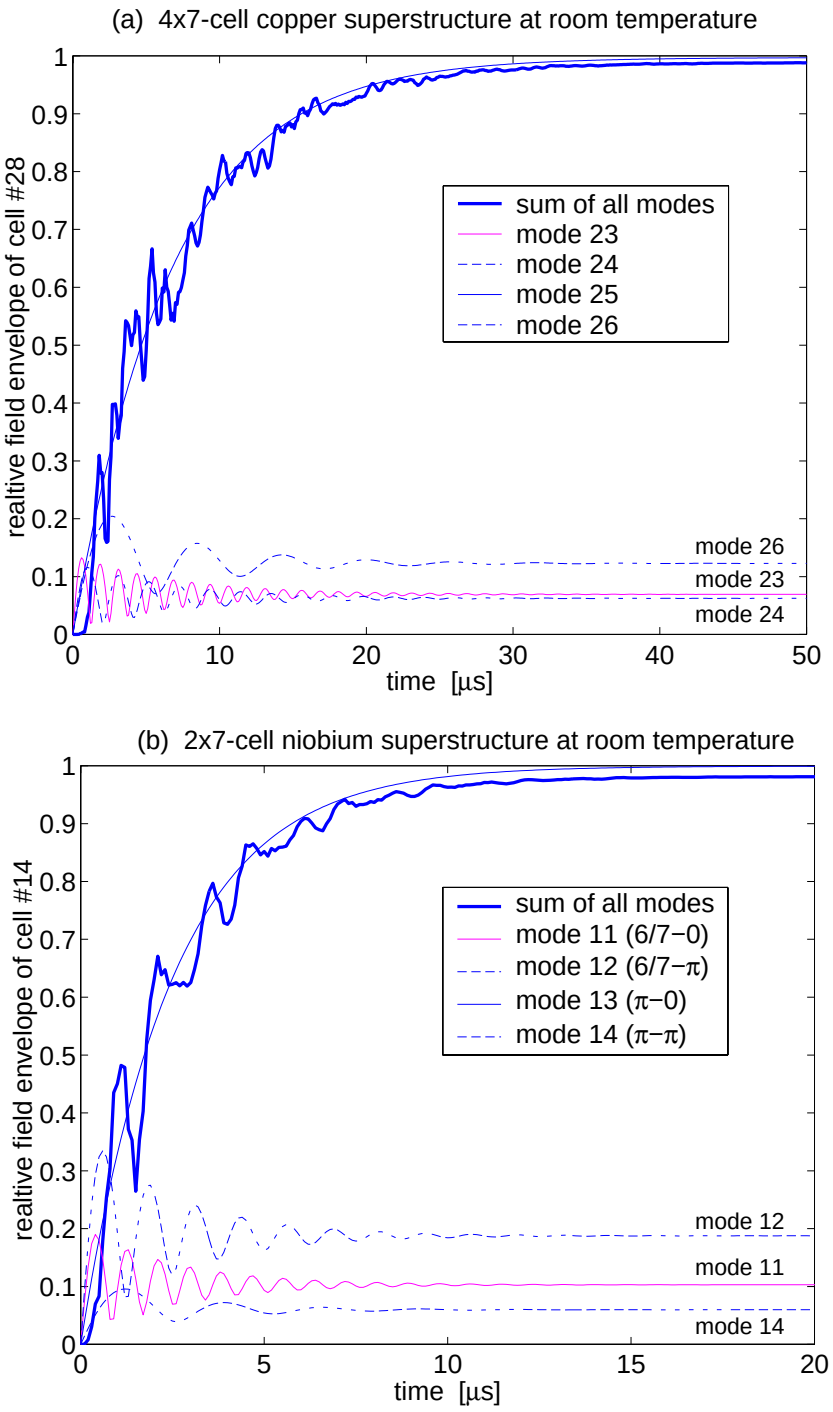

Figure 7.2: Computed transient state in the last cell of a superstructure at room temperature. Shown is the absolute value of the field envelope of the last cell and the contributions of different TM_{010} eigenmodes. (a) 4×7-cell copper superstructure. (b) 2×7-cell niobium superstructure at room temperatue. The RF input power is switched on at $t = 0$ μs. The frequency of the input wave equals the accelerating mode frequency. The structures are driven via an input antenna close to cell # 1.

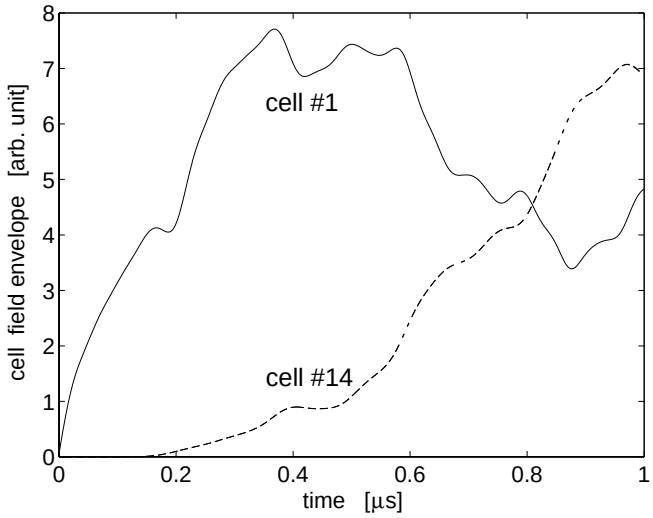

Figure 7.3: Computed absolute values of the field envelope coefficient for the first and the last cell of a superconducting 2×7-cell superstructure during filling ($Q_e^{(13,13)} = 2.733 \cdot 10^6$).

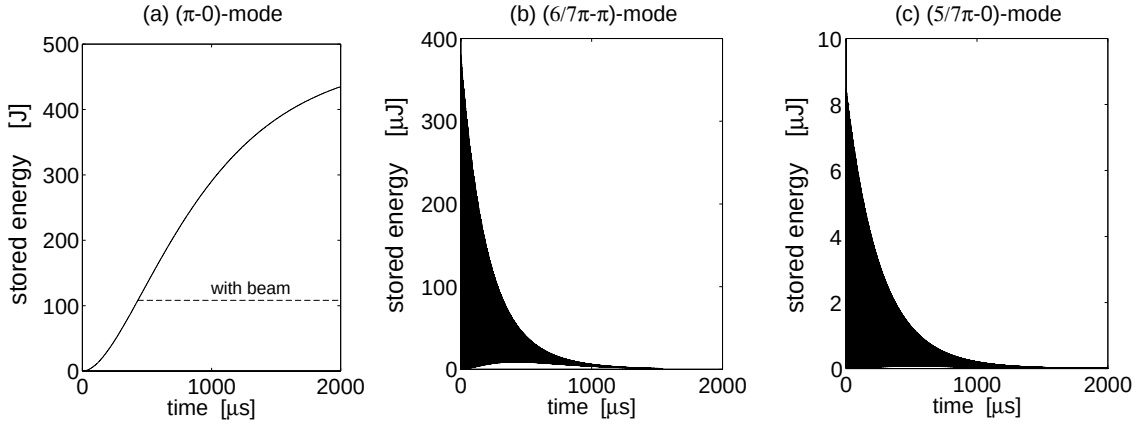

Figure 7.4: Computed field energy $U^{(l)} = \frac{1}{2}\varepsilon_0 a^{(l)}(a^{(l)})^*$ of selected TM_{010} eigenmodes during filling of a superconducting 2×7-cell superstructure without beam ($Q_e^{(13,13)} = 2.733 \cdot 10^6$). The steady state accelerating voltage of the $\pi - 0$ mode is 75.80 MV. The first bunch would be injected after 462 μs at a accelerating voltage of 37.9 MV. (a) $\pi - 0$ mode. (b) $6/7\pi - \pi$ mode. (c) $5/7\pi - 0$ mode. The stored energy oscillates rapidly, as indicated by the black color. The dashed line indicates the stored energy with a bunch-train injected after 462 μs filling, see also figure 7.7

Solving the differential equation (5.40) for the coefficients of the electric fields of the TM_{010} eigenmodes

$$\frac{d^2}{dt^2}\mathcal{E}^{(l)}(t)+\left(\omega^{(l)}\right)^2\frac{d}{dt}\mathcal{E}^{(l)}(t) = -\frac{1}{\varepsilon_0}\frac{d}{dt}\int_V \vec{j}_b\cdot\vec{e}^{(l)}(\vec{r})dv \tag{7.3}$$

for the current density $\vec{j}_q(t) = qc\delta(z-z_b(t))\vec{u}_z$ yields

$$\Delta\mathcal{E}_q^{(l)}(t) = \Delta a_q^{(l)}(t)e^{i\omega^{(l)}(t-t_0)} = \left\{\frac{-q}{\varepsilon_0}\int_{-L_{cav}/2}^{L_{cav}/2}\vec{u}_z\cdot\vec{e}^{(l)}(z)e^{-i\omega^{(l)}z/c}dz\right\}e^{i\omega^{(l)}(t-t_0)} \quad . \tag{7.4}$$

Here L_{cav} is the length of the cavity and $\vec{e}^{(l)}$ is the orthonormal eigenfunction of the TM_{010} mode l. At $t=t_0$ the charge passes the center of the cavity. Note that (7.4) is valid immediately after the charge has passed the cavity but not for later times, since we have neglected losses. The integral in (7.4) can by computed numerically from the eigenfunctions of the TM_{010} modes. Comparing (7.4) with the equation (5.58), defining the $(R_{sh}/Q_0)^{(l)}$ value of a mode,

$$\left(\frac{R_{sh}}{Q_0}\right)^{(l)} = \frac{(V_{acc}^{(l)})^2}{2\omega^{(l)}U^{(l)}} = \frac{1}{\varepsilon_0\omega^{(l)}}\left|\int_{-L_{cav}/2}^{L_{cav}/2}\vec{u}_z\cdot\vec{e}^{(l)}(z)e^{-i\omega^{(l)}z/c}dz\right|^2 \quad , \tag{7.5}$$

we find for the change $\Delta V_{acc,q}^{(l)}$ in the accelerating voltage of a mode induced by the relativistic charge

$$|\Delta V_{acc,q}^{(l)}| = \omega^{(l)}\left(\frac{R_{sh}}{Q_0}\right)^{(l)}|q| \quad . \tag{7.6}$$

In the next step we consider a relativistic bunch with a gaussian charge distribution

$$q(z-z_0(t)) = \frac{Q_b}{\sqrt{2\pi}\sigma_b}\exp\left(-\frac{(z-z_0(t))^2}{2\sigma_b^2c^2}\right) \quad , \tag{7.7}$$

where Q_b is the bunch charge and σ_b is the bunch length in time (standard deviation). Integrating (7.4) for the charge distribution (7.7) yields for the bunch induced mode coefficient

$$\Delta\mathcal{E}_b^{(l)}(t) = \left\{\frac{-q}{\varepsilon_0}\int_{-L_{cav}/2}^{L_{cav}/2}\vec{u}_z\cdot\vec{e}^{(l)}(z)\exp(-i\omega^{(l)}z/c)dz\right\}\exp(i\omega^{(l)}(t-t_0))\exp\left(-\frac{(\omega^{(l)})^2\sigma_b^2}{2}\right). \tag{7.8}$$

Here the center z_0 of the bunch passes the center of the cavity for $t=t_0$. Accordingly the bunch induced change in the accelerating voltage is given by

$$|\Delta V_{acc,b}^{(l)}| = \omega^{(l)}\left(\frac{R_{sh}}{Q_0}\right)^{(l)}|Q_b|\exp\left(-\frac{(\omega^{(l)})^2\sigma_b^2}{2}\right) \quad . \tag{7.9}$$

The length σ_b of the electron bunches at the TESLA-Test-Facility and at the TESLA collider is below 1 mm. We see from (7.9) that these bunches can be treated as point-like charges Q_b for the TM_{010} modes ($f^{(l)} \approx 1.3$ GHz), since $\omega^{(l)}\sigma_b/c \ll 1$. In the following this case will be considered.
The integral in (7.8) has to be evaluated from the TM_{010} eigenfunctions $\vec{e}^{(l)}$ of the

cavity, which are calculated by numerical field codes. Alternatively we can approximately describe the TM_{010} cavity eigenfunctions in terms of the TM_{010} eigenfunctions $\vec{e}_n^{(1)}$ of the cells

$$\vec{e}^{(l)} = \sum_{n=1}^{N} v_n^{(l)} \vec{e}_n^{(1)}(\vec{r}) \qquad , \tag{7.10}$$

see (5.149) in chapter 5. Recall that $\vec{v}^{(l)}$ are the TM_{010} cell amplitude eigenvectors of the cavity, as found from the lumped element model of a cavity. Inserting (7.10) into (7.8) gives

$$\Delta a_b^{(l)} = \frac{-Q_b}{\varepsilon_0} \sum_{n=1}^{N} v_n^{(l)} e^{-i\omega^{(l)} d_{n,c}/c} \int_{-L_{cell,n}/2}^{L_{cell,n}/2} \vec{u}_z \cdot \vec{e}_n^{(1)}(z) e^{-i\omega^{(l)} z/c} dz \qquad , \tag{7.11}$$

where $d_{n,c}$ is the distance between the center of cell n and the center of the entire multicell structure. Accordingly the $(R_{sh}/Q_0)^{(l)}$ values of the TM_{010} cavity modes are approximately

$$\begin{aligned} \left(\frac{R_{sh}}{Q_0}\right)^{(l)} &= \frac{1}{\varepsilon_0 \omega^{(l)}} \left| \sum_{n=1}^{N} v_n^{(l)} e^{-i\omega^{(l)} d_{n,c}/c} \int_{-L_{cell,n}/2}^{L_{cell,n}/2} \vec{u}_z \cdot \vec{e}_n^{(1)}(z) e^{-i\omega^{(l)} z/c} dz \right|^2 \\ &\approx \left| \sum_{n=1}^{N} v_n^{(l)} e^{-i\omega^{(l)} d_{n,c}/c} \sqrt{\left(\frac{R_{sh}}{Q_0}\right)_n^{(1)}} \right|^2 \qquad . \end{aligned} \tag{7.12}$$

Here the small differences between the eigenfrequencies $\omega^{(l)}$ have been neglected in evaluating the integral. The quantity $(R_{sh}/Q_0)_n$ is the corresponding ratio of shunt impedance and unloaded quality factor for a single cell n. Further in (7.12) we make use of the fact, that the TM_{010} cell eigenfunctions $\vec{e}_n^{(1)}$ are of even symmetry with repect to the middle plane of the cell, i.e. that the integral yields a positive real number. A similar treatment gives for the amplitude coefficient induced by a short bunch

$$\Delta a_b^{(l)} = \frac{-Q_b}{\sqrt{\varepsilon_0}} \sum_{n=1}^{N} v_n^{(l)} e^{-i\omega^{(l)} d_{n,c}/c} \sqrt{\left(\frac{R_{sh}}{Q_0}\right)_n^{(1)} \omega^{(l)}} \qquad . \tag{7.13}$$

A cavity with beam loading can be simulated by superposing the bunch induced fields calculated from this equation to the fields computed for the excitation by a generator current. Conservation of energy requires that the energy gain ΔE_{bunch} of a bunch is opposite to the change ΔU_b of the total field energy by the bunch-induced fields

$$\Delta E_{bunch} = Q_b V_{acc} = -\Delta U_b \qquad . \tag{7.14}$$

Accordingly the energy gain of the beam can directly be calculated from the change of the total field energy of all TM_{010} eigenmodes. The $(R_{sh}/Q_0)_n$ values of the cells have to be calculated with numerical eigenmode codes. For the cells of the 2×7-cell prototype superstructure one finds, that the $(R_{sh}/Q_0)_n$ values of the four end-cells are lowered by about 30 % in comparison with the center cells [Sek 00]. The reason for this is the leakage of the fields into the beam tubes (114 mm diameter) at the end-cells. Figure 7.5 shows the $(R_{sh}/Q_0)^{(l)}$ values of the TM_{010} eigenmodes for the

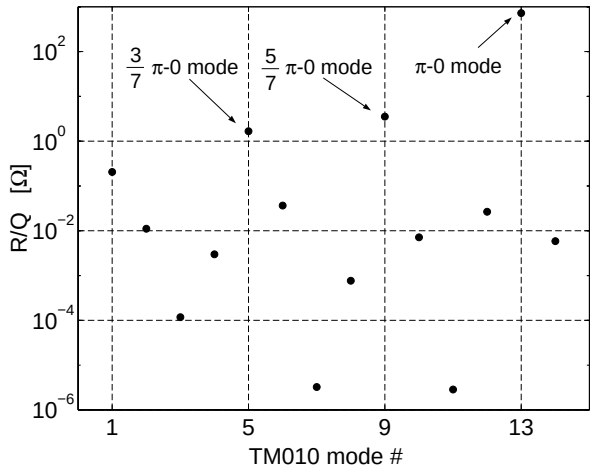

Figure 7.5: $(R_{sh}/Q_0)^{(l)}$ values of the TM_{010} modes of a 2×7-cell superstructure, as calculated from equation (7.12). It is considered that $(R_{sh}/Q_0)_n$ values of the four end-cells are 2/3 of the value for a center cell [Sek 00]. The $\pi - 0$ mode is the accelerating eigenmode.

2×7-cell structure, as calculated from equation (7.12). The accelerating $(\pi - 0)$ mode ($l = 13$) has the largest $(R_{sh}/Q_0)^{(13)} = 729\ \Omega$. The $(\frac{3}{7}\pi - 0)$ mode and the $(\frac{5}{7}\pi - 0)$ mode will also interact with the beam, but their $(R_{sh}/Q_0)^{(l)}$ is a few 10^{-3} of the fundamental mode $(R_{sh}/Q_0)^{(13)}$.
The resulting energy variation of the bunches has been calculated by computer simulations. For this purpose a TESLA-type bunch train of 2820 bunches is considered. The first bunch of the train is injected at $t_f = 2Q_e^{(13,13)}/\omega^{(13)} ln(2) = 462\ \mu$s. The bunches are 337 ns spaced [TDR 01]. Each bunch is composed of $2 \cdot 10^{10}$ relativistic electrons. Figure 7.6 shows the computed bunch-to-bunch energy variation as well as the fluctuation of the field envelope in cell #1. The field is sampled immediately before a bunch is injected into the superstructure, thus showing the modulation of the accelerating voltage in this cell as "seen" by the beam. It is found, that the bunch-to-bunch energy gain variation is more than one order of magnitude smaller than the fluctuation of the individual fields in the cells. The modulation of the field amplitude in the cell is caused by the non-fundamental modes, which are excited by the generator and the beam. The amplitude of excitation depends on the frequency of the modes, their time constant and the generator and beam coupling to the modes, see (5.143) and (7.13). Figure 7.7 shows the field energy $U^{(l)} = \frac{1}{2}\varepsilon_0 a^{(l)}(a^{(l)})^*$ of selected modes as a function of time. With increasing frequency separation to the generator frequency $f_g = 1.3$ GHz, the mode excitation by the generator current is getting smaller. For a single bunch the amplitude coefficient $\Delta a_b^{(l)}$ induced by the bunch is proportional to the square root of the $(R_{sh}/Q_0)^{(l)}$ of mode l, see equation (7.12) and (7.13). The excitation by a bunch train depends also on the distance between the eigenfrequencies and the Fourier components of the bunched beam, since this determines how the bunch-induced transients add up. For the parameters of the computation discussed here it is found, that beside the fundamental mode mainly the $(\frac{3}{7}\pi - 0)$ mode of the 2×7-cell superstructure is excited by the beam. This is

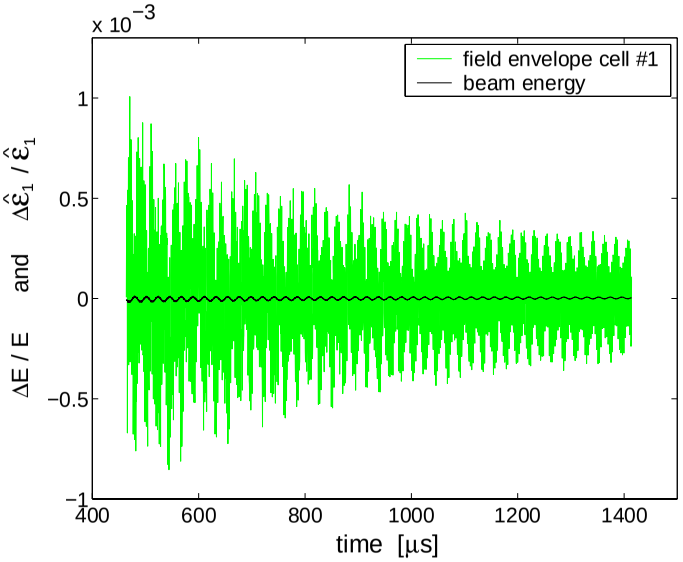

Figure 7.6: Computed energy gain variation and modulation of the field envelope in the first cell for a 2×7-cell superstructure ($\mathcal{K}_{cc} = 0.01934$, $\mathcal{K}_{rr} = 3.6{\cdot}10^{-4}$, $Q_e^{(13,13)} = 2.733{\cdot}10^6$, $f^{(13)} = 1.3$ GHz). The nominal energy gain is 37.9 MeV. The envelope field is sampled immediately before the injection of the bunches. The used $(R_{sh}/Q_0)^{(l)}$ values of the TM_{010} modes are shown in figure 7.5.

due to the small, but non-vanishing $(R_{sh}/Q_0)^{(5)}$ value of the $(\frac{3}{7}\pi - 0)$ mode and its spacing of only 46 kHz to the nearest beam harmonics.
Figure 7.6 shows that the bunch-to-bunch energy gain variation is more than an order of magnitude smaller than the fluctuation of the accelerating fields of the individual cells. The reason for this is that the bunches are accelerated by the *sum of the accelerating fields* of all cells. This sum nearly vanishes for all eigenmodes except for the fundamental $(\pi - 0)$ mode. This cancellation is the physical origin of the small $(R_{sh}/Q_0)^{(l)}$ values of the non-fundamental modes shown in figure 7.5. Figure 7.8 compares the individual cell field fluctuation with the fluctuation of the total accelerating voltage in the 2×7-cell superstructure. The total accelerating voltage is mainly modulated by the bunch-induced transients of the accelerating mode and the refilling between the bunches. The computed energy gain variation for the 2×7-cell superstructure is shown in figure 7.9. The nominal energy gain is 37.9 MeV. It is found, that the bunch-to-bunch energy variation for the whole TESLA bunch-train in this structure is predicted to be smaller than $5 \cdot 10^{-5}$, thus well below the intra-bunch energy spread. This demonstrates, that the energy flow from the input coupler through the whole 2×7-cell superstructure is sufficient to replenish the stored energy in all cells without causing unacceptable energy spread. The variation in energy becomes smaller at the end of the bunch-train due to the decay of the interfering modes. As discussed above, the fluctuation is dominated by the $(\frac{3}{7}\pi - 0)$ mode for the parameters used in this simulation; see also figure 7.7. Accordingly by shifting the eigenfrequency of this mode such, that the distance to

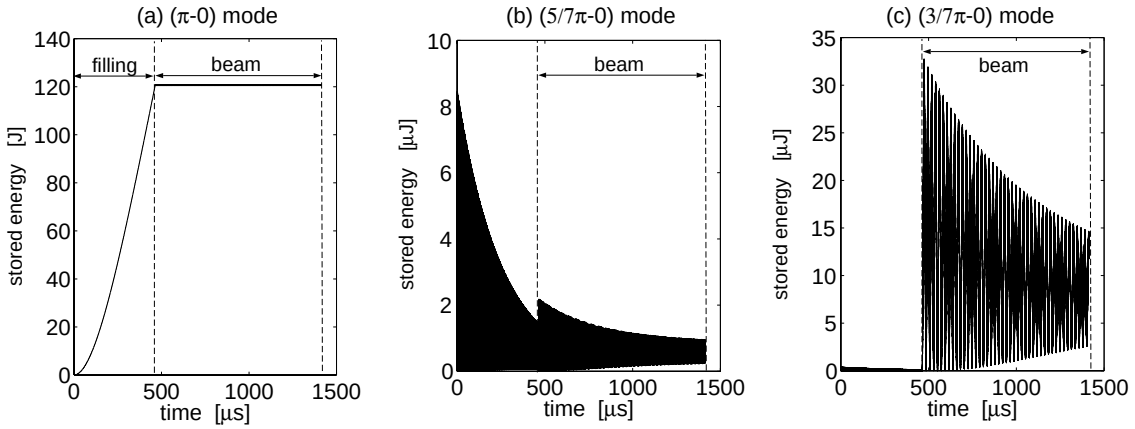

Figure 7.7: Computed field energy in a 2×7-cell superstructure as function of time during cavity filling and beam acceleration ($\mathcal{K}_{cc} = 0.01934$, $\mathcal{K}_{rr} = 3.6 \cdot 10^{-4}$, $Q_e^{(13,13)} = 2.733 \cdot 10^6$, $f^{(13)} = 1.3$ GHz). (a) Fundamental $\pi - 0$ mode. (b) $\frac{5}{7}\pi - 0$ mode. (c) $\frac{3}{7}\pi - 0$ mode.

the nearest beam harmonics is increased, the fluctuation of the cell fields and the energy gain variation becomes even smaller, see figure 7.10.

The expected small bunch-to-bunch energy variation for the 2×7-cell superstructure of less than $5 \cdot 10^{-5}$ has been confirmed by other independend codes: HOMDYN [Fer 96] and MAFIA [Doh 98]. In the HOMDYN code the beam interaction with the eigenmodes is computed from the TM_{010} eigenmode fields and eigenfrequencies, which have to be numerically calculated [Sek 94]. Figure 7.11 shows the resulting $(R_{sh}/Q_0)^{(l)}$ values for a 2×7-cell superstructure as well as the bunch-to-bunch energy gain variation for a TESLA bunch-train, as simulated with HOMDYN. The computed energy variation is in good agreement with the results discussed above, see figure 7.9. Note that slightly different parameters have been used for the 2×7-cell superstructure in the two simulations.

As discussed in chapter 4, the 2×9-cell superstructure and the 4×7-cell superstructure have been proposed for the TESLA collider. The HOMDYN code has been used to computed the bunch-to-bunch energy gain variation for a TESLA bunch-train, see figure 7.12. As for the 2×7-cell superstructure the relative spread in the energy gain is predicted to be less than $5 \cdot 10^{-5}$.

These results indicate, that the energy flow in the proposed superstructures is sufficiently high to refill all cells in the time interval between two subsequent bunches, without causing significant energy spread. The predicted bunch-to-bunch energy variation is well below the limit for the TESLA collider for all three superstructure types.

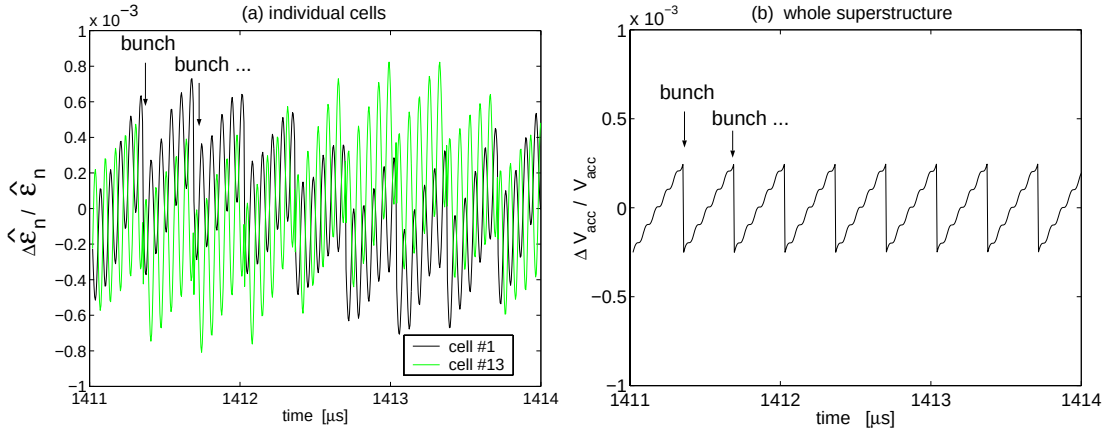

Figure 7.8: (a) Computed fluctuation of the absolute value of the field amplitude of cell #1 and #13 for a 2×7-cell superstructure ($\mathcal{K}_{cc} = 0.01934$, $\mathcal{K}_{rr} = 3.6 \cdot 10^{-4}$, $Q_e^{(13,13)} = 2.733 \cdot 10^6$, $f^{(13)} = 1.3$ GHz). Shown are the last 3 μs of the bunch train. The nominal energy gain of the structure is 37.9 MeV. (b) Corresponding fluctuation of the total accelerating voltage in the 2×7-cell structure.

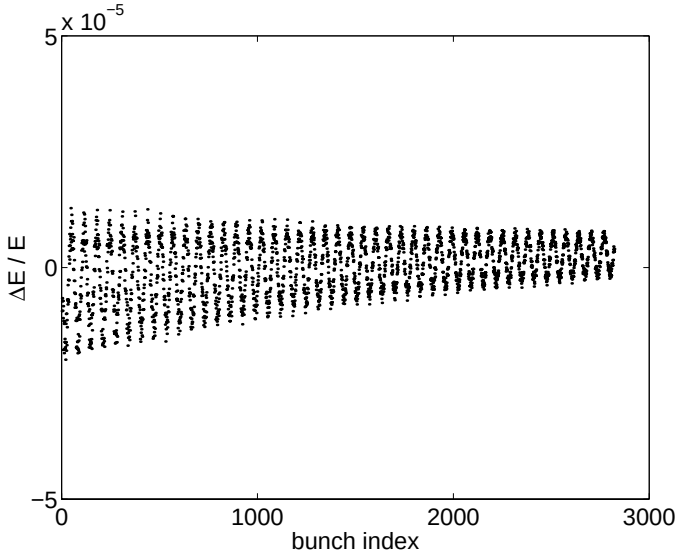

Figure 7.9: Computed bunch-to-bunch energy gain variation for a train of 2820 bunches (TESLA parameters) in a 2×7-cell superstructure ($\mathcal{K}_{cc} = 0.01934$, $\mathcal{K}_{rr} = 3.6 \cdot 10^{-4}$, $Q_e^{(13,13)} = 2.733 \cdot 10^6$, $f^{(13)} = 1.3$ GHz). The nominal energy gain is 37.9 MeV. The used $(R_{sh}/Q_0)^{(l)}$ values of the TM_{010} modes are shown in figure 7.5.

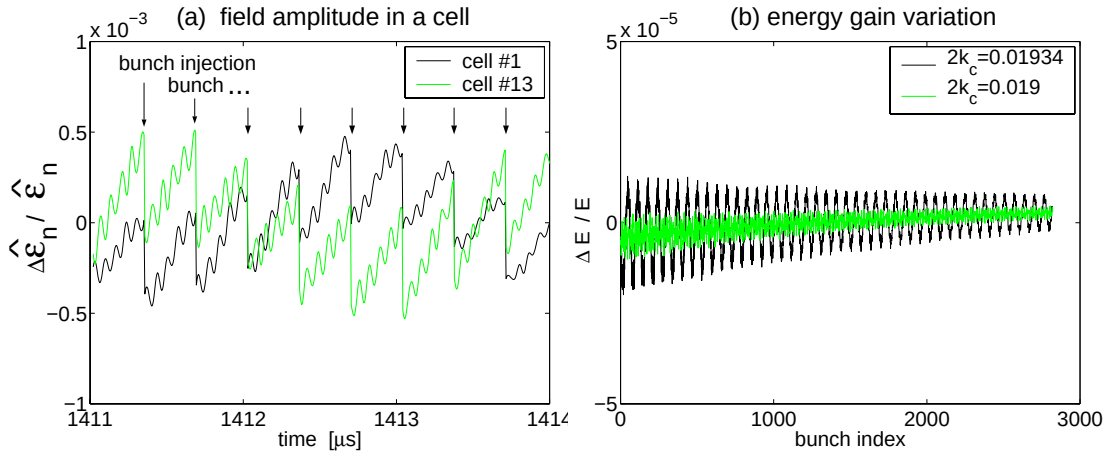

Figure 7.10: Computed modulation of the field amplitude and the energy gain in a 2×7-cell superstructure ($\mathcal{K}_{rr} = 3.6 \cdot 10^{-4}$, $Q_e^{(13,13)} = 2.733 \cdot 10^6$, $f^{(13)} = 1.3$ GHz). The nominal energy gain is 37.9 MeV. The cell-to-cell coupling factor is shifted from $\mathcal{K}_{cc} = 0.019$ to $\mathcal{K}_{cc} = 0.019$ to shift the $\frac{3}{7}\pi - 0$ mode eigenfrequency by 258 kHz. (a) Fluctuation of the absolute value of the field envelope coefficient of cell #1 and #13. Shown are the last 3 μs of the bunch train. (b) Bunch-to-bunch energy gain variation for a TESLA bunch-train of 2820 bunches (cell-to-cell coupling factor $\mathcal{K}_{cc} = 0.01934$ and $\mathcal{K}_{cc} = 0.019$).

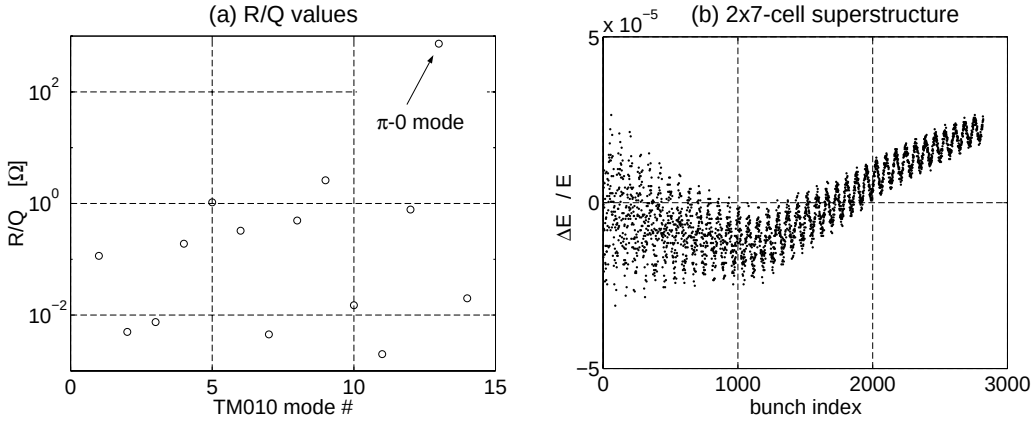

Figure 7.11: Interaction between the beam and the TM_{010} modes in a 2×7-cell superstructure. (a) $(R_{sh}/Q_0)^{(l)}$ values of the eigenmodes calculated by a numerical code [Sek 94]. Computation done by J. Sekutowicz, DESY [Sek 00]. (b) Computed bunch-to-bunch energy gain variation for a train of 2820 bunches (TESLA parameters). Nominal energy gain 35.6 MeV. Computation done by M. Ferrario, INFN, with HOMDYN [Fer 96].

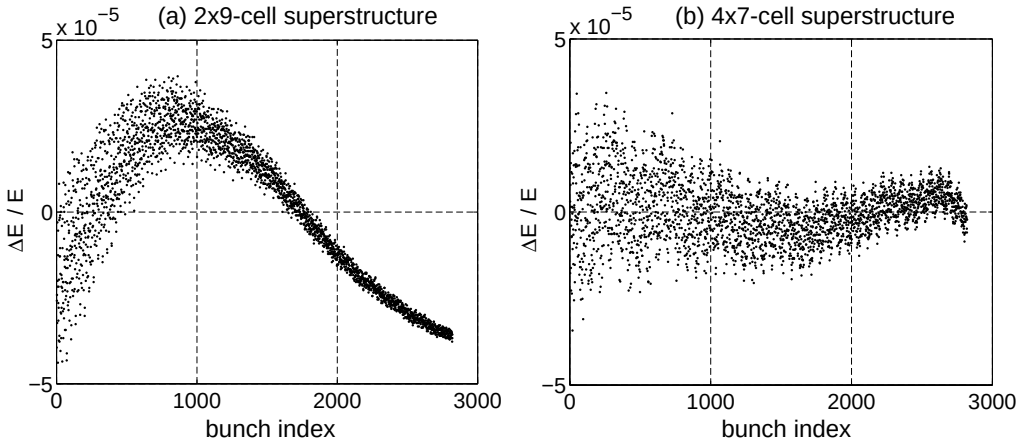

Figure 7.12: Computed bunch-to-bunch energy gain variation for a train of 2820 bunches (TESLA parameters) in: (a) 2×9-cell superstructure (nominal energy gain 71 MeV), and (b) 4×7-cell superstructure (nominal energy gain 46 MeV)[TDR 01]. Computations done by M. Ferrario, INFN, with HOMDYN [Fer 96].

8 RF Field Control for Superstructures

In the previous chapters it has been discussed how the relatively small TM_{010} eigenfrequency spacing in a superstructure affects the amplitude homogeneity tuning and the bunch-to-bunch energy spread. In this chapter we study the consequences of the small eigenfrequency spacing for the RF control system. For the 9-cell cavites at the TESLA-Test-Faciliy a digital RF control system has been developed [Schi 98], as briefly described in section 2.2. We will find that an additional analog bandpass filter in the field detection (see figure 8.1) is sufficient to adapt the TTF control system for superstructures and to guarantee stability of the control loop.

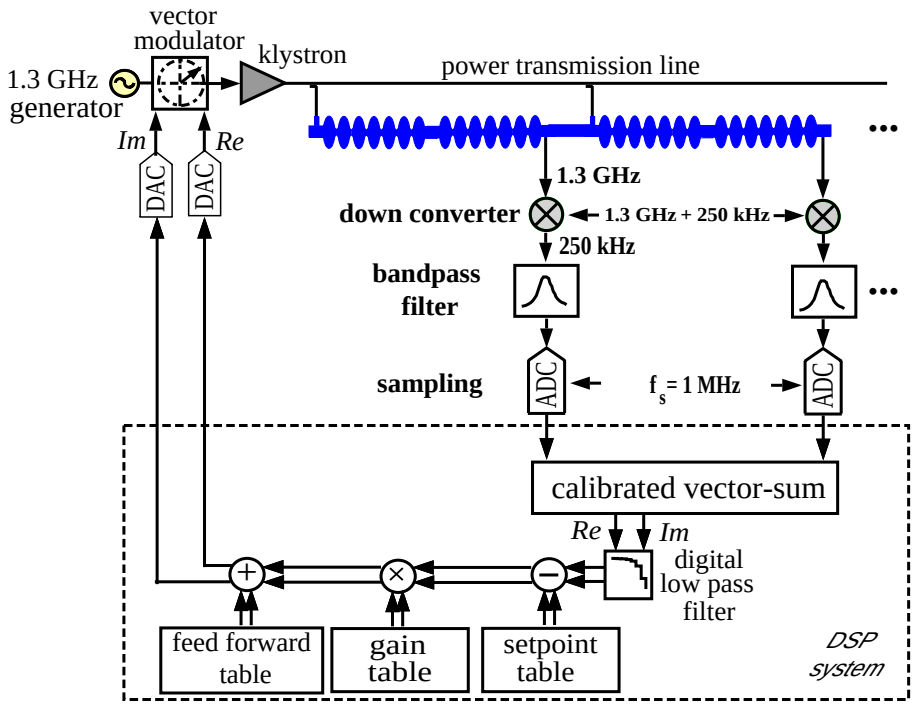

Figure 8.1: Schematic view of the TTF RF control system [Schi 98], as adapted for field stabilization in superstructures. The down-converted pick-up antenna signal is filtered by a bandpass filter before it is sampled with an ADC (Analog-Digital-Converter). The control system is stabilizing the vector-sum of the fields of several superstructures.

8.1 Accelerating Field Detection

In the TTF control system [Schi 98] the real and imaginary components of the cavity field are stabilized. The fundamental mode 1.3 GHz signal of a pick-up antenna close to one end-cell of each cavity is down-converted to an intermediate frequency (IF) of 250 kHz, which contains the amplitude and phase information of the RF signal. Accordingly the eigenfrequencies $f^{(l)}$ of the non-fundamental TM_{010} modes are converted to

$$f_{if}^{(l)} = f_{lo} - f^{(l)} = 1.3 \text{ GHz } + 250 \text{ kHz } - f^{(l)} \quad . \tag{8.1}$$

Here f_{lo} is the frequency of a local oscillator, which serves as the frequency offset in the down-conversion, see [Schi 98] for details. Figure 8.2 (a) shows the TM_{010} eigenfrequencies of a 2×7-cell superstructure. The down-converted frequencies of the modes are shown in figure 8.2 (b). According to the 1 MHz electron-bunch

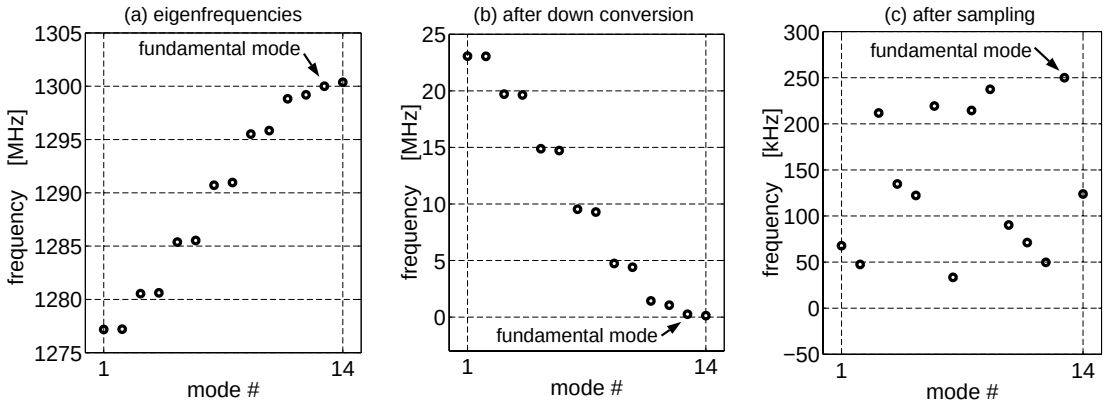

Figure 8.2: Frequencies in the field detection signal of a 2×7-cell superstructure. (a) TM_{010} eigenfrequencies. (b) Frequencies $f_{if}^{(l)}$ after down-conversion. (c) Frequencies after down-conversion and sampling with 500 kHz.

repetition rate at the TTF linac, the down-converted signal is sampled with a rate of 1MHz. This yields four samples per period of the 250 kHz IF signal. Since the samples are 90° apart, two subsequent voltages can be taken as the real and the imaginary parts of a complex field vector, which is representing the acclerating field of the fundamental mode. Accordingly the real and the imaginary parts are updated every 2 μs, corresponding to an effective sampling rate of 500 kHz. Also the field of non-fundamental modes is measured, down-converted and sampled with 500 kHz rate. Due to aliasing, all IF frequencies above 250 kHz are mapped onto frequencies between 0 to 250 kHz, see figure 8.2 (c). The sampled field probe signal is fluctuating on account of the non-fundamental modes, see figure 8.3. However, the accelerating voltage experienced by a beam is totally dominated by the fundamental mode, since the non-fundamental TM_{010} modes have only small (R_{sh}/Q_0) values, see chapter 7. Thus it is desirable to suppress the pick-up antenna signal of the non-fundamental eigenmodes. To achieve this, analog bandpass filters with

a center frequency of 250 kHz and a bandwidth of about 100 kHz to 200 kHz will be placed after the down-converters, see figure 8.1. These filters do not attenuate the fundamental mode signal, since its down-converted frequency is 250 kHz, but suppress the non-fundamental mode signals, see figure 8.3. Note that this suppres-

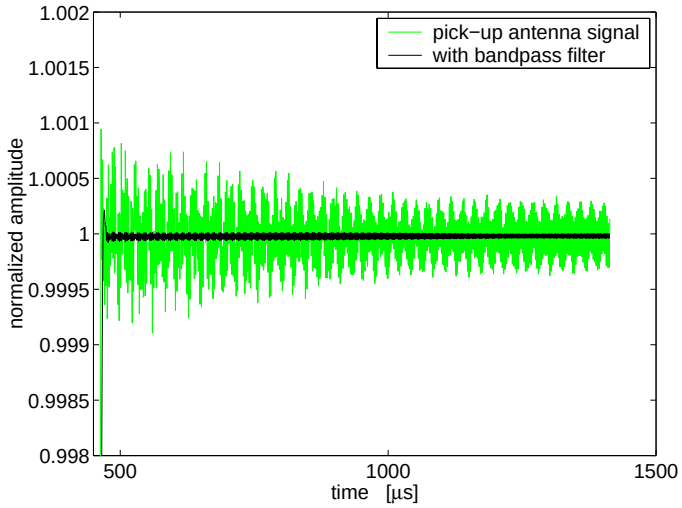

Figure 8.3: Computed amplitude signal of a pick-up antenna close to cell #14 of a 2×7-cell superstructure, which is sampled with to the bunch repetition rate. Shown is the amplitude of the unfiltered signal, which is fluctuating on account of the pick-up signal of the non-fundamental modes. The corresponding bunch-to-bunch energy variation is shown in figure 7.6 (see also figure 7.7). Also shown is the filtered signal (Butterworth 8^{th} order analog filter with 100 kHz bandwidth).

sion is more important for superstructures than for 9-cell cavites, since the excitation of non-fundamental modes by the driving generator is stronger on account of the smaller frequency spacing between the fundamental mode and the neighboring TM_{010} modes. Accordingly in the present control system for the 9-cell cavities at the TTF linac no analog bandpass filter is needed.

8.2 Stability Analysis

By filtering the measured signal, which is used for controlling of the accelerating voltage, robustness and stability of the control loop can be guaranteed. This will be illustrated in the following for the 2×7-cell prototype superstructure. In order to cover the most critical case with respect to stability, an fictive controller is considered (see figure 8.4), which provides frequency independent feedback gain. Moreover it is assumed that the generator, which is driving the superstructure, has also infinite bandwidth. Therefore stability has to be guaranteed by the bandpass filter, since this filter is the only bandwidth limiting element in the control loop beside the superstructure itself, see figure 8.4. Accordingly if the fictive control loop shown in figure 8.4 is stable, stablility is also guaranteed for the controller, which is

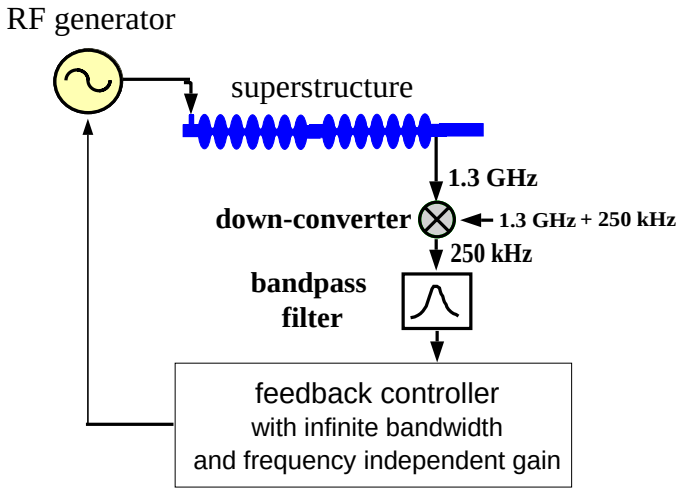

Figure 8.4: Schematic view of the fictive control loop, which is considered in the stability analysis of the feedback system for superstructures (total delay in the feedback loop: 5 μs).

proposed for the superstructures, see figure 8.1. The total delay in the control loop is assumed to be 5 μs as it is in the present TTF RF field control system. A control loop is stable at a given frequency, if the total phase advance along the loop is a multiple of 2π. For this phase advance an oscillation with the considered frequency is supressed by the negative feedback of the control loop. In the control loop for the cavity RF field (see figure 8.1 and 8.4), the phase advance along the loop is adjusted for negative feedback at the frequency of the fundamental mode, since the accelerating field needs to be stabilized. However, the phase advance along the loop depends on the frequency. If the phase advance reaches $-180°$, the negative control loop feedback is turned into positive feedback. Accordingly the loop is unstable if its gain at this frequency is larger than one (unity gain, 0 dB).
Figure 8.5 (a) shows the computed amplitude of the field probe signal for the 2×7-cell superstructure as function of the generator frequency. Hereby it is considered that the pick-up antenna is close to cell #14 and that the generator current amplitude is independent of the frequency. After after mixing with $f_{lo} = 1300.25$ MHz the fundamental mode frequency 1.3 GHz is mapped to 250 kHz. The computed frequency spectrum of the pick-up signal after down-conversion is shown in figure 8.5 (b). Subsequently the down-converted signal is filtered by the bandpass filters (Butterworth 8^{th} order analog bandpass filter with 100 kHz bandwidth), as shown by the lower curve in figure 8.5 (b). The center frequency of the bandpass filter is adjusted to 250 kHz, thus the signal of the fundamental $\pi - 0$ mode is not attenuated, whereas the signal of the non-fundamental TM_{010} modes is supressed. The filter characteristics of the bandpass filter is shown in figure 8.6 for selected bandwidths.

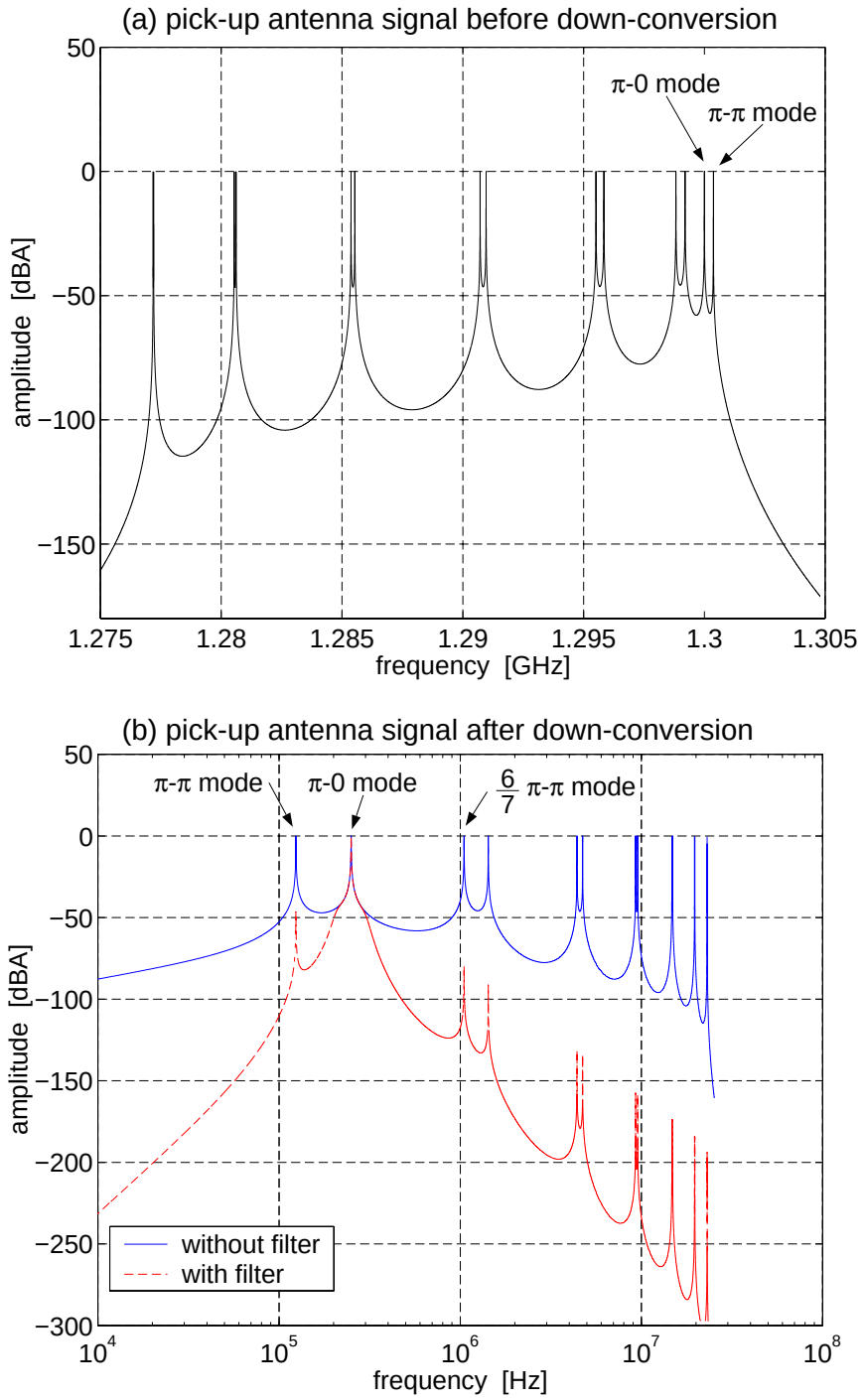

Figure 8.5: Computed TM_{010} resonance spectrum of a superconducting 2×7-cell superstructure for a driving RF generator with constant amplitude ($\mathcal{K}_{cc} = 0.019$, $\mathcal{K}_{rr} = 3.6 \cdot 10^{-4}$, $Q_0^{(1)} = 10^{10}$, $Q_e^{(13,13)} = 2.733 \cdot 10^6$). (a) Amplitude of the field probe signal measured via a pick-up antenna close to cell #14. (b) Field probe signal after mixing with $f_{lo} = 1300.25$ MHz and filtering (Butterworth 8^{th} order analog bandpass filter with 100 kHz bandwidth).

For the control loop shown in figure 8.4 the amplitude of the filtered pick-up antenna signal gives the frequency dependence of the loop gain, since the controller and the generator are considered to have frequency independent gain. Stability of the control loop requires, that the gain at all frequencies with positive feedback is below one. Figure 8.7 shows the loop gain and the loop phase advance (minus multiples of 2π) at frequencies near to the fundamental-mode frequency. It is found that the gain-margin between the gain at the fundamental mode frequency and the frequencies with positive feedback (180° phase advance) is 80 (38 dB) for the parameters of the example dicussed here. This gain-margin gives the critical loop gain for the

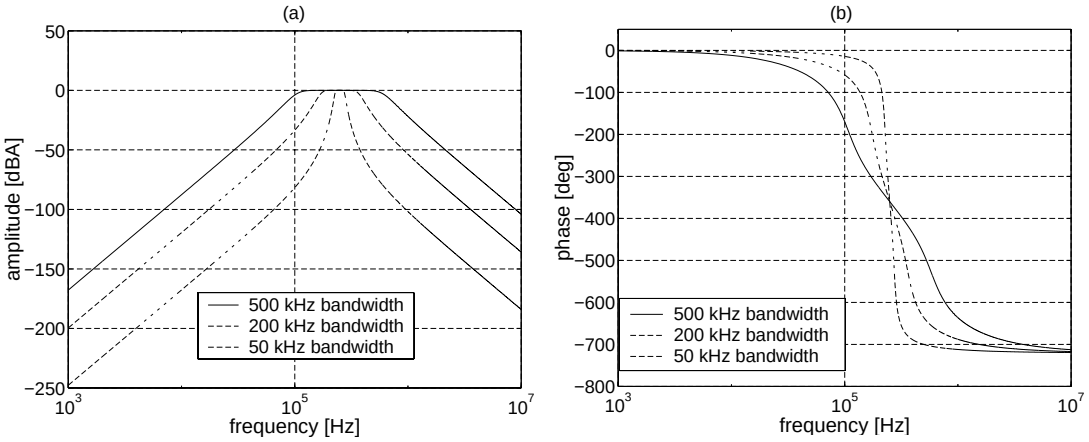

Figure 8.6: Computed filter characteristics of Butterworth 8^{th} order analog bandpass filters with selected bandwidths. The center frequency is 250 kHz. (a) Amplitude response as function of frequency. (b) Phase advance as function of frequency.

negative feedback on the fundamental eigenmode field. However, a loop gain below but close to this critical gain results in overshooting and oscillation around a given setpoint for the accelerating field [Schi 98]. According to the methode of Ziegler and Nichols [Lun 97] the optimal gain K_{opt} for a proportional gain controller is half of the critical gain K_{crit}

$$K_{opt} = 0.5 \cdot K_{crit} \quad . \tag{8.2}$$

Accordingly for the example shown in figure 8.7 the optimal feedback gain at the fundamental mode frequency is 40.

Up to now only frequencies near to the fundamental mode frequencies have been considered in the stability analysis. Figure 8.8 shows the frequency dependence of the loop gain for the full frequency range of the TM_{010} modes for the fictive control loop. It is found that the gain has local maxima at the mode eigenfrequencies after down-conversion. The phase advance of the control loop at these frequencies strongly depends on the eigenfrequencies and the time delay in the loop. To guarantee robustness against parameter fluctuations the worst case needs to be considered, i.e. positive feedback at the eigenfrequencies of the non-fundamental modes. Accordingly stability of the control loop requires, that the gain at these frequencies is below one, as is discussed above. The gain at the eigenfrequencies of the non-

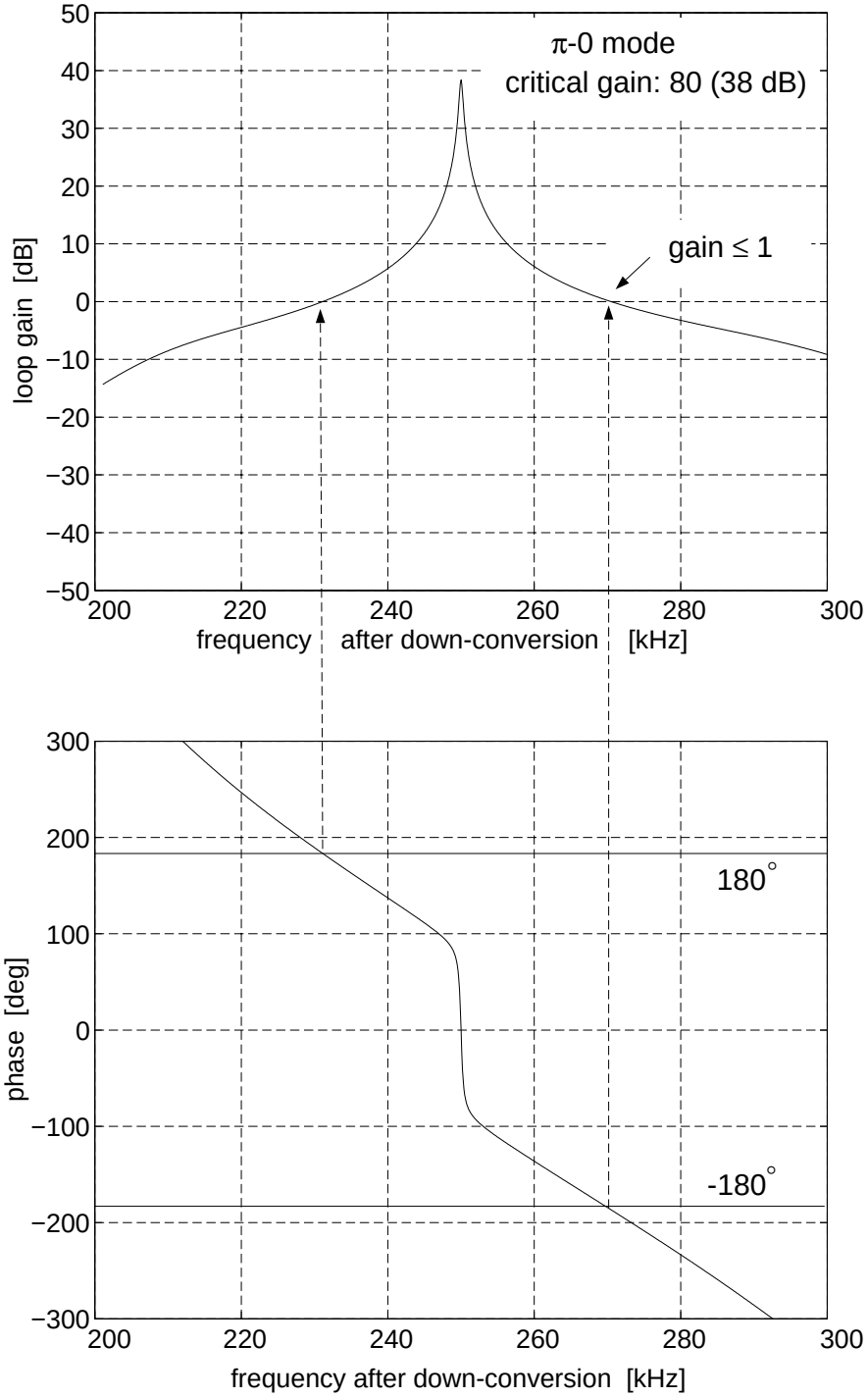

Figure 8.7: Computed loop gain and phase advance near to fundamental-mode frequency after down-conversion for the control loop, which is shown in figure 8.4 (2×7-cell superstructure, $Q_e^{(13,13)} = 2.733 \cdot 10^6$, 5 μs loop delay, Butterworth 8^{th} order analog bandpass filter with 100 kHz bandwidth).

fundamental modes is lowered by the bandpass filters. For a filter with 100 kHz bandwidth, the $\pi - \pi$ mode of the 2×7-cell superstructure cannot cause instability if the fundamental mode feedback gain is lower than 210, see figure 8.8. For this feedback gain the loop gain at the $\pi - \pi$ frequency reaches the critical value of one (0 dB). The gain at the other non-fundamental mode frequencies is still below one, as can be seen from figure 8.8, thus they do not cause instability.
The smaller the bandwidth of the filter, the lower is the loop gain at the non-fundamental modes. Unfortunately a smaller bandwidth gives a stronger frequency dependence of the phase advance of the filter near to the fundamental mode frequency, see figure 8.6. This lowers the critical gain-margin (and therefore the optimal gain) for the stability near to the fundamental mode frequency, since the instability points with positive feedback (180° phase advance) are shifted towards the fundamental mode frequency, see figure 8.7. Therefore the benefit of a smaller filter bandwidth for the non-fundamental mode frequencies has to be balanced against the lowered gain-margin for the fundamental mode. Figure 8.9 shows the gain-margin for the fundamental mode as well as the maximum feedback gain for control stability at the non-fundamental mode frequencies as function of the filter bandwidth. It is found that the optimum full bandwidth of a Butterworth 8^{th} order bandpass filter is 140 kHz for a 2×7-cell superstructure and 190 kHz for a 2×9-cell superstructure. For these filter parameters stability of the control loop is guaranteed up to a fundamental mode feedback gain of 50 and 60, respectively. These feedback gains are comparable to the gain presently used for the field control in the TTF 9-cell cavities at the TESLA-TEST-Facility linac. Measurements at the TTF linac have shown, that the control performance goals for the TESLA collider are met for these feedback gains in combination with a feedforward control [TDR 01].
A similar stability analysis for the field control in 4×7-cell superstructures gives, that a full filter bandwidth of 140 kHz and a maximum gain of 50 guarantees control stability [Min 01].

8.3 Conclusion

The RF control system presently in operation for the 9-cell cavities at the TTF linac can be used for proposed superstructures by inserting an analog bandpass filters at the IF output of the down-converters. Properly adjusted, these filters effectively remove contributions of the non-fundamental modes to the pick-up antenna signal. This ensures that the accelerating voltage of the fundamental mode is stabilized by the feedback control. Moreover the bandpass filters guarantee stability of the RF control loop and robustness against parameter fluctuations.

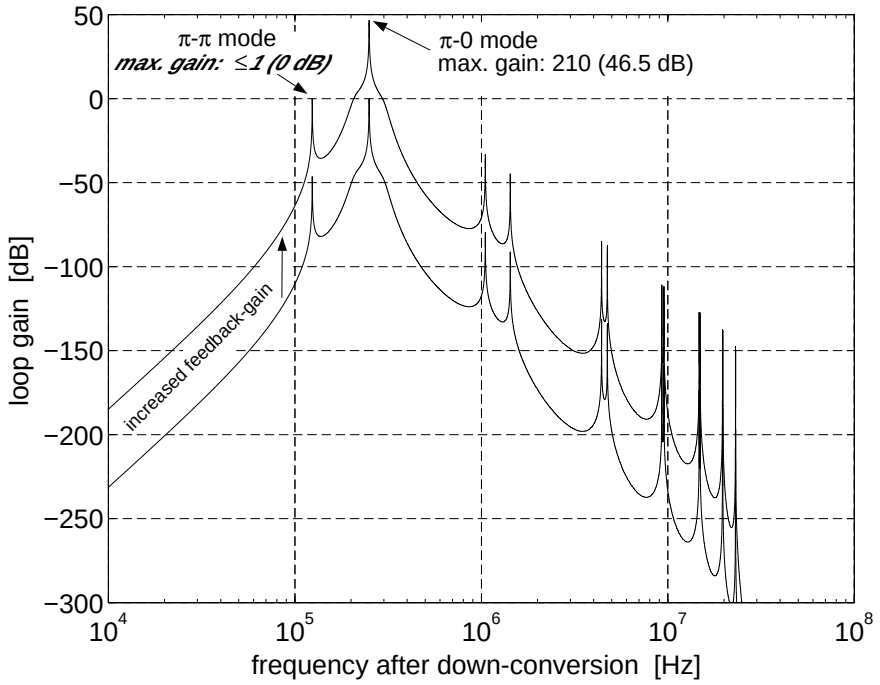

Figure 8.8: Computed loop gain of the control loop, which is shown in figure 8.4 as function of frequency after down-conversion (2×7-cell superstructure, $Q_e^{(13,13)} = 2.733 \cdot 10^6$, 5 μs loop delay, Butterworth 8^{th} order analog bandpass filter with 100 kHz bandwidth). Shown is the loop gain for two different feedback gains of the controller.

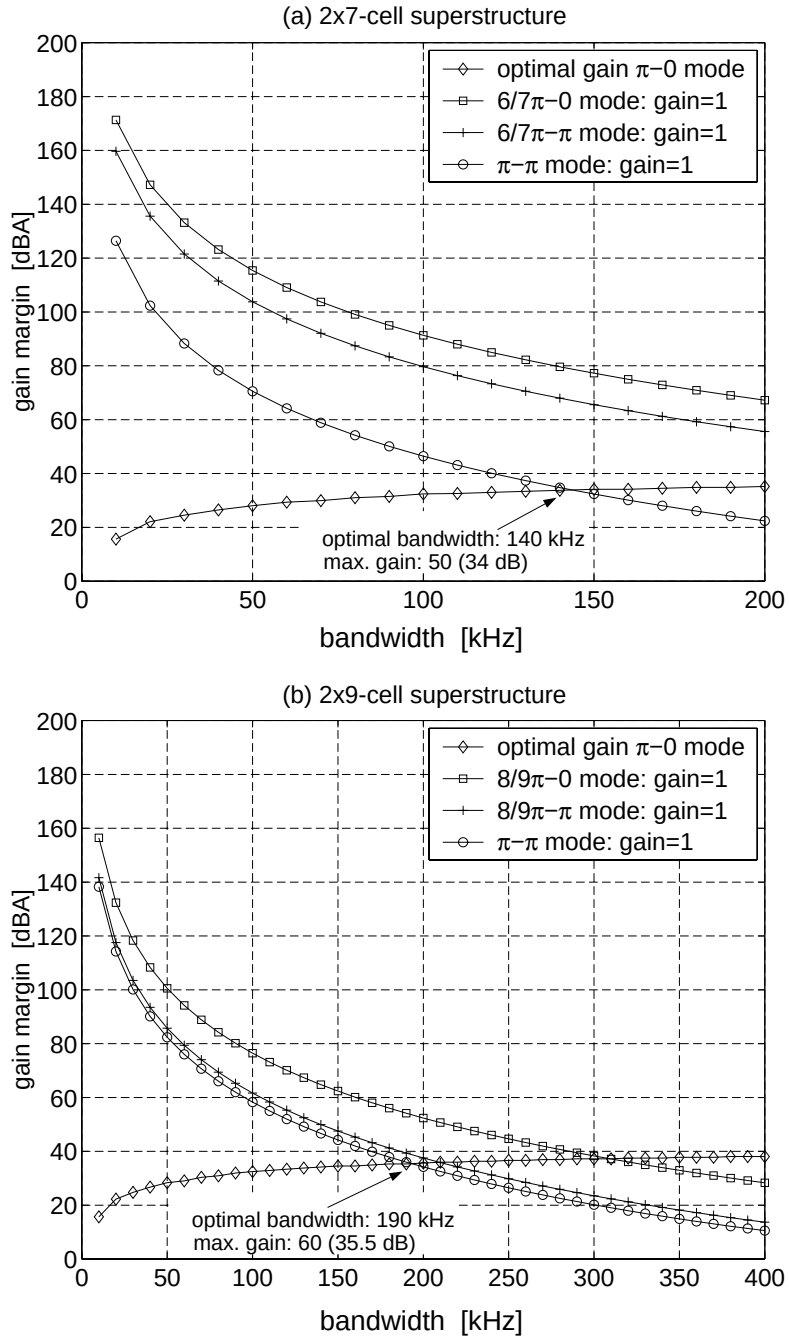

Figure 8.9: Maximum feedback gain K_{fb} for the control loop shown in figure 8.4 at the fundamental mode frequency (5 μs loop delay) as function of the full bandwidth of the Butterworth 8^{th} order analog bandpass filter. The curves show the optimal gain if only the fundamental $\pi - 0$ mode is considered as well as the maximum gain for the stability condition $K_{fb} \leq 1$ at the frequencies of the neighboring modes. (a) 2×7-cell superstructure. (b) 2×9-cell superstructure.

9 Higher-Order Mode Damping in Superstructures

In this chapter the higher-order modes (HOMs) and their damping in superstructures is discussed. The HOM damping has been extensively studied on copper versions of the 2×7 and 4×7-cell superstructure for frequencies up to 3.1 GHz.
A special feature of superstructures is the possibility to adjust the frequencies of trapped higher-order modes.

9.1 Higher-Order Mode Excitation

A charge passing through a cavity is accelerated by the fundamental mode, which is driven by a generator. However, the charge itself can also excite modes. In chapter 7 we studied this for the TM_{010} monopole modes of a multicell cavity. In this chapter we will consider the so-called higher-order modes, which have frequencies above the TM_{010} modes. In the following we shall briefly discuss the excitation of these modes by a train of bunches. A charge passing on axis through a cavity can only excite monopole modes, because the longitudinal electric field vanishes on axis for all other modes, see section 5.2. However, if the charge is moving off axis through the cavity, it can also excite dipole modes and HOMs with higher multipole order.
Monopole modes:
Let us consider a bunch with a charge Q_b and a gaussian profile with a length σ_b in time (standard deviation). When the bunch has passed a cavity on axis, the accelerating voltage of a monopole mode m is changed by

$$\begin{aligned} \Delta V_{acc,b}^{(m)} &= \omega^{(m)} \left(\frac{R_{sh}}{Q_0}\right)^{(m)} Q_b \exp\left(-\frac{(\omega^{(m)})^2 \sigma_b^2}{2}\right) \exp(i\omega^{(m)} t) \\ &\approx \omega^{(m)} \left(\frac{R_{sh}}{Q_0}\right)^{(m)} Q_b \exp(i\omega^{(m)} t) \quad , \end{aligned} \tag{9.1}$$

see chapter 7. Here $\omega^{(m)}$ is the eigenfrequency of the monopole mode. The approximation in (9.1) is valid for a short bunch, i.e. for $\omega^{(m)}\sigma_b \ll 1$, as we will consider in the following. The (R_{sh}/Q_0)-value of a monopole mode is given by

$$\left(\frac{R_{sh}}{Q_0}\right)^{(m)} = \frac{|V_{acc}^{(m)}|^2}{2\omega^{(m)} U^{(m)}} \quad , \tag{9.2}$$

where $U^{(m)}$ is the stored energy, as is derived in section 5.5.
In the next step we consider a train of identical bunches, equally spaced in time

by ΔT_b. The excited voltage is found by using the superposition principle. For this we have to take into account, that the exited RF field is oscillating and is decaying exponentially between the bunches on account of losses. Within the bunch spacing ΔT_b the field changes by a factor $\exp(-(\omega_{1/2}^{(m)} - i\omega^{(m)})\Delta T_b)$. Recall that $\omega_{1/2}^{(m)} = \omega^{(m)}/2Q_L^{(m)}$ is the bandwidth of the mode m and $Q_L^{(m)}$ is the so-called loaded quality factor of this mode. It is usefull to write

$$\omega^{(m)} = (\Delta\omega^{(m)} + \omega_h) \quad , \tag{9.3}$$

where

$$\omega_h = \frac{2\pi h}{\Delta T_b} \quad , h = \text{integer}, \tag{9.4}$$

is the closest harmonic of the bunch repetition frequency [Pad 98]. Superposing all induced voltages for a mode yields for the total change of the accelerating voltage after bunch n of a bunch-train has passed the cavity

$$V_{acc,tr}^{(m)}(t = n\Delta T_b) = V_{acc,sst}^{(m)}(1 - \exp(-(\omega_{1/2}^{(m)} - i\Delta\omega^{(m)})n\Delta T_b) \quad , \tag{9.5}$$

where the steady-state beam induced voltage is given by the result of a geometrical progression

$$V_{acc,sst}^{(m)} = \frac{\Delta V_{acc,b}^{(m)}}{1 - \exp(-\omega_{1/2}^{(m)}\Delta T_b)\exp(i\Delta\omega^{(m)}\Delta T_b)} \quad . \tag{9.6}$$

Figure 9.1 shows the steady-state beam induced voltage (normalized to the voltage induced by a single bunch) as a function of $\Delta f^{(m)}\Delta T_b$ for two different damping factors $f_{1/2}^{(m)}\Delta T_b$. We see that a substantial resonant built-up occurs, if the damping is small and the mode eigenfrequency is close to a Fourier component of the bunched beam, i.e. $\Delta f^{(m)} \to 0$. If we consider the case $\omega_{1/2}^{(m)}\Delta T_b \ll 1$ and short bunches ($\omega^{(m)}\sigma_b \ll 1$), the maximum steady-state excitation for $\Delta\omega^{(m)} = 0$ is approximately given by

$$V_{acc,sst}^{(m)}(\Delta\omega^{(m)} = 0) \approx \frac{\Delta V_{acc,b}^{(m)}}{\omega_{1/2}^{(m)}\Delta T_b} = 2Q_L^{(m)}\left(\frac{R_{sh}}{Q_0}\right)^{(m)} I_b \quad . \tag{9.7}$$

Here $I_b = Q_b/T_b$ is the time-averaged beam current. Accordingly the maximum beam induced steady-state voltage is proportional to the impedance $Q_L^{(m)} \cdot (R_{sh}/Q_0)^{(m)}$. Usually the damping of a monopole mode in a superconducting cavity is dominated by the energy extraction via the HOM couplers of the cavity, i.e. $Q_L^{(m)} \approx Q_{ext}^{(m)}$. The quantity $Q_{ext}^{(m)}$ is the external quality factor of mode m due to the damping by the HOM couplers. Then we find the following relation for the power, which is dissipated in the loads of the HOM couplers by a resonant excited monopole mode

$$P_{max}^{(m)} = \frac{\omega^{(m)}U^{(m)}(\Delta\omega^{(m)} = 0)}{Q_{ext}^{(m)}} = I_b V_{acc,sst}^{(m)}(\Delta\omega^{(m)} = 0) \approx 2Q_{ext}^{(m)}\left(\frac{R_{sh}}{Q_0}\right)^{(m)} I_b^2 \quad . \tag{9.8}$$

It is important to note that the power transferred by the HOM couplers increases proportional to the external quality factor of a mode, since the steady-state induced

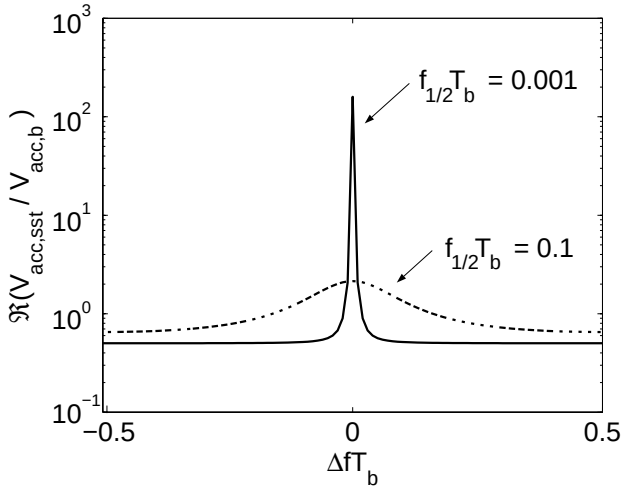

Figure 9.1: Normalized real part of the steady-state beam induced voltage as function of $\Delta f^{(m)} \Delta T_b$, see equation (9.6). Example: $T_b = 1$ μs, $f^{(m)} = 2$ GHz, $f_{1/2}^{(m)} = 0.1/T_b = 100$ kHz and $f_{1/2}^{(m)} = 0.001/T_b = 1$ kHz correspond to $Q_L^{(m)} = 10^4$ and $Q_L^{(m)} = 10^6$.

stored energy $U^{(m)}$ for $\Delta\omega^{(m)} = 0$ is proportional to the square of the external quality factor.

Dipole modes:

Higher-order modes (dipole, quadrupole, ...) can only be excited if the beam passes off axis through a cavity. For a pill-box cavity of length L_c and radius R the longitudinal electric field for TM_{abp} modes is

$$E_z = E_0 \cos\left(\frac{p\pi z}{L_c}\right) J_a\left(\frac{u_{ab} r}{R}\right) \cos(a\varphi) \quad . \tag{9.9}$$

The fields in a pill-box cavity and the mode nomenclature are discussed in detail in section 5.2. For $u_{ab} r/R \ll 1$ the approximation $J_1(u_{1b} r/R) \approx u_{1b} r/(2R)$ is valid. We find that the longitudinal electric field of a dipole mode ($a = 1$) increases linearly with r for small distances from the axis. E_z vanishes on the axis.

The accelerating voltage in a cavity can be expanded in a multipole series. For an axially symmetric cavity with beam tubes it can be shown that the accelerating voltage for a beam path parallel to the cavity axis varies with r and φ as [Zot 79]

$$V_{acc}(r) = V_{acc,R_0} \left(\frac{r}{R_0}\right)^a \cos(a\varphi) \quad . \tag{9.10}$$

Here V_{acc,R_0} is the accelerating voltage of a mode at a characteristic transversal position $r = R_0$, e.g. the beam tube radius. The integer index a gives the multipole order of the mode. According to (9.10) the accelerating voltage of a mode of a multipole order a falls off more rapidly towards the cavity axis as a increases. Hence for beam stability studies the most important modes with deflecting fields are the dipole modes of a cavity ($a = 1$).

By analogy with the monopole modes we shall define a (R_d/Q_0)-value for the dipole modes. Since the accelerating voltage increases linearly with the distance from the cavity axis, an appropiate choice is

$$\left(\frac{R_d}{Q_0}\right)^{(m)} = \frac{|V^{(m)}_{acc,R_0}|^2}{2\omega^{(m)}U^{(m)}R_0^2} \quad , \tag{9.11}$$

where (R_d/Q_0) is in Ω/m^2.
Each dipole mode exists in two orthogonal polarisations. The damping of the two polarisations via the HOM-couplers may differ. Accordingly in the following the measured external quality factors for each polarisation will be listed. In an axially symmetric cavity both polarisations have the same frequency. Since this symmetry is assumed in the numerical field calculations, only one calculated eigenfrequency value is listed per dipole mode.

9.2 HOM's in Superstructures

The eigenfields and frequencies of higher-order modes in the 2×7-cell and 4×7-cell superstructure have been computed for the first groups of monopole modes ([Sek 00, Sek 94]) and dipole modes (MAFIA code, [Che 00, Kla 86]). The obtained eigenfrequencies and (R/Q) values of the strongest monopole modes are listed in the tables 9.1 and 9.3, while the strongest dipole modes are listed in the tables 9.2 and 9.4. In figure 9.6 (a) and figure 9.7 (a) the (R/Q) values of the superstructure dipole modes (normalized to the number of cells) are compared to the (R/Q) values of the TTF 9-cell cavity. It can be seen, that the superstructures and the 9-cell cavity are comparable, if (R/Q) is normalized to the number of cells per structure. This can be attributed to the fact that the structures have identical center-cells.

9.3 Requirements on Damping

For a linear accelerator the desired beam parameters (particularly energy spread and beam emittance) determine the required HOM damping in the cavities. In order to estimate the effect of the higher-order modes on the beam parameters, the multi-bunch beam dynamics in the main linac of the TESLA collider has been simulated [Bab 01]. In the following the obtained requirements on the HOM damping for a TESLA collider based on superstructures will be presented, as taken from [Bab 01].
Monopole modes:
Monopole modes excited by a bunch-train react on the bunches and modulate their energy. However, for the TESLA collider with a large number of accelerating structures, the resulting energy modulation nearly averages out because of the natural frequency spread of the monopole modes [TDR 01]. Simulations for the 4×7-cell superstructure have shown, that quality factors of a few 10^5 result in a relative bunch-to-bunch energy variation in the order of 10^{-6} [Bab 01]. Compared to the intra-bunch energy spread of approximately $5{\cdot}10^{-4}$ [TDR 01] this is neglectible. The needed damping of the monopole modes is therefore not determined by the required

energy stability, but by the power capability of cables and feedthroughs of the HOM couplers. Recall that the power transferred by the HOM couplers increases proportional to the external quality factor, see equation (9.8) in section 9.1. Accordingly sufficient damping in the order of $5 \cdot 10^4$ has to be ensured for the modes with the highest (R_{sh}/Q_0)-values, to stay within the mean power capability of several watts [Sek 00], even for the worst case of resonant mode excitation.

frequency (simulation) [GHz]	(R_{sh}/Q_0) (simulation) [Ω]	Q_{ext} (meas.)
2.1259	64.4	$6.47{\cdot}10^2$
2.3052	29.1	$1.45{\cdot}10^3$
2.4340	14.9	$7.51{\cdot}10^3$
2.4530	134.8	$1.41{\cdot}10^4$
2.4764	109.4	$< 5 \cdot 10^4$

Table 9.1: TM_{011} monopole modes of the 2 × 7-cell superstructure with high (R_{sh}/Q_0) values, as obtained from numerical computations [Sek 00]. The Q_{ext}-values are taken from measurements on the copper model, see section 9.4.

frequency (simulation) [GHz]	(R_d/Q_0) (simulation) [Ω/cm^2]	Q_{ext} (meas.) pol. 1	Q_{ext} (meas.) pol. 2
TE$_{111}$−like			
1.6938	2.0	$2.68{\cdot}10^3$	$5.96{\cdot}10^3$
1.7233	11.2	$7.12{\cdot}10^4$	$8.81{\cdot}10^3$
1.7283	3.1	$1.29{\cdot}10^5$	$2.13{\cdot}10^4$
1.7638	5.9	$1.35{\cdot}10^4$	$1.28{\cdot}10^4$
TM$_{110}$−like			
1.8527	1.3	$2.36{\cdot}10^4$	$2.03{\cdot}10^3$
1.8563	1.2	$1.82{\cdot}10^4$	$9.00{\cdot}10^3$
1.8664	1.1	$1.38{\cdot}10^4$	$3.18{\cdot}10^3$
1.8687	2.6	$3.96{\cdot}10^4$	$1.26{\cdot}10^4$
1.8762	2.8	$1.50{\cdot}10^4$	$1.48{\cdot}10^4$
1.8773	2.1	$1.50{\cdot}10^4$	$1.12{\cdot}10^5$
1.9099	1.1	$5.39{\cdot}10^4$	$1.71{\cdot}10^2$
TE-like			
2.5741	13.1	$1.49{\cdot}10^4$	$1.54{\cdot}10^4$
2.6423	2.2	$6.05{\cdot}10^3$	$3.80{\cdot}10^3$
2.9474	1.3	$8.92{\cdot}10^3$	$5.18{\cdot}10^4$

Table 9.2: Dipole modes of the 2 × 7-cell superstructure with high (R_d/Q_0) values, as obtained from MAFIA computations [Che 00]. The Q_{ext}-values are taken from measurements on the copper model, see section 9.4.

frequency (simulation) [GHz]	(R_{sh}/Q_0) (simulation) [Ω]	Q_{ext} (meas.)
2.1607	17.3	$2.28{\cdot}10^3$
2.4365	78.7	$1.97{\cdot}10^4$
2.4507	144.8	$8.41{\cdot}10^3$
2.4519	15.9	$8.56{\cdot}10^3$
2.4530	21.0	$1.25{\cdot}10^5$

Table 9.3: TM_{011} monopole modes of a 4×7-cell superstructure with high (R_{sh}/Q_0) values, as obtained from numerical computations [Che 00]. The Q_{ext}-values are taken from measurements on the copper model, see section 9.4.

frequency (simulation) [GHz]	(R_d/Q_0) (simulation) [Ω/cm^2]	Q_{ext} (meas.) pol. 1	Q_{ext} (meas.) pol. 2
TE$_{111}$−like			
1.7163	7.5	$4.52{\cdot}10^3$	$1.77{\cdot}10^3$
1.7203	17.4	$1.07{\cdot}10^3$	$2.76{\cdot}10^3$
1.7246	2.4	$1.31{\cdot}10^3$	$1.87{\cdot}10^4$
1.7257	3.1	$7.07{\cdot}10^3$	$4.17{\cdot}10^3$
1.7603	2.0	$1.00{\cdot}10^3$	$1.00{\cdot}10^3$
1.7622	9.2	$3.61{\cdot}10^3$	$9.10{\cdot}10^3$
TM$_{110}$−like			
1.8527	2.5	$4.32{\cdot}10^3$	$3.32{\cdot}10^3$
1.8666	2.0	$7.07{\cdot}10^3$	$4.57{\cdot}10^3$
1.8680	3.6	$1.69{\cdot}10^4$	$1.77{\cdot}10^4$
1.8766	5.3	$8.55{\cdot}10^3$	$2.85{\cdot}10^4$
1.8772	4.9	$6.04{\cdot}10^4$	$1.58{\cdot}10^4$
TE-like			
2.5726	≤23.0	$1.56{\cdot}10^4$	$5.01{\cdot}10^4$
2.5731	≤23.2	$4.13{\cdot}10^4$	$5.82{\cdot}10^4$
2.5737	≤2.5	$3.34{\cdot}10^4$	$1.34{\cdot}10^4$
2.5742	≤4.0	$3.04{\cdot}10^4$	$2.19{\cdot}10^4$

Table 9.4: Dipole modes of the 4×7-cell superstructure with high (R_d/Q_0) values, as obtained from MAFIA computations [Che 00]. The Q_{ext}-values are taken from measurements on the copper model, see section 9.4.

Dipole modes:
If a dipole mode is excited by the beam, the deflecting field of the dipole mode will act on the subsequent bunches and causes a multi-bunch emittance[1] growth. For the TESLA main linac the normalized beam emittance in the vertical plane at injection is specified to $2 \cdot 10^{-8}$ m·rad, while the desired normalized vertical emittance at the end of the linac is $3 \cdot 10^{-8}$ m·rad, or below [TDR 01]. Beam dynamics simulations for a TESLA linac equipped with 4×7-cell superstructures indicate, that it is sufficient to damp all dipole modes with $(R_d/Q_0) \leq 7.5\ \Omega/\mathrm{cm}^2$ to a level of $Q_L = 2 \cdot 10^5$, while the loaded quality factors of the dipole modes with higher (R_d/Q_0) should not exceed $Q_L = 1 \cdot 10^5$ [Bab 01]. As is discussed above, it can be expected that similar limits also apply for the 2×7-cell and the 2×9-cell superstructures. Refer to [Bab 01] for details.

9.4 Measurements on Copper Models

In order to verify the numerical higher-order mode calculations and to test the HOM damping, copper versions of the 2×7-cell superstructure and the 4×7-cell structure have been built, see figure 9.2. The RF parameters of the structurs are listed in table

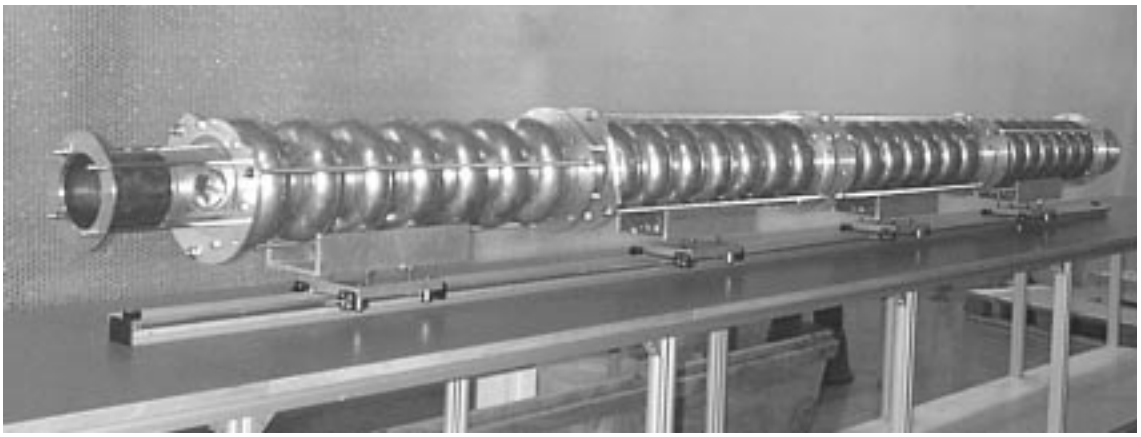

Figure 9.2: Copper model of the 4x7-cell superstructure. The RF parameters of the structure are listed in table 4.3.

4.2 and table 4.3, respectively. For monopole and dipole modes with frequencies up to 3.1 GHz the on-axis profile of the electric field amplitude[2] has been measured in the copper structures and compared to the computations. In general the agreement is quite good. To give an example, figure 9.3 shows the computed and the measured field profile for a TE_{111} dipole mode on the 4×7-cell superstructure, which has a high (R_d/Q_0)-value (see also table 9.4). For some modes it was found, that the cavities of a superstructure stay almost uncoupled. This is shown in figure 9.4 for

[1] A multi-bunch emittance of a bunch-train is defined via the positions of the bunch centers in the transversal phase space.

[2] Note that the amplitude of the electric field is measured and not only its longitudinal component.

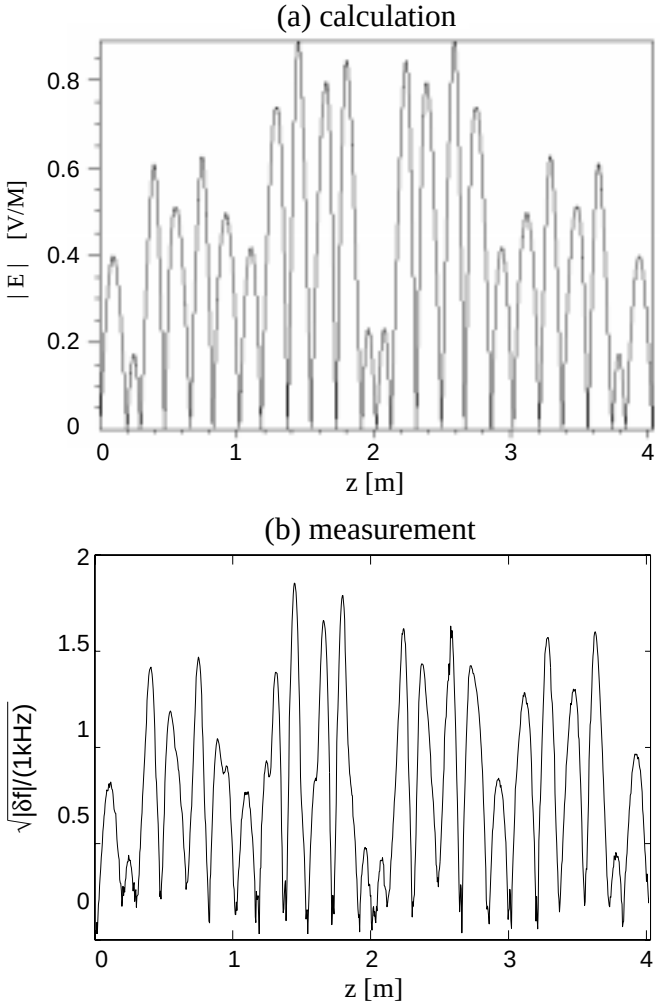

Figure 9.3: 4×7-cell superstructure: On-axis electric field profile of the TE_{111} dipole mode with the highest (R_d/Q_0)-value ($f = 1.720$ GHz, $(R_d/Q_0) = 17.4\ \Omega/\mathrm{cm}^2$). (a) MAFIA calculation of the electric field profile [Che 00]. (b) Bead pull result for one polarisation of the dipole mode, measured on the copper model.

a dipole mode of the 2×7-cell superstructure. This can be attributed to imperfections of the cell shapes in the copper structure. The cell frequencies are tuned for a homogeneous amplitude profile of the accelerating mode (see chapter 6), but not for obtaining equal HOM amplitudes in the cavities. Accordingly for higher-order modes the individual cells and cavities can have significant differences in frequencies and cell-to-cell coupling. For modes with low fields in the interconnecting tubes (see for example figure 9.4), i.e. low cavity-to-cavity coupling, these differences can result in a field pattern which is concentrated in one cavity. Obviously this perturbation has impact on the HOM damping, since only the HOM couplers close to the cavities with a high field amplitude can extract the mode energy. Accordingly it is desirable to study the HOM damping on several superstructures to verify that sufficient damping is ensured under varying conditions for the HOMs.

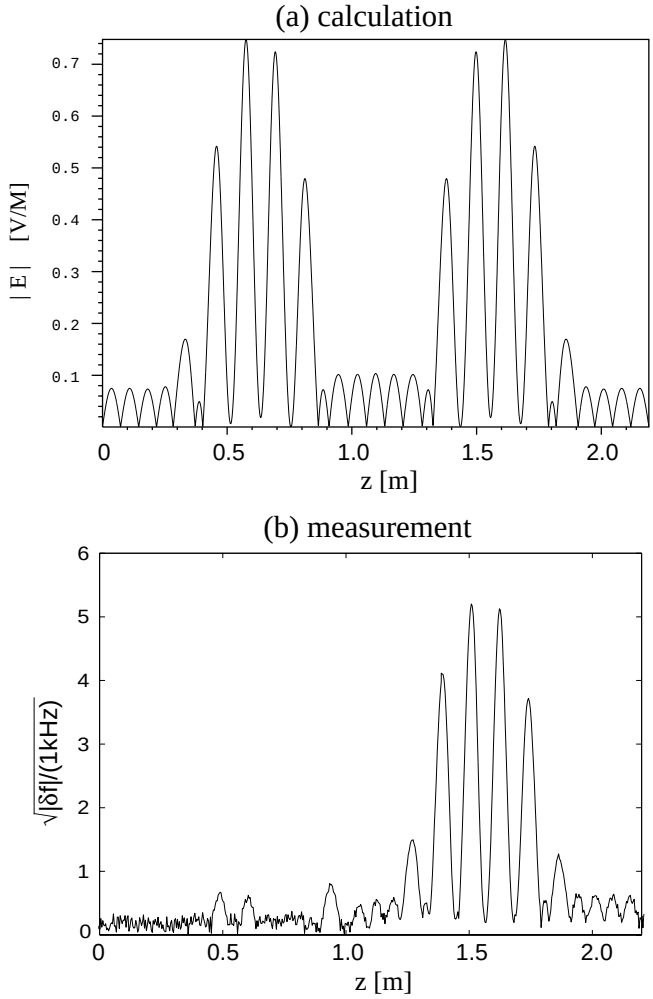

Figure 9.4: 2×7-cell superstructure: On-axis electric field profile of a TE-like dipole mode with high (R_d/Q_0) ($f = 2.574$ GHz, $(R_d/Q_0) \leq 13.1\ \Omega/\mathrm{cm}^2$). (a) MAFIA calculation of the electric field profile [Che 00]. (b) Bead pull result for one polarisation of the dipole mode, measured on the copper model.

In the next step the quality factors of the HOMs have been studied. In the superconducting state, the HOMs can have very high quality factors in the order of $Q_0 \approx 10^{10}$ and damping by HOM couplers is essential to fulfill the requirements on damping. These couplers are mounted close to the end-cells of the cavity, see for example figure 4.2. The HOM couplers in the TTF 9-cell cavities couple to the electric and magnetic field. A 1.3 GHz notch filter supresses energy extraction from the accelerating mode ($Q_{ext} > 10^{11}$). The extracted average power from the fundamental mode is well below 1 W during high gradient pulsed cavity operation at 25 MV/m [Sek 93]. In order to get an estimation on the HOM damping in the superstructures, the copper versions have been equipped with HOM couplers, which are similar to the welded HOM coupler version of the 9-cell cavities [Sek 93]. The antenna tip was lengthened by 5 mm to increase the coupling to the electric field.

Figure 9.5 shows a copper version of the HOM pick-up antenna with a coupling loop for the magnetic field and an antenna tip for the electric field. The field energy is extracted via a coaxial cable connected to a 50 Ω load. Note that the HOM cou-

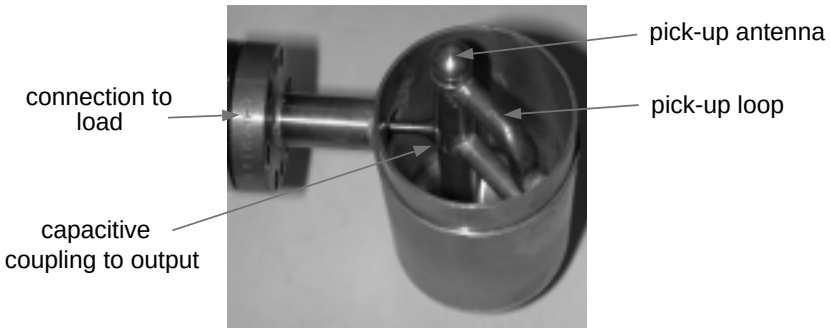

Figure 9.5: Copper version of the HOM coupler, which has been used in the damping measurements. This coupler is based on the welded HOM coupler version of the TTF 9-cell cavities [Sek 93]. The antenna tip is lengthened by 5 mm to increase the coupling to the electric field.

plers of the niobium cavities are also made from niobium to minimize losses at the 2 K level. The copper superstructures are equipped with one HOM coupler at each end-tube and at each interconnection tube, see also figure 4.6 and 4.8. Each inner coupler damps the fields from two neighbouring cavities. Accordingly the 2×7-cell copper structure has a total number of three HOM dampers, wheras the 4×7-cell copper structure is equipped with five HOM couplers. The damping scheme with couplers at the interconnection tubes is one of the major benefits of the superstructure concept.

The damping by the HOM-couplers has been measured on the copper structures for monopole and dipole modes. In a superconducting cavity usually the losses are dominated by the external losses due to the couplers, i.e $Q_L^{(m)} \approx Q_{ext}^{(m)}$. Accordingly in the following the external quality factors $Q_{ext}^{(m)}$ of the HOMs will be discussed.

Monopole modes:

The measured external quality factors of TM_{011} modes with high (R_{sh}/Q_0) values are listed in table 9.1 and table 9.3 for the 2×7-cell copper structure and the 4×7-cell structure, respectively. The monopole modes are well damped. The $Q_{ext}^{(m)}$ values of the modes with the strongest coupling to the beam stay below $5 \cdot 10^4$. As is discussed in section 9.3, this ensures that not more than a few watts of average power will be coupled out in pulsed cavity operation with the nominal TESLA beam current of 9.5 mA.

Dipole modes:

The measured external quality factors for the dipole modes with high (R_d/Q_0) values are given in the tables 9.2 and 9.4. The values for both polarisations are listed. The measured values for modes with $(R_d/Q_0) > 0.1\ \Omega/\mathrm{cm}^2$ are shown in the figures 9.6 (b) and 9.7 (b) for the 2×7-cell structure and the 4×7-cell structure, respectivly. As can be seen, most of the modes are damped much stronger than needed. This relaxes the damping level required for modes with lower damping. Only a few

modes have Q_{ext} values above $2 \cdot 10^5$, but these modes have low (R_d/Q_0) values below 1 Ω/cm^2. The resulting impedance $Q_L^{(m)} \cdot (R_d/Q_0)^{(m)}$. values of the dipole modes are shown in figures 9.6 (c) and 9.7 (c). Note that the total impedance of all modes is dominated by a few modes, which are also damped sufficiently.

It is important to understand, that the presented measurements can only give an estimation on the HOM damping in the superstructures. The copper model measurements indicate that the used damping scheme fulfills the overall HOM damping requirements for the TESLA collider. However, the individual external quality factors of the modes depend on the exact shape of the accelerating structure and on the boundary conditions at the end of the structure. Accordingly the external quality factors will fluctuate from structure to structure. This has recently been observed for the 9-cell cavities of the TESLA-Test-Facility linac [Bab 01, Mag 01]. Two 2×7-cell niobium superstructures are under construction and will be installed in the TTF linac in 2002, see chapter 10. We plan to repeat the beam-based HOM measurements for these structures to confirm that the overall mode damping is sufficient, and to gain more experience.

The HOM damping in the 2×9-cell superstructure has not been studied yet. A copper version of this structure will be aviable soon for HOM measurements. Results similar to those of the 2×7-cell structure can be expected. Further we envision to perform also beam-based HOM measurements on 2×9-cell superstructures.

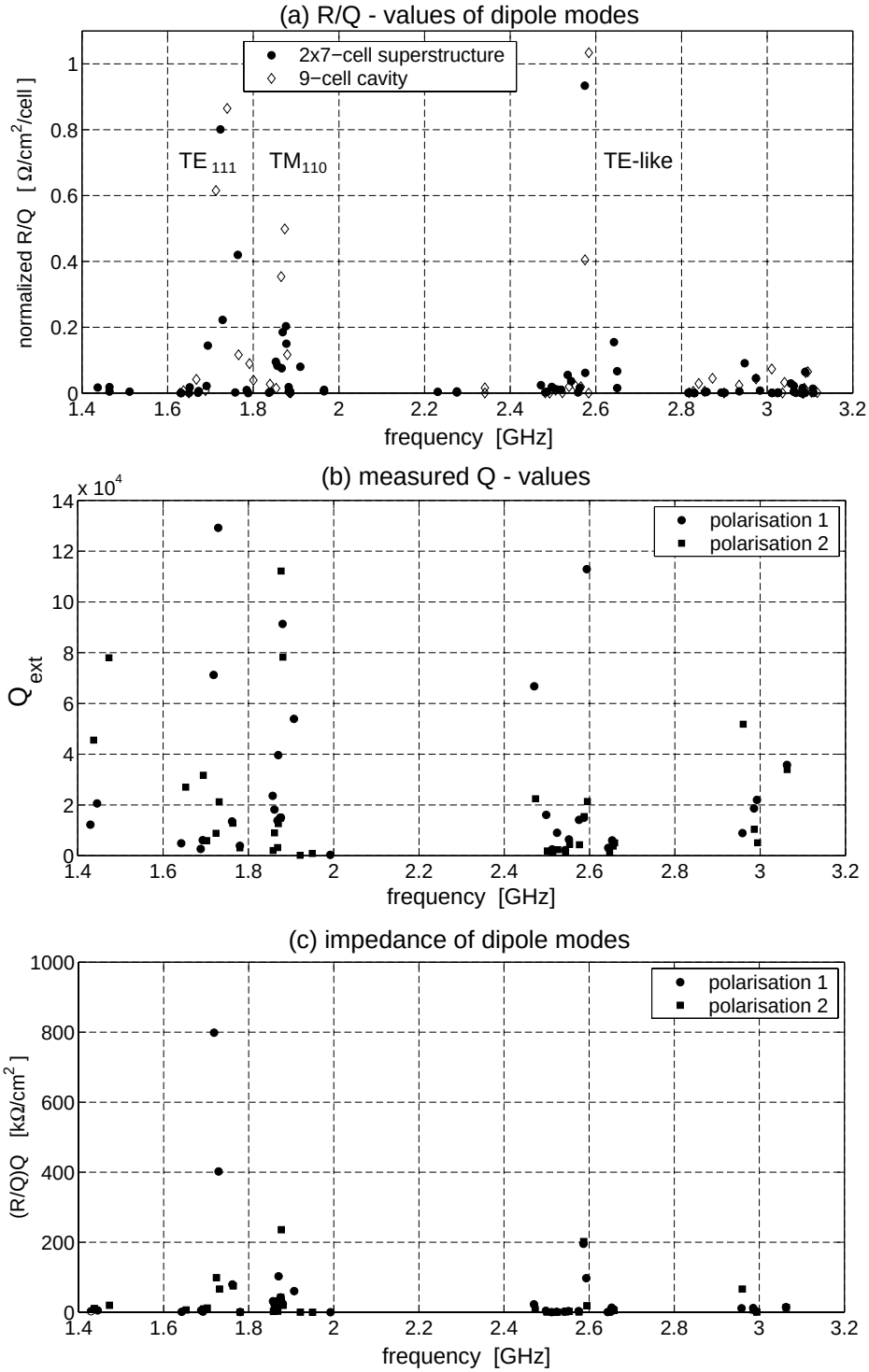

Figure 9.6: Dipole mode parameters of a 2×7-cell superstructure. (a) Computed (R_d/Q_0) values for dipole modes of a 2×7-cell structure ([Che 00]) and a TTF 9-cell cavity ([Wan 01]), normalized to the number of cells per structure. The values are shown as a function of the calculated eigenfrequencies. (b) External quality factors Q_{ext} of dipole modes with $(R_d/Q_0) > 0.1\ \Omega/\mathrm{cm}^2$, as measured on the copper 2×7-cell structure. The values for both polarisations of the dipole modes are shown as function of the measured eigenfrequencies. (c) Resulting impedance values $(R_d/Q_0) \cdot Q_{ext}$ for the 2×7-cell structure versus measured frequency.

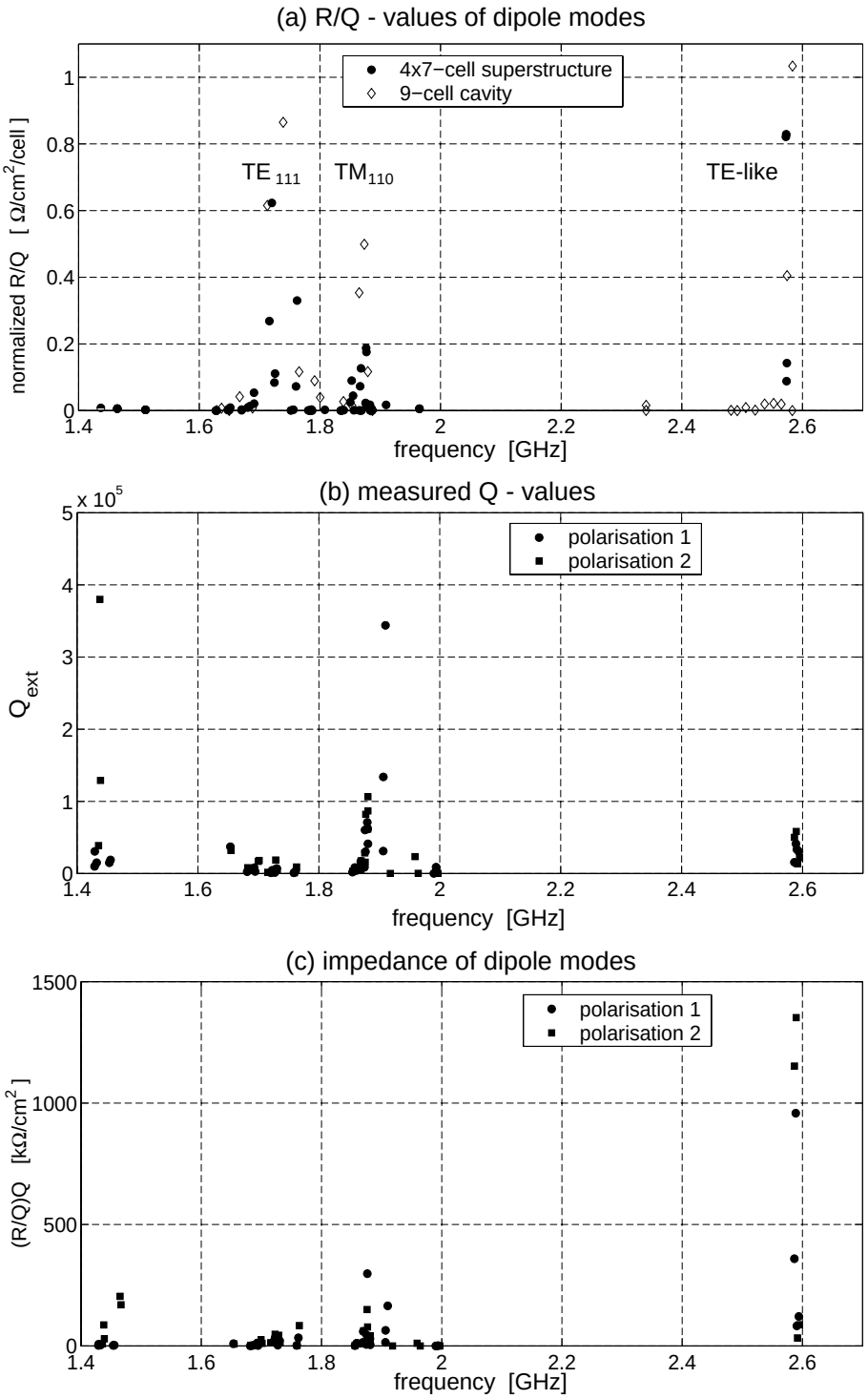

Figure 9.7: Dipole mode parameters of a 4×7-cell superstructure. (a) Computed (R_d/Q_0) values for dipole modes of a 4×7-cell structure ([Che 00]) and a TTF 9-cell cavity ([Wan 01]), normalized to the number of cells per structure. The values are shown as function of the calculated eigenfrequencies. Above 2 GHz, only selected modes with high impedance are shown. (b) External quality factors Q_{ext} of dipole modes with $(R_d/Q_0) > 0.1\ \Omega/\mathrm{cm}^2$, as measured on the copper 4×7-cell structure. The values for both polarisations of the dipole modes are shown as a function of the measured eigenfrequencies. Above 2 GHz, only selected modes with high impedance have been measured. (c) Resulting impedance values $(R_d/Q_0) \cdot Q_{ext}$ for the 4×7-cell structure versus measured frequency.

9.5 Tuning of HOM Frequencies

Measurements on the TESLA 9-cell cavities have shown an rms frequency spread of the higher-order modes in the order of a few 10^{-3} [Bab 01], which is caused by small cavity fabrication errors. This natural frequency spread turns out to be an advantage for the beam dynamics, since the effective long-range wakefield of the HOMs is reduced by averaging over many cavities [TDR 01]. Without frequency spread the long-range wakefields would add coherently along the linac. For normal conducting RF structures a artificial cell-to-cell detuning for the HOMs is therefore needed [Bab 01], while for the superconducting cavities a cavity-to-cavity frequency variation is naturally given. However, the frequency variation also means, that by chance a dipole mode can be excited resonantely in a cavity. If the (R_d/Q_0)-value and the quality factor are high for this mode, it will locally give a strong transverse kick to the beam. Sufficient HOM damping has to keep these kicks within acceptable limits.

These considerations are also valid for the superstructures. However, a special feature of the superstructures provides -at least in principle- additional safty: The frequencies of some higher-order modes can be adjusted (within several kHz) during linac operation. The reason for this is the possibility to tune the cavities of a superstructure individually. To illustrate the HOM frequency adjustment, we consider a 2×7-cell superstructure and assume that a given dipole mode has a high quality factor and is resonantly excited by the beam. If now the fundamental mode frequency of the first cavity is lowered by a few kHz, and the frequency of the second cavity is correspondingly increased, the two frequency shifts chancel for the accelerating mode and the field homogeneity is only slightly reduced (see figure 5.21). Suppose the considered dipole mode with high quality factor has an unbalanced stored energy in the two cavities of the superstructure, then the two tuning steps will not cancel for this mode (see also equation (6.20)). For example the dipole mode shown in figure 9.4 is sensitive to tuning the second cavity, but its frequency is nearly unchanged, if the first cavity is tuned. Obviously the HOM frequency tuning procedure is most effective for modes, which have strongly unbalanced stored energies in the individual cavities. This is usually the case for modes, which have low fields in the interconnecting tubes (small cavity-to-cavity coupling). These modes have also low fields at the HOM-couplers at the interconnecting tubes, thus the quality factors might become high and a resonant excitation could be harmful for the beam.

Note that the maximum range of frequency adjustment for a HOM depends on the sensitivity of the frequency to a cavity length change, on the distribution of the stored energy and on the tolerable inhomogeneity of the accelerating mode. Measurements on the copper superstructures have shown, that frequency shifts up to several kHz are feasible for many modes, which are almost trapped.

10 A 2x7-cell Niobium Prototype Superstructure

For a final proof of principle of the superstructure concept a beam measurement is required. Therefore two 2×7-cell prototype superstructures are in preparation for a beam test. This test is scheduled for beginning of 2002 and will be the first test of a coupled-cavity standing-wave structure. A cryomodule housing two superconducting 2×7-cell prototypes will be installed in the linac at the TESLA-Test-Facility.

10.1 Construction of the Prototype

The layout of the prototype superstructure module is presented in chapter 4, see particularly figure 4.6 and table 4.2. In summary, each of the two 2×7-cell superstructures will be equipped with one input coupler, three HOM-couplers (one at each end tube and one at the interconnecting tube), two frequency tuning systems (one for each cavity) and four pick-up antennas near the end-cells.
In order to achieve a short schedule of the prototype construction, several existing components of the 9-cell cavities have been adapted for the superstructure test. In the following we will briefly discuss the main components of the prototype module with two 2×7-cell structures.

Cavities

Four 7-cell niobium cavities (plus two spare cavities) have been fabricated similar to the TESLA 9-cell cavities by deep drawing and electron-beam welding [TDR 01], see figure 10.1. After the removal of the damage layer on the inner cavity surface, the cavities were annealed at 800°C to out-gas dissolved hydrogen and to relieve mechanical stress. Subsequently to these major fabrication steps, which may perturb the cell geometry, the cell frequencies have been tuned for a homogenious amplitude profile of the accelerating mode using special end-cups at the beam tubes. The end-cups simulate a complete superstructure by matching the RF boundary conditions at the cavity end-tubes. This pre-tuning and the proper functioning of the end-cups has been verified by joining two 7-cell cavities by a flange connection. The assembled 2×7-cell prototype superstructure with a $\lambda/2$ interconnecting tube is shown in figure 10.2. Refer to chapter 6 for a detailed discussion of this tuning procedure. We believe that the subsequent preparation steps will preserve the amplitude homogeneity. Future measurements have to confirm this assumption.
After a light surface removal by chemistry the cleaned 7-cell cavities will be tested

Figure 10.1: Niobium 7-cell cavities for the 2 × 7-cell prototype superstructure.

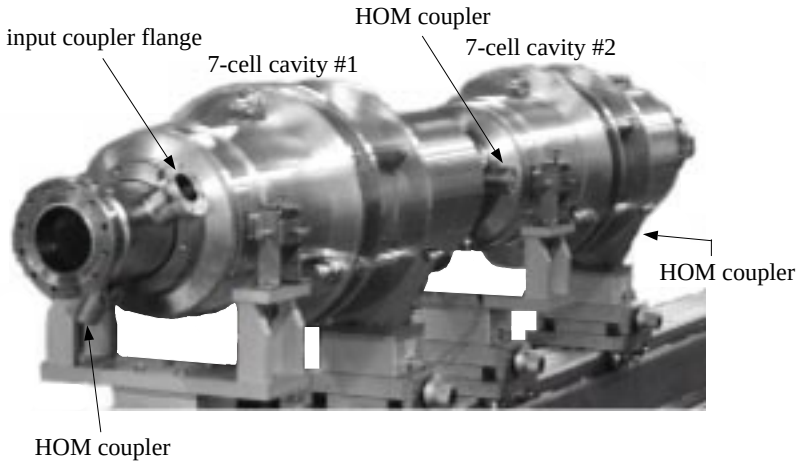

Figure 10.2: Niobium 2 × 7-cell prototype superstructure. The two cavities are joined by a flange connection for field profile measurements. Before installation in the cryomodule, the cavities will be connected by an electron-beam weld.

in cw-mode to investigate their field performance for quality control. The existing cw-test cryostats constructed for the 9-cell cavities can be used without modifications. This would not be the case for a whole 2 × 7-cell structure due to its length of 2.08 m. Therefore we decided to test the cavities before joining them. Note that this will be not necessary for the superstructure cavities of the TESLA collider, since a larger test cryostat will be built.
After the performance test the cavities are welded into their liquid helium container. Finally the 7-cell cavities will be connected by electron-beam welding to build two 2 × 7-cell superstructures. The prototypes will get a final light chemistry and water rinsing before mounting them to the cryomodule.

Input coupler

The TTF input couplers are based on a 70 Ω coaxial line with 40 mm diameter. The latest version (called TTF type III, [Moe 99]) has demonstrated a power capa-

bility of more than 1 MW [Moe 01], thus providing a sufficient performance for the prototype superstructures.
For future superstructures the diameter of the cold coupler section will be increased from 40 mm to 60 mm [TDR 01]. Since the multipacting levels are shifted with the fourth power of the diameter ($P_{mp} \propto d^4$, [Cou 99]) and become weaker at higher power, the increased diameter provides an additional safty margin for the operation at high gradients.

HOM coupler

In order to reduce the effort for the construction of the Nb prototypes, the existing welded HOM coupler version [Sek 93] of the TESLA 9-cell cavities is used for the 2×7-cell superstructures. Its antenna loop couples to the electric and magnetic field with a rejection filter at 1.3 GHz. For the 2×7-cell superstructures the antenna tip of the HOM coupler is lengthened by 5 mm to provide a sufficient damping of the higher-order-modes, see chapter 9.

Frequency tuner

The reduced distance between two cavities in a superstructure leaves no space for the present frequency tuner of the TESLA 9-cell cavities [CDR 97], since this tuner is placed at the interconnecting tube. Therefore a new tuner design has been developed [Kai 99, Pet 01]. The principle of this tuner is to change the length of the LHe container and thereby to adjust the cavity frequency. The container is made of two tubes, which are joined at the center via a bellow. The opposite side of the tubes is connected to the beam tubes of the cavity.
Recently a protytpe of this new tuner (see figure 10.3) has been tested successfully at cryogenic temperatures. An improved version will be used for the two 2×7-cell superstructures. One tuner will be equipped with piezoelements to test a fast frequency adjustment, see chapter 3.

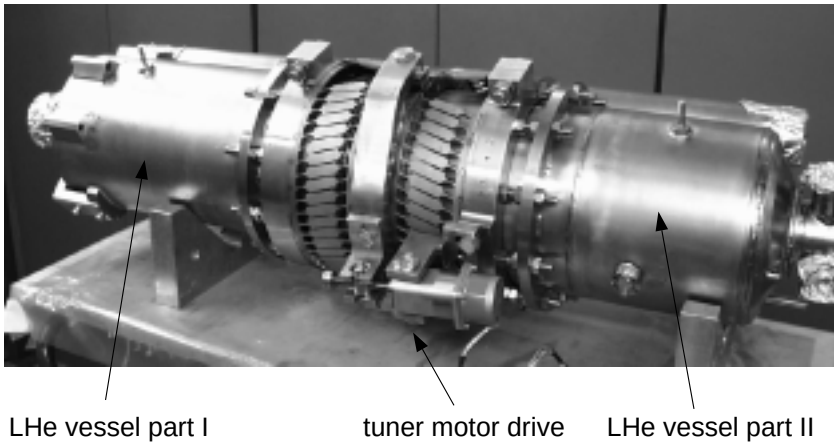

Figure 10.3: Prototype tuner for superstructure cavities (design by H. B. Peters and H. Kaiser, DESY). The two vessel parts are joint via a bellow. The tuning system is changing the distance between the two parts.

Cryostat

Since the cryostat for the cavities is an expensive component, we adapted the cryostat of a future TTF cavity module for the superstructure test. After the test, this cryostat will be equipped with eight TESLA 9-cell cavities and will serve as a spare module for the TTF linac. The two cavities of a 2×7-cell superstructure have a fixed spacing. Accordingly tuning one cavity will change the length of the whole superstructure. Therefore in the cryostat the cavities will be mounted on sliding supports with low friction. Each structure has a fix point in the cryostat at the input coupler position.

10.2 Measurement Program

The beam test at the TESLA-Test-Facility will allow us to study in a full system test all aspects related to the concept of coupling cavities. The cryomodule with the two superstructures will be located directly behind the RF photo-cathode gun, replacing an existing module with eight 9-cell cavities, see figure 10.4. This position has the

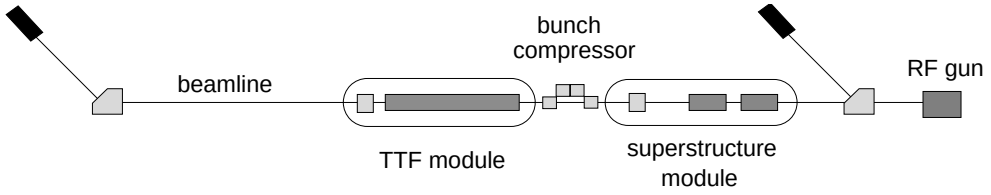

Figure 10.4: Layout of the TTF linac during test of the prototype superstructure (not to scale). The first cryomodule will house two 2×7-cell prototype superstructures, whereas the second module is equipped with eight 9-cell cavities. Both modules have superconducting magnets at the beam-exit side.

advantage of a low beam energy (a few MeV), thus providing a high sensitivity in measuring the excitation of higher-order-modes and their impact on the beam.
In the full system test of the superconducting 2×7-cell structures we will be able

- to check the frequency spectrum of monopole and dipole modes and their loaded quality factor,
- to test the methods proposed to equalize the fields in the two cavities per superstructure at cryogenic temperatures in the linac, see chapter 6,
- to find field limitations of the cavities or HOM-couplers,
- to test the proposed modified RF field control system, and
- to test the new frequency tuner design.

Moreover based on beam measurements (see for example [Mag 01]) we can

- confirm the refilling of all cells between the bunches and verify the predicted low bunch-to-bunch energy spread,

- measure the energy deposition in monopole modes, and
- investigate the damping of deflecting dipole modes and estimate their impedance.

This measurements will also help us to verify the computations and the measurements on room temperature models of the superstructure.

CHAPTER 11

11 Summary and Outlook

The superconducting technology for a linear collider with a center-of-mass energy well above 500 GeV is in progress. Beside of a cavity surface preparation by electrolytic polishing, a fast resonance frequency control within the RF pulses and the superstructure concept of coupled cavities are considered as two important steps towards 800 GeV.
The initial experiments with a fast piezoelectric tuner have demonstrated a successful control of the cavity resonance frequency during pulsed cavity operation. This Lorentz-force detuning cancellation permits an efficient cavity operation at the TESLA-800 accelerating gradient of 35 MV/m. Moreover the piezoelectric tuner has shown to be a valuable tool to study the mechanical modes of a multicell cavity and their excitation in pulsed cavity operation. In the near future detailed investigations are planned to verify the reliability of the fast tuner and to increase our knowledge of the mechanical behavior of cavities during pulsed operation. We envision to extend the resonance frequency control to microphonics detuning, which would be especially valuable for superconducting linacs with a low average beam current, i.e. small cavity bandwidth, as they are proposed for rare isotope accelerators [Kel 01, Gri 01] and for new light sources [Gru 00].
In 1998 a structure of coupled multicell cavities (superstructure) has been proposed for the TESLA collider [Sek 99]. Since then different types of superstructures have been investigated in detail. In this structures the HOM damping as well as the field homogeneity of the accelerating mode are handled at the cavity sub-unit level, since HOM couplers are located at the interconnecting beam tubes and each cavity is equipped with its own frequency tuning system. This is the essential advantage of these structures, as compared to standard multicell cavity. Two types of superstructures have been proposed for the TESLA main linacs: the first one consisting of four 7-cell cavities, and more recently, a 2×9-cell structure. Building the TESLA collider with these superstructures instead of 9-cell cavities increases the active acceleration length by about 6 % and reduces the number of main power couplers in the machine by a factor of 2-3. The studies presented in this dissertation indicate the operability of these structure types and furthermore the fulfillment of the requirements for the TESLA collider. This includes

- the amplitude profile measurement of the accelerating mode and its tuning,
- the bunch-to-bunch energy variation due to excited TM_{010} modes,
- the RF field control,

- the higher-order mode damping.

For the amplitude profile adjustment at room temperature as well as for its optimization during linac operation new concepts have been developed and successfully tested on copper superstructures. Based on obtained results and because of its favorable length the 2×9-cell superstructure appears most attractive and is expected to become the referred layout of the TESLA collider.
For a first full system test of a superstructure with beam two 2×7-cell niobium prototypes are presently under construction and will be installed in the linac at TESLA-Test-Facility. Further we envision a similar test for the 2×9-cell structures to gain more experience. It is believed, that the combination of the superstructure concept with a surface preparation by electrolytic polishing and a fast piezoelectric tuner will provide the technology for an 800 GeV superconducting linear collider [TDR 01].

Bibliography

[Bab 01] N. I. Baboi et al.,
Studies on Higher Order Modes in Accelerating Structures for Linear Colliders,
PhD thesis, Hamburg University, (2001).

[Ban 99] R. Bandelmann, et al.,
Nb Prototype of the Superstructure for the TESLA Linear Collider,
in *Proc. of the 9th Workshop on RF Superconductivity*, Santa Fe, USA, (1999).

[Bat 75] S. Battisti et al.,
Radiation Damage to Electronic Components, CERN Report, CERN 75-18, Geneva, (1975).

[Bev 64] R. M. Bevensee,
Electromagnetic Slow Wave Systems,
John Wiley and Sons, New York, (1964).

[Bou 99] S. Bousson,
Advances in Superconducting RF Cavity Stiffening by Thermal Spraying,
in *Proc. of the 9th Workshop on RF Superconductivity*, Santa Fe, USA, (1999).

[Bro 89] I. N. Bronstein, K. A. Semendjajew,
Taschenbuch der Mathematik, B. G. Teubner Verlagsgesellschaft, Leipzig, 24th edition, (1989).

[CDR 97] *Conceptual Design Report of a 500 GeV e^+e^- Linear Collider with Integrated X-ray Laser Facility*,
Editors R. Brinkmann, G. Materlik, J. Rossbach, A. Wagner,
DESY 1997-048, ECFA 1997-182, (1997).

[Che 00] H. Chen (Tsinghua University, Beijing),
private communication.

[Cou 99] *Coupler Workshop at DESY, April 26-27 1999*,
Editor D. Proch, TESLA-Report, TESLA 99-10, (1999).

[Doh 98] M. Dohlus et al.,
Filling and Beam Loading in TESLA Superstructures,
TESLA-Report, TESLA 98-14, (1998).

[Fer 96] M. Ferrario et al.,
Multi-Bunch Energy Spread Induced by Beam Loading in a Standing Wave Structure,
Particle Accelerators, Vol. 52, p. 1-30, (1996).

[Gri 01] T. Grimm et al.,
Superconducting RF Activities at NSCL,
in *Proc. of the 10th Workshop on RF Superconductivity*, Tsukuba, Japan, (2001), to be published.

[Gru 00] S. Gruner, D. Bilderback, M. Tigner,
Synchrotron Radiation Sources for the Future,
White paper, http://erl.chess.cornell.edu/Papers/Papers.htm, (2000).

[Hae 92] E. Häbel, A. Mosnier, J. Sekutowicz,
Cavity Shape Optimization for Superconducting Linear Colliders,
in *Proc. of HEACC 92*, Hamburg, Germany, (1992).

[Jack 75] J. D. Jackson,
Classical Electrodynamics,
Wiley, New York, 2nd edition, (1975).

[Kai 99] H. Kaiser,
New Approches to Tuning the TESLA Resonator,
in *Proc. of the 9th Workshop on RF Superconductivity*, Santa Fe, USA, (1999).

[Kel 01] M. P. Kelly,
Superconducting RF Activities at the Argonne National Lab,
in *Proc. of the 10th Workshop on RF Superconductivity*, Tsukuba, Japan, (2001), to be published.

[Kla 86] R. Klatt et al.,
MAFIA - A Three Dimensional Electromagnetic CAD System for Magnets, RF Structures and Transient Wake-Field Calculations,
in *Proc. of Linear Accelerator Conference*, Stanford, USA, (1986).

[Kop 93] K. Kopittzki,
Einführung in die Festkörperphysik,
3rd edition, B. G. Teubner Verlag, Stuttgart, (1993).

[Kre 01] G. Kreps (DESY, Hamburg),
private communication.

[Lau 87] U. Lauströer et al.,
URMEL and URMEL-T User Guide (Modal Analysis of Cylindrically Symmetric Cavities; Evaluation of RF-Fields in Waveguides), (1987).

[Leu 01] A. Leuschner (DESY, Hamburg),
private communication.

[Lie 98] M. Liepe and S. N. Simrock,
Adaptive Feed Forward for the Digital RF Control System at the TESLA Test Facility,
in *Proc. of the 1998 European Particle Accelerator Conference*, Stockholm, Sweden, p. 1735, (1998).

[Lil 01] L. Lilje,
Experimantal Investigations on Superconducting Niobium Cavities at Highest Radiofrequency Fields,
PhD thesis, Hamburg University, DESY-Thesis 2001-034, (2001).

[Lun 97] J. Lunze,
Regelungstechnik 2,
Springer Verlag, Berlin Heidelberg, (1997).

[Mag 01] C. Magne et al.,
Measurements with Beam of the Deflecting Higher Order Modes in the TTF Superconducting Cavities,
in *Proc. of the PAC 2001*, Chicago, USA, (2001), to be published.

[Mai 52] L. Maier, J. Slater,
Fields Strength Measurements in Resonant Cavities,
in *Journal of Applied Physics*, Vol. 23, No. 1, (1952).

[Men 87] M. T. Menzel, H. K. Stokes,
User's Guide for the POISSON/SUPERFISH Group of Codes,
Accelerator Theorie and Simulatoin Group, AT-6, Los Alamos National Laboratory, LA-UR-87-115, Los Alamos, (1987).

[Min 01] S. Michizono, M. Liepe, S. N. Simrock,
Design of Low Level RF Control for the TESLA Superstructure,
in *Proc. of the 2001 Particle Accelerator Conference*, Chicago, (2001), to be published.

[Moe 99] W. D. Möller,
High Power Coupler for the TESLA Test Facility,
in *Proc. of the 9th Workshop on RF Superconductivity*, Santa Fe, USA, (1999).

[Moe 01] W. D. Möller (DESY, Hamburg),
private communication.

[Nag 67] D. Nagel, E. Knapp, B. Knapp,
Coupled Resonant Model for Standing Wave Accelerator Tanks,
Rev. of Sci. Instrum. 38, number 11, (1967).

[Nov 98] A. Novokhatski, A. Mosnier,
Wakefield Dynamics in Quasi Periodic Structures,
IEEE Press, (1998).

[Pad 98] H. Padamsee, J. Knobloch, T. Hays,
RF Superconductivity for Accelerators,
John Wiley and Sons, New York, (1998).

[Pet 01] H. B. Peters (DESY, Hamburg),
private communication.

[PI 01] *Theory and Applications of Piezo Actuators and PZT Nano-Positioning Systems*,
Physik Instrumente, http://www.physikinstrumente.com/tutorial/index.html,
(September 2001).

[PM 01] *Piezo Stack and Ring Actuators Catalogue: Comments on Technical Data*,
PIEZOMECHANIK GmbH, http://www.piezomechanik.com/p_14b.htm,
(September 2001).

[Schi 98] T. Schilcher,
Vecor-sum Control of Pulsed Accelerating Fields in Lorentz-Force Detuned Superconducting Cavities,
TESLA-Report, TESLA 98-05, (1998).

[Sek 90] J. Sekutowicz, et al.,
A Different Tuning Methode for Accelerating Cavities,
in *Proc. of the 4th Workshop on RF Superconductivity*, Tsukuba, Japan, (1990).

[Sek 93] J. Sekutowicz,
Higher Order Mode Coupler for TESLA,
in *Proc. of the 6th Workshop on RF Superconductivity*, Newport News, USA, (1993).

[Sek 94] J. Sekutowicz,
2D FEM Code with Third Order Approximation for RF Cavity Computation,
in *Proc. of the LINAC 94*, Tsukuba, Japan, (1994).

[Sek 98] J. Sekutowicz, M. Ferrario, C. Tang,
Superconducting Superstructure for the TESLA collider,
TESLA Report, TESLA 98-08, (1998).

[Sek 99] J. Sekutowicz, M. Ferrario, C. Tang,
Superconducting Superstructure for the TESLA collider: A Concept,
Phys. Ref. ST Accelerators and Beams 2:062001, (1999).

[Sek 00] J. Sekutowicz (DESY, Hamburg),
private communication.

[Sek 01] J. Sekutowicz et al.,
Status of the Superstructure,
in *Proc. of the 10th Workshop on RF Superconductivity*, Tsukuba, Japan, (2001), to be published.

[Sim 01] S. N. Simrock (DESY, Hamburg),
private communication.

[Sla 50] J. C. Slater,
Microwave Electronics ,
D. Van Nostrand Company, Princeton, (1950).

[TDR 01] *TESLA Technical Design Report Part II: The Accelerator*,
Editors R. Brinkmann, K. Flöttmann, J. Rossbach, P. Schmüser, N. Walker, H. Weise, DESY 2001-011, ECFA 2001-209, (2001).

[TTF 95] *TESLA Test Facility Design Report*,
Editor D. A. Edwards, TESLA-Report, TESLA 95-01, (1995).

[Wan 01] R. Wanzenberg (DESY, Hamburg),
private communication.

[Zick 96] B. Zickgraf,
Ermüdungsverhalten von Multilayer-Aktoren aus Piezokeramik,
VDI Verlag, Düsseldorf, (1996).

[Zot 79] B. Zotter, K. Bane,
Transverse Resonances of Periodically Widened Cylindrical Tubes with Circular Cross Section,
Technical Report, SLAC/PEP-Note 308, (1979).

List of Figures

List of Tables